Thermal Dehydroxylation Kinetics and Investigation of Factors Affecting the Dehydroxylation of Serpentine Minerals to Improve CO_2 Sequestration through Mineral Carbonation

Sana Zahid, BSc (Hons), MSc

This thesis is presented for the degree of

Doctor of Philosophy

Murdoch University

Geochemistry and Mineral Sciences, Murdoch University, 90 South Street,

Murdoch, WA 6150, Australia

2020

Declaration

I hereby declare that the material embodied in this thesis is the result of original research and contains as its main content work that has not previously been submitted for a degree or diploma at any tertiary education institution. To the best of my knowledge and belief, this thesis is the result of original research. It contains no material previously published or written by another person, except where due reference has been made in the text.

Signature: Date: 27/01/2021

Sana Zahid

Supervisory Statement

We, the undersigned, attest that Higher Research Degree candidate, Sana Zahid, has performed all the experiments, analysed data and has written all papers included in this thesis. Dr Hans C. Oskierski, Professor Bogdan Z. Dlugogorski, Assoc Prof Gamini Senanayake and Assoc Prof Mohammednoor Altarawneh provided the necessary advice on experimental program, project direction and assisted with the editing of the papers, consistent with normal supervisors-candidate relations.

Dr Hans C. Oskierski Date: 28/01/2021

Professor Bogdan Z. Dlugogorski Date: 28/01/2021

Assoc Prof Gamini Senanayake Date: 28/01/2021

Assoc Prof Mohammednoor Altarawneh Date: 31/01/2021

Dedication

I would like to dedicate my thesis to my beloved parents; Zahid Iqbal (deceased) and Shahnaz Begum, my husband (Jalil Ahmed) and my Son (Qawi Ahmed)

Acknowledgements

All praise belongs to Almighty Allah, the only real creator and owner of everything. All respects are for His Holy Prophet Mohammed (PBUH), whose teachings are a true source of acquaintance and guidance for the whole of humanity.

First and foremost, I would like to thank Allah, who has given me the courage and strength throughout my research work and helped me at all moments of my life. I am very thankful to my family for motivating me and for being a source of moral support to complete my research.

This research work reflects the support of many kind people around me. Firstly, I would like to express my profound gratitude to my supervisors, Dr Hans C. Oskierski, Professor Bogdan Z. Dlugogorski, Assoc Prof Gamini Senanayake, Assoc Prof Mohammednoor Altarawneh and Dr Helen E. A. Brand for their encouragement, valuable advice, and their continuous support during my doctoral study. Their mentorship, understanding, motivation and valuable comments have played a vital role in completing the present research. Special thanks to Professor Bogdan Dlugogorski and Dr Hans Oskierski for their ideas, time patience, and enormous support during my PhD.

I am grateful to Murdoch University for the award of a Murdoch International Postgraduate Scholarship (MIPS) and acknowledges the Australian Institute of Nuclear Science (AINSE) Limited for providing a Postgraduate Research Award (PGRA), which provided valuable financial support and access to the Australian synchrotron facilities for this research. Part of this work was carried out on the powder diffraction beamline at the Australian Synchrotron,

ANSTO, under Proposal ID 13048 and 10844. I express my profound gratitude for my co-supervisor at ANSTO, Dr Helen E A Brand for supporting the above grants and providing access to the PXRD beamline at the Australian synchrotron under her supervision.

Special thanks to all administrative staff at Murdoch University, especially Dr Juita, Dr Ibukun Oluwoye, Mr Kris Parker, Mr Andrew Foreman, Mr Kenneth Seymour, Mr Stewart Kelly, Dr Marc Hampton, and Dr Fang Xia for their professional and technical assistance. I acknowledge my gratitude for my fellow students and staff of Fire Safety and Combustion Kinetics Research Laboratory, Dr Juita, Dr Ibukun Oluwoye, Dr Jakub Skut, Dr Anam Saeed, Dr Sidra Jabeen, Ms Saleha Qudsia, Dr Kamal Siddique, Dr Zhe Zeng, Dr Nassim Zeinali, Dr Arif Abdullah, Mr Thamsanqa Ncube, Ms Kanwal Shabbir, Ms Kudzai Angeline Mchibwa, Mr Goruck Soban, Dr Jomana Al-Nu'airat, Dr Alaa Kamaluldeen, Mr Mahmoud Alhadad, Mr James Mulwanda, Mr. Johannes Chischi and Mr Elie Kabende. They have been a source of insightful discussions that helped me in my project and taught me the virtues of teamwork.

My heartiest acknowledgment goes to my beloved mother (Shahnaz Begum) and my sisters (Adeela, Nabeela, Rabia and Saba) for their unconditional love, encouragement, and support throughout my life. I am also very grateful to all my relatives and in-laws for their prayers and encouragements. I express my immense thanks to my husband, Jalil Ahmed, for his unconditional encouragement and support throughout my PhD journey. Last but not least, my Son (Qawi Ahmed) for his prayers, patience and understanding. Enormous thanks are due to all my friends who encouraged me to fulfil this project. I thank you all.

Abstract

Thermal dehydroxylation of serpentine minerals ($Mg_3Si_2O_5(OH)_4$) is a crucial step for mineral carbonation, a promising technique for the safe and permanent disposal of CO_2 emissions. Thermal dehydroxylation enhances the dissolution kinetics of these minerals through amorphisation of mineral structure but at the expense of an additional energy penalty. Therefore, this thesis aims to generate an in-depth understanding of structural changes and dehydroxylation kinetics under different heat-treatment conditions to provide an energy-efficient solution for the commercialisation of mineral carbonation.

Isoconversional kinetic analysis based on thermogravimetric (TGA) and differential scanning calorimetric (DSC) analyses demonstrate the multistep nature of antigorite dehydroxylation, with activation energies (E_α) varying between 290 and 515 kJ mol^{-1}. The high resolution, *in-situ* synchrotron powder X-ray diffraction (PXRD) for the first time enables the identification of two amorphous metaserpentine components (α and β) along with minor semi-crystalline chlorite-like γ-metaserpentine formation during antigorite dehydroxylation. The amorphous α and β-metaserpentine components originate simultaneously and then transform to forsterite and enstatite, respectively, and chlorite-like formation reveals an additional reaction pathway for the Al_2O_3-rich antigorite dehydroxylation process. The combination of TGA-DSC-based kinetics and PXRD data illustrates that only ~49% dehydroxylation of Al-rich antigorite can be achieved before forming less-reactive forsterite and E_α increase.

The effect of the partial pressure of water vapours (P_{H2O}), grain size, and mineralogy on the structural changes during dehydroxylation of serpentine minerals by *in-situ* synchrotron PXRD illustrates that the lizardite is a more suitable feedstock for mineral carbonation compared to antigorite because it: a) produces almost all amorphous content before forsterite formation; b) yields 2-3 times higher amorphous content than antigorite; and, c) reduces the

energy requirements to nearly half due to high amorphous production and a lower dehydroxylation temperature. In particular, low P_{H2O} and small-sized lizardite particles make this mineral especially suitable for mineral carbonation. The small-sized particles also favour antigorite dehydroxylation, and the high P_{H2O} does not significantly affect its dehydroxylation. Overall, higher dehydroxylation temperatures and overlapping of amorphisation with forsterite formation make antigorite infeasible for subsequent mineral carbonation. Moreover, this study also suggests that the amorphous α and β-metaserpentine components are precursors of forsterite, and enstatite, respectively, in both serpentine polymorphs, *i.e.*, antigorite and lizardite. In antigorite, the formation of both amorphous components coincides and reaches the maximum amorphous content at the same temperature. In contrast, in lizardite, the β-metaserpentine lags the α-metaserpentine component, and it is nearly 80% at the higher amorphous production. This coexistence of both amorphous components also exhibits the maximum possible exploitation of serpentine feedstock for mineral carbonation due to the infeasibility of the preferential production of one amorphous component over the other.

Also, *in-situ* synchrotron-PXRD yielded measurements for the isoconversional kinetic analysis. As opposed to TGA-DSC, which provides insight into the coupled dehydroxylation-amorphisation-crystallisation process, synchrotron-PXRD can resolve processes affecting individual mineral phases. This enables kinetic analysis of antigorite dehydroxylation separately from forsterite formation, demonstrating the initial gradual increase in E_α is due to diffusion limitation, whereas the sharp rise in E_α during the later stages of dehydroxylation occurs because of forsterite formation. Consequently, this study highlights that the trade-off between amorphicity and forsterite formation is vital for developing an economical heat treatment of antigorite to store CO_2 by mineral carbonation.

List of Acronyms and Abbreviations

AINSE	Australian Institute of Nuclear Science and Engineering
ANSTO	Australian Nuclear Science and Technology Organisation
AS	Australian Synchrotron
CCS	Carbon capture and storage
COD	Crystallographic open database
DSC	Differential scanning calorimetry
DTG	Differential thermogravimetry
Endo	Endothermic peaks
Exo	Exothermic peaks
Gt	Gigatonnes
IPCC	Intergovernmental Panel for Climate Change
LOI	Loss on ignition
MIPS	Murdoch International Postgraduate Scholarship
NETL	National Energy Technology Laboratory
NIST	National Institute of Standards and Technology
NMR	Nuclear magnetic resonance
PGRA	Postgraduate research awards
Pt:Rh	Platinum Rhodium
PXRD	Powder X-ray diffraction
SRM	Standard reference material
STA	Simultaneous thermal analyser

TGA	Thermogravimetric analysis
TGA-DSC	Thermogravimetric analysis-differential scanning calorimetry
XRD	X-ray diffraction
XRF	X-ray fluorescence

List of Minerals

Al_2O_3	Aluminium oxide/ Corundum Powder
Atg	Antigorite
Chl	Chlorite
En	Enstatite
Fo	Forsterite
Hem	Hematite
LaB_6	Lanthanum hexabromide
Liz	Lizardite
Mag	Magnetite
Mgs	Magnesite
Prp	Pyrope
Qtz	Quartz
α-MS	α-metaserpentine (Low-angle magnesium-rich amorphous component)
β-MS	β-metaserpentine (High-angle silica-rich amorphous component)
γ-MS	γ-metaserpentine (Low-angle semi-crystallise chlorite-like component)

Table of Contents

1 Table of Contents

CHAPTER 1: Introduction

1 Introduction

1.1 Significance of the study

The continued increase in anthropogenic CO_2 emission per year (34 Gt in 2021) from the burning of fossil fuels accelerates the adverse effects of global warming on the environment (Lackner *et al.*, 1997; McKelvy *et al.*, 2004; Metz *et al.*, 2005). These adverse effects motivate both the governments and concerned individuals to find economical ways of capturing, and safely and permanently storing anthropogenic emission of CO_2. Mineral carbonation offers a promising technology for safe and permanent disposal of CO_2 through its conversion to stable carbonates (Dlugogorski and Balucan, 2014; Gerdemann *et al.*, 2007; Hariharan *et al.*, 2014b; Huijgen and Comans, 2005; Kirchofer *et al.*, 2013; Liu and Gadikota, 2018; Maroto-Valer *et al.*, 2005; Miller *et al.*, 2019; Oskierski *et al.*, 2019; Viti, 2010; Wilson *et al.*, 2014).

Mineral carbonation is categorised into *in-situ* carbonation and *ex-situ* carbonation. *In-situ* carbonation involves the transportation and injection of CO_2 into the original rock formations, while *ex-situ* carbonation encompasses the mining, crushing, and grinding of minerals, which can react with CO_2, at their original location, and possibly carrying them to industrial sites (Dlugogorski and Balucan, 2014; McKelvy *et al.*, 2004) away from mine sites. *Ex-situ* carbonation has evolved as a preferable option to sequester CO_2 over *in-situ* carbonation and geological storage at locations where geological formations have insufficient CO_2 storage capacities; south-eastern Australia or northern Europe (Romanov *et al.*, 2015). Moreover, geological sites that are more prone to seismic activities are impractical for CO_2

disposal because of leakage risk. On the other hand, the slow dissolution kinetics and energy requirements for the activation of serpentine minerals hinders the industrial implementation of mineral carbonation.

Thermal dehydroxylation increases the dissolution rates necessary for industrial-scale applications, but the energy requirements are a challenge (Alexander *et al.*, 2007; Dlugogorski and Balucan, 2014; Drief and Nieto, 1999; Kim and Chung, 2002; Maroto-Valer *et al.*, 2005; McKelvy *et al.*, 2004; Sanna *et al.*, 2014b). Thermal dehydroxylation produces amorphous content below 700 °C, which, on further heating, converts to less reactive crystalline phases: forsterite and enstatite (Brindley and Hayami, 1963; Dlugogorski and Balucan, 2014; McKelvy *et al.*, 2004). A properly optimised thermal activation of the serpentine mineral could decrease the energy requirements (Du Breuil *et al.*, 2019b; Farhang *et al.*, 2017; Pasquier *et al.*, 2014). The energy requirements for thermal dehydroxylation of serpentine minerals, as reported in recent studies (Balucan *et al.*, 2013; Balucan *et al.*, 2011), are still too high for the implementation of mineral carbonation in a practical process for sequestration of CO_2, necessitating further research (Neeraj and Yadav, 2020). However, the energy requirement and optimisation of thermal dehydroxylation are based on the high-pressure mineral carbonation, which allows the dissolution of even forsterite by decreasing the solution's pH whereas the enstatite phase remains insoluble (Balucan *et al.*, 2013; McKelvy *et al.*, 2004; O'Connor *et al.*, 2005; Rim *et al.*, 2020). Most recent literature has shifted from high-pressure carbonation to lower pressure carbonation to reduce the energy requirements for CO_2 sequestration by eliminating the need to purify and pressurise the CO_2 gas from point source emissions (Hariharan *et al.*, 2013; Pasquier *et al.*, 2014; Sanna *et al.*, 2014b; Werner *et al.*, 2014; Werner *et al.*, 2013). Nevertheless, the low-pressure mineral carbonation does not allow the dissolution of either the forsterite or enstatite phase (Rausis *et*

al., 2020; Rim *et al.*, 2020). In either case, the amorphous phase formation is vital in achieving the lower cost for mineral carbonation (Du Breuil *et al.*, 2019b; Farhang *et al.*, 2017; Pasquier *et al.*, 2014; Rim *et al.*, 2020). Therefore, a profound understanding of thermal dehydroxylation can help select the optimum dehydroxylation process conditions to achieve the highest amorphous materials in activated rock while minimising the formation of crystalline phases of forsterite and enstatite.

This thesis investigates the dehydroxylation kinetics of antigorite, the factors affecting the appearance and disappearance of intermediate phases, and the formation of recrystallised products during the heat treatment of two serpentine polymorphs, *i.e.*, antigorite and lizardite. We expect to gain profound insights into the kinetics of antigorite and understand the crystallographic and mineralogical variation of heat-treated antigorite and lizardite minerals to develop new energy-efficient strategies effective heat treatment of these minerals.

1.2 Mineral carbonation

Mineral carbonation involves the conversion of Mg, Ca and Fe-rich silicate or oxide minerals into their respective carbonates. This process occurs naturally during the weathering of silicate rocks to stable carbonates. The CO_2 in the atmosphere converts to carbonic acid by its reaction with either surface or meteoric water. In freshwater, with its pH typical below 7.5, the carbonic acid dissociates into protons (H^+) bicarbonate anions (HCO_3^-), whereas in seawater (pH $\approx$ 8.2), bicarbonate ions dissociate further into protons and carbonate anions (CO_3^{2-}). This is because pK_{a1} and pK_{a2} of carbonic acid correspond to 6.36 and 10.33, respectively. Carbonic acid provides acidity/protons to break down silicate minerals to

produce divalent cation (M^{2+} where M= Mg, Ca). The released divalent cations can react with carbonate ions to form stable carbonate minerals and SiO_2, under alkaline conditions as shown in the following reaction sequence Equation 1.1 to Equation 1.5 (Power *et al.*, 2013).

$$CO_{2(g)} \leftrightarrow CO_{2(aq)} \quad (1.1)$$

$$CO_{2(aq)} + H_2O_{(l)} \leftrightarrow H_2CO_{3(aq)} \quad (1.2)$$

$$H_2CO_{3(aq)} \leftrightarrow HCO_3^-{}_{(aq)} + H^+{}_{(aq)} \quad (1.3)$$

$$HCO_3^-{}_{(aq)}) \leftrightarrow CO_3^{2-}{}_{(aq)} + H^+{}_{(aq)} \quad (1.4)$$

$$M^{2+}{}_{(s)} + CO_3^{2-}{}_{(aq)} \leftrightarrow MCO_{3(s)} \quad (1.5)$$

Different feedstocks such as wollastonite (Balucan and Dlugogorski, 2013; Ding *et al.*, 2016; Lackner *et al.*, 1995; O'Connor *et al.*, 2004; Xu *et al.*, 2019), olivine (Béarat *et al.*, 2006; Ji *et al.*, 2018; Wang *et al.*, 2019), serpentine (Balucan and Dlugogorski, 2013; Balucan *et al.*, 2013; Critelli *et al.*, 2015; Du Breuil *et al.*, 2019b; Farhang *et al.*, 2017; Gerdemann *et al.*, 2007; Ghoorah *et al.*, 2014; Hariharan *et al.*, 2014b; Lackner *et al.*, 1995; Liu and Gadikota, 2018; Miller *et al.*, 2019; Mouedhen *et al.*, 2017; O'Connor *et al.*, 2000; Sanna *et al.*, 2013; Viti, 2010), brucite (Béarat *et al.*, 2002; Larachi *et al.*, 2018; McKelvy *et al.*, 2000), ultramafic mining waste (Azadi *et al.*, 2019; Bloise, 2018; Huot *et al.*, 2003; Wilson *et al.*, 2009) and industrial wastes (Liu and Gadikota, 2018; Rahmani, 2018; Song *et al.*, 2019; Stolaroff *et al.*, 2005) have been explored for their potential to sequester CO_2 via mineral carbonation. However, some of the above feedstocks, such as brucite, industrial waste, and ultramafic mining wastes, are highly reactive. They also require less amount of the mineral to sequester 1 tonne of CO_2, but due to the limited availability, they cannot be suitably

exploited for CO_2 sequestration on a global scale (Gualtieri *et al.*, 2012). Therefore, serpentinite minerals are considered to be one of the leading candidates for mineral carbonation for two reasons; (i) the presence of well-distributed and abundant resources of these minerals and (ii) natural weathering of these minerals to carbonates demonstrating its thermodynamic feasibility (Balucan and Dlugogorski, 2013; Dlugogorski and Balucan, 2014; McKelvy *et al.*, 2004).

1.2.1 Serpentine feedstock

Serpentine minerals are hydrated magnesium silicates with a composition of 35-40 % SiO_2 and MgO each and around ~13% water (Dlugogorski and Balucan, 2014; Moody, 1976; Whittaker and Zussman, 1956; Wicks and O'Hanley, 1988). These minerals are present in chemically similar, structurally different polymorphs (Balucan and Dlugogorski, 2013; Gualtieri *et al.*, 2012; Sanna *et al.*, 2013; Tarling *et al.*, 2018; Whittaker and Zussman, 1956; Wicks and O'Hanley, 1988) as shown in Figure 1.1: (i) antigorite (wave-like structure); (ii) chrysotile (concentric layered structure); and (iii) lizardite (planer structure).

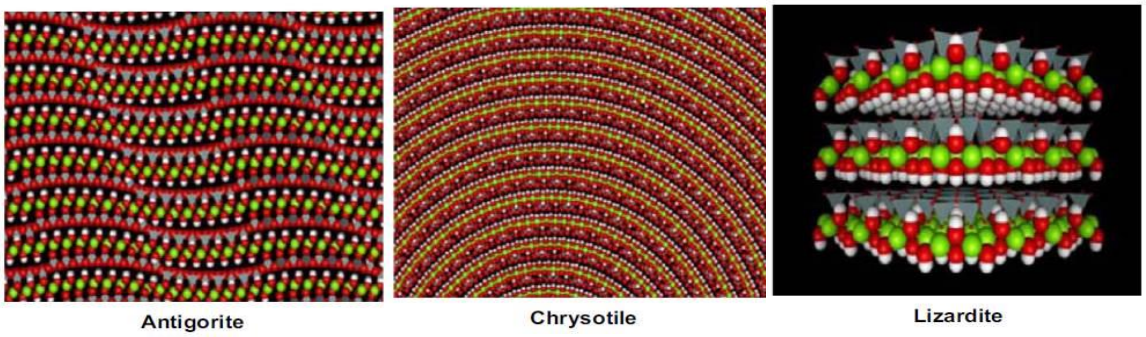

Figure 1.1. The structures of serpentine polymorphs, *i.e.*, antigorite, chrysotile and lizardite. The Mg, O and H atoms of the octahedral layer are represented by green, red and white spheres, respectively. The grey tetrahedra

represent the silica layer. Note the wave-like pattern of antigorite, parallel sheets for lizardite and concentric structure of chrysotile (Dlugogorski and Balucan, 2014; McKelvy *et al.*, 2005; Wicks and O'Hanley, 1988)

Although the carbonation is thermodynamically favourable (Equation 1.6) at lower temperatures, the slower reaction kinetics of Mg-rich serpentine mineral impedes the commercialisation of this process (Gualtieri *et al.*, 2012; Lackner *et al.*, 1995; Viti, 2010).

$$Mg_3Si_2O_5(OH)_4 + 3CO_2 = 3MgCO_3 + 2SiO_2 + 2H_2O \qquad \Delta H = +64 \text{ kJ mol}^{-1} CO_2 \qquad (1.6)$$

Several attempts have been made to increase serpentinite minerals' reactivity through chemical, mechanical and thermo-mechanical treatment and heat treatment and a combination of pre-treatments (McKelvy *et al.*, 2004). However, an economically viable option is still not available to sequester the CO_2 on the global scale of emission (Alizadehhesari *et al.*, 2012; Gualtieri *et al.*, 2012; Viti, 2010). Although Balucan *et al.* (2011) point out the previous overestimates of energy during heat treatment of serpentine minerals, which were primarily based on the electrical power (O'Connor *et al.*, 2005) and suggested that the use of thermal energy along with heat integration energy may result in a suitable option among the pre-treatment steps (Balucan *et al.*, 2011; Dlugogorski and Balucan, 2014). Additionally, the heat integration may utilise the exothermic heat of mineral carbonation to compensate for part of the energy penalty during heat-treatment, as shown in the schematic below (Figure 1.2.).

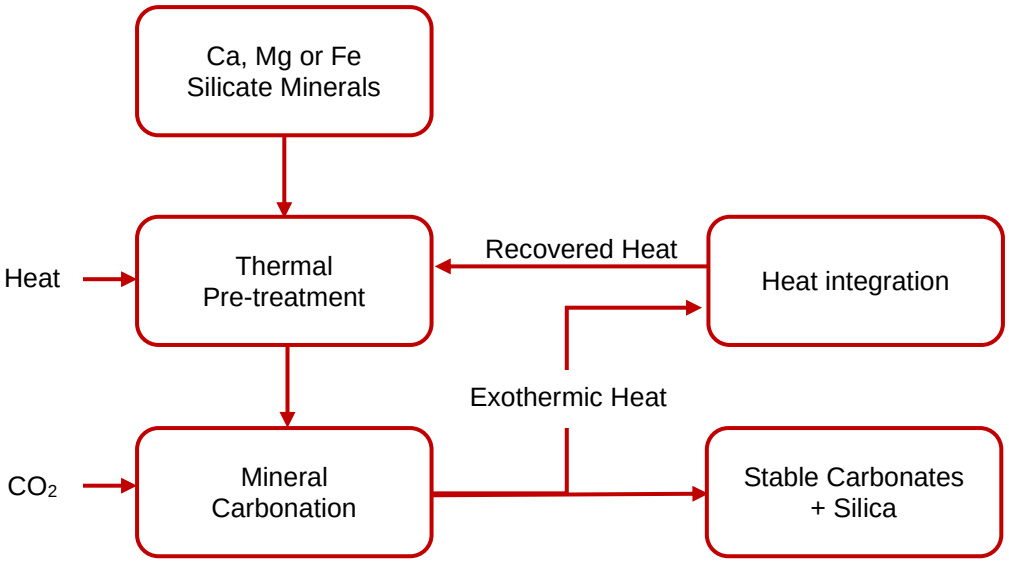

Figure 1.2. Schematic for the conservation of exothermic heat of mineral carbonation for thermal dehydroxylation of serpentine minerals

1.2.2 Thermal dehydroxylation

Heat activation of serpentine minerals result in the formation of intermediate amorphous phases through dehydroxylation, *i.e.*, the release of hydroxyl groups from the brucite-like octahedral layers (Bloise, 2018; Brindley and Millhollen, 1966). The high amorphicity ultimately increases the reactivity of these minerals for the subsequent processes of leaching and carbonation. Since the dehydroxylation of serpentine through heat treatment is one of the energy-intensive steps, it is essential to optimise the heat treatment to achieve the highest reactivity at the lowest possible cost and energy requirement. The dehydroxylation of serpentine via heat treatment occurs at a temperature above 650 °C, 685 °C and 700 °C for chrysotile, lizardite, and antigorite, respectively (Brindley and Zussman, 1957; Martinez, 1961). Antigorite, which is the most stable serpentine polymorph, exhibits the highest dehydroxylation temperature (Drief and Nieto, 1999). Therefore, antigorite serves as the

benchmark to estimate the maximum energy requirements for these minerals (Brindley and Hayami, 1963).

Previous studies provided the energy estimates for serpentine dehydroxylation for high-pressure mineral carbonation based on either full dehydroxylation or various degrees of dehydroxylation (Balucan *et al.*, 2013; Gerdemann *et al.*, 2007), usually represented as the percentage residual hydroxyl (% OH_{res}). The value of % OH_{res} represents the amount of water, or OH content retained in the sample after heat treatment, *e.g.*, the value of % OH_{res} before and after complete dehydroxylation is 100 % and 0 %, respectively. Among these studies, Balucan *et al.* (2013) provided the lowest cost estimates of AU$1.25 for the heat-treatment of serpentine minerals to 20 % OH_{res} using the direct combustion of natural gas while eliminating the secondary CO_2 emissions (Balucan *et al.*, 2013). However, the optimal 20 % residual hydroxyl has been suggested for all serpentine polymorphs for subsequent high-pressure mineral carbonation, irrespective of their different thermal behaviour during dehydroxylation (Balucan *et al.*, 2013). This is because the lower pH caused by high-pressure mineral carbonation can dissolve the forsterite phase (Zulumyan *et al.*, 2018).

On the other hand, recent literature is focused on the optimisation of carbonation of heat-activated serpentine minerals for large-scale mineral carbonation at the flue gas conditions (Du Breuil *et al.*, 2019b; Farhang *et al.*, 2019; Farhang *et al.*, 2017; Hariharan and Mazzotti, 2017b; Hariharan *et al.*, 2014b; Hariharan *et al.*, 2013; Kemache *et al.*, 2017; Mouedhen *et al.*, 2017; Pasquier *et al.*, 2014; Rim *et al.*, 2020). However, the dissolution of forsterite and enstatite phases is not possible under these conditions. Since antigorite dehydroxylation is accompanied by an overlap between amorphisation and forsterite formation, the structural variation, *i.e.*, amorphisation and crystalline forsterite and enstatite formations, also need to

be considered while optimising the cost for the thermal dehydroxylation of these minerals especially for the low-pressure mineral carbonation. Hence, it is realised that the enhanced understanding of thermal dehydroxylation can help to optimise the mineral carbonation process further.

1.3 Isoconversional kinetic modelling

Previously developed kinetic models for dehydroxylation of serpentine are based on the model-fitting approach (Alizadehhesari *et al.*, 2012; Balucan *et al.*, 2011; Brindley *et al.*, 1967a; Brindley *et al.*, 1967b; Cattaneo *et al.*, 2003; Chollet *et al.*, 2011; Gualtieri *et al.*, 2012; Perrillat *et al.*, 2005), which either involves the selection of a model based on phenomenological judgement (Brindley and Hayami, 1963; Cattaneo *et al.*, 2003; Gualtieri *et al.*, 2012; Perrillat *et al.*, 2005) or based on the best fit of experimental data to well established solid-state reaction models (Alizadehhesari *et al.*, 2012; Balucan *et al.*, 2011). However, in both of these approaches, the value of activation energy (E) and Arrhenius factor (A) depends on the selected reaction model [$f(\alpha)$] (Alizadehhesari *et al.*, 2012; Balucan *et al.*, 2011; Gualtieri *et al.*, 2012; Weber and Greer, 1965). Moreover, the traditional methodology also suffers from the inconsistency between isothermal and non-isothermal E and A (Vyazovkin and Wight, 1998). Therefore, a considerable variation in the kinetic parameters exists throughout the literature for dehydroxylation of serpentine minerals (Balucan and Dlugogorski, 2013; Brindley *et al.*, 1967a; Dlugogorski and Balucan, 2014; McKelvy *et al.*, 2004; Pawley and Bromiley, 2003; Viti, 2010). These drawbacks were noted by Dlugogorski and Balucan (2014) in their review papers which reviewed the literature on mineral carbonation until 2012 and suggested the employment of multiple heating rates and

isoconversional methodology to obtain a unique set of kinetic parameters. Additionally, the use of several heating rates eliminates the ambiguous determination of kinetic triple from a limited dataset, as several kinetic models, each with a different set of kinetic parameters can potentially describe a single TG-experiment (Dlugogorski and Balucan, 2014).

On the other hand, isoconversional analysis involves the estimation of the model-independent activation energy (E_α) (Vyazovkin, 2015a, b; Vyazovkin and Wight, 1998), *i.e.*, it assumes the activation energy (E_α) remains constant over a small extent of conversion (α) compared to the whole range of conversion and then attempts to infer mechanism from the shape of E_α. Most recent literature successfully performed the isoconversional kinetic modelling on lizardite (Trittschack and Grobéty, 2012; Zhou *et al.*, 2017), chrysotile, brucite (Trittschack and Grobéty, 2013) and antigorite (Liu *et al.*, 2019) showed the multistep nature of dehydroxylation of serpentine minerals. However, the study on the antigorite dehydroxylation through this approach aims to model a reaction kinetics to predict the water release rates, which acts as a trigger for the seismicity in subduction zones (Liu *et al.*, 2019). Therefore, the multistep nature of dehydroxylation of serpentine minerals and significant disparity in activation energy based on model fitting approach, require the development of unique kinetic parameters using isoconversional kinetic modelling to establish a better understanding of reaction kinetics for dehydroxylation of serpentinite.

1.4 Research objectives

This research aims to study the implication of thermal dehydroxylation of antigorite to gauge the usefulness of this mineral for the sequestration of CO_2. The thesis investigates the

kinetics of antigorite and the formation of intermediate and product phases during thermal dehydroxylation of two serpentine polymorphs, *i.e.*, antigorite and lizardite, to provide the limitations and suggestions for effective heat treatment strategies. In order to achieve this, the thesis targets fulfilling the following objectives:

i. To develop the knowledge of intermediate phases and their corresponding onset formation temperatures and determine the kinetic parameters of thermal dehydroxylation to pin down the practical limitation of antigorite as a feedstock for mineral carbonation.

ii. To understand the effects of various parameters such as feedstock composition, dehydroxylation temperature, particle size and partial pressure of water vapours on crystallographic structural variation during heat treatment of two serpentine polymorphs (antigorite and lizardite) from crystallographic measurements afforded by the *in-situ* synchrotron powder X-ray diffraction (PXRD).

iii. To develop the individual isoconversional kinetics of antigorite dehydroxylation and forsterite crystallisation reaction steps during heat treatment of serpentine minerals using TGA-DSC and *in-situ* synchrotron PXRD, with the latter having the ability to resolve the individual phases.

This study drives the implication for industrial dehydroxylation and subsequent mineral carbonation to store anthropogenic CO_2 emissions from point sources, into stable carbonates based on the enhanced understanding of thermal dehydroxylation kinetics of antigorite, and

the effects of various parameters on intermediate phases during dehydroxylation of serpentine minerals especially antigorite and lizardite.

1.5 Thesis organisation

In view of the above aims and objectives, the thesis is organised as follows.

Chapter 2 of this thesis gives a brief literature review of the dehydroxylation of serpentine minerals for the mineral carbonation process. It discusses the *in-situ* and *ex-situ* mineral carbonation technologies, available feedstocks, reaction chemistry, feed pre-treatment, contributions in the field of thermal dehydroxylation, the kinetics and carbonation of heat-activated serpentine minerals, to describe the existing thermal dehydroxylation strategies as compared to those suggested in this thesis and to point out knowledge gaps.

Chapter 3 describes the multistep nature of dehydroxylation of antigorite through isoconversional kinetic modelling using the non-isothermal TGA-DSC analysis. The combined use of isoconversional activation energy and understanding of corresponding crystallographic changes via *in-situ* synchrotron PXRD analysis provides an insight into the effect of structural changes on the dehydroxylation kinetics.

Chapter 4 compares the effects of mineralogy, particle size and partial pressure of water vapours on the formation of amorphous and crystalline phases during the dehydroxylation of serpentine polymorphs (*i.e.,* antigorite and lizardite) using *in-situ* synchrotron PXRD. This

chapter also compares the energy requirements for the heat treatment of antigorite and lizardite minerals in relation to the formation of amorphous phases.

In **Chapter 5,** dehydroxylation kinetics based on TGA-DSC are used for the validation of synchrotron PXRD-based kinetics. Additionally, we deploy the synchrotron PXRD to resolve the individual phases and study the kinetics of dehydroxylation and forsterite formation independently using the isoconversional kinetic modelling.

Chapter 6 provides concluding remarks on the most significant results of this thesis and their implication for mineral carbonation. Based on these conclusions, the areas for futures research are suggested.

Finally, Appendix comprises the information that we pulled out from individual chapters to allow the discussion to flow smoothly, but which we considered essential to include in the thesis for its completeness.

1.6 References

Alexander, G., Mercedes Maroto-Valer, M., Gafarova-Aksoy, P. (2007) Evaluation of reaction variables in the dissolution of serpentine for mineral carbonation. Fuel 86, 273-281.

Alizadehhesari, K., Golding, S.D., Bhatia, S.K. (2012) Kinetics of the dehydroxylation of serpentine. Energy & Fuels 26, 783-790.

Azadi, M., Edraki, M., Farhang, F., Ahn, J. (2019) Opportunities for mineral carbonation in Australia's mining industry. Sustainability 11.

Balucan, R.D., Dlugogorski, B.Z. (2013) Thermal activation of antigorite for mineralisation of CO_2. Environmental Science & Technology 47, 182-190.

Balucan, R.D., Dlugogorski, B.Z., Kennedy, E.M., Belova, I.V., Murch, G.E. (2013) Energy cost of heat activating serpentinites for CO_2 storage by mineralisation. International Journal of Greenhouse Gas Control 17, 225-239.

Balucan, R.D., Kennedy, E.M., Mackie, J.F., Dlugogorski, B.Z. (2011) Optimisation of antigorite heat pre-treatment via kinetic modelling of the dehydroxylation reaction for CO_2 mineralisation. Greenhouse Gases: Science and Technology 1, 294-304.

Bloise, A.C., Manuela; Gualtieri, Alessandro F. (2018) Effect of grinding on chrysotile, amosite and crocidolite and implications for thermal treatment. Minerals 8.

Brindley, G.W., Achar, B.N.N., Sharp, J.H. (1967a) Kinetics and mechanism of dehydroxylation processes: II. Temperature and vapour pressure dependence of dehydroxylation of serpentine. American Mineralogist 52, 1697-1705.

Brindley, G.W., Hayami, R. (1963) Kinetics and mechanisms of dehydration and recrystallisation of serpentine—I. Clays and Clay Minerals 12, 35-47.

Brindley, G.W., Millhollen, G.L. (1966) Chemisorption of water at high temperatures on kaolinite: Effect on dehydroxylation. Science 152, 1385.

Brindley, G.W., Sharp, J.H., Patterson, J.H., Narahari, B.N. (1967b) Kinetics and mechanism of dehydroxylation processes, I. Temperature and vapour pressure dependence of dehydroxylation of kaolinite. American Mineralogist 52, 201-211.

Brindley, G.W., Zussman, J. (1957) A structural study of the thermal transformation of serpentine minerals to forsterite. American Mineralogist 42, 461-474.

Critelli, T., Marini, L., Schott, J., Mavromatis, V., Apollaro, C., Rinder, T., De Rosa, R., Oelkers, E.H. (2015) Dissolution rate of antigorite from a whole-rock experimental study of serpentinite dissolution from 2<pH<9 at 25°C: Implications for carbon mitigation via enhanced serpentinite weathering. Applied Geochemistry 61, 259-271.

Ding, W., Yang, H., Ouyang, J., Long, H. (2016) Modified wollastonite sequestrating CO_2 and exploratory application of the carbonation products. RSC Advances 6, 78090-78099.

Dlugogorski, B.Z., Balucan, R.D. (2014) Dehydroxylation of serpentine minerals: Implications for mineral carbonation. Renewable and Sustainable Energy Reviews 31, 353-367.

Drief, A., Nieto, F. (1999) The effect of dry grinding on antigorite from Mulhacen, Spain. Clays and Clay Minerals 47, 417-424.

Du Breuil, C., César-Pasquier, L., Dipple, G., Blais, J.-F., Iliuta, C.M., Mercier, G. (2019a) Mineralogical transformations of heated serpentine and their impact on dissolution during aqueous-phase mineral carbonation reaction in flue gas conditions. Minerals 9.

Du Breuil, C., Pasquier, L.-C., Dipple, G., Blais, J.-F., Iliuta, C.M., Mercier, G. (2019b) Mineralogical transformations of heated serpentine and their impact on dissolution during aqueous-phase mineral carbonation reaction in flue gas conditions. Minerals 9.

Farhang, F., Oliver, T.K., Rayson, M.S., Brent, G.F., Molloy, T.S., Stockenhuber, M., Kennedy, E.M. (2019) Dissolution of heat-activated serpentine for CO2 sequestration: The effect of silica precipitation at different temperature and pH values. Journal of CO2 Utilization 30, 123-129.

Farhang, F., Rayson, M., Brent, G., Hodgins, T., Stockenhuber, M., Kennedy, E. (2017) Insights into the dissolution kinetics of thermally activated serpentine for CO_2 sequestration. Chemical Engineering Journal 330, 1174-1186.

Gerdemann, S.J., O'Connor, W.K., Dahlin, D.C., Penner, L.R., Rush, H. (2007) *Ex-situ* aqueous mineral carbonation. Environmental Science & Technology 41, 2587-2593.

Ghoorah, M., Dlugogorski, B.Z., Oskierski, H.C., Kennedy, E.M. (2014) Study of thermally conditioned and weak acid-treated serpentinites for mineralisation of carbon dioxide. Minerals Engineering 59, 17-30.

Gualtieri, A.F., Giacobbe, C., Viti, C. (2012) The dehydroxylation of serpentine group minerals. American Mineralogist 97, 666.

Hariharan, S., Mazzotti, M. (2017) Kinetics of flue gas CO_2 mineralisation processes using partially dehydroxylated lizardite. Chemical Engineering Journal 324, 397-413.

Hariharan, S., Werner, M., Hänchen, M., Zingaretti, D., Baciocchi, R., Mazzotti, M. (2014) Dissolution kinetics of thermally activated serpentine for mineralisation at flue gas conditions. Energy Procedia 63, 5887-5891.

Hariharan, S.B., Werner, M., Zingaretti, D., Baciocchi, R., Mazzotti, M. (2013) Dissolution of Activated Serpentine for Direct Flue-Gas Mineralisation. Energy Procedia 37, 5938-5944.

Huijgen, W., Comans, R. (2005) Mineral CO_2 sequestration by carbonation of industrial residues. The Netherlands: Energy Research Centre of the Netherlands (ECN).

Ji, S., Zhu, J., He, H., Tao, Q., Zhu, R., Ma, L., Chen, M., Li, S., Zhou, J. (2018) Conversion of serpentine to smectite under hydrothermal condition: Implication for solid-state transformation. American Mineralogist 103, 241-251.

Kemache, N., Pasquier, L.-C., Cecchi, E., Mouedhen, I., Blais, J.-F., Mercier, G. (2017) Aqueous mineral carbonation for CO_2 sequestration: From laboratory to pilot scale. Fuel Processing Technology 166, 209-216.

Kim, D.-J., Chung, H.-S. (2002) Effect of grinding on the structure and chemical extraction of metals from serpentine. Particulate Science and Technology 20, 159-168.

Kirchofer, A., Becker, A., Brandt, A., Wilcox, J. (2013) CO_2 mitigation potential of mineral carbonation with industrial alkalinity sources in the United States. Environmental Science & Technology 47, 7548-7554.

Larachi, F., Aksenova, D., Yousefi, B., Maldague, X.P.V., Beaudoin, G. (2018) Thermochemical monitoring of brucite carbonation using passive infrared thermography. Chemical Engineering and Processing - Process Intensification 130, 43-52.

Liu, C., Wang, D., Shen, K., Liu, T., Yi, L. (2019) Kinetics of antigorite dehydration: Rapid dehydration as a trigger for lower-plane seismicity in subduction zones. American Mineralogist 104, 282-290.

Liu, M., Gadikota, G. (2018) Chemo-morphological coupling during serpentine heat treatment for carbon mineralisation. Fuel 227, 379-385.

Maroto-Valer, M.M., Fauth, D.J., Kuchta, M.E., Zhang, Y., Andrésen, J.M. (2005) Activation of magnesium-rich minerals as carbonation feedstock materials for CO_2 sequestration. Fuel Processing Technology 86, 1627-1645.

Martinez, E. (1961) The effect of particle size on the thermal properties of serpentine minerals. American Mineralogist 46, 901-912.

McKelvy, M.J., Chizmeshya, A.V., Diefenbacher, J., Bearat, H., Wolf, G. (2004) Exploration of the role of heat activation in enhancing serpentine carbon sequestration reactions. Environmental Science & Technology 38, 6897-6903.

Mellini, M., Trommsdorff, V. & Compagnoni, R. (1987) Antigorite polysomatism: behaviour during progressive metamorphism. Contributions to Mineralogy and Petrology 97, 147-155.

Miller, Q.R.S., Schaef, H.T., Kaszuba, J.P., Gadikota, G., McGrail, B.P., Rosso, K.M. (2019) Quantitative review of olivine carbonation kinetics: Reactivity trends, mechanistic insights, and research frontiers. Environmental Science & Technology Letters 6, 431-442.

Mouedhen, I., Kemache, N., Pasquier, L.-C., Cecchi, E., Blais, J.-F., Mercier, G. (2017) Effect of pCO_2 on direct flue gas mineral carbonation at pilot scale. Journal of Environmental Management 198, 1-8.

Neeraj, Yadav, S. (2020) Carbon storage by mineral carbonation and industrial applications of CO2. Materials Science for Energy Technologies 3, 494-500.

O'Connor, W.K., Dahlin, D.C., Nilsen, D.N., Gerdemann, S.J., Rush, G.E., Walters, R.P., Turner, P.C., (2001) Research status on the sequestration of carbon dioxide by direct aqueous mineral carbonation. Pittsburgh Coal Conference, University of Pittsburgh, 1249 Benedum Hall, Pittsburgh, PA 15261, United States.

O'Connor, W.K., Dahlin, D.C., Rush, G.E., Gerdemann, S.J., Penner, L.R., (2005) Energy and economic evaluation of *ex-situ* aqueous mineral carbonation. Rubin, E.S., Keith, D.W., Gilboy, C.F., Wilson, M., Morris, T., Gale, J., Thambimuthu, K. (Eds.), Greenhouse Gas Control Technologies 7. Elsevier Science Ltd, Oxford, pp. 2011-2015.

Oskierski, H.C., Beinlich, A., Mavromatis, V., Altarawneh, M., Dlugogorski, B.Z. (2019) Mg isotope fractionation during continental weathering and low-temperature carbonation of ultramafic rocks. Geochimica et Cosmochimica Acta 262, 60-77.

Pasquier, L.-C., Mercier, G., Blais, J.-F., Cecchi, E., Kentish, S. (2014) Reaction mechanism for the aqueous-phase mineral carbonation of heat-activated serpentine at low temperatures and pressures in flue gas conditions. Environmental Science & Technology 48, 5163-5170.

Pawley, A.R., Bromiley, G.D. (2003) The stability of antigorite in the systems MgO-SiO_2-H_2O (MSH) and MgO-Al_2O_3-SiO_2-H_2O (MASH): The effects of Al^{3+} substitution on high-pressure stability. American Mineralogist 88, 99-108.

Rahmani, O. (2018) CO_2 sequestration by indirect mineral carbonation of industrial waste red gypsum. Journal of CO2 Utilization 27, 374-380.

Rim, G., Marchese, A.K., Stallworth, P., Greenbaum, S.G., Park, A.-H.A. (2020) 29Si solid-state MAS NMR study on leaching behaviours and chemical stability of different Mg-silicate structures for CO_2 sequestration. Chemical Engineering Journal 396, 125204.

Romanov, V., Soong, Y., Carney, C., Rush, G.E., Nielsen, B., O'Connor, W. (2015) Mineralisation of carbon dioxide: A literature review. ChemBioEng Reviews 2, 231-256.

Sanna, A., Uibu, M., Caramanna, G., Kuusik, R., Maroto-Valer, M.M. (2014) A review of mineral carbonation technologies to sequester CO_2. Chemical Society Reviews 43, 8049-8080.

Sanna, A., Wang, X., Lacinska, A., Styles, M., Paulson, T., Maroto-Valer, M.M. (2013) Enhancing Mg extraction from lizardite-rich serpentine for CO_2 mineral sequestration. Minerals Engineering 49, 135-144.

Song, X., Xiaoyu, C., Lin, Q., Yanna, L. (2019) A review of mineral carbonation from industrial waste. IOP Conference Series: Earth and Environmental Science 401, 012008.

Tarling, M.S., Smith, S.A.F., Viti, C., Scott, J.M. (2018) Dynamic earthquake rupture preserved in a creeping serpentinite shear zone. Nature Communications 9, 3552.

Trittschack, R., Grobéty, B. (2012) Dehydroxylation kinetics of lizardite. European Journal of Mineralogy 24, 47-57.

Trittschack, R., Grobéty, B., (2013) The dehydroxylation of chrysotile: A combined *in-situ* micro-Raman and micro-FTIR study, American Mineralogist, p. 1133.

Viti, C. (2010) Serpentine minerals discrimination by thermal analysis. American Mineralogist 95, 631.

Wang, F., Dreisinger, D., Jarvis, M., Hitchins, T. (2019) Kinetics and mechanism of mineral carbonation of olivine for CO_2 sequestration. Minerals Engineering 131, 185-197.

Weber, J.N., Greer, R.T. (1965) Dehydration of serpentine: heat of reaction and reaction kinetics at PH_2O=1 ATM. American Mineralogist 50, 450-464.

Wilson, S.A., Harrison, A.L., Dipple, G.M., Power, I.M., Barker, S.L.L., Ulrich Mayer, K., Fallon, S.J., Raudsepp, M., Southam, G. (2014) Offsetting of CO_2 emissions by air capture in mine tailings at the Mount Keith Nickel Mine, Western Australia: Rates, controls and prospects for carbon-neutral mining. International Journal of Greenhouse Gas Control 25, 121-140.

Xu, X., Liu, W., Chu, G., Zhang, G., Luo, D., Yue, H., Liang, B., Li, C. (2019) Energy-efficient mineral carbonation of $CaSO_4$ derived from wollastonite via a roasting-leaching route. Hydrometallurgy 184, 151-161.

Zhou, S., Wei, Y., Li, B., Ma, B., Wang, C., Wang, H. (2017) Kinetics study on the dehydroxylation and phase transformation of $Mg_3Si_2O_5(OH)_4$. Journal of Alloys and Compounds 713, 180-186.

Chapter 2: Literature Review

2 Literature review

2.1 Introduction

The anthropogenic CO_2 emissions are increasing at the rate of Gigatons (Gt) each year, leading to severe climate changes and global warning by accumulating into the atmosphere (IPCC, 2014). To mitigate the severe effects of climate change and global warming, Paris agreement in 2015 recommended constraining the atmospheric warning to < 2 ℃ by 2100 through the implementation of CO_2 sequestration technologies to remove CO_2 from the atmosphere and point sources in addition to the renewable energy resources (UNFCCC, 2015). Mineral carbonation offers one of the promising technologies to store anthropogenic CO2 emissions permanently. The abundance and natural weathering of serpentinite minerals to carbonate favours the exploitation of serpentinite rocks for CO_2 sequestration. However, the slow reaction kinetics hinder the commercialisation of this process. To overcome this kinetic barrier and to increase the reactivity during carbonation, serpentinite rocks must be activated by dehydroxylation at high temperature. Since this is the most energy-intensive step of the mineral carbonation process, a detailed understanding of structural changes with temperature and associated kinetic parameters for dehydroxylation of serpentinite is required to identify the most cost and energy effective activation strategy. This study aims to develop a detailed kinetic model using isoconversional methodology considering the multistep process of dehydroxylation, and the analysis of structural changes during heat activation for the inferences on the reaction mechanism.

After the brief overview about the motivation of carbon capture and storage as a result of CO_2 emissions, this review briefly provides the necessary overview of mineral carbonation, discusses the benefits and challenges of *in-situ* and *ex-situ* mineral carbonation, raw material, reaction chemistry and available pre-treatments for mineral carbonation. After that, it evaluates the thermal pre-treatment for dehydroxylation of serpentine minerals in the previous literature with a focus on the factors affecting the thermal dehydroxylation and dehydroxylation phases that result in higher reactivity for subsequent mineral carbonation. This review also provides an account of previous kinetic evaluations of thermal dehydroxylation of serpentine minerals to be used as the basis for isoconversional kinetic modelling. The current CO_2 sequestration through mineral carbonation of heat-treated serpentine minerals is also reviewed to evaluate the effectiveness of heat activation in increasing reactivity. Finally, this review concludes by providing a summary of unresolved problems, gaps in knowledge and possible future research directions for the development of economical and energy-efficient thermal activation of serpentine minerals for large-scale CO_2 storage by mineral carbonation

2.2 CO_2 emission and the need for carbon capture and storage (CCS)

Continued emissions of anthropogenic CO_2 have resulted in severe climate change through global warming (Dey and Dhal, 2019; Friedlingstein *et al.*, 2019; IPCC, 2014; Neeraj and Yadav, 2020; Viti, 2010). Moreover, global energy demands and availability of inexpensive fossil fuels will continue to increase the CO_2 concentration in the atmosphere (Field and Raupach, 2004; IPCC, 2014). Figure 2.1 shows the increase in the CO_2 emissions from 1850 to 2018, which have risen from only a few $GtCO_2$ per year to around 37 $GtCO_2$ per year in

2018 (Friedlingstein *et al.*, 2019). It can be noted that fossil fuel consumption, cement industry and flaring resulted in a rapid and massive increase in CO_2 emissions after the 1950s.

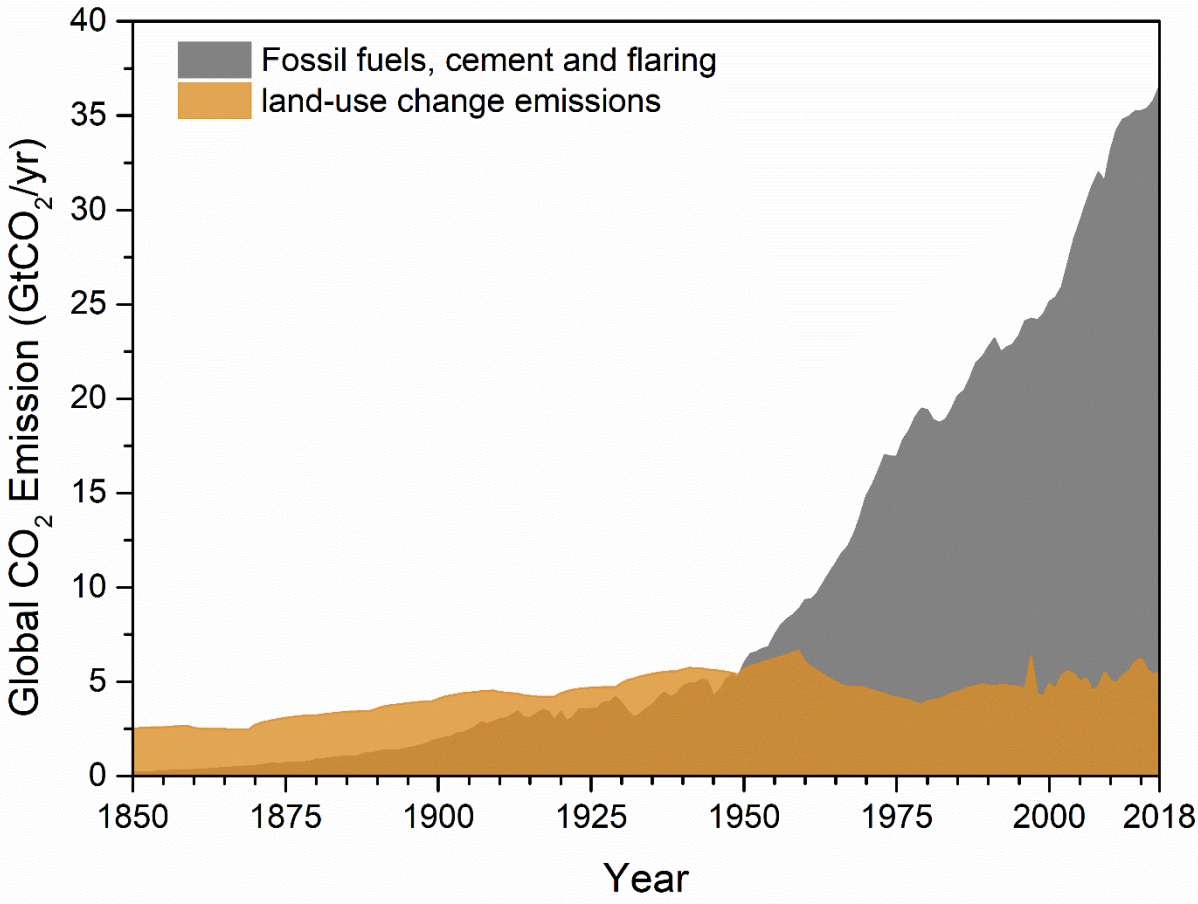

Figure 2.1. Global anthropogenic CO_2 emissions, the data is taken from the Global carbon budget 2019 (Friedlingstein *et al.*, 2019).

So, growing concerns about climate change as a result of CO_2 emissions and Paris agreement to constrain the global warming to < 2 ℃ has motivated the research in carbon capture and storage (CCS) technologies during the last decades (Mouedhen *et al.*, 2017; Neeraj and Yadav, 2020; Romanov *et al.*, 2015). Multiple technologies have been explored for CO_2 sequestration, but the economically viable option is still a challenge (Neeraj and Yadav, 2020). Geological storage offers a mature solution for the disposal of CO_2 at the scale of global CO_2 emissions (Dlugogorski and Balucan, 2014; Neeraj and Yadav, 2020) and the cost

for geological storage is low if CO_2 capture, storage and transportation are not included (Romanov *et al.*, 2015). However, significant challenges for geological storage such as permanency and long-term site monitoring still need to be resolved (Durand, 2011; Metz *et al.*, 2005; Power *et al.*, 2013). An alternative approach for the CO_2 disposal is mineral carbonation which has an excellent potential to provide a long term and permanent sequestration of CO_2 on the global scale (Béarat *et al.*, 2006; Dlugogorski and Balucan, 2014; Lackner *et al.*, 1995; Neeraj and Yadav, 2020; Power *et al.*, 2013).

2.3 Mineral carbonation

Mineral carbonation involves the storage of CO_2 through its conversion to stable carbonates (Lackner *et al.*, 1995; Neeraj and Yadav, 2020; Power *et al.*, 2013). CO_2 in the form of either gas and/or aqueous form reacts with calcium (Ca), magnesium (Mg) and Iron (Fe)-rich silicate or hydroxide minerals and converts into carbonate minerals mimicking natural weathering of serpentine minerals and silicate minerals, *i.e.*, pyroxene as shown in equations (2.1) and (2.2), respectively. (Lackner *et al.*, 1995; Seifritz, 1990; Wilson *et al.*, 2009).

$$Mg_3Si_2O_5(OH)_{4(s)} + 3HCO_3^-{}_{(aq)} + 3H^+{}_{(aq)} \leftrightarrow 3MgCO_{3(s)} + 2SiO_{2(s)} + 5H_2O_{(l)} \quad (2.1)$$

$$(Ca, Mg, Fe)\ SiO_{3\ (s)} + CO_{2\ (g)} \rightarrow (Fe, Mg, Ca)\ CO_{3(s)} + SiO_{2\ (s)} \quad (2.2)$$

Mineral carbonation can be divided into *in-situ* (below ground) and *ex-situ* (above ground) mineral carbonation.

2.3.1 *In-situ* mineral carbonation

In-situ mineral carbonation is like geological storage in which part of the injected CO_2 reacts with Ca and Mg bearing minerals to form stable carbonates underground. However, it is aimed to accelerate the natural process of mineral carbonation through the introduction of water captured CO_2 into the reactive rocks containing a high concentration of Ca, Mg and Fe cations for rapid mineralisation (Sigfusson *et al.*, 2015). Although CO_2 could be introduced in liquid or gaseous form in the reactive rocks, the mineralisation may be slowed due to the need for CO_2 to dissolve in formation waters (Snæbjörnsdóttir *et al.*, 2020). Kelemen and Matter (2008) reported that the higher conversion rates of CO_2 in peridotite rocks would lead to complete storage of CO_2 in the form of stable carbonates before cracking due to heating, hydration and carbonation (Kelemen and Matter, 2008). Moreover, some rocks such as basalt and ultramafic rocks are very reactive to sequester CO_2. Recent literature reports the capturing of > 95% injected CO_2 within two years under the reservoir conditions for basaltic rocks (Kelemen *et al.*, 2019; Matter *et al.*, 2016). Although only 10 % of the earth's surface is covered with basalt, it can capture 33 % of all the CO_2 consumed by natural weathering of silicate rocks (Dessert *et al.*, 2003). As the mass and volume of the phases formed during carbonation are higher than that of the starting material, it is believed that the mineral carbonation will clog the available pores which will substantially decrease the permeability of the rock (Gysi and Stefánsson, 2008; Snæbjörnsdóttir *et al.*, 2018). A recent study showed that the volume expansion during precipitation reaction leads to the cracking and opening of fracture, which may promote the further carbonation by exposing new surface (Kelemen *et al.*, 2019; Kelemen and Hirth, 2012; Zhu *et al.*, 2016). However, Snæbjörnsdóttir *et al.* (2020) argued that this phenomenon would only occur after considerable neutralisation of the injected CO_2 solution due to the dissolution of host rock at some distance from the injection

well, as the dissolution of mineral will also create pores and flow paths near the injection well depending up the acidity of CO_2 water solution (Snæbjörnsdóttir *et al.*, 2020). The fundamental investigation to address the dissolution rates of the host rocks, kinetics and effect of the composition of injected fluid on mineral carbonation at the reservoir conditions, and profound understanding of reservoir environment, *e.g.*, permeability, geomechanics and microstructure of peridotite rocks, are still needed (Kelemen *et al.*, 2019; Power *et al.*, 2013; Romanov *et al.*, 2015; Snæbjörnsdóttir *et al.*, 2020). Furthermore, *in-situ* mineral carbonation also has some challenges related to a high amount of water required for carbonation, and suspected mobilisation of trace and hazardous metals (Oelkers *et al.*, 2008). Despite the success of Carbfix and Wallula projects, a considerable effort is still required to speed up the widespread implementation of *in-situ* mineral carbonation through an understanding of the limitation and potential of this method under diverse conditions (Snæbjörnsdóttir *et al.*, 2020).

2.3.2 *Ex-situ* mineral carbonation

Ex-situ mineral carbonation, on the other hand, occurs above ground (Romanov *et al*. 2015) and is suitable for CO_2 point sources where suitable geological storage is not available (Khoo *et al.*, 2011; Snæbjörnsdóttir *et al.*, 2020), and seismic activity is hindering the exploitation of geological storage (Power *et al.*, 2013). Lackner and co-workers at the Los Alamos National Laboratory were the first to study the mineral carbonation at the industrial scale (Lackner *et al.*, 1995). Figure 2 provides an overview of *ex-situ* mineral carbonation.

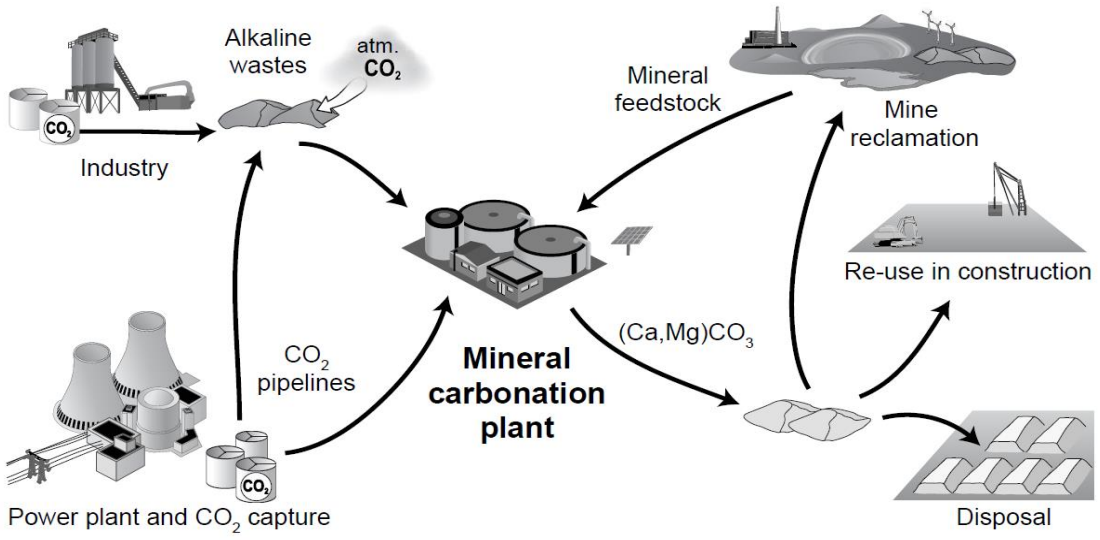

Figure 2.2 Material fluxes and processes associated with industrial carbonation of mineral feedstock and industrial alkaline wastes (modified after IPCC 2005)(Metz *et al.*, 2005).

According to the US National Energy Technology Laboratory (NETL) report (2007), *ex-situ* mineral carbonation was considered unfeasible because of the (i) required scope of mineral operations and (ii) energy requirements for the feed pre-treatment (Huijgen and Comans, 2005). This conclusion led researchers towards the exploration of more economical pre-treatment steps and alternative feedstocks. Some industrial wastes such as fly ash, steel and iron industry waste are also potentially reactive and could be suitable for the small-scale industrial point source emissions (Neeraj and Yadav, 2020; Romanov *et al.*, 2015; Snæbjörnsdóttir *et al.*, 2020). However, CO_2 sequestration at the global scale requires an abundant feedstock and serpentine, being the most abundant among potential candidates, fulfils this requirement (Harrison *et al.*, 2013; Neeraj and Yadav, 2020; Snæbjörnsdóttir *et al.*, 2020). Despite the higher cost of the *ex-situ* mineral carbonation, the unavailability of potential geological storage near CO_2 point source emissions necessitates the exploration in the field of *ex-situ* mineral carbonation for offsetting the local CO_2 emissions (Béarat *et al.*, 2006; Neeraj and Yadav, 2020; Snæbjörnsdóttir *et al.*, 2020). Additionally, the fundamental

knowledge of dissolution kinetics and mineralisation can benefit both the *in-situ* and *ex-situ* mineral carbonation. The major challenges for the commercialisation of mineral carbonation are a) enhancement of chemical reaction kinetics and b) energy cost associated with feed activation (Neeraj and Yadav, 2020; Romanov *et al.*, 2015).

2.4 Raw materials for mineral carbonation

Different raw materials have been explored by various researchers for CO_2 sequestration using mineral carbonation. During the last few years, the focus has shifted towards industrial waste streams for mineral carbonation due to their higher reactivity and small particle size and their generation at primary CO_2 emission sources (Kelly *et al.*, 2011). For example, fly ash (Loo *et al.*, 2017; Montes-Hernandez *et al.*, 2009; Tamilselvi Dananjayan *et al.*, 2016; Ukwattage *et al.*, 2013), steel slag (Chang *et al.*, 2012; Huijgen and Comans, 2006; Reddy *et al.*, 2019; Sarperi *et al.*, 2014; Ukwattage *et al.*, 2017), cement kiln dust (Huntzinger *et al.*, 2009; Rahmani, 2018), alkaline paper mill wastes (R. Perez-Lopez, 2008), ultramafic waste materials (Azadi *et al.*, 2019; Bloise, 2018; Pronost *et al.*, 2011) are promising feedstocks for mineral carbonation. On the other hand, natural mineral such as wollastonite (Ding *et al.*, 2016; Ghoorah *et al.*, 2014; Xu *et al.*, 2019; Yan *et al.*, 2013), olivine (Béarat *et al.*, 2006; Ji *et al.*, 2018; Wang *et al.*, 2019), serpentine (Alizadehhesari *et al.*, 2012; Balucan *et al.*, 2013; Critelli *et al.*, 2015; Du Breuil *et al.*, 2019b; Farhang *et al.*, 2017; Hariharan *et al.*, 2013; Liu and Gadikota, 2018; McKelvy *et al.*, 2004; Miller *et al.*, 2019; Mouedhen *et al.*, 2017; Sanna *et al.*, 2014b) and brucite (Assima *et al.*, 2014; Harrison *et al.*, 2013; Larachi *et al.*, 2018; Schaef *et al.*, 2011) have also been studied by many researchers for mineral carbonation. However, brucite reactivity is highest among the existing natural minerals, but the resources

of brucite are too small to accommodate CO_2 emission at the global scale (Power *et al.*, 2013). Lackner *et al.* (1995) proposed that the serpentine minerals are well distributed and abundant enough to sequester all the CO_2 emissions from the burning of fossil fuels (Lackner *et al.*, 1995). So, serpentine being the most abundant, well-distributed and thermodynamically feasible resource for mineral carbonation, is a leading candidate to sequester CO_2 globally (Harrison *et al.*, 2013; Li and Hitch, 2018). However, a significant challenge for its exploitation lies in its slower dissolution kinetics and energy requirements for the pre-treatment.

Table 2.1 summarises the different feedstocks for mineral carbonation and their theoretical amount required to sequester 1 ton of CO_2 except the values for industrial wastes are based on experimental results in the literature.

Table 2.1

Different feedstocks and their amounts needed to sequester one tonne of CO_2

Feedstocks	Chemical formula	Tonnes of mineral required to sequester 1 ton of CO2	Studied by
Serpentine	$Mg_3Si_2O_5(OH)_4$	2.1	*e.g.*, (Alizadehhesari *et al.*, 2012; Balucan *et al.*, 2013; Critelli *et al.*, 2015; Du Breuil *et al.*, 2019b; Farhang *et al.*, 2017; Hariharan *et al.*, 2013; Liu and Gadikota, 2018; McKelvy *et al.*, 2004; Miller *et al.*, 2019; Mouedhen *et al.*, 2017; Sanna *et al.*, 2014b)
Brucite	$Mg(OH)_2$	1.33	*e.g.*, (Larachi *et al.*, 2018; Schaef *et al.*, 2011)
Wollastonite	$CaSiO_3$	2.64	*e.g.*, (Ding *et al.*, 2016; Ghoorah *et al.*, 2014; Xu *et al.*, 2019; Yan *et al.*, 2013),
Forsterite	Mg_2SiO_4	1.6	*e.g.*, (Béarat *et al.*, 2006; Ji *et al.*, 2018; Wang *et al.*, 2019)
Ultramafic Mining waste	Mg-rich minerals, *e.g.*, serpentine, brucite and olivine	45	*e.g.*, (Azadi *et al.*, 2019; Bloise, 2018; Pronost *et al.*, 2011)
Steel Slag	MgO, CaO and FeO	3.4-15*	*e.g.*, (Chang *et al.*, 2012; Huijgen and Comans, 2006; Reddy *et al.*, 2019; Sarperi *et al.*, 2014; Ukwattage *et al.*, 2017)
Fly Ash	MgO, CaO and Fe_2O_3	12-38*	*e.g.*, (Loo *et al.*, 2017; Montes-Hernandez *et al.*, 2009; Tamilselvi Dananjayan *et al.*, 2016; Ukwattage *et al.*, 2013)

* The required amount of waste to sequester 1 tonne of CO_2 varies depending on the waste composition.

2.5 Reaction chemistry

The carbonation of Mg, Ca, and Fe-rich minerals occur through two distinct reaction steps, the dissolution of the feedstock followed by precipitation of carbonate minerals. The dissolution of serpentine is naturally a slow process, whereas the subsequent carbonate precipitation is a spontaneous exothermic reaction. Since the overall process is exothermic (Eq 1.6), the carbonation process is thermodynamically favoured (Alizadehhesari *et al.*, 2012; Harrison *et al.*, 2013; Metz *et al.*, 2005; Neeraj and Yadav, 2020).

However, the slow dissolution of serpentine minerals (Critelli *et al.*, 2015; Thom *et al.*, 2013; Wilson *et al.*, 2009) impedes the commercialisation of this process (Dlugogorski and Balucan, 2014; Neeraj and Yadav, 2020; Sanna *et al.*, 2014b).

2.6 Feed pre-treatments

Different feed pre-treatments such as chemical (Maroto-Valer *et al.*, 2005; Sanna *et al.*, 2014a), thermal (Balucan *et al.*, 2011; Du Breuil *et al.*, 2019b; Farhang *et al.*, 2017; Ghoorah *et al.*, 2014; Hariharan *et al.*, 2014b; Liu and Gadikota, 2018; McKelvy *et al.*, 2004; O'connor *et al.*, 2005; Pasquier *et al.*, 2014; Werner *et al.*, 2014), mechanical (Gerdemann *et al.*, 2007; Li and Hitch, 2018; O'connor *et al.*, 2005) have been employed to enhance the reactivity of serpentine (Huijgen and Comans, 2005). All these pre-treatments increase the carbonation rate of the silicate mineral by destroying their crystal structures (Aminu *et al.*, 2017). Figure 2.3 displays the steps of mineral carbonation, along with some essential feed pre-treatments.

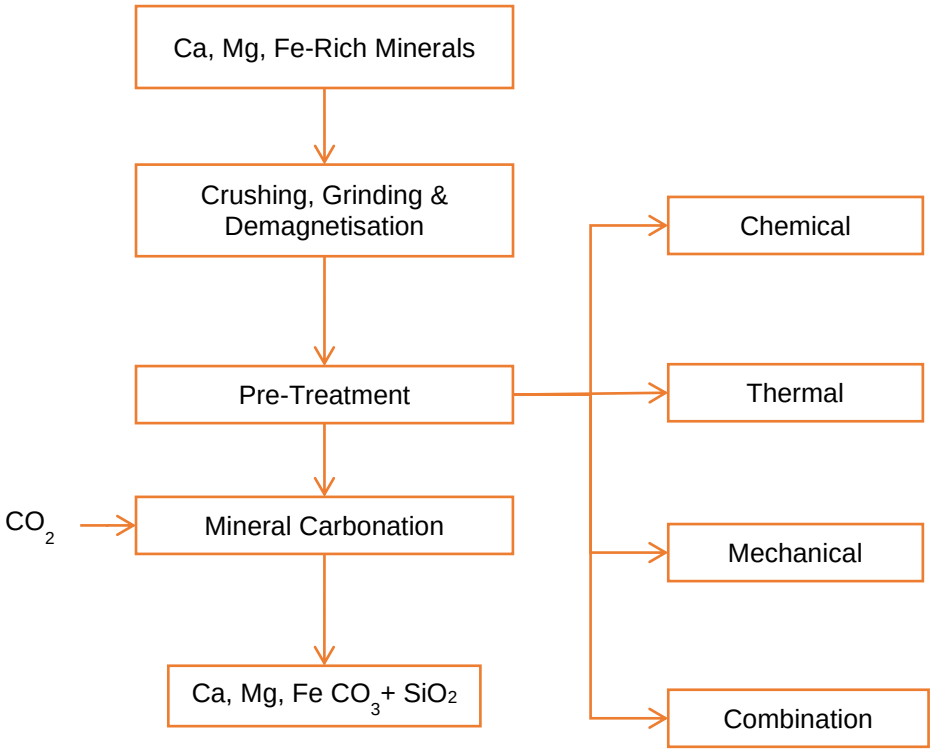

Figure 2.3 Feed pre-treatments for mineral carbonations

2.6.1 Chemical pre-treatment:

The prime purpose of the chemical pre-treatment is to enhance the dissolution kinetics of the Mg-rich silicates through polarisation and weakening of Mg bonds. For example, Lackner *et al.* (1995) employed hydrochloric acid (HCl) as a leaching agent to liberate Mg ions and then utilised it for the production of $Mg(OH)_2$ which can readily be carbonated. However, the enormous energy penalty to generate $Mg(OH)_2$ limits the applicability of this process (Lackner *et al.*, 1995). Similarly, Maroto-Valer *et al.* (2005) performed serpentine mineral activation using various acids and bases. Sulphuric acid (H_2SO_4) was found to be the best chemical to increase the specific surface area due to the removal hydroxyl groups and

leaching of Mg, and they found that the overall degree of conversion for carbonation was ~53 % (Maroto-Valer *et al.*, 2005). However, a recent study found that the extraction of Mg from serpentine mineral using NH_4HSO_4 has better efficiency than the previously reported for H_2SO_4 (Wang and Maroto-Valer, 2011b).

Moreover, various chemical, *e.g.*, ammonium salts, organic and inorganic acids, sodium and potassium hydroxides, have been investigated to increase Mg extraction of the serpentine mineral for mineral carbonation (Azdarpour *et al.*, 2015; Sanna *et al.*, 2016; Sanna *et al.*, 2014a; Teir *et al.*, 2007). Teir *et al.* (2007) found that the makeup cost for the acid-base process, *i.e.*, NaOH and HCl required for carbonation at high temperature and pressure to sequester one tonne of CO_2 is 1300 US$ whereas for using HNO_3 the cost increased to 1600 US$ $(tCO_2)^{-1}$ (Teir *et al.*, 2007). Although the use of a cheaper base such as ammonium hydroxide (NH_4OH) can reduce the cost for HNO_3 and HCl acid-base process to 940 US$ $(tCO_2)^{-1}$ and 600 US$ $(tCO_2)^{-1}$ respectively (Teir *et al.*, 2007), still the cost is very high for the practical implementation of mineral carbonation using chemical pre-treatment. Wang and Maroto-Valer (2011a) reported the carbonation of serpentine minerals using a pH swing process at the ambient pressure conditions could result in pure carbonates production and high dissolution rates (Wang and Maroto-Valer, 2011a). Although the use of NH_4HSO_4 resulted in the extraction of 100 % Mg from the serpentine minerals at 100 ℃ in 3 hr, the cost for the chemical recovery through evaporation remained a significant challenge (Wang and Maroto-Valer, 2011a). Sanna *et al.* (2016) suggested using liquid-liquid extraction for the recovery of the chemical compared to the use of heat for evaporation as this will decrease the energy requirement by 35 % (Sanna *et al.*, 2016). Arce Ferrufino *et al.* (2018) checked the feasibility of HCl and NH_4OH for the pH swing mineral carbonation at the ambient pressure, and they also found that the iron-rich lizardite found in mining waste produced high

purity hydromagnesite along with silica and iron oxide at 90 ℃ (Arce Ferrufino *et al.*, 2018). Iron in the sample act as a catalyst in this process, and they found that the recovery of chemical NH_4Cl can be performed below 250 ℃. Despite the significant efforts, the implementation of mineral carbonation through this challenging due to the high cost of the recycling and disposing of chemicals (Li and Hitch, 2018; Li *et al.*, 2018; Maroto-Valer *et al.*, 2005).

2.6.2 Mechanical pre-treatment:

The mechanical pre-treatment is useful to increase the specific surface area of the particles by size reduction which results in higher reactivity (Huijgen and Comans, 2006; Li and Hitch, 2018; Sanna *et al.*, 2014b). It aims to achieve higher disorder in the mineral by reducing particle size to < 300 μm, necessary to release valuable grains of mineral (Sanna *et al.*, 2014b). The NETL (Gerdemann *et al.*, 2007) developed a scheme for a direct mineral carbonation process, as shown in Figure 2.4.

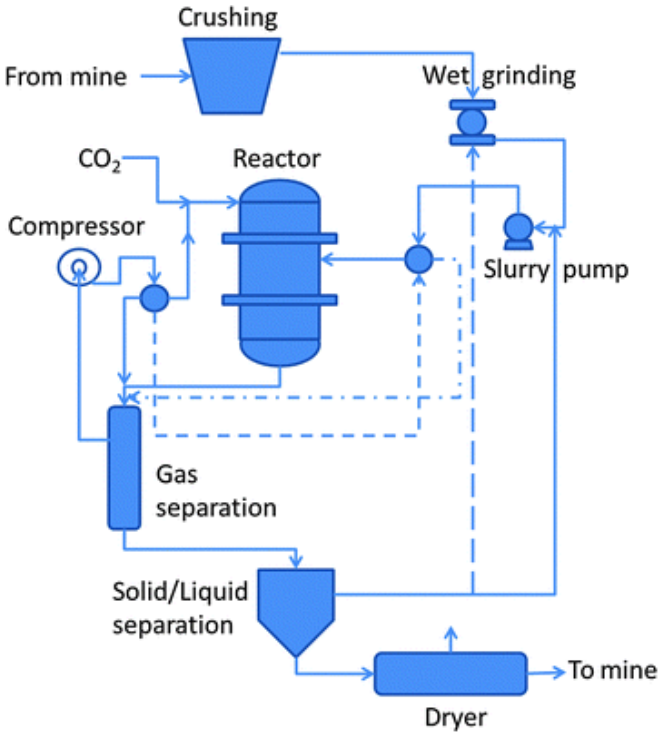

Figure 2.4. Scheme of the NETL process (Gerdemann *et al.*, 2007)

Gerdemann *et al.* (2007) performed the activation of olivine, serpentinite and wollastonite by grinding the mineral to < 75µm and they found that the carbonation of these minerals at 100 - 185 ℃ and 4 - 15 MPa proceeded very slow reaching 50 % extent of the reaction for serpentinite whereas heat-treated serpentine achieved a maximum of 65% conversion in 1 h. Olivine achieved 80 % conversion in 6 h, and wollastonite proved to be more reactive than Mg-rich minerals, *i.e.*, olivine and serpentinites, reaching carbonation over 70 % in 1 h (Gerdemann *et al.*, 2007). Park and Fan (2004) studied the effect of physical activation, *i.e.*, surface agitation through ultrasound, acoustic and integral (*in-situ*) grinding to increase the dissolution of serpentine mineral and pH swing process. They found that the internal (*in-situ*) grinding to remove the SiO_2 layer alone did not provide suitable results. However, the use of Mg leaching solvent along with grinding resulted in rapid dissolution of serpentine (Park and Fan, 2004).

McKelvy *et al.* (2005) studied the mechanical activation by grinding at 300 rpm resulted in the temperature rise of 250 ℃ which enhanced the reactivity by removing structural hydroxyl which transforms to adsorbed water during the dry grinding of serpentinites. However, high-intensity grinding of up to 500 rpm failed during the thermomechanical activation of lizardite due to the sintering of particles (McKelvy *et al.*, 2005). Fabian *et al.* (2010) studied the influence of grinding on the CO_2 storage capacity of olivine and found that although higher attrition resulted in higher conversion rates, the energy consumption was very high (Fabian *et al.*, 2010). Huijgen and Comans (2005) and Zevenhoven and co-workers arrived at similar conclusions (Huijgen and Comans, 2005; Sipilä *et al.*, 2008). However, Li and Hitch, 2018 critically reviewed the mechanical activation of olivine, serpentine and partially serpentinised olivine and suggested that the mechanical pre-treatment could be practical for the olivine by integrating mineral carbonation with the mechanical pre-treatment and by using high purity carbonation product to partly offset the cost of the overall process (Li and Hitch, 2018). However, they suggested combining chemical and thermal pre-treatment for the mineral carbonation of serpentine minerals as mechanical treatment was not very successful due to the sintering of serpentine particles at high attrition grinding (Li and Hitch, 2018). Sanna *et al.* (2014b) also reviewed the activation through mechanical treatment and concluded that the combination of thermal and chemical options are preferred over thermo-mechanical treatment (Sanna *et al.*, 2014b).

2.6.3 Heat pre-treatment

Heat activation of serpentine minerals involves the removal of hydroxyl groups from the structure of serpentine minerals, resulting in the formation of intermediate amorphous phases

which convert to crystalline phases such as forsterite and enstatite at higher temperatures (Dlugogorski and Balucan, 2014; McKelvy *et al.*, 2004; Viti, 2010). Forsterite and enstatite formation decreases the amorphicity, which results in slower dissolution kinetics (Dlugogorski and Balucan, 2014; Du Breuil *et al.*, 2019b; Farhang *et al.*, 2017; McKelvy *et al.*, 2005). The amorphisation of the structure increases Mg^{+2} leaching and enhances the mineral carbonation process (Balucan *et al.*, 2011; Dlugogorski and Balucan, 2014; Du Breuil *et al.*, 2019b). While dehydroxylation of serpentine through heat treatment results in higher reactivity, it also imposes a considerable energy penalty to the carbonation process (Neeraj and Yadav, 2020; O'connor *et al.*, 2005; Snæbjörnsdóttir *et al.*, 2020). Thus, it is essential to optimise this energy-intensive step to achieve the reactivity suitable for the commercialisation of this process.

Balucan *et al.* (2011) performed practical fuel cost analysis for the activation of serpentine. They reported that the previous energy estimates based on the electrical energy (O'connor *et al.*, 2005) were impractical because the efficiency to convert heat energy to electrical power is only 35 %. The use of thermal heat for partial dehydroxylation and lower CO_2 intensive fuel would provide a practical option for activation of serpentine (Balucan *et al.*, 2013; Balucan *et al.*, 2011). The suggested strategy for serpentine activation involves the prograde heating to produce the activated serpentine while recovering 80 % of the sensible heat through heat integration. (Balucan *et al.*, 2013). In this way, the cost for the activation of serpentine can be reduced to 1.25 AUD per tonne of available active serpentine (Balucan *et al.*, 2013). However, this study targets 20% residual hydroxyls as the optimum for heat activation. Since recent literature emphasises the production of highest amorphous content to achieve the higher reactivity (Du Breuil *et al.*, 2019b; Farhang *et al.*, 2017), the calculations of heat activation cost should also consider the maximum amorphisation of serpentine.

The dehydroxylation of serpentine is affected by several factors such as temperature, particle size, the partial pressure of water vapours, type of purge gas and heating rates. Balucan and Dlugogorski (2013) studied the effects of heating rate, particle size, types, and flow of purge gas, on dehydroxylation of antigorite in detail using thermogravimetric and differential scanning calorimetric (TGA-DSC) analysis. They observed that oxidising purge gas, lower heating rates and larger particle size delay the dehydroxylation reaction. They suggested the demagnetisation of samples to avoid the formation of a hematite layer under oxidising purge gas. Consequently, they recommended proper sizing, prior demagnetisation, rapid heating and the use of fluidised bed reactor for commercialisation of this process (Balucan *et al.*, 2013). Fagerlund *et al.* (2009) also suggested the use of fluidised bed reactor for the enhancement of reaction kinetics (Fagerlund *et al.*, 2009). Moreover, Alizadehhesari *et al.* (2012) also studied the effect of particle size and heating rate and found that the higher heating rates and larger particle size resulted in higher heat of reaction and heat transfer resistance between solid and gas.

Balucan *et al.* (2011) investigated the most stable serpentinite, *i.e.,* antigorite to estimate the highest energy requirements during heat activation of serpentine minerals. They provided optimised conditions for dehydroxylation via heat treatment of antigorite based on kinetic modelling. They reported that the optimal heat activation of antigorite requires ≤ 30 min, which includes prograde heating at the rate of 30 ℃ min^{-1} followed by isothermal heating at 730 ℃. Moreover, it has been observed that heat activation within 500-800 ℃ resulted in a major mass loss with the formation of forsterite at 725 ℃ and enstatite above 800℃. However, enstatite formation deactivates the mineral; therefore, the optimum temperature for heat treatment should be less than 800 ℃ (Balucan *et al.,* 2011). Dlugogorski and Balucan

(2014) provided a thorough review of thermal dehydroxylation, factors affecting the reaction kinetics and associated heat requirement for dissolution and carbonation of serpentine mineral. They suggested to avoid the recrystallisation of disordered phases to forsterite and enstatite for proper activation of serpentine minerals as the most reactive serpentine does not require the full dehydroxylation of serpentine to have the highest reactivity as perceived previously (Dlugogorski and Balucan, 2014).

Further, they pointed out that the partial pressure of water vapour must be low to avoid the inhibition of hydroxyl group liberation from the minerals. Moreover, the type of heat treatment also affects thermal events, *e.g.*, dehydroxylation, the formation of forsterite and enstatite and it was observed in prograde heating the thermal event occurs at higher temperatures than in isothermal heating (Dlugogorski and Balucan, 2014). However, all the above studies only focus on optimising thermal dehydroxylation of serpentine independent of carbonation step or referring to the carbonations at high temperature and pressure conditions.

Du Breuil *et al.* (2019b) recently studied the mineralogical transformation during thermal dehydroxylation of lizardite and its effect on the dissolution during aqueous phase mineral carbonation under flue gas conditions. They found two amorphous phases (α- meta and amorphous meta component) during the thermal dehydroxylation and reported that the higher amorphous meta component leads to the higher dissolution of the minerals (Du Breuil *et al.*, 2019b). Farhang *et al*. (2017) also concluded that the higher amorphous meta serpentine phase results in higher dissolution rates. However, it is essential to note that the strong acids or lower pH can also result in high dissolution rates of the serpentine minerals even in the presence of some forsterite (Rim *et al.*, 2020). Although the use of strong acids or the pure CO_2 leads to higher acidity, this also adds additional costs. Hence, recent studies point out

that the formation of the reactive amorphous phase, particle size and pH are the critical parameters for determining the dissolution rates of the serpentine minerals at the flue gas conditions (Du Breuil *et al.*, 2019b; Farhang *et al.*, 2017), this emphasises the need for understanding the effects of above parameters on structural variation during heat treatment.

2.7 Kinetic model development

Despite the importance of the profound understanding of thermal dehydroxylation of the serpentine mineral for the commercialisation of mineral carbonation, only a few attempts have been made to understand the dehydroxylation phenomenon through kinetic modelling.

2.7.1 Model fitting approach

Only limited literature is available on the kinetic modelling of dehydroxylation of serpentine (Alizadehhesari *et al.*, 2012; Balucan *et al.*, 2011; Chollet *et al.*, 2011; Gualtieri *et al.*, 2012; Hariharan *et al.*, 2014b; Liu *et al.*, 2019; Perrillat *et al.*, 2005; Trittschack and Grobéty, 2012; Trittschack *et al.*, 2014; Zhou *et al.*, 2017). However, most of the available literature is based on the kinetic modelling of dehydroxylation based on model-fitting approach (Alizadehhesari *et al.*, 2012; Balucan *et al.*, 2011; Chollet *et al.*, 2011; Gualtieri *et al.*, 2012; Hariharan *et al.*, 2014b; Perrillat *et al.*, 2005). This approach does not provide the model's uniqueness for the system under study (Burnham and Dinh, 2007; Vyazovkin and Sbirrazzuoli, 2006; Vyazovkin and Wight, 1998). For example, Alizadehhesari *et al.* (2012) performed kinetic modelling based on the model-fitting approach. The experimental data was analysed based

on the assumed reaction model among the reaction models for solid-state kinetics shown in Table 2.2 for thermally stimulation solid-state reactions (Alizadehhesari *et al.*, 2012).

Table 2.2

The kinetic function of the most common mechanism operating in solid-state reactions (Alizadehhesari *et al.*, 2012)

Mechanism	***f*(α)**	***g*(α)**
One-dimensional diffusion	$1/2\ \alpha^{-1}$	α^{2}
Two-dimensional diffusion	$[-\ln(1-\alpha)]^{-1}$	$(1-\alpha)\ln(1-\alpha)+\alpha$
Three-dimensional diffusion	$3/2(1-\alpha)^{2/3}[1-(1-\alpha)^{1/3}]^{-1}$	$[1-(1-\alpha)^{1/3}]^{2}$
Ginstling Brounshtein	$3/2[(1-\alpha)^{1/3}-1]^{-1}$	$(1-2/3\ \alpha)-(1-\alpha)^{2/3}$
Contracting cylinder	$2(1-\alpha)^{1/2}$	$1-(1-\alpha)^{1/2}$
Contracting sphere	$3(1-\alpha)^{2/3}$	$1-(1-\alpha)^{1/3}$
Avrami–Erofeev	$2(1-\alpha)[-\ln(1-\alpha)]^{1/2}$	$[-\ln(1-\alpha)]^{1/2}$
Avrami–Erofeev	$3(1-\alpha)[-\ln(1-\alpha)]^{2/3}$	$[-\ln(1-\alpha)]^{1/3}$
Avrami–Erofeev	$4(1-\alpha)[-\ln(1-\alpha)]^{3/4}$	$[-\ln(1-\alpha)]^{1/4}$
Second-order	$(1-\alpha)^{2}$	$(1-\alpha)^{-1}-1$

The estimation of kinetic triplets, *e.g.*, activation energy (E_α), Arrhenius factor (A) and function of reaction $f(\alpha)$ was based on the selected model under non-isothermal approach. They suggested that dehydroxylation reaction for antigorite is a two-step process with 1st step being the nucleation followed by a three-dimensional diffusion-controlled kinetic mechanism, and heat of reaction is 108, 128 and 169 kJ mol^{-1} for the particle size of 90 - 106, 300 - 355 and 425 - 500 µm respectively measured at 100 °C min^{-1} (Alizadehhesari *et al.*, 2012). Gualtieri *et al.* (2012) also performed the kinetic modelling based on the model-fitting approach and studied the antigorite and lizardite dehydroxylation Avrami models, and they found that chrysotile, lizardite and antigorite follows a diffusion-controlled reaction mechanism as observed by Alizadehhesari *et al.* (2012). However, they suggested one-

dimensional diffusion for antigorite with activation energy 255 kJ mol^{-1}, and two-dimensional diffusion for lizardite with 221 kJ mol^{-1} in a temperature range of 612 - 708 ℃ (Gualtieri *et al.*, 2012). These values are considerably higher than the value of 108 kJ mol^{-1} calculated by Alizadehhesari *et al.* (2012). Furthermore, Balucan *et al.* (2011) also used contracting sphere model to define the dehydroxylation reaction mechanism model to optimise heat pre-treatment for antigorite. They reported 160 kJ mol^{-1} of activation energy for antigorite using three-dimensional phase boundary reaction model. It can be observed that the calculated activation energies are not consistent within the literature, and different researchers described the removal of hydroxyl groups from serpentine differently. Furthermore, the variation is activation energy may arise from using various techniques, *i.e.*, TGA or XRD, heating program, isothermal or non-isothermal, particle size distribution, heat and mass transfer limitations and composition of the sample. In addition, heat and mass transfer limitations caused by particle size, sample mass and gas flow rates are also leads to the disparsity in the estimation of activation energy {Fedunik-Hofman, 2019 #228}.

2.7.2 Isoconversional methodology

Isoconversional methodology for kinetic modelling gained popularity as researchers realised that the estimation of kinetic parameters based on an assumed model at a single heating rate generates uncertain results (Burnham and Dinh, 2007). Moreover, non-unique results sometimes provide a completely different mechanism based on the best fit of experimental data. Hence, isoconversional methodology can evaluate kinetic parameters independent of the reaction model (Burnham and Dinh, 2007; Vyazovkin and Sbirrazzuoli, 2006; Vyazovkin and Wight, 1998). The advanced isoconversional approach has its roots in Friedman

(Friedman, 1964) and Ozawa-Flynn-Wall methods (Flynn and Wall, 1966; Ozawa, 1965), and is thus a comparatively new approach to kinetic modelling. Friedman (1964) proposed the differential isoconversional method, as shown in Equation 2.3, which requires numerical differentiation of the experimental curve, the extent of conversion versus temperature.

$$ln\left(\frac{d\alpha}{dt}\right)_{\alpha,i} = ln[A_\alpha f(\alpha)] - \frac{-E_\alpha}{RT_{\alpha,i}} \tag{2.3}$$

The numerical differentiation gives unstable activation energy values due to noisy rate data (Vyazovkin and Sbirrazzuoli, 2006). Flynn and Wall (1966) and Ozawa (1965) took the foundation for the integral isoconversional method (as shown in Eq. 2.4) which uses the Doyle approximation to solve the integral of activation energy and temperature function I(*E*, *T*) (Vyazovkin and Wight, 1998).

$$g(\alpha) \equiv \frac{A}{\beta}\int_0^{T_\alpha} \exp\left(\frac{-E}{RT}\right) dT = \frac{A}{\beta} I(E,T) \tag{2.4}$$

Vyazovkin and Sbirrazzuoli (2006) provided the most accurate way to estimate I (*E*, *T*) through numerical integration. This method is based on the minimisation of the following function (Eq. 2.5).

$$\phi(E_a) = \sum_{i=1}^{n}\sum_{j\neq i}^{n} \frac{I\left(E_\alpha, T_{\alpha,i}\right)\beta_j}{I\left(E_\alpha, T_{\alpha,j}\right)\beta_i} \tag{2.5}$$

However, the calculated values of activation energy differ when calculated through the above three methods. Previously, these differences were attributed to different approximations used

for the temperature integral. However, Sbirrazzuoli *et al.* (2009) showed that the major contributor is the assumption of constant activation energy. Since the constant activation energy is not valid for the complex and multistep reaction mechanisms (Sbirrazzuoli *et al.*, 2009), Vyazovkin and Sbirrazzuoli (2006) provided an advance isoconversional method for kinetic modelling of multistep and complex processes. Moreover, it has also been reported that all the above approaches gave satisfactory result over a small-time interval. However, for a longer time interval, the integral method may lead to erroneous results.

Modern isoconversional techniques to study the kinetics of solid-state reaction started to gain interest only recently. Only a few studied the dehydroxylation kinetics of serpentine minerals using isoconversional methodology (Liu *et al.*, 2019; Trittschack and Grobéty, 2012; Trittschack *et al.*, 2014; Zhou *et al.*, 2017). They studied the dehydroxylation kinetics of brucite, chrysotile and lizardite (Trittschack and Grobéty, 2012, 2013). One recent study performed isoconversional kinetic analysis of the dehydroxylation of antigorite, and the focus is on the dehydroxylation as a trigger to seismicity and its application to mineral carbonation is not discussed (Liu *et al.*, 2019). The modern isoconversional method proposed by Vyazovkin and Sbirrazzuoli (2006) facilitates the estimation of activation energy independent of reaction model, the measurement of the pre-exponential factor (A) is now also possible with this approach (Vyazovkin and Sbirrazzuoli, 2006). Another isoconversional approach of Galwey's can be combined with Vyazovkin's method to evaluate the pre-exponential factor and reaction model (Galwey, 2003). So, Ortega *et al.* (2010) explained the multistep nature of dehydroxylation of kaolinite using the isoconversional method of Vyazovkin and Galwey. They found that the activation energy can be calculated independently using modern isoconversional methodology of Vyazovkin while Galwey's procedure was successful for describing the kinetics of dehydroxylation of kaolinite (Ortega *et al.*, 2010). However,

Trittschack *et al.* (2014) found that Galwey's procedure could not successfully describe the mechanism of solid-state reactions during serpentine dehydroxylation. Since the kinetic study through isoconversional methodology only recently gained momentum, the information on solid-state reaction mechanisms is limited. Therefore, they suggested that spectroscopy, microscopy and ab initio calculations may help to develop inferences on the mechanism of dehydroxylation of serpentine mineral (Ortega *et al.*, 2010; Trittschack and Grobéty, 2012).

2.8 Carbonation of heat-treated serpentine

Several attempts have been made to increase carbonate conversion using heat-treated serpentine (Du Breuil *et al.*, 2019b; Farhang *et al.*, 2017; Hariharan and Mazzotti, 2017b; Hariharan *et al.*, 2014b; Hariharan *et al.*, 2013; Mouedhen *et al.*, 2017; O'connor *et al.*, 2005; Pasquier *et al.*, 2014; Rim *et al.*, 2020). Earlier studies were focussed on the carbonation using strong acids at the high pressure (pure CO_2) and high-temperature conditions to increase the Mg leaching from the serpentine mineral, but the higher energy requirements of this process make it infeasible for the large-scale mineral carbonation (Balucan *et al.*, 2011; McKelvy *et al.*, 2005; O'connor *et al.*, 2005; Teir *et al.*, 2007). However, the interest in carbonation at the flue gas conditions recently gained momentum which could reduce the cost of the process by avoiding the energy-intensive CO_2 capturing (Hariharan *et al.*, 2014b; Mouedhen *et al.*, 2017; Pasquier *et al.*, 2014; Werner *et al.*, 2014; Werner *et al.*, 2013). Hariharan *et al.* (2013) studied the dissolution of thermally activated (75 % dehydroxylated) serpentine for direct mineral carbonation. They found that the use of the CO_2-water system resulted in 60% conversion of Mg in the first 30 min followed by a slow dissolution phase due to silica diffusive barrier (Hariharan *et al.*, 2013). Moreover, they found similar

conversions using HCl under identical condition. Later, Werner *et al.* (2013) employed a single reactor to introduce serpentine step by step to avoid the increase in pH, which hinders the dissolution of serpentine. They also introduced concurrent grinding to prevent the formation of the silica layer. Although this resulted in a higher degree of carbonation, overall conversion did not exceed 20% (Werner *et al.*, 2013). Therefore, they suggested performing the dissolution and precipitation steps in separate reactors (Hariharan *et al.*, 2013; Werner *et al.*, 2013). The carbonation of heat-activated lizardite minerals using double-step carbonation at the flue gas conditions resulted in the higher dissolution and carbonation of 50.2% and 35.6 % respectively (Werner *et al.*, 2014). They suggested that efficient Mg extraction is key to the overall efficiency of the system (Werner *et al.*, 2014). The same group also developed kinetic models to predict the dissolution of partially dehydroxylated lizardite (Hariharan *et al.*, 2016; Hariharan *et al.*, 2014a), precipitation of hydromagnesite (Hariharan and Mazzotti, 2017a) and the passivation behaviour of amorphous silica (Hariharan and Mazzotti, 2017b).

Pasquier *et al.* (2014) investigated the CO_2 solubility and Mg leaching by reacting heat-treated serpentine with 18.2 vol% of CO_2 gas stream and observed 85 % conversion of Mg into carbonates while the model prediction was 98%. This lower conversion was attributed to carbonate precipitation being slower than CO_2 dissolution in water. To overcome this problem, they suggested the occasional introduction of freshwater to avoid water saturation with CO_2, which hinder the precipitation of carbonates. However, they reported that this technique remained effective for only three batches of water. Moreover, another cycle of grinding followed by heat treatment also showed remarkable results but only for one batch (Pasquier *et al.*, 2014). Finally, it was found that the Mg conversion was 63% within 3 h while after 18 h, 95% of Mg was carbonated. Furthermore, they reported that the purity of

carbonate produced during carbonation could offset the part of the processing cost of the process.

However, it can be noted that most of the above studies focus on enhancing the dissolution of heat-activated serpentine, especially lizardite through inhibiting the formation of silica. Only a little attention is given to optimise the heat activation step of the serpentine minerals. A few recent studies tried to optimise the heat activation of lizardite to offset the overall cost of the mineral carbonation (Du Breuil *et al.*, 2019b; Farhang *et al.*, 2017; Rim *et al.*, 2020). For example, Du Breuil *et al.* (2019b) and Farhang *et al.* (2017) Farhang *et al*. (2017) both studied the effect of amorphous phase on the mineral carbonation at the flue gas conditions. However, Du Breuil *et al.* (2019b) observed the highest dissolution for lizardite sample heat activated at 750 ℃ for 15 min which is in contrast to other literature (Farhang *et al.*, 2017; Rim *et al.*, 2020) who propose the heat activation at 630 ℃ and 640 ℃ for 4 hr. According to Du Breuil *et al.* (2019b), this difference in dissolution may be attributed to the different mineralogy, carbonation conditions and methodology to evaluate the carbonation efficiency (Du Breuil *et al.*, 2019b). Recent studies reported the presence of two intermediate phases [α-metaserpentine (semi-crystalline) and amorphous metaserpentine] as observed by McKelvy *et al.* (2004) and concluded that the high amorphous metaserpentine component results in the higher dissolution of lizardite sample (Du Breuil *et al.*, 2019b; Farhang *et al.*, 2017; McKelvy *et al.*, 2005). Additionally, Rim *et al.* (2020) studied the mineral carbonation of lizardite, heat-activated at 640 ℃ for 4 hours and showed that the order of solubilities of different phases observed using ^{29}Si Nuclear magnetic resonance (^{29}Si NMR) analysis is Q^1 (dehydroxylate I) > Q^2 (enstatite) ≫ Q^0 (forsterite) > Q^3 (dehydroxylate II and serpentine), where Q^n represents a phase with "n" number of bridging oxygen atoms in the SiO_4-tetrahedron. Recent studies have shown that use of strong acids could completely dissolve

the crystalline forsterite phase (Matus *et al.*, 2020; Rim *et al.*, 2020) *e.g.*, Rim and co-workers also showed that the use of 2 M HNO_3 results in the Mg extraction up to 90.6 %. However, the heat treatment must be optimised to maximise the amorphous metaserpentine component, which can result in the highest Mg extraction during the mineral carbonation process. In contrast, Rausis *et al.* (2020) showed the formation of two amorphous phases using Raman spectroscopy. They concluded that the amorphous metaserpentine component is poorly reactive silica-rich amorphous phase during the carbonation at mild temperature and pressure conditions.

Although both of the above studies show the formation of amorphous phase formation is a controlling factor for these minerals' reactivity during the carbonation step, a discrepancy exists in the connection of amorphous phases observed in NMR and Raman analysis with amorphous phases observed during XRD analysis. Overall, the above studies signify the importance of understanding intermediate phases and optimising the heat treatment step for the mineral carbonation at the flue gas conditions for the large-scale implementation of mineral carbonation.

2.9 Gaps in the current literature

The growing research on mineral carbonation using heat-treated serpentine minerals emphasise that the deployment of the industrial scale mineral carbonation requires significant efforts for the optimisation of heat-treatment of serpentine mineral, for the enhancement of the dissolution and carbonation efficiencies at the ambient conditions along with the production of value-added end products to offset part of the overall cost of mineral

carbonation. Therefore, the existing knowledge on the dehydroxylation of these minerals along with the high carbon price is not sufficient to implement economic and energy-efficient technology. As the formation of amorphous phase during thermal dehydroxylation is critical for optimising the heat treatment step, the proposed research will provide a profound understanding of the structural variation and mineralogical changes necessary to understand the dehydroxylation temperature to achieve highest amorphous content. Additionally, since the different serpentine minerals have different dehydroxylation temperatures, the optimised temperature to reach highest amorphous content will need the optimisation separately. Also, variation in thermal dehydroxylation kinetics necessitates accurate kinetics parameters to optimise the heat -treatment step for the mineral carbonation. The proposed research will try to minimise the gaps in the knowledge around heat treatment of serpentine minerals, which will help provide energy-efficient solutions for serpentine dehydroxylation.

Based on the above literature review the proposed research will focus on the following points

- ✓ *In-situ* thermal decomposition analysis of serpentine mineral to understand the structural changes during dehydroxylation
- ✓ Factors affecting the structural changes during thermal dehydroxylation
- ✓ Development of isoconversional kinetic model for dehydroxylation of serpentine

2.10 References

Alexander, G., Mercedes Maroto-Valer, M., Gafarova-Aksoy, P. (2007) Evaluation of reaction variables in the dissolution of serpentine for mineral carbonation. Fuel 86, 273-281.

Alizadehhesari, K., Golding, S.D., Bhatia, S.K. (2012) Kinetics of the dehydroxylation of serpentine. Energy & Fuels 26, 783-790.

Aminu, M.D., Nabavi, S.A., Rochelle, C.A., Manovic, V. (2017) A review of developments in carbon dioxide storage. Applied Energy 208, 1389-1419.

Arce Ferrufino, G.L.A., Okamoto, S., Dos Santos, J.C., de Carvalho, J.A., Avila, I., Romero Luna, C.M., Gomes Soares Neto, T. (2018) CO2 sequestration by pH-swing mineral carbonation based on HCl/NH_4OH system using iron-rich lizardite 1T. Journal of CO_2 Utilization 24, 164-173.

Ashley, P.M., Brownlow, J.W. (1993) Silica-carbonate alteration zones in the Great Serpentinite Belt, southern New England Orogen: their nature and significance, In New England Orogen, (eds. P.G. Flood and J.C. Aitchison). University of New England, Armidale, Australia, 197-214.

Assima, G.P., Larachi, F., Molson, J., Beaudoin, G. (2014) Comparative study of five Québec ultramafic mining residues for use in direct ambient carbon dioxide mineral sequestration. Chemical Engineering Journal 245, 56-64.

Azadi, M., Edraki, M., Farhang, F., Ahn, J. (2019) Opportunities for mineral carbonation in Australia's mining industry. Sustainability 11.

Azdarpour, A., Asadullah, M., Mohammadian, E., Hamidi, H., Junin, R., Karaei, M.A. (2015) A review on carbon dioxide mineral carbonation through pH-swing process. Chemical Engineering Journal 279, 615-630.

Balucan, R.D., Dlugogorski, B.Z. (2013) Thermal activation of antigorite for mineralisation of CO_2. Environmental Science & Technology 47, 182-190.

Balucan, R.D., Dlugogorski, B.Z., Kennedy, E.M., Belova, I.V., Murch, G.E. (2013) Energy cost of heat activating serpentinites for CO_2 storage by mineralisation. International Journal of Greenhouse Gas Control 17, 225-239.

Balucan, R.D., Kennedy, E.M., Mackie, J.F., Dlugogorski, B.Z. (2011) Optimisation of antigorite heat pre-treatment via kinetic modelling of the dehydroxylation reaction for CO2 mineralisation. Greenhouse Gases: Science and Technology 1, 294-304.

Béarat, H., McKelvy, M.J., Chizmeshya, A.V.G., Gormley, D., Nunez, R., Carpenter, R.W., Squires, K., Wolf, G.H. (2006) Carbon sequestration via aqueous olivine mineral carbonation: Role of passivating layer formation. Environmental Science & Technology 40, 4802-4808.

Benhelal, E., Rashid, M.I., Rayson, M.S., Brent, G.F., Oliver, T., Stockenhuber, M., Kennedy, E.M. (2019) Direct aqueous carbonation of heat-activated serpentine: Discovery of undesirable side reactions reducing process efficiency. Applied Energy 242, 1369-1382.

Bloise, A.C., Manuela; Gualtieri, Alessandro F. (2018) Effect of grinding on chrysotile, amosite and crocidolite and implications for thermal treatment. Minerals 8.

Brindley, G.W., Hayami, R. (1963) Kinetics and mechanisms of dehydration and recrystallisation of serpentine—I. Clays and Clay Minerals 12, 35-47.

Brindley, G.W., Hayami, R. (1965) Mechanism of formation of forsterite and enstatite from serpentine. Mineralogical Magazine and Journal of the Mineralogical Society 35, 189-195.

Brindley, G.W., Millhollen, G.L. (1966) Chemisorption of water at high temperatures on kaolinite: Effect on dehydroxylation. Science 152, 1385.

Brindley, G.W., Sharp, J.H., Patterson, J.H., Narahari, B.N. (1967b) Kinetics and mechanism of dehydroxylation processes, I. Temperature and vapour pressure dependence of dehydroxylation of kaolinite. American Mineralogist 52, 201-211.

Brindley, G.W., Zussman, J. (1957) A structural study of the thermal transformation of serpentine minerals to forsterite. American Mineralogist 42, 461-474.

Bromiley, G.D., Pawley, A.R. (2003) The stability of antigorite in the systems MgO-SiO_2-H_2O (MSH) and MgO-Al_2O_3-SiO_2-H_2O (MASH): The effects of Al^{3+} substitution on high-pressure stability. American Mineralogist 88, 99-108.

Burnham, A.K., Dinh, L. (2007) A comparison of isoconversional and model-fitting approaches to kinetic parameter estimation and application predictions. Journal of Thermal Analysis and Calorimetry 89, 479-490.

Candela, P.A., Crummett, C.D., Earnest, D.J., Frank, M.R., Wylie, A.G. (2007) Low-pressure decomposition of chrysotile as a function of time and temperature. American Mineralogist 92, 1704-1713.

Capitani, G., Mellini, M. (2004) The modulated crystal structure of antigorite: The *m* = 17 polysome. American Mineralogist 89, 147-158.

Chang, E.E., Pan, S.-Y., Chen, Y.-H., Tan, C.-S., Chiang, P.-C. (2012) Accelerated carbonation of steelmaking slags in a high-gravity rotating packed bed. Journal of Hazardous Materials 227-228, 97-106.

Chollet, M., Daniel, I., Koga, K.T., Morard, G., van de Moortèle, B. (2011) Kinetics and mechanism of antigorite dehydration: Implications for subduction zone seismicity. Journal of Geophysical Research: Solid Earth 116, B04203.

Critelli, T., Marini, L., Schott, J., Mavromatis, V., Apollaro, C., Rinder, T., De Rosa, R., Oelkers, E.H. (2015) Dissolution rate of antigorite from a whole-rock experimental study of serpentinite dissolution from 2<pH<9 at 25°C: Implications for carbon mitigation via enhanced serpentinite weathering. Applied Geochemistry 61, 259-271.

Dessert, C., Dupré, B., Gaillardet, J., François, L.M., Allègre, C.J. (2003) Basalt weathering laws and the impact of basalt weathering on the global carbon cycle. Chemical Geology 202, 257-273.

Dey, S., Dhal, G.C. (2019) Materials progress in the control of CO and CO_2 emission at ambient conditions: An overview. Materials Science for Energy Technologies 2, 607-623.

Ding, W., Yang, H., Ouyang, J., Long, H. (2016) Modified wollastonite sequestrating CO_2 and exploratory application of the carbonation products. RSC Advances 6, 78090-78099.

Dlugogorski, B.Z., Balucan, R.D. (2014) Dehydroxylation of serpentine minerals: Implications for mineral carbonation. Renewable and Sustainable Energy Reviews 31, 353-367.

Drief, A., Nieto, F. (1999) The effect of dry grinding on antigorite from Mulhacen, Spain. Clays and Clay Minerals 47, 417-424.

Du Breuil, C., Pasquier, L.-C., Dipple, G., Blais, J.-F., Iliuta, C.M., Mercier, G. (2019) Mineralogical transformations of heated serpentine and their impact on dissolution during aqueous-phase mineral carbonation reaction in flue gas conditions. Minerals 9.

Durand, B., (2011) Carbon dioxide capture and storage, France, p. 32.

Fabian, M., Shopska, M., Paneva, D., Kadinov, G., Kostova, N., Turianicová, E., Briančin, J., Mitov, I., Kleiv, R.A., Baláž, P. (2010) The influence of attrition milling on carbon dioxide sequestration on magnesium–iron silicate. Minerals Engineering 23, 616-620.

Fagerlund, J., Teir, S., Nduagu, E., Zevenhoven, R. (2009) Carbonation of magnesium silicate mineral using a pressurised gas/solid process. Energy Procedia 1, 4907-4914.

Farhang, F., Oliver, T.K., Rayson, M.S., Brent, G.F., Molloy, T.S., Stockenhuber, M., Kennedy, E.M. (2019) Dissolution of heat-activated serpentine for CO2 sequestration: The effect of silica precipitation at different temperature and pH values. Journal of CO2 Utilization 30, 123-129.

Farhang, F., Rayson, M., Brent, G., Hodgins, T., Stockenhuber, M., Kennedy, E. (2017) Insights into the dissolution kinetics of thermally activated serpentine for CO_2 sequestration. Chemical Engineering Journal 330, 1174-1186.

Fedoročková, A., Hreus, M., Raschman, P., Sučik, G. (2012) Dissolution of magnesium from calcined serpentinite in hydrochloric acid. Minerals Engineering 32, 1-4.

Field, C.B., Raupach, M.R. (2004) The global carbon cycle: integrating humans, climate and the natural world. Island Press, Washington.

Flynn, J.H., Wall, L.A. (1966) General treatment of thermogravimetry of polymers. Journal of Research of the National Bureau of Standards Section a-Physics and Chemistry A 70, 487-+.

Fouda, M.F.R., Amin, R.E.-S., Abd-Elzaher, M.M. (1996) Extraction of magnesia from Egyptian serpentine ore via reaction with different acids. I. Reaction with sulfuric acid. Bulletin of the Chemical Society of Japan 69, 1907-1912.

Friedlingstein, P., Jones, M.W., O'Sullivan, M., Andrew, R.M., Hauck, J., Peters, G.P., Peters, W., Pongratz, J., Sitch, S., Le Quéré, C., Bakker, D.C.E., Canadell, J.G., Ciais, P., Jackson, R.B., Anthoni, P., Barbero, L., Bastos, A., Bastrikov, V., Becker, M., Bopp, L., Buitenhuis, E., Chandra, N., Chevallier, F., Chini, L.P., Currie, K.I., Feely, R.A., Gehlen, M., Gilfillan, D., Gkritzalis, T., Goll, D.S., Gruber, N., Gutekunst, S., Harris, I., Haverd, V., Houghton, R.A., Hurtt, G., Ilyina, T., Jain, A.K., Joetzjer, E., Kaplan, J.O., Kato, E., Klein Goldewijk, K., Korsbakken, J.I., Landschützer, P., Lauvset, S.K., Lefèvre, N., Lenton, A., Lienert, S., Lombardozzi, D., Marland, G., McGuire, P.C., Melton, J.R., Metzl, N., Munro, D.R., Nabel, J.E.M.S., Nakaoka, S.I., Neill, C., Omar, A.M., Ono, T., Peregon, A., Pierrot, D., Poulter, B., Rehder, G., Resplandy, L., Robertson, E., Rödenbeck, C., Séférian, R., Schwinger, J., Smith, N., Tans, P.P., Tian, H., Tilbrook, B., Tubiello, F.N., van der Werf, G.R., Wiltshire, A.J., Zaehle, S. (2019) Global carbon budget 2019. Earth Syst. Sci. Data 11, 1783-1838.

Friedman, H.L. (1964) Kinetics of thermal degradation of char-forming plastics from thermogravimetry. Application to a phenolic plastic. Journal of Polymer Science Part C: Polymer Symposia 6, 183-195.

Fumagalli, P., Poli, S. (2004) Experimentally determined phase relations in hydrous peridotites to 6·5 GPa and their consequences on the dynamics of subduction zones. Journal of Petrology 46, 555-578.

Galwey, A.K. (2003) Perennial problems and promising prospects in the kinetic analysis of nonisothermal rate data. Thermochimica Acta 407, 93-103.

Gao, W., Wen, J., Li, Z. (2014) Dissolution kinetics of magnesium from calcined serpentine in NH_4Cl solution. Industrial & Engineering Chemistry Research 53, 7947-7955.

Gerdemann, S.J., O'Connor, W.K., Dahlin, D.C., Penner, L.R., Rush, H. (2007) *Ex-situ* aqueous mineral carbonation. Environmental Science & Technology 41, 2587-2593.

Ghoorah, M., Dlugogorski, B.Z., Oskierski, H.C., Kennedy, E.M. (2014) Study of thermally conditioned and weak acid-treated serpentinites for mineralisation of carbon dioxide. Minerals Engineering 59, 17-30.

Gualtieri, A.F., Giacobbe, C., Viti, C. (2012) The dehydroxylation of serpentine group minerals. American Mineralogist 97, 666.

Gysi, A.P., Stefánsson, A. (2008) Numerical modelling of CO_2-water-basalt interaction. Mineralogical Magazine 72, 55.

Hariharan, S., Mazzotti, M. (2017a) Growth Kinetics of Synthetic Hydromagnesite at 90 °C. Crystal Growth & Design 17, 317-327.

Hariharan, S., Mazzotti, M. (2017b) Kinetics of flue gas CO_2 mineralisation processes using partially dehydroxylated lizardite. Chemical Engineering Journal 324, 397-413.

Hariharan, S., Repmann-Werner, M., Mazzotti, M. (2016) Dissolution of dehydroxylated lizardite at flue gas conditions: III. Near-equilibrium kinetics. Chemical Engineering Journal 298, 44-54.

Hariharan, S., Werner, M., Hänchen, M., Mazzotti, M. (2014a) Dissolution of dehydroxylated lizardite at flue gas conditions: II. Kinetic modelling. Chemical Engineering Journal 241, 314-326.

Hariharan, S., Werner, M., Hänchen, M., Zingaretti, D., Baciocchi, R., Mazzotti, M. (2014b) Dissolution kinetics of thermally activated serpentine for mineralisation at flue gas conditions. Energy Procedia 63, 5887-5891.

Hariharan, S.B., Werner, M., Zingaretti, D., Baciocchi, R., Mazzotti, M. (2013) Dissolution of Activated Serpentine for Direct Flue-Gas Mineralisation. Energy Procedia 37, 5938-5944.

Harrison, A.L., Power, I.M., Dipple, G.M. (2013) Accelerated carbonation of brucite in mine tailings for carbon sequestration. Environmental Science & Technology 47, 126-134.

He, S., Zhang, W., Liu, L., Huang, Y., He, J., Xie, W., Wu, P., Du, C. (2014) Baseline correction for Raman spectra using an improved asymmetric least squares method. Analytical Methods 6, 4402-4407.

Huijgen, W., Comans, R. (2005) Mineral CO_2 sequestration by carbonation of industrial residues. The Netherlands: Energy Research Centre of the Netherlands (ECN).

Huijgen, W.J.J., Comans, R.N.J. (2006) Carbonation of steel slag for co2 sequestration: Leaching of products and reaction mechanisms. Environmental Science & Technology 40, 2790-2796.

Huntzinger, D.N., Gierke, J.S., Kawatra, S.K., Eisele, T.C., Sutter, L.L. (2009) Carbon dioxide sequestration in cement kiln dust through mineral carbonation. Environmental Science & Technology 43, 1986-1992.

IPCC, (2014) Climate change 2014: Mitigation of climate change. IPCC.

Ji, S., Zhu, J., He, H., Tao, Q., Zhu, R., Ma, L., Chen, M., Li, S., Zhou, J. (2018) Conversion of serpentine to smectite under hydrothermal condition: Implication for solid-state transformation. American Mineralogist 103, 241-251.

Kelemen, P., Benson, S.M., Pilorgé, H., Psarras, P., Wilcox, J. (2019) An overview of the status and challenges of CO_2 storage in minerals and geological formations. Frontiers in Climate 1, 9.

Kelemen, P.B., Hirth, G. (2012) Reaction-driven cracking during retrograde metamorphism: Olivine hydration and carbonation. Earth and Planetary Science Letters 345-348, 81-89.

Kelemen, P.B., Matter, J. (2008) *In-situ* carbonation of peridotite for CO_2 storage. Proceedings of the National Academy of Sciences 105, 17295-17300.

Kelly, K.E., Silcox, G.D., Sarofim, A.F., Pershing, D.W. (2011) An evaluation of *ex-situ*, industrial-scale, aqueous CO_2 mineralisation. International Journal of Greenhouse Gas Control 5, 1587-1595.

Kemache, N., Pasquier, L.-C., Cecchi, E., Mouedhen, I., Blais, J.-F., Mercier, G. (2017) Aqueous mineral carbonation for CO_2 sequestration: From laboratory to pilot scale. Fuel Processing Technology 166, 209-216.

Khawam, A., Flanagan, D.R. (2005) Role of isoconversional methods in varying activation energies of solid-state kinetics: I. isothermal kinetic studies. Thermochimica Acta 429, 93-102.

Khoo, H.H., Sharratt, P.N., Bu, J., Yeo, T.Y., Borgna, A., Highfield, J.G., Bjorklof, T.G., Zevenhoven, R. (2011) Carbon capture and mineralisation in Singapore: preliminary environmental impacts and costs via LCA. Industrial & Engineering Chemistry Research 50, 11350-11357.

Kim, D.-J., Chung, H.-S. (2002) Effect of grinding on the structure and chemical extraction of metals from serpentine. Particulate Science and Technology 20, 159-168.

Kirchofer, A., Becker, A., Brandt, A., Wilcox, J. (2013) CO_2 mitigation potential of mineral carbonation with industrial alkalinity sources in the United States. Environmental Science & Technology 47, 7548-7554.

Lackner, K.S., Wendt, C.H., Butt, D.P., Joyce, E.L., Sharp, D.H. (1995) Carbon dioxide disposal in carbonate minerals. Energy 20, 1153-1170.

Larachi, F., Aksenova, D., Yousefi, B., Maldague, X.P.V., Beaudoin, G. (2018) Thermochemical monitoring of brucite carbonation using passive infrared thermography. Chemical Engineering and Processing - Process Intensification 130, 43-52.

Li, J., Hitch, M. (2018) Mechanical activation of magnesium silicates for mineral carbonation, a review. Minerals Engineering 128, 69-83.

Li, J., Hitch, M., Power, I.M., Pan, Y. (2018) Integrated mineral carbonation of ultramafic mine deposits—a review. Minerals 8.

Li, W., Li, W., Li, B., Bai, Z. (2009) Electrolysis and heat pre-treatment methods to promote CO_2 sequestration by mineral carbonation. Chemical Engineering Research and Design 87, 210-215.

Liu, C., Wang, D., Shen, K., Liu, T., Yi, L. (2019) Kinetics of antigorite dehydration: Rapid dehydration as a trigger for lower-plane seismicity in subduction zones. American Mineralogist 104, 282-290.

Liu, M., Gadikota, G. (2018) Chemo-morphological coupling during serpentine heat treatment for carbon mineralisation. Fuel 227, 379-385.

Liu, M., Gadikota, G. (2020) Single-step, low temperature and integrated CO_2 capture and conversion using sodium glycinate to produce calcium carbonate. Fuel 275, 117887.

Loo, L., Maaten, B., Konist, A., Siirde, A., Neshumayev, D., Pihu, T. (2017) Carbon dioxide emission factors for oxy-fuel CFBC and aqueous carbonation of the Ca-rich oil shale ash. Energy Procedia 128, 144-149.

MacKenzie, K.J.D., Meinhold, R.H. (1994) Thermal reactions of chrysotile revisited: A 29Si and 25Mg MAS NMR study. American Mineralogist 79, 43-50.

Maroto-Valer, M.M., Fauth, D.J., Kuchta, M.E., Zhang, Y., Andrésen, J.M. (2005) Activation of magnesium rich minerals as carbonation feedstock materials for CO_2 sequestration. Fuel Processing Technology 86, 1627-1645.

Martinez, E. (1961) The effect of particle size on the thermal properties of serpentine minerals. American Mineralogist 46, 901-912.

Matter, J.M., Stute, M., Snæbjörnsdottir, S., Oelkers, E.H., Gislason, S.R., Aradottir, E.S., Sigfusson, B., Gunnarsson, I., Sigurdardottir, H., Gunnlaugsson, E., Axelsson, G., Alfredsson, H.A., Wolff-Boenisch, D., Mesfin, K., Fernandez de la Reguera Taya, D., Hall, J., Dideriksen, K., Broecker, W.S. (2016) Rapid carbon mineralisation for permanent disposal of anthropogenic carbon dioxide emissions. Science 352, 1312-1314.

McKelvy, M.J., Chizmeshya, A.V.G., Diefenbacher, J., Béarat, H., Wolf, G. (2004) Exploration of the role of heat activation in enhancing serpentine carbon sequestration reactions. Environmental Science & Technology 38, 6897-6903.

McKelvy, M.J., Diefenbacher, J., Nunez, R., Carpenter, R.W., Chizmeshya, A.V.G., (2005) Simultaneous mechanical and heat activation: A new route to enhance serpentine carbonation reactivity and lower CO_2 mineral sequestration process cost, United States.

Mellini, M., Trommsdorff, V. & Compagnoni, R. (1987) Antigorite polysomatism: behaviour during progressive metamorphism. Contributions to Mineralogy and Petrology 97, 147-155.

Metz, B., Davidson, O., Coninck, H.d., Loos, M., Meyer, L. (2005) IPCC special report on carbon dioxide capture and storage. Cambridge University Press, New York, NY (United States), United States.

Miller, Q.R.S., Schaef, H.T., Kaszuba, J.P., Gadikota, G., McGrail, B.P., Rosso, K.M. (2019) Quantitative review of olivine carbonation kinetics: Reactivity trends, mechanistic insights, and research frontiers. Environmental Science & Technology Letters 6, 431-442.

Molina-Montes, E., Donadio, D., Hernández-Laguna, A., Sainz-Díaz, C.I. (2008a) DFT research on the dehydroxylation reaction of pyrophyllite 2. Characterization of reactants, intermediates, and transition states along the reaction path. The Journal of Physical Chemistry A 112, 6373-6383.

Molina-Montes, E., Donadio, D., Hernández-Laguna, A., Sainz-Díaz, C.I., Parrinello, M. (2008b) DFT research on the dehydroxylation reaction of pyrophyllite 1. First-principle molecular dynamics simulations. The Journal of Physical Chemistry B 112, 7051-7060.

Montes-Hernandez, G., Pérez-López, R., Renard, F., Nieto, J.M., Charlet, L. (2009) Mineral sequestration of CO_2 by aqueous carbonation of coal combustion fly-ash. Journal of Hazardous Materials 161, 1347-1354.

Mouedhen, I., Kemache, N., Pasquier, L.-C., Cecchi, E., Blais, J.-F., Mercier, G. (2017) Effect of pCO_2 on direct flue gas mineral carbonation at pilot scale. Journal of Environmental Management 198, 1-8.

Muravyev, N.V., Koga, N., Meerov, D.B., Pivkina, A.N. (2017) Kinetic analysis of overlapping multistep thermal decomposition comprising exothermic and endothermic processes: thermolysis of ammonium dinitramide. Physical Chemistry Chemical Physics 19, 3254-3264.

Nakano, M., Wada, T., Koga, N. (2015) Exothermic Behavior of Thermal Decomposition of Sodium Percarbonate: Kinetic Deconvolution of Successive Endothermic and Exothermic Processes. The Journal of Physical Chemistry A 119, 9761-9769.

Neeraj, Yadav, S. (2020) Carbon storage by mineral carbonation and industrial applications of CO2. Materials Science for Energy Technologies 3, 494-500.

O'Connor, W.K., Dahlin, D.C., Nilsen, D.N., Gerdemann, S.J., Rush, G.E., Walters, R.P., Turner, P.C., (2001) Research status on the sequestration of carbon dioxide by direct aqueous mineral carbonation. Pittsburgh Coal Conference, University of Pittsburgh, 1249 Benedum Hall, Pittsburgh, PA 15261, United States.

O'Connor, W.K., Dahlin, D.C., Rush, G.E., Gerdemann, S.J., Penner, L.R., (2005) Energy and economic evaluation of *ex-situ* aqueous mineral carbonation, Rubin, E.S., Keith, D.W., Gilboy, C.F., Wilson, M., Morris, T., Gale, J., Thambimuthu, K. (Eds.), Greenhouse Gas Control Technologies 7. Elsevier Science Ltd, Oxford, pp. 2011-2015.

O'connor, W., Dahlin, D., Rush, G., Gerdemann, S., Penner, L., Nilsen, D. (2005) Aqueous mineral carbonation: Mineral availability, pre-treatment, reaction parametrics, and process studies. National Energy Technology Laboratory, US DOE. Available online: http://www. webcitation. org/query.

Oelkers, E.H., Gislason, S.R., Matter, J. (2008) Mineral carbonation of CO_2. Elements 4, 333.

Ortega, A., Macías, M., Gotor, F.J. (2010) The multistep nature of the kaolinite dehydroxylation: Kinetics and mechanism. Journal of the American Ceramic Society 93, 197-203.

Oskierski, H.C., Beinlich, A., Mavromatis, V., Altarawneh, M., Dlugogorski, B.Z. (2019) Mg isotope fractionation during continental weathering and low temperature carbonation of ultramafic rocks. Geochimica et Cosmochimica Acta 262, 60-77.

Oskierski, H.C., Dlugogorski, B.Z., Jacobsen, G. (2013) Sequestration of atmospheric CO_2 in chrysotile mine tailings of the Woodsreef Asbestos Mine, Australia: Quantitative mineralogy, isotopic fingerprinting and carbonation rates. Chemical Geology 358, 156-169.

Ozawa, T. (1965) A new method of analyzing thermogravimetric data. Bulletin of the Chemical Society of Japan 38, 1881-1886.

Park, A.-H.A., Fan, L.-S. (2004) Mineral sequestration: physically activated dissolution of serpentine and pH swing process. Chemical Engineering Science 59, 5241-5247.

Pasquier, L.-C., Mercier, G., Blais, J.-F., Cecchi, E., Kentish, S. (2014) Reaction mechanism for the aqueous-phase mineral carbonation of heat-activated serpentine at low temperatures and pressures in flue gas conditions. Environmental Science & Technology 48, 5163-5170.

Pawley, A. (2003) Chlorite stability in mantle peridotite: the reaction clinochlore+enstatite=forsterite+pyrope+H2O. Contributions to Mineralogy and Petrology 144, 449-456.

Pawley, A.R., Bromiley, G.D. (2003) The stability of antigorite in the systems MgO-SiO_2-H_2O (MSH) and MgO-Al_2O_3-SiO_2-H_2O (MASH): The effects of Al^{3+} substitution on high-pressure stability. American Mineralogist 88, 99-108.

Peng, J., Peng, S., Jiang, A., Wei, J., Li, C., Tan, J. (2010) Asymmetric least squares for multiple spectra baseline correction. Analytica Chimica Acta 683, 63-68.

Perrillat, J.-P., Daniel, I., Koga, K.T., Reynard, B., Cardon, H., Crichton, W.A. (2005) Kinetics of antigorite dehydration: A real-time X-ray diffraction study. Earth and Planetary Science Letters 236, 899-913.

Power, I.M., Harrison, A.L., Dipple, G.M., Wilson, S.A., Kelemen, P.B., Hitch, M., Southam, G. (2013a) Carbon mineralisation: From natural analogues to engineered systems. Reviews in Mineralogy and Geochemistry 77, 305.

Power, I.M., Wilson, S.A., Dipple, G.M. (2013b) Serpentinite carbonation for CO_2 sequestration. Elements 9, 115.

Prigiobbe, V., Hänchen, M., Werner, M., Baciocchi, R., Mazzotti, M. (2009) Mineral carbonation process for CO_2 sequestration. Energy Procedia 1, 4885-4890.

Pronost, J., Beaudoin, G., Tremblay, J., Larachi, F., Duchesne, J., Hébert, R., Constantin, M. (2011) Carbon sequestration kinetic and storage capacity of ultramafic mining waste. Environmental Science & Technology 45, 9413-9420.

R. Perez-Lopez, G.M.-H., J.-M. Nieto, F. Renard, L. Charlet (2008) Carbonation of alkaline paper mill waste to reduce CO_2 greenhouse gas emissions into the atmosphere. Applied Geochemistry, Elsevier 23 8.

Rahmani, O. (2018) CO_2 sequestration by indirect mineral carbonation of industrial waste red gypsum. Journal of CO2 Utilization 27, 374-380.

Rausis, K., Ćwik, A., Casanova, I. (2020) Insights into the direct carbonation of activated lizardite: The identification a poorly reactive amorphous Mg-rich silicate phase. International Journal of Greenhouse Gas Control 100, 103114.

Reddy, K.R., Gopakumar, A., Chetri, J.K. (2019) Critical review of applications of iron and steel slags for carbon sequestration and environmental remediation. Reviews in Environmental Science and Bio/Technology 18, 127-152.

Rietmeijer, F.J.M., Nuth, J.A., Mackinnon, I.D.R. (1986) Analytical electron microscopy of Mg・SiO smokes: A comparison with infrared and XRD studies. Icarus 66, 211-222.

Rim, G., Marchese, A.K., Stallworth, P., Greenbaum, S.G., Park, A.-H.A. (2020) 29Si solid state MAS NMR study on leaching behaviors and chemical stability of different Mg-silicate structures for CO_2 sequestration. Chemical Engineering Journal 396, 125204.

Romanov, V., Soong, Y., Carney, C., Rush, G.E., Nielsen, B., O'Connor, W. (2015) Mineralisation of Carbon Dioxide: A Literature Review. ChemBioEng Reviews 2, 231-256.

Saadatkhah, N., Carillo Garcia, A., Ackermann, S., Leclerc, P., Latifi, M., Samih, S., Patience, G.S., Chaouki, J. (2020) Experimental methods in chemical engineering: Thermogravimetric analysis—TGA. The Canadian Journal of Chemical Engineering 98, 34-43.

Sanna, A., Gaubert, J., Maroto-Valer, M.M. (2016) Alternative regeneration of chemicals employed in mineral carbonation towards technology cost reduction. Chemical Engineering Journal 306, 1049-1057.

Sanna, A., Lacinska, A., Styles, M., Maroto-Valer, M.M. (2014a) Silicate rock dissolution by ammonium bisulphate for pH swing mineral CO_2 sequestration. Fuel Processing Technology 120, 128-135.

Sanna, A., Uibu, M., Caramanna, G., Kuusik, R., Maroto-Valer, M.M. (2014b) A review of mineral carbonation technologies to sequester CO_2. Chemical Society Reviews 43, 8049-8080.

Sanna, A., Wang, X., Lacinska, A., Styles, M., Paulson, T., Maroto-Valer, M.M. (2013) Enhancing Mg extraction from lizardite-rich serpentine for CO_2 mineral sequestration. Minerals Engineering 49, 135-144.

Sarperi, L., Surbrenat, A., Kerihuel, A., Chazarenc, F. (2014) The use of an industrial by-product as a sorbent to remove CO2 and H2S from biogas. Journal of Environmental Chemical Engineering 2, 1207-1213.

Sawai, M., Katayama, I., Hamada, A., Maeda, M., Nakashima, S. (2013) Dehydration kinetics of antigorite using *in-situ* high-temperature infrared microspectroscopy. Physics and Chemistry of Minerals 40, 319-330.

Sbirrazzuoli, N., Vincent, L., Mija, A., Guigo, N. (2009) Integral, differential and advanced isoconversional methods: Complex mechanisms and isothermal predicted conversion–time curves. Chemometrics and Intelligent Laboratory Systems 96, 219-226.

Scambelluri, M., Pettke, T., Rampone, E., Godard, M., Reusser, E. (2014) Petrology and trace element budgets of high-pressure peridotites indicate subduction dehydration of serpentinized mantle (Cima di Gagnone, Central Alps, Switzerland). Journal of Petrology 55, 459-498.

Schaef, H.T., Windisch Jr, C.F., McGrail, B.P., Martin, P.F., Rosso, K.M. (2011) Brucite [Mg(OH2)] carbonation in wet supercritical CO_2: An *in-situ* high-pressure X-ray diffraction study. Geochimica et Cosmochimica Acta 75, 7458-7471.

Schmitt, B., Brönnimann, C., Eikenberry, E.F., Hülsen, G., Toyokawa, H., Horisberger, R., Gozzo, F., Patterson, B., Schulze-Briese, C., Tomizaki, T. (2004) Development of single photon counting detectors at the Swiss Light Source. Nuclear Instruments and Methods in Physics Research Section A: Accelerators, Spectrometers, Detectors and Associated Equipment 518, 436-439.

Seifritz, W. (1990) CO_2 disposal by means of silicates. Nature 345, 486.

Sigfusson, B., Gislason, S.R., Matter, J.M., Stute, M., Gunnlaugsson, E., Gunnarsson, I., Aradottir, E.S., Sigurdardottir, H., Mesfin, K., Alfredsson, H.A., Wolff-Boenisch, D., Arnarsson, M.T., Oelkers, E.H. (2015) Solving the carbon-dioxide buoyancy challenge: The design and field testing of a dissolved CO_2 injection system. International Journal of Greenhouse Gas Control 37, 213-219.

Sipilä, J., Teir, S., Zevenhoven, R. (2008) Carbon dioxide sequestration by mineral carbonation: Literature review update 2005–2007. Åbo Akademi Rep. VT 1.

Snæbjörnsdóttir, S.Ó., Gislason, S.R., Galeczka, I.M., Oelkers, E.H. (2018) Reaction path modelling of *in-situ* mineralisation of CO_2 at the CarbFix site at Hellisheidi, SW-Iceland. Geochimica et Cosmochimica Acta 220, 348-366.

Snæbjörnsdóttir, S.Ó., Sigfússon, B., Marieni, C., Goldberg, D., Gislason, S.R., Oelkers, E.H. (2020) Carbon dioxide storage through mineral carbonation. Nature Reviews Earth & Environment 1, 90-102.

Song, X., Xiaoyu, C., Lin, Q., Yanna, L. (2019) A review of mineral carbonation from industrial waste. IOP Conference Series: Earth and Environmental Science 401, 012008.

Stackhouse, S., Coveney, P.V., Benoit, D.M. (2004) Density-functional-theory-based study of the dehydroxylation behavior of aluminous dioctahedral 2:1 layer-type clay minerals. The Journal of Physical Chemistry B 108, 9685-9694.

Staudigel, H., Schreyer, W. (1977) The upper thermal stability of clinochlore, $Mg_5Al[AlSi_3O_{10}](OH)_8$, at 10–35 kbar P_{H2O} Contributions to Mineralogy and Petrology 61, 187-198.

Svoboda, R. (2019) Reaction/crystallisation kinetics studied via *in-situ* XRD: experimental conditions versus methods of kinetic analysis. Philosophical Magazine 99, 2941-2956.

Tamilselvi Dananjayan, R.R., Kandasamy, P., Andimuthu, R. (2016) Direct mineral carbonation of coal fly ash for CO_2 sequestration. Journal of Cleaner Production 112, 4173-4182.

Tarling, M.S., Smith, S.A.F., Viti, C., Scott, J.M. (2018) Dynamic earthquake rupture preserved in a creeping serpentinite shear zone. Nature Communications 9, 3552.

Teir, S., Kuusik, R., Fogelholm, C.-J., Zevenhoven, R. (2007) Production of magnesium carbonates from serpentinite for long-term storage of CO2. International Journal of Mineral Processing 85, 1-15.

Thom, J.G.M., Dipple, G.M., Power, I.M., Harrison, A.L. (2013) Chrysotile dissolution rates: Implications for carbon sequestration. Applied Geochemistry 35, 244-254.

Trittschack, R., Grobéty, B. (2012) Dehydroxylation kinetics of lizardite. European Journal of Mineralogy 24, 47-57.

Trittschack, R., Grobéty, B., (2013) The dehydroxylation of chrysotile: A combined *in-situ* micro-Raman and micro-FTIR study, American Mineralogist, p. 1133.

Trittschack, R., Grobéty, B., Brodard, P. (2014) Kinetics of the chrysotile and brucite dehydroxylation reaction: a combined non-isothermal/isothermal thermogravimetric analysis and high-temperature X-ray powder diffraction study. Physics and Chemistry of Minerals 41, 197-214.

Ukwattage, N.L., Ranjith, P.G., Li, X. (2017) Steel-making slag for mineral sequestration of carbon dioxide by accelerated carbonation. Measurement 97, 15-22.

Ukwattage, N.L., Ranjith, P.G., Wang, S.H. (2013) Investigation of the potential of coal combustion fly ash for mineral sequestration of CO_2 by accelerated carbonation. Energy 52, 230-236.

UNFCCC, P.A. (2015) United Nations framework convention on climate change. report of the conference of the parties on itss twenty first session, held in Paris from 30 November to 13 December 2015.

Vickery, N.M., Brown, R.E., Percival, I.G. (2010) Manilla 1:100000 geological sheet 9036 explanatory notes. . NSW Geol. Surv., Maitland, Australia.

Viti, C. (2010) Serpentine minerals discrimination by thermal analysis. American Mineralogist 95, 631.

Viti, C., Giacobbe, C., Gualtieri, A.F. (2011) Quantitative determination of chrysotile in massive serpentinites using DTA: Implications for asbestos determinations. American Mineralogist 96, 1003-1011.

Vyazovkin, S., (2015a) Isoconversional methodology, Isoconversional kinetics of thermally stimulated processes. Springer International Publishing, Switzerland, pp. 27-62.

Vyazovkin, S., (2015b) Some basics en route to isoconversional methodology, Isoconversional Kinetics of Thermally Stimulated Processes. Springer, pp. 1-25.

Vyazovkin, S., Sbirrazzuoli, N. (2006) Isoconversional kinetic analysis of thermally stimulated processes in polymers. Macromolecular Rapid Communications 27, 1515-1532.

Vyazovkin, S., Wight, C.A. (1998) Isothermal and non-isothermal kinetics of thermally stimulated reactions of solids. International Reviews in Physical Chemistry 17, 407-433.

Wallwork, K.S., Kennedy, B.J., Wang, D. (2007) The high resolution powder diffraction beamline for the Australian Synchrotron. AIP Conference Proceedings 879, 879-882.

Wang, D., Liu, X., Liu, T., Shen, K., Welch, D.O., Li, B. (2017) Constraints from the dehydration of antigorite on high-conductivity anomalies in subduction zones. Scientific Reports 7, 16893.

Wang, F., Dreisinger, D., Jarvis, M., Hitchins, T. (2019) Kinetics and mechanism of mineral carbonation of olivine for CO_2 sequestration. Minerals Engineering 131, 185-197.

Wang, X., Maroto-Valer, M. (2011a) Integration of CO2 capture and storage based on pH-swing mineral carbonation using recyclable ammonium salts. Energy Procedia 4, 4930-4936.

Wang, X., Maroto-Valer, M.M. (2011b) Dissolution of serpentine using recyclable ammonium salts for CO_2 mineral carbonation. Fuel 90, 1229-1237.

Weber, J.N., Greer, R.T. (1965) Dehydration of serpentine: heat of reaction and reaction kinetics at PH_2O=1 ATM. American Mineralogist 50, 450-464.

Werner, M., Hariharan, S., Mazzotti, M. (2014) Flue gas CO_2 mineralisation using thermally activated serpentine: From single- to double-step carbonation. Energy Procedia 63, 5912-5917.

Werner, M., Hariharan, S.B., Bortolan, A.V., Zingaretti, D., Baciocchi, R., Mazzotti, M. (2013) Carbonation of activated serpentine for direct flue gas mineralisation. Energy Procedia 37, 5929-5937.

White, C.E., Provis, J.L., Proffen, T., Riley, D.P., van Deventer, J.S.J. (2010) Density functional modelling of the local structure of kaolinite subjected to thermal dehydroxylation. The Journal of Physical Chemistry A 114, 4988-4996.

Whittaker, E.J.W., Zussman, J. (1956) The characterization of serpentine minerals by X-ray diffraction. Mineralogical Magazine and Journal of the Mineralogical Society 31, 107-126.

Wilson, S.A., Dipple, G.M., Power, I.M., Thom, J.M., Anderson, R.G., Raudsepp, M., Gabites, J.E., Southam, G. (2009) Carbon dioxide fixation within mine wastes of ultramafic-hosted ore deposits: Examples from the Clinton Creek and Cassiar chrysotile deposits, Canada. Economic Geology 104, 95-112.

Wilson, S.A., Harrison, A.L., Dipple, G.M., Power, I.M., Barker, S.L.L., Ulrich Mayer, K., Fallon, S.J., Raudsepp, M., Southam, G. (2014) Offsetting of CO_2 emissions by air capture in mine tailings at the Mount Keith Nickel Mine, Western Australia: Rates, controls and prospects for carbon neutral mining. International Journal of Greenhouse Gas Control 25, 121-140.

Xu, X., Liu, W., Chu, G., Zhang, G., Luo, D., Yue, H., Liang, B., Li, C. (2019) Energy-efficient mineral carbonation of $CaSO_4$ derived from wollastonite via a roasting-leaching route. Hydrometallurgy 184, 151-161.

Yan, H., Zhang, J., Zhao, Y., Zheng, C. (2013) CO_2 sequestration from flue gas by direct aqueous mineral carbonation of wollastonite. Science China Technological Sciences 56, 2219-2227.

Zhang, M., Redfern, S.A.T., Salje, E.K.H., Carpenter, M.A., Wang, L. (2010) H2O and the dehydroxylation of phyllosilicates: An infrared spectroscopic study. American Mineralogist 95, 1686-1693.

Zhou, S., Wei, Y., Li, B., Ma, B., Wang, C., Wang, H. (2017) Kinetics study on the dehydroxylation and phase transformation of $Mg_3Si_2O_5(OH)_4$. Journal of Alloys and Compounds 713, 180-186.

Zhu, W., Fusseis, F., Lisabeth, H., Xing, T., Xiao, X., De Andrade, V., Karato, S.-i. (2016) Experimental evidence of reaction-induced fracturing during olivine carbonation. Geophysical Research Letters 43, 9535-9543.

Chapter 3: Kinetics of Antigorite Dehydroxylation for CO_2 Sequestration

3 Abstract

The slow dissolution of serpentine minerals hinders the large-scale implementation of CO_2 sequestration by mineral carbonation. Heat treatment, resulting in amorphisation of the serpentine mineral structure, is thus required to increase reactivity during carbonation. This study employs thermal analyses (TGA-DSC) in conjunction with *in-situ* synchrotron powder X-ray diffraction (PXRD) to record concurrent mass loss, heat flow, and mineralogical changes during thermal treatment of antigorite. Isoconversional kinetic modelling demonstrates that thermal decomposition of antigorite is a complex multistep reaction, with activation energies (E_α) varying between 290 and 515 kJ mol^{-1}. The combination of isoconversional kinetics with *in-situ* synchrotron PXRD provides, for the first time, insight into the relationship between activation energies and phase changes during antigorite dehydroxylation, suggesting that changes in the local crystal structure related to intermediate phase and forsterite formation are responsible for the steep increase in activation energy above 650 °C. The use of synchrotron XRD enables identification of three intermediate phases forming during antigorite dehydroxylation. Formation of a semi-crystalline chlorite-like phase (γ metaserpentine) represents an additional reaction pathway for the decomposition of Al_2O_3-rich antigorite, whereas two distinct amorphous components (α and β-metaserpentine) form simultaneously from antigorite but then convert into forsterite and enstatite at the higher temperature, respectively. For the Al_2O_3-rich antigorite, which we use as an example feedstock, only about 49 % dehydroxylation can be achieved prior to the onset

of forsterite formation and the associated increase in activation energy. This suggests that Mg extraction during the practical implementation of mineral carbonation under lean flue gas conditions would be severely limited by the high thermal stability of Al_2O_3-bearing antigorite.

3.1 Introduction

Sequestration of CO_2 through mineral carbonation is considered as one of the most promising technologies for safe and permanent disposal of CO_2 (Gerdemann *et al.*, 2007; Huijgen and Comans, 2005; Kirchofer *et al.*, 2013; Liu and Gadikota, 2018, 2020; Maroto-Valer *et al.*, 2005; McKelvy *et al.*, 2004; Miller *et al.*, 2019; Prigiobbe *et al.*, 2009; Rim *et al.*, 2020; Werner *et al.*, 2014). Natural weathering of serpentine into stable carbonates (Oskierski *et al.*, 2019; Oskierski *et al.*, 2013b; Wilson *et al.*, 2014) demonstrates the thermodynamic feasibility of the mineral carbonation process, and the abundance and wide distribution of serpentine minerals distinguish them as an excellent raw material for CO_2 sequestration (Lackner *et al.*, 1995). However, the slow dissolution of serpentine minerals currently hinders large-scale commercialisation of mineral carbonation (Dlugogorski and Balucan, 2014; Pasquier *et al.*, 2014; Power *et al.*, 2013). The dissolution rate of serpentine minerals can be improved through thermal dehydroxylation (Alexander *et al.*, 2007; Dlugogorski and Balucan, 2014; Drief and Nieto, 1999; Kim and Chung, 2002; Maroto-Valer *et al.*, 2005; McKelvy *et al.*, 2004; Sanna *et al.*, 2014b), which induces amorphisation of the serpentine structure and enhances the reactivity of the mineral during subsequent carbonation (Dlugogorski and Balucan, 2014; Ghoorah *et al.*, 2014; Li *et al.*, 2009; Liu and Gadikota, 2018; McKelvy *et al.*, 2004). Hence, thermal dehydroxylation is crucial for the economic

feasibility of the mineral carbonation process (Gao *et al.*, 2014; Hariharan and Mazzotti, 2017b; Hariharan *et al.*, 2014b; Mouedhen *et al.*, 2017) and an intimate understanding of the dehydroxylation is thus required to optimise reactivity while limiting additional energy cost (Balucan *et al.*, 2013).

The dehydroxylation of serpentine minerals result in the formation of amorphous phases between 550 to 750 ℃, which convert to forsterite above 700 ℃ and enstatite above 800 ℃ (Brindley and Hayami, 1963, 1965; Du Breuil *et al.*, 2019b; MacKenzie and Meinhold, 1994; McKelvy *et al.*, 2004). Figure 3.1 and Equations 3.1 to 3.3 illustrate the commonly accepted reaction scheme for the dehydroxylation of serpentine minerals, based on NMR observations of chrysotile and lizardite dehydroxylation (MacKenzie and Meinhold, 1994; Rim *et al.*, 2020).

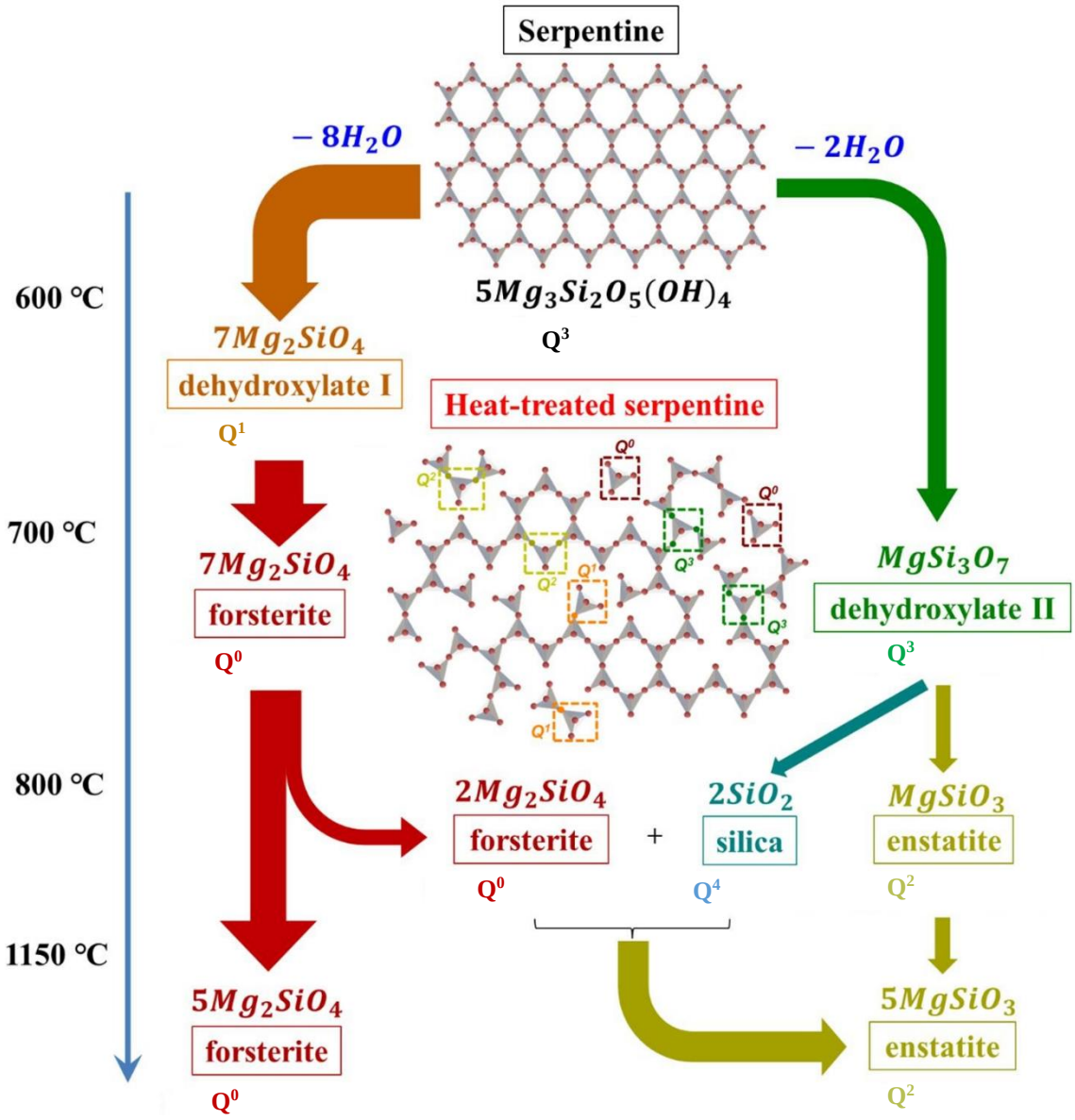

Figure 3.1. Schematic of thermal decomposition of serpentine after MacKenzie and Meinhold (1994) and modified from Rim *et al*. (2020)

serpentine → dehydroxylate I + dehydroxylate II + water

$5Mg_3Si_2O_5(OH)_4 \rightarrow 7Mg_2SiO_4 + MgSi_3O_7 + 10H_2O$ (3. 1)

dehydroxylate II → enstatite + silica (3. 2)

$$MgSi_3O_7 \rightarrow MgSiO_3 + 2SiO_2$$

$$\begin{array}{lll} \text{dehydroxylate I} & + \text{silica} & \rightarrow \text{forsterite} + \text{enstatite} \\ 7Mg_2SiO_4 & + 2SiO_2 & \rightarrow 5Mg_2SiO_4 + 4MgSiO_3 \end{array} \quad (3.\ 3)$$

However, the nomenclature for amorphous phases formed during serpentine dehydroxylation is inconsistent, variably referring to serpentine anhydride (Brindley and Zussman, 1957), talc-like phases (d > 10 Å; *e.g.*, Candela *et al.* (2007), dehydroxylate I (Mg_2SiO_4 at σ = -72 to -74 ppm) and dehydroxylate II ($MgSi_3O_7$ at σ = -97 ppm) (MacKenzie and Meinhold, 1994; Rim *et al.*, 2020) or *α*-metaserpentine (d = 14.7 Å) and amorphous metaserpentine ($2.1 \leq d \leq 5.2$ Å) (McKelvy *et al.*, 2004; Rausis *et al.*, 2020)

Most earlier literature (Alizadehhesari *et al.*, 2012; Balucan *et al.*, 2011; Chollet *et al.*, 2011; Gualtieri *et al.*, 2012; Perrillat *et al.*, 2005; Sawai *et al.*, 2013) relied on kinetic analysis of serpentine dehydroxylation by model-fitting, which seeks to generate a phenomenological understanding of the reaction mechanism based on the best fit of experimental data to well-defined reaction models. However, model fitting assumes a single-step reaction mechanism and constant activation energy (E) for the entire dehydroxylation process (Alizadehhesari *et al.*, 2012; Balucan *et al.*, 2011; Gualtieri *et al.*, 2012). Its applicability to reaction kinetics of solid-state systems and multistep processes with varying activation energy is considered dubious (Khawam and Flanagan, 2005; Ortega *et al.*, 2010; Vyazovkin, 2015b; Vyazovkin and Sbirrazzuoli, 2006; Vyazovkin and Wight, 1998). More recent studies (Liu *et al.*, 2019; Trittschack and Grobéty, 2012; Trittschack *et al.*, 2014), have confirmed that the dehydroxylation of chrysotile (Trittschack *et al.*, 2014), lizardite (Trittschack and Grobéty, 2012) and antigorite (Liu *et al.*, 2019) are multistep reactions and thus prone to

misinterpretation during kinetic analysis by model fitting. Conversely, isoconversional kinetic modelling considers activation energy (E_α) over small intervals of the extent of conversion (α) (Vyazovkin and Sbirrazzuoli, 2006; Vyazovkin and Wight, 1998), yielding a better mechanistic understanding of the reaction, which is independent of a reaction model (Ortega *et al.*, 2010; Trittschack and Grobéty, 2012, 2013; Vyazovkin and Sbirrazzuoli, 2006).

In this study, we employ thermogravimetric and calorimetric analyses, in conjunction with *in-situ* synchrotron powder X-ray diffraction (PXRD), to investigate concurrent weight loss, heat flow and structural changes during dehydroxylation of antigorite. This approach allows simultaneous monitoring of the removal of volatile species, energy requirements and phase changes, especially the formation of amorphous phases that determine reactivity during subsequent carbonation but are challenging to detect by laboratory XRD. We present a model-free kinetic analysis of antigorite dehydroxylation based on the isoconversional interpretation of thermogravimetric and calorimetric data. The resulting temperature-resolved records of mass loss, heat flow, phase changes, and activation energy provide hitherto unavailable insights into the dehydroxylation of antigorite, which have important implications for the optimisation of serpentine heat treatment strategies for large scale CO_2 sequestration.

3.2 Experimental section

3.2.1 Sample preparation

This study investigates serpentinised harzburgite from the Great Serpentinite Belt, a dismembered ophiolite sequence in Northern New South Wales, Australia (Oskierski *et al.*, 2013b). Antigorite at Attunga has formed through contact metamorphism during the intrusion of the Attunga Creek Monzogranite (Ashley and Brownlow, 1993; Oskierski *et al.*, 2013b; Vickery *et al.*, 2010). The sample was crushed, ground in an agate ring mill for 2 – 3 minutes and sieved to obtain a size fraction <45 µm, which represents the minimum size considered as economically feasible for mineral carbonation (Balucan *et al.*, 2011; Huijgen and Comans, 2005). Samples were then demagnetised to remove the majority of Fe-rich phases such as magnetite.

3.2.2 X-ray fluorescence (XRF) and LOI analyses

A PANalytical MagiX FAST XRF was used for the analysis of the chemical composition of the demagnetised powdered sample using a glass bead prepared by lithium tetraborate/lithium metaborate fusion. Loss on ignition (LOI) was determined through a robotic LabFit TGA-4000, thermogravimetric analyser.

3.2.3 Synchrotron powder X-ray diffraction

The powder X-ray diffraction (PXRD) analysis was performed at the PXRD beamline at the Australian Synchrotron (Wallwork *et al.*, 2007) to monitor phase changes during the prograde heating of antigorite. The X-ray wavelength (0.688987(2) Å) was calibrated using NIST SRM LaB_6 660b and diffractograms were recorded using a MYTHEN II detector (Schmitt *et*

al., 2004) over a 2θ range of 2 – 77°, with an acquisition rate of one scan per minute. Diffractograms were collected on samples in oscillating capillaries (0.7 mm OD x 0.01 mm wall thickness) heated from 100 °C to 915 °C at 8 °C min^{-1} under a continuous flow of N_2. Temperature calibration was based on the α to β-quartz phase transition temperature (573 °C) of a pure quartz sample and the melting point of reagent grade NaCl (801 °C) (see Fig.S3.1 in section 1 of Appendix A).

Planer structural disorder in serpentine minerals makes modelling of their crystal structures and their quantification in mixtures challenging (Wilson *et al.,* 2006). Wilson *et al.* (2006) demonstrated that the amount of disordered serpentine minerals could be determined with satisfactory precision (± 5-10 % relative error) by modelling serpentine minerals as amorphous phases using the Pawley method. However, this method can only account for one amorphous phase per sample (Wilson *et al.,* 2006). Consequently, this method cannot be applied to serpentine dehydroxylation, which involves serpentine and the formation of multiple amorphous phases. Also, identification of a suitable internal standard for *in-situ* experiments up to 1000 ° C was challenging and prevented implementation of the Pawley or Rietveld refinements. Therefore, we use non-overlapping peak reflections to monitor the evolution of different phases as done in several previous studies (Cattaneo *et al.,* 2003).

PDViPeR software was used to process the XRD data for phase identification in Crystal Impact Match! software, utilising the crystallography open database (COD). The background signal from the glass capillary was constant over the experimental temperature range. The evolution of amorphous phases was determined as the difference in integrated intensity between the amorphous background and the capillary background; both modelled using the asymmetric least square smoothing method in Origin software (see Fig. S3.2 in section 2 of

Appendix A) He *et al.* (2014); Peng *et al.* (2010). Non-overlapping peaks of crystalline phases were numerically integrated using Origin software after subtraction of the amorphous background. Reaction progress (α) was obtained by normalising integrated intensities of amorphous and crystalline phases to the maximum integrated intensity of the respective phases.

3.2.4 Thermal analyses

A simultaneous thermal analyser Netzsch STA-449F3 was used for concurrent thermogravimetric (TGA) and differential scanning calorimetric (DSC) analyses. Sensitivity calibration was performed using a sapphire disc standard (dimensions 0.25 mm × 6 mm) in a covered Pt-Rh crucible under a constant argon flow of 40 mL min^{-1}. Additionally, a routine furnace burn-off at 1000 ℃ for 10 min under a synthetic airflow of 100 mL min^{-1} served to eliminate all residual impurities. The non-isothermal runs were carried out in a covered Pt-Rh crucible (Pt:Rh = 80:20, Ø 6.8 mm × 4 mm) at a heating rate of 2.5, 5.0, 7.5, 8.0 and 10.0 ℃ min^{-1} from 20 – 1000 ℃ under argon flow of 40 mL min^{-1}, employing 10.0 ± 0.05 mg of powdered antigorite sample. Blank runs (*i.e.,* without sample) under identical conditions enabled TGA thermal buoyancy and DSC baseline corrections. The fraction of residual hydroxyls decreasing from 100 to 0 % between 500 - 800 ℃ to represent the progress of dehydroxylation (Fig. S3.5).

3.2.5 Estimation of isoconversional kinetic parameters

The isoconversional method assumes that the reaction model remains constant over a small degree of conversion and independent of the heating rate (Vyazovkin and Sbirrazzuoli, 2006). The extent of conversion (α) can be calculated from the baseline subtracted DSC (Fig. S3.6) and TGA data using Equations 3.4 and 3.5, respectively:

$$\alpha = \frac{\Delta H_i}{\Delta H_T} = \left(\frac{A_i}{A_T}\right) \quad (3.4)$$

$$\alpha = \left(\frac{m_i - m_t}{m_i - m_f}\right) \quad (3.5)$$

where ΔH_i represents the instantaneous change in enthalpy as calculated by the area under the heat flow curve (*i.e.*, A_i) over a small interval of conversion, and ΔH_T (or A_T) denotes the total reaction enthalpy as computed by the total area under the heat flow curve. The area between the onset and end of the endothermic/exothermic peak corresponds to the total heat flow A_T, in DSC. This study only based on the kinetics of endothermic dehydroxylation peak. Similarly, for the TGA-based kinetics (Eq. 3.5), m_i, m_t, and m_f, signify the initial mass, mass at any instant, and the final mass, respectively. The onset and end of the corresponding differential thermogravimetric (DTG) curves served to mark the region that corresponds to the initial (m_i) and final mass (m_f) in TGA data for the calculation of the extent of conversion.

Equation 3.6 describes the rate of reaction in solid-state, as a function of the temperature-dependent rate constant *k(T)*, and the representative reaction model $f(\alpha)$.

$$\frac{d\alpha}{dt} = k(T)\, f(\alpha) \quad (3.6)$$

Substituting the Arrhenius expression for the temperature-dependent rate constant, and heating rate (β =dT/dt) into Equation 3.7 yields the generalised non-isothermal dependency in Equation 3.4.

$$\frac{d\alpha}{dT} = \frac{A}{\beta}.e^{\frac{-E}{RT(t)}}.f(\alpha) \tag{3. 7}$$

Equation 3.7 can be solved using numerical differentiation of the experimental extent of conversion (Vyazovkin and Sbirrazzuoli, 2006). Alternatively, one can apply its integral form (Eq. 3.8) for approximate solutions (Vyazovkin, 2015a, b).

$$\int_0^{\alpha} \frac{d\alpha}{A.f(\alpha)} = \frac{1}{\beta}\int_0^{T} e^{\frac{-E}{RT(t)}}\,dT = \frac{1}{\beta}[I\,(E_\alpha, T_\alpha)] \tag{3. 8}$$

There are many alternative solutions for Equation 3.8. However, the advanced Vyazovkin method offers excellent accuracy (Vyazovkin and Sbirrazzuoli, 2006). For a set of n experiments carried out at different heating rates, the activation energy (E_α) minimises Equation 3.9 at a particular α. The parameters i and j represent the experiments performed at different heating rates.

$$n(n-1) = \emptyset(E_\alpha) = \sum_{i=1}^{n}\sum_{j\neq i}^{n}\frac{I\,(E_\alpha, T_{\alpha,i})\beta_j}{I\,(E_\alpha, T_{\alpha,j})\beta_i} \tag{3. 9}$$

We use numerical interpolation of the raw data to obtain the temperatures at the desired extent of conversion, selecting an interval of 0.025 over the entire fractional conversion range

(*i.e.*, α = 0.025, 0.05, 0.075, 0.01,..., 0.975). Additionally, we evaluate the isoconversional pre-exponential factor (*A*) considering the compensation based on Equation 3.10.

$$\ln A_i = \frac{E_i}{RT} + \ln\left(\frac{(\frac{d\alpha}{dt})}{f(\alpha)}\right)_i = a + bE_i \qquad (3.\ 10)$$

Where A_i and E_i represent a pair of pre-exponential factor and activation energy for "i^{th}" solid-state reaction models listed in the supplementary information (Table S3.2). The straight-line plot, for E_α and A_α pairs from all reaction models, is then used to estimate the coefficients "*a*" and "*b*" for the compensation effect.

$$\ln A_\alpha = a + bE_\alpha \qquad (3.\ 11)$$

Finally, we use Equation 3.11 to find the isoconversional pre-exponential factor A_α for a given extent of conversion using isoconversional E_a values.

3.3 Results and discussion

3.3.1 Sample characterisation

Synchrotron PXRD at room temperature (Fig. S3.7) shows that the sample consists of antigorite (COD ref. code: 96-900-3104) along with minor traces of magnetite (96-900-0927), quartz (96-153-6390) and hematite (96-900-0140). Antigorite is identified based on the characteristic (330) peak at 2θ = 25.4° (d = 1.6 Å), which is absent from the other

serpentine polymorphs (Whittaker and Zussman, 1956). The chemical composition and loss on ignition of 12.04 % (Table 3.1) are also consistent with antigorite, which shows the lowest mass loss among the serpentine polymorphs due to the absence of three brucite units every half wavelength (Mellini, 1987).

Table 3.1

XRF analysis for the demagnetised sample of antigorite. The chemical composition of antigorite is expressed in $\%_{wt./wt.}$ and LOI represents the volatile components based on loss on ignition at 1000 °C. The table lists Ni rather than NiO.

Species	SiO_2	Al_2O_3	MgO	Fe_2O_3	Cr_2O_3	CaO	Na_2O	P_2O_5	SO_3	Ni	LOI	Total
$\%_{wt./wt.}$	41.86	1.69	38.90	4.07	0.247	0.740	0.050	0.008	0.056	0.195	12.04	99.86

3.3.2 Phase changes during dehydroxylation of antigorite

Figure 3.2 illustrates the phase changes during antigorite dehydroxylation recorded by prograde *in-situ* synchrotron PXRD.

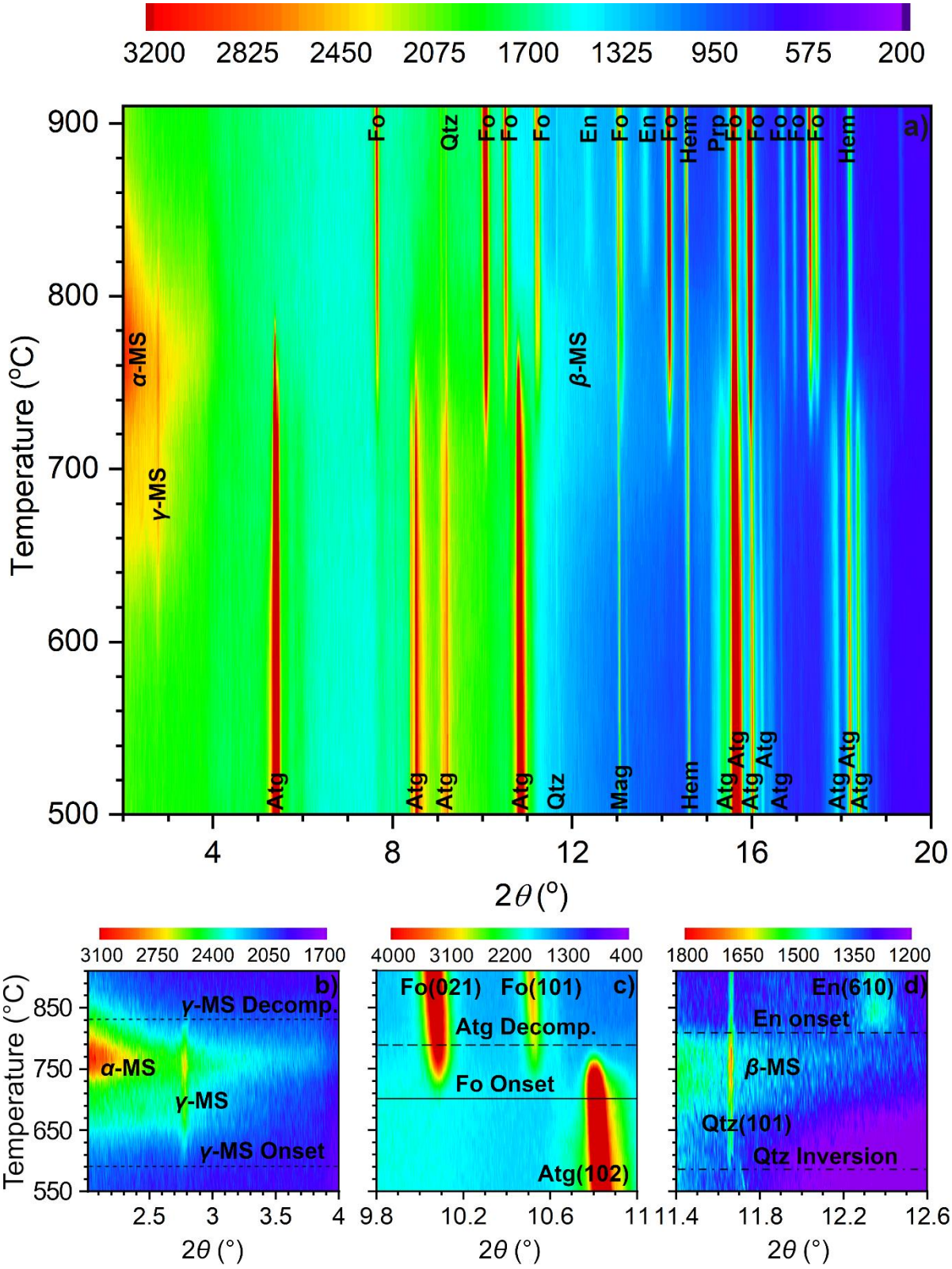

Figure 3.2. a) Phase changes during heating of antigorite at 8 °C min^{-1} recorded by *in-situ* synchrotron PXRD. **b)** Details of the amorphous α-metaserpentine and chlorite-like semi-crystalline γ-metaserpentine components and. **c)** Details of the (102) peak reflection of antigorite and the (021) and (101) peaks of forsterite. **d)** Details

of the (101) peak of quartz, the amorphous β-metaserpentine component and the (610) peak of enstatite. Peaks/phases are labelled as Atg: antigorite, Fo: forsterite, En: enstatite, Hem: hematite, Mag: magnetite, Prp: pyrope and Qtz: quartz α-MS: α-metaserpentine, β-MS: β-metaserpentine, γ-MS: γ-metaserpentine. Red lines show events during dehydroxylation: Fo Onset: onset of forsterite formation, Atg Decomp.: decomposition of antigorite, En Onset: onset of enstatite formation, Qtz Inversion: α to β inversion of quartz and γ-MS Onset: onset of γ-metaserpentine.

The intensity of antigorite, *e.g.*, the (001) peak at d = 7.3 Å (2θ = 5.4°), starts to decrease between 530 °C and 575 °C, reflecting the breakdown of the antigorite structure and formation of intermediate phases until all antigorite peaks have disappeared at 790 °C (Fig. 3.2a and 3.2c, Fig. S3.3). The amorphous phases are characterised by broad increases in intensity for at d > 9.9 Å (4° > 2θ) for the α-metaserpentine (dehydroxylate I) and between 2.7 < d < 3.4 Å (11.7 < 2θ < 14.5°) for the β-metaserpentine (dehydroxylate II), respectively (Fig. 3.2 and S3.2). In *ex-situ* XRD, the amorphous metaserpentine component is commonly described as a broad hump with d values between 5.2 and 2.1 Å (McKelvy *et al.*, 2004; Rausis *et al.*, 2020) but we observe that the amorphous background between 5.0 and 3.4 Å decreases during heating (Fig. S3.3). This is likely due to the recrystallisation of antigorite, which also reduces the background below other antigorite peaks, *e.g.*, around the (001) peak at d = 7.3 Å (Fig. S3.2). Therefore, we use the d range between 3.4 and 2.7 Å (11.7 < 2θ < 14.5°) to represent the evolution of the β-metaserpentine component (Fig. S3.2). Above 589 °C, we observe the formation of a minor, broad peak at d = 14.3 Å (2θ = 2.77°), which can be interpreted as the semi-crystalline (002) peak of chlorite (Chl), consistent chlorite-like phase observed in previous studies (Brindley and Zussman, 1957; Bromiley and Pawley, 2003; Chollet *et al.*, 2011; Scambelluri *et al.*, 2014). The maximum intensities of chlorite-like phase and both amorphous α and β-metaserpentine components are reached at 700 °C, and 765 °C, respectively (Fig. 3.2b, Fig.5, Fig. S3.3). Forsterite (Fo), *e.g.*, the (020) and (021)

peaks at d = 5.1 Å (2θ = 7.7°) and 3.9 Å (2θ = 10.1°), respectively, starts forming at around 700 °C before antigorite has completely decomposed (Fig. 3.2a and 3.2c). Formation of enstatite (En), *e.g.*, the (221) and (610) reflections at d value of 3.2 Å (2θ = 12.4°) and 2.9 Å (2θ = 13.6°), respectively, commences at 805 °C after the complete decomposition of antigorite (Fig. 3.2a and 3.2d). The observed temperatures for the decomposition of antigorite into forsterite and enstatite are in good agreement with previous literature (Balucan *et al.*, 2011; Gualtieri *et al.*, 2012; Viti, 2010). A small amount of pyrope (Prp), *i.e.*, the (402) reflection at d = 2.6 Å (2θ = 15.3°) (Fig. 3.2a), forms above 750 °C as a result of chlorite decomposition (Pawley, 2003; Staudigel and Schreyer, 1977). The quartz inversion from α to β-quartz occurs at 576 °C (Fig. 3.2d), demonstrating the validity of the external temperature calibration. Magnetite (Mag) and hematite (Hem) peaks remain unchanged during the dehydroxylation process (Fig. 3.2a).

3.3.3 Thermogravimetry and differential scanning analyses

Figure 3.3 depicts the thermogravimetric (TGA), differential thermogravimetric (DTG) and differential scanning calorimetry (DSC) traces for the dehydroxylation of antigorite at 2.5, 5, 7.5 and 10 °C min^{-1}.

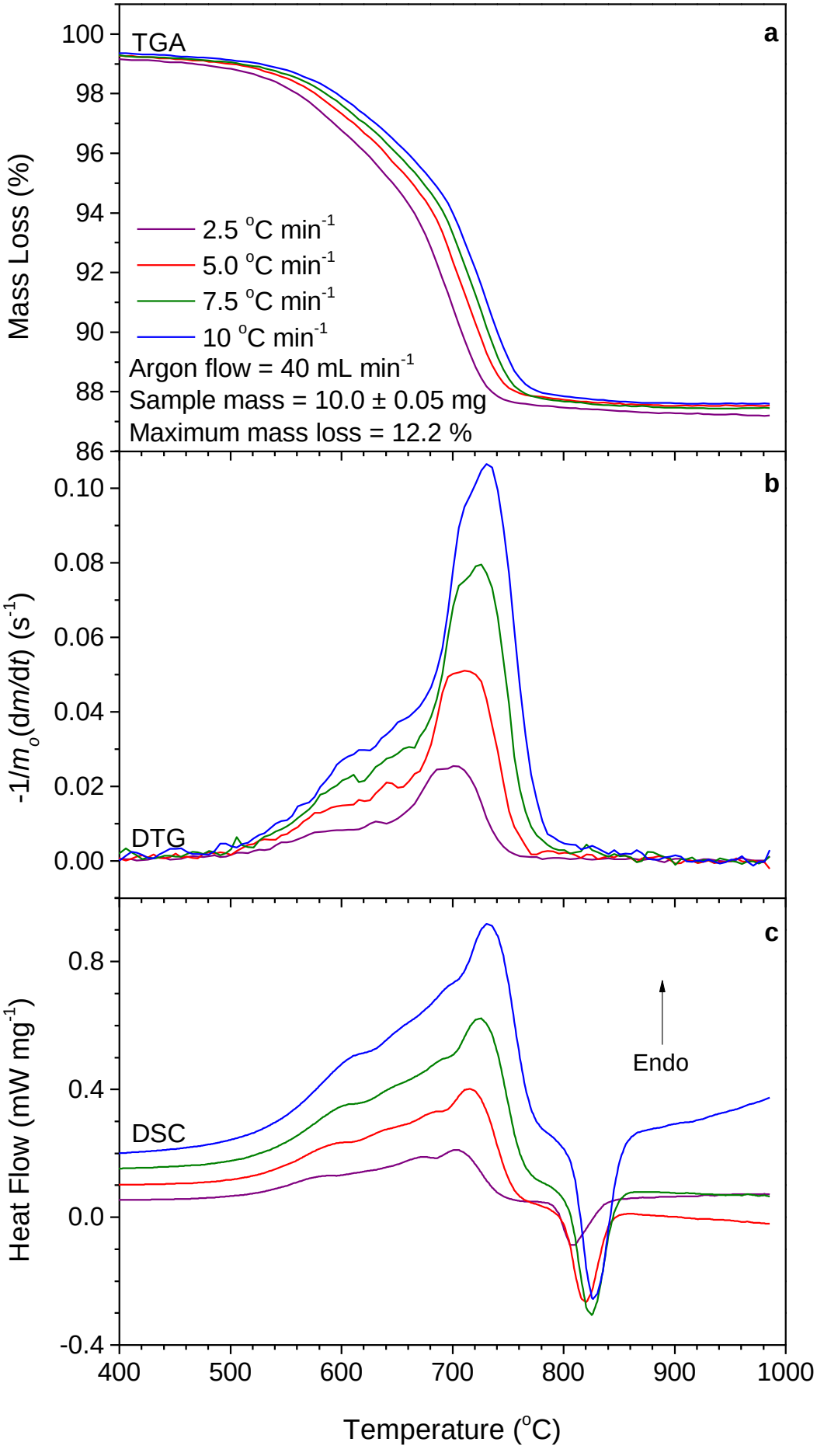
TGA
a
Mass Loss (%)
2.5 °C min-1
5.0 °C min-1
7.5 °C min-1
10 °C min-1
Argon flow = 40 mL min-1
Sample mass = 10.0 ± 0.05 mg
Maximum mass loss = 12.2 %
b
-1/mo(dm/dt) (s-1)
DTG
c
Heat Flow (mW mg-1)
DSC
Endo
Temperature (°C)

Figure 3.3. a) TGA **b)** Normalised DTG and **c)** DSC results for the dehydroxylation of antigorite at 2.5, 5, 7.5 and 10 °C min^{-1} are shown from 400 °C to 1000 °C.

The maximum mass loss of 12.2% is consistent with the theoretical mass loss of antigorite ranging between 12.0 – 12.3 % (Mellini, 1987). The initial mass loss of < 0.8 % below 500 °C may be attributed to a negligible amount of adsorbed moisture, whereas the majority of the mass loss occurs during the dehydroxylation of antigorite between 500 – 800 °C. Four convoluted endothermic peaks between 500 °C and 800 °C and the exothermic peak above 800 °C are in good agreement with previous TGA-DSC data on antigorite dehydroxylation as shown in Table S3.1 of Appendix A (Balucan *et al.*, 2013; Viti, 2010).

3.3.4 Isoconversional kinetics

Multiple maxima in DSC and DTG traces along with multiple overlapping reactions observed during synchrotron PXRD analysis suggest the dehydroxylation reaction is not a single step mechanism. Therefore, isoconversional treatment is required to correctly describe the kinetics of the dehydroxylation of antigorite (Vyazovkin and Sbirrazzuoli, 2006). Raw and interpolated plots of the extent of conversion (α) and temperature needed for the isoconversional kinetic modelling for prograde TGA and DSC data and calculation of pre-exponential factors based on the compensation effect are shown in section 5 of Appendix A. Figure 3.4 displays the activation energy (E_α) and pre-exponential factor (A) derived from prograde DSC and TGA data calculated using Vyazovkin's isoconversional method (Vyazovkin and Sbirrazzuoli, 2006).

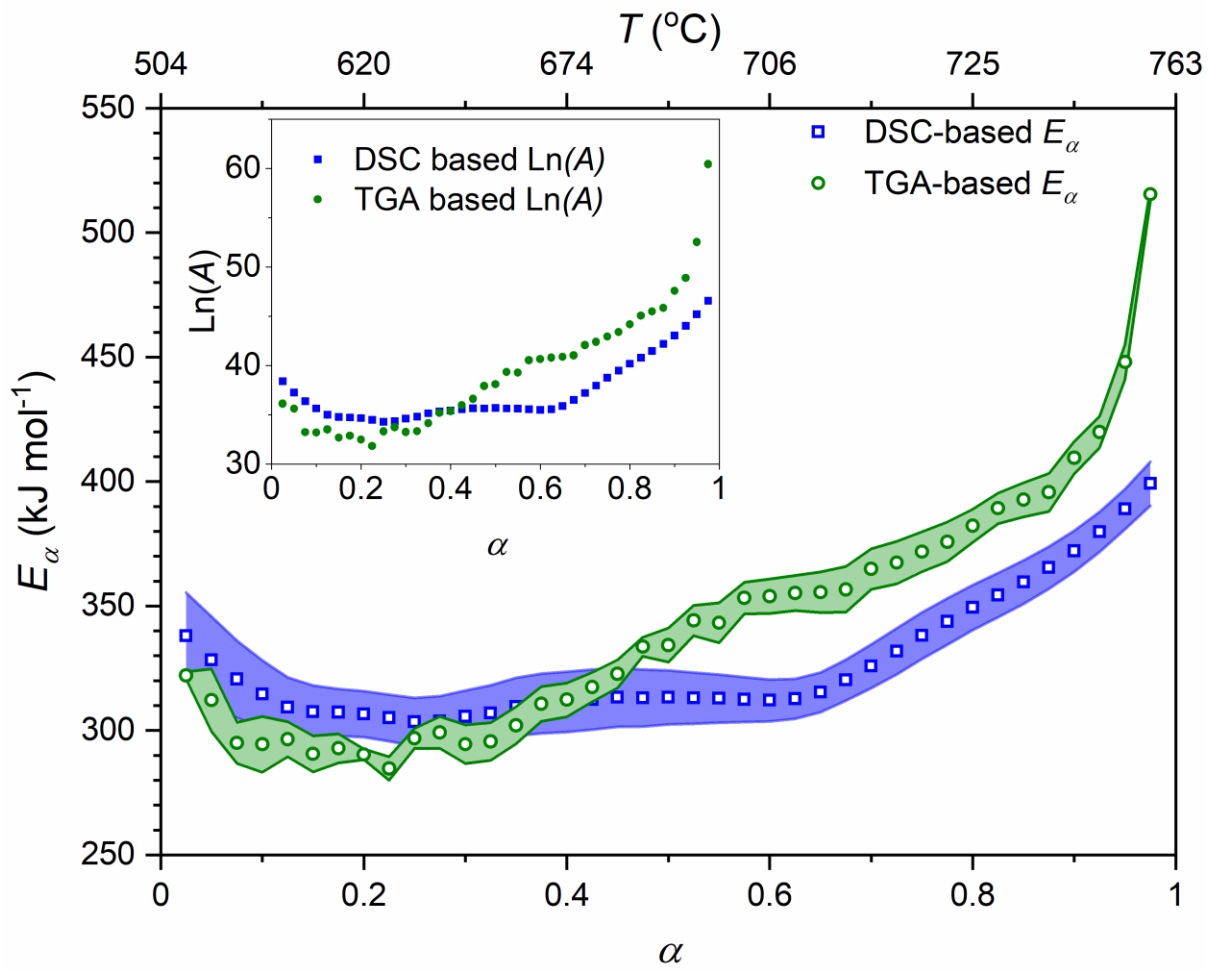

Figure 3.4. Variation of activation energy (E_α) with the extent of conversion (α) based on TGA and DSC data. The area around the data points shows the standard error. The variation in pre-exponential factor (A) with α is shown in the inset. The error in Ln(A) is smaller than the symbols used.

The activation energy based on TGA, first decreases from 322 ± 17 kJ mol^{-1} to 290 ± 7 kJ mol^{-1} for $0.025 < \alpha < 0.2$ and then remains relatively constant between 290 and 299 kJ mol^{-1} for $0.2 < \alpha < 0.325$ with a maximum standard error of ± 8 kJ mol^{-1}. For $0.325 < \alpha < 0.575$ TGA-based E_α shows an increase from 295 to 355 ± 8 kJ mol^{-1}, then reaches a plateau at 355 ± 9 kJ mol^{-1} for α between 0.575 and 0.675 and rapidly increases to 409 ± 6 kJ mol^{-1} for α = 0.9. Then, at $\alpha > 0.95$, the activation energy is 448 ± 6 kJ. The activation energy based on DSC ranges from 340 - 400 kJ mol^{-1} and can be divided into three steps: A decrease in E_α from 340 ± 17 kJ mol^{-1} to 307 ± 10 kJ mol^{-1} in the interval $0.025 < \alpha < 0.175$, followed by nearly constant E_α between 303 to 312 kJ mol^{-1} with maximum standard error of ± 12 kJ mol^{-}

[1] for $0.175 < \alpha < 0.625$ and an increase in E_α from 312 ± 12 kJ mol^{-1} to 400 ± 9 kJ mol^{-1} for $0.625 < \alpha < 0.975$. The E_α based on DSC is higher, similar within error and lower than E_α based on TGA for $\alpha < 0.325$, $0.325 < \alpha < 0.45$ and $\alpha > 0.45$, respectively. Above $\alpha = 0.575$, the E_α based on DSC remains 30 to 40 kJ mol^{-1} lower than E_α based on TGA.

3.4 Insights from simultaneous TGA-DSC, isoconversional modelling and *in-situ* synchrotron PXRD

Figure 3.5 provides a direct comparison between mass loss, heat flow, the variation of activation energy and phase evolution for the dehydroxylation of antigorite between 425 °C and 900 °C.

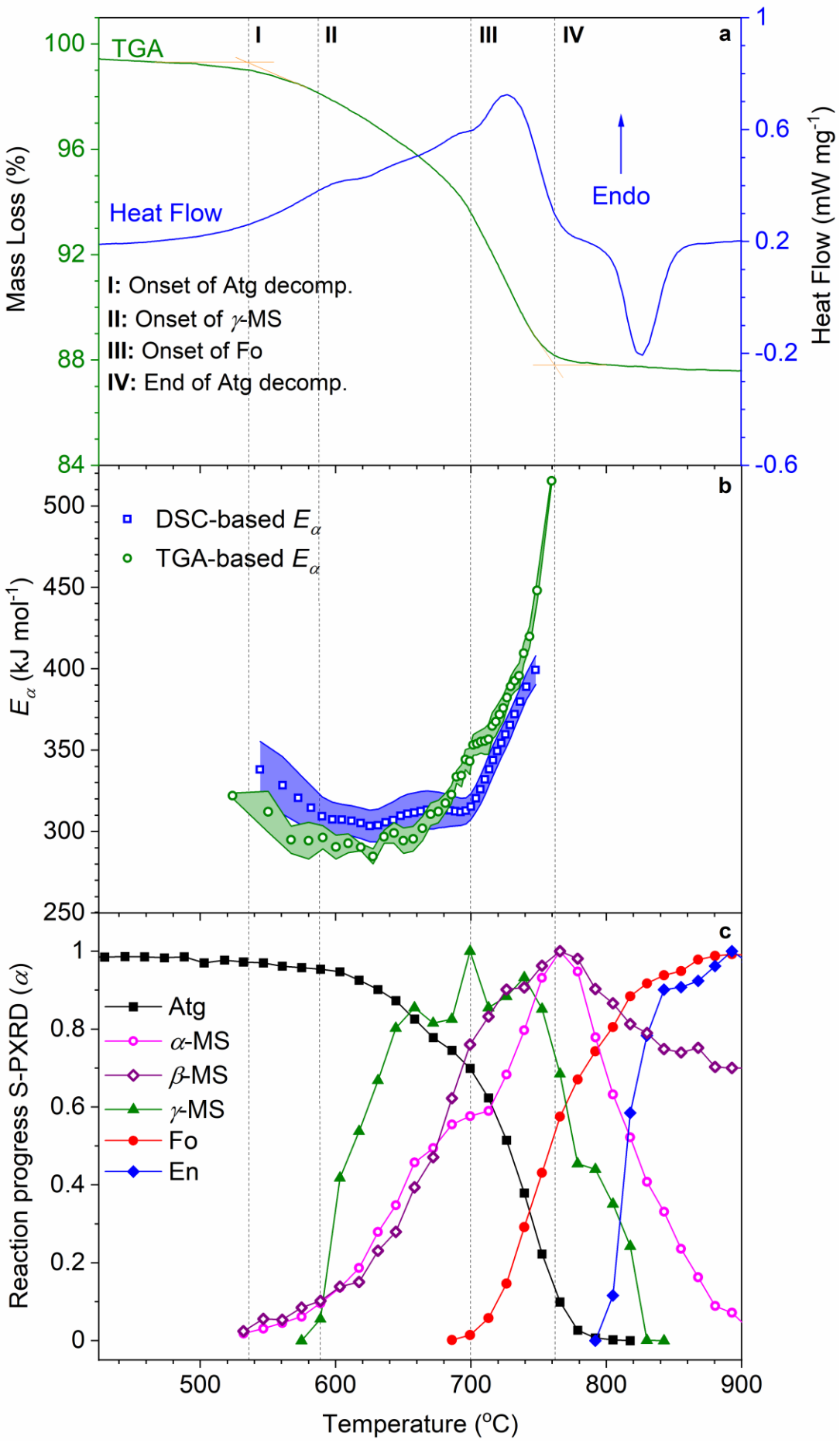
a
TGA
Heat Flow
Endo
I
II
III
IV
I: Onset of Atg decomp.
II: Onset of γ-MS
III: Onset of Fo
IV: End of Atg decomp.
Mass Loss (%)
Heat Flow (mW mg-1)
b
DSC-based Eα
TGA-based Eα
Eα (kJ mol-1)
c
Atg
α-MS
β-MS
γ-MS
Fo
En
Reaction progress S-PXRD (α)
Temperature (°C)

Figure 3.5. a) TGA and DSC plot for the dehydroxylation of antigorite at 8 °C min^{-1}. Events, shown as dotted vertical lines, are based on synchrotron PXRD except for the onset and end of antigorite dehydroxylation, which are based on TGA. **b)** Variation in activation energy with average temperature based on the constant extent of conversion over four different heating rates (2.5, 5, 7.5 and 10 °C min^{-1}) **c)** Synchrotron PXRD reaction progress (α) is based on changes of normalised integrated peak intensities during heating at 8 °C min^{-1}. Phases are labelled as Atg: antigorite, En: enstatite, Fo: forsterite, α-MS: α-metaserpentine, β-MS: β-metaserpentine and γ-MS: γ-metaserpentine. Solid and open symbols show the crystalline and amorphous phases, respectively.

The onset of antigorite dehydroxylation, determined based on TGA data, is at 536 °C (start of stage I in Fig. 3.5). The formation of the amorphous α and β-metaserpentine components concurs with the slower decrease in the (001) peak of antigorite in stage I (536 °C to 589 °C), which is associated with a constant increase in heat flow, demonstrating the endothermic nature of the dehydroxylation. Both TGA and DSC-based activation energies initially decrease until the onset of chlorite-like formation (γ-MS) at 589 °C (Fig. 3.5). A similar decrease in activation energy has been interpreted as the transition from nucleation-limited to growth-limited kinetics for the thermal dehydroxylation of kaolinite (Ortega *et al.*, 2010).

In stage II of the dehydroxylation (589 °C to 700 °C), mass loss and decrease in antigorite peak area are accompanied by the formation of intermediate chlorite-like phase and growth of amorphous components (α and β-metaserpentine). A dip in the endothermic heat flow peak of the dehydroxylation (Fig. 3.5a) may be associated with the (exothermic) growth of these intermediate phases or may reflect the presence of minor amounts of other serpentine polymorphs and their dehydroxylation (Viti, 2010; Viti *et al.*, 2011). Both TGA and DSC-based activation energies remain constant throughout this stage, with DSC-based E_a generally being higher than the TGA-based E_a. This initial stage of dehydroxylation reflects the removal of adjacent hydroxyl groups which diffuse through the mineral structure and leave

from the surface of particles in the form of water (Trittschack and Grobéty, 2012, 2013; Wang *et al.*, 2017). This is consistent with ab initio quantum mechanical calculations on pyrophyllite, which show that the reaction of adjacent hydroxyl groups is the rate-limiting step at the start of dehydroxylation of dioctahedral phyllosilicates (Molina-Montes *et al.*, 2008). Besides minor chlorite-like phase formation, the primary reaction at this stage is the conversion of antigorite to the amorphous phases as suggested earlier by Brindley *et al*., (1965) and Mackenzie and Meinhold (1994)

Formation of chlorite-like phase is consistent with the elevated Al_2O_3 content of the sample (1.69 %, Table 3.1) and can be described by reaction equation 3.12 (Brindley and Zussman, 1957; Bromiley and Pawley, 2003; Chollet *et al.*, 2011).

Al-component of serpentine	→ chlorite (clinochlore)	(3. 12)
$2(Mg_{2.5}Al_{0.5})(Al_{0.5}Si_{1.5})O_5(OH)_4$	→ $Mg_5Al(Si_3Al)O_{10}(OH)_8$	

Higher Al_2O_3 content stabilises antigorite to higher temperatures and pressures, and it leads to the formation of intermediate chlorite (Bromiley and Pawley, 2003; Scambelluri *et al.*, 2014) in addition to the amorphous phases (Bromiley and Pawley, 2003; Gualtieri *et al.*, 2012; Perrillat *et al.*, 2005). Both chlorite-like and amorphous components retain some water/hydroxyls in their structure, explaining the slower initial mass loss between 536 ℃ and 700 ℃ (Bromiley and Pawley, 2003). Above 589 ℃, the amount of chlorite-like phase and both amorphous components continue to increase along with antigorite decomposition. TGA-based E_a shows an increase in activation energy, crossing to higher values than DSC-based E_a, which reflects the hindrance of the diffusion of water to the surface of particles due to the formation of the amorphous structure (Trittschack and Grobéty, 2013).

Stage III, from 700 ℃ to 762 ℃, is characterised by the onset of forsterite formation, which is associated with a dip in the heat flow curve due to the exothermic crystallisation of forsterite. Forsterite formation is also associated with an increase in the mass-loss rate and thus faster escape of water from the sample. This is consistent with the appearance of a water-free dehydroxylation product (forsterite) instead of water-retaining intermediates (chlorite-like and amorphous phases) formed at lower temperatures. The onset of forsterite formation also coincides with a decrease in amorphous α-MS, whereas the amorphous β-MS is not affected (Fig. 3.5c). This suggests that forsterite formation is directly coupled to the α-MS but not to the β-MS, consistent with the accepted reaction scheme, in which forsterite and enstatite form from the Mg-rich (dehydroxylate I) and Si-rich (dehydroxylate II) dehydroxylation intermediates, respectively (Mackenzie and Meinhold, 1994; Rim *et al*., 2020). A small amount of pyrope is also observed in this stage which can be related to the decomposition of chlorite-like phase via reaction Equation 3.13 (Fumagalli and Poli, 2004; Pawley, 2003; Scambelluri *et al.*, 2014).

$$\begin{array}{lllll} \text{Chlorite (Clinochlore)} & + \text{enstatite} \rightarrow & \text{forsterite} & + \text{pyrope} & + \text{water} \\ Mg_5Al(Si_3Al)O_{10}(OH)_8 & + 2MgSiO_3 \rightarrow & 2Mg_2SiO_4 & + Mg_3Al_2(SiO_4)_3 & + 4\ H_2O \end{array} \quad (3.\ 13)$$

Both TGA and DSC-based E_a increase strongly after the onset of forsterite formation, suggesting a change in the rate-limiting step of the dehydroxylation reaction. The increasing E_a is commonly ascribed to either a shift from reactions between adjacent hydroxyls to the reactions between more distant hydroxyl groups (Molina-Montes *et al.*, 2008; Trittschack and Grobéty, 2012), or the hindrance of water diffusion by increased amorphous content and growth of forsterite crystals (Ortega *et al.*, 2010; Trittschack and Grobéty, 2013), TGA

measures mass loss and thus records the hindrance to diffusion of water molecules as a result of amorphous metaserpentine components or forsterite formation. In contrast, DSC captures the overall heat flow, integrating both endothermic dehydroxylation and exothermic forsterite crystallisation. The lower activation energy in DSC relative to TGA can thus be attributed to the hindrance of water diffusion by secondary phase formation or to exothermic forsterite crystallisation reducing heat flow requirements for dehydroxylation.

The last stage (IV) above 762 °C is marked by the complete decomposition of antigorite which coincides with the maximum peak area of the amorphous metaserpentine components, demonstrating the coupling of these phases with the dehydroxylation reaction (Eq. 3.1; Fig. 3.5c). Once antigorite is exhausted, forsterite formation seems to slow down. At 805 °C, enstatite starts to form, and the heat flow curve crosses from endothermic to exothermic. Overlap of the endothermic dehydroxylation peak with the exothermic crystallisation peaks of forsterite and enstatite is typical for antigorite and usually absent in lizardite or chrysotile (Viti, 2010). Increasing peak areas of enstatite (and to a lesser degree forsterite) after complete decomposition of antigorite imply that above 805 °C enstatite forms from the amorphous *β*-MS component (Fig. 3.5c) or by the reaction between forsterite and silica (Rietmeijer *et al.*, 1986). It is noteworthy that the *β*-MS is not fully decomposed with nearly 30 % conversion in the studied temperature range, suggesting that it is coupled to enstatite formation, which is not complete at the final temperature of 900 °C.

3.5 Environmental technology implications for the heat treatment of serpentinised ultramafic rocks for CO_2 sequestration

Isoconversional kinetic analysis of both TGA and DSC results shows that the dehydroxylation of antigorite is a complex multistep process. The increase of activation energy observed during prograde heating demonstrates that the rate-limiting step of the dehydroxylation changes with reaction progress. Model-fitting approaches, which assume a single-step reaction and use the "reaction order" for mechanistic interpretation, thus cannot capture the actual kinetics of antigorite dehydroxylation. This is also reflected in the enormous disparity of activation energies for antigorite dehydroxylation in the literature, ranging from 160 kJ mol^{-1} to 643 kJ mol^{-1} (Alizadehhesari *et al.*, 2012; Balucan *et al.*, 2011; Dlugogorski and Balucan, 2014; Gualtieri *et al.*, 2012; Liu *et al.*, 2019). The mechanistic understanding of serpentine dehydroxylation is still developing but previous studies on the other serpentine polymorphs (Trittschack and Grobéty, 2012; Trittschack *et al.*, 2014) and dioctahedral phyllosilicates (Molina-Montes *et al.*, 2008; Stackhouse *et al.*, 2004; White *et al.*, 2010), including ab initio quantum mechanical calculations, have identified the reaction between adjacent hydroxyls as the rate-limiting step during initial dehydroxylation. As dehydroxylation progresses, neighbouring hydroxyls react first to form water (Zhang *et al.*, 2010) that diffuses towards the particle surface, gradually increasing the distance between the remaining hydroxyls and therefore the average activation energy of dehydroxylation (Trittschack and Grobéty, 2012). Dehydroxylation is associated with changes in the local crystal structure from antigorite to amorphous α-MS and β-MS components or chlorite-like phase, and then to forsterite. These local structural changes influence the diffusion of volatile species but have not yet been incorporated into ab initio calculations (Molina-Montes *et al.*, 2008; Stackhouse *et al.*, 2004; White *et al.*, 2010). The increase in TGA-based activation energies for antigorite dehydroxylation above 650 ℃ (Fig. 3.5b) coincides with increasing amounts of the amorphous phases and above 700 ℃ with forsterite formation (Fig. 3.5c). This suggests that the increase in activation energy and thus the change in the rate-limiting

step are related to rearrangements of the local crystal structure, either through the hindrance of hydroxyl interaction or of subsequent diffusion towards particle surfaces.

Previous studies show that, the amorphisation of serpentine results in higher reactivity for subsequent mineral carbonation (Farhang *et al.*, 2017; Fedoročková *et al.*, 2012; Fouda *et al.*, 1996; Sbirrazzuoli *et al.*, 2009), especially under mild flue gas conditions, which do no extract Mg from forsterite (Du Breuil *et al.*, 2019b; Rim *et al.*, 2020). Optimisation of Mg leaching from heat-activated serpentine thus requires a detailed understanding of amorphous phase formation during heat treatment and amorphous phase reactivity during carbonation. This is commonly hampered by inconsistencies in the nomenclature of amorphous intermediate phases (*e.g.*, Dlugogorski and Balucan (2014); MacKenzie and Meinhold (1994); McKelvy *et al.* (2004) and difficulties identifying amorphous phases in conventional laboratory XRD and consequently in reconciling XRD with ^{29}Si NMR data (*e.g.*, Rausis *et al.* (2020); Rim *et al.* (2020). The synchrotron radiation used in this study provides significantly better signal-to-noise ratios than laboratory XRD, thus enabling identification of a chlorite-like phase (d ~ 14.2 Å) and two distinct amorphous components (α-MS at d > 9.9 Å and β-MS at d between 3.4 Å and 2.7 Å) forming during antigorite dehydroxylation. Our data suggest that the formation of the intermediate chlorite-like phase and its transformation into pyrope represent an additional dehydroxylation pathway for Al_2O_3 bearing serpentine (Fig. S3.13). Considering its semi-crystalline nature and low abundance, it is unlikely that the chlorite-like phase contributes significantly to Mg leaching during subsequent carbonation, consistent with the persistence of a 14.7 Å phase during leaching under mild flue gas conditions (Rim *et al.* 2020). Our data further demonstrate that antigorite dehydroxylation is directly coupled to the formation of both amorphous components, which reach maximum abundance simultaneously (Fig. 3.5c). In the first instance, this implies that practical heat

activation strategies for a given antigorite can only be optimised for maximum amorphous content, not for high yields of one of the amorphous phases. However, other factors such as the serpentine polymorph, original make-up of the rock or heating rate may favour one amorphous phase over the other.

Contrary to a previous study, which achieved full amorphisation of lizardite before forsterite formation (McKelvy *et al.*, 2004), an overlap between serpentine amorphisation and forsterite formation has been observed for all three serpentine polymorphs (Balucan *et al.*, 2011; Gualtieri *et al.*, 2012; Trittschack and Grobéty, 2012, 2013). For the antigorite studied here, this overlap is severe, *i.e.*, forsterite starts forming when only about 49 % of the antigorite is dehydroxylated (51 % residual OH) (Fig. S3.5). With forsterite formation occurring at a relatively constant temperature, the overlap is caused by the higher thermal stability of the antigorite polymorph relative to lizardite (Gualtieri *et al.*, 2012; Viti, 2010), which has been attributed to higher interlayer bond strength related to the inversion of the tetrahedral sheet in the antigorite structure (Capitani and Mellini, 2004). Additional stabilisation of antigorite to higher temperature results from the increased Al_2O_3 content of the studied sample (Bromiley and Pawley, 2003). Practical heating strategies for Al_2O_3-rich antigorite thus cannot achieve full amorphisation and, instead, must consider the trade-off between amorphicity and formation of forsterite along with energy requirements. Heat treatment to maximum amorphous phase content at 765 °C and 2.4 % residual hydroxyls (Fig. S3.5) avoids enstatite formation but is associated with about 56 % of total forsterite being formed (Fig. 3.5c). Furthermore, this heat treatment requires removing almost all residual hydroxyls for which the DSC and TGA-based activation energies increase from 312 kJ mol^{-1} and 343 kJ mol^{-1} to above 400 and 500 kJ mol^{-1}, respectively (Fig. 3.5b). A heat treatment at 700 °C and 49 % residual hydroxyls (Fig. S3.5), below the onset temperature of forsterite formation, would

thus be more effective. This heat treatment avoids the increase in activation energy, accepting that only about 49 % of antigorite can be converted into more reactive intermediate phases. None of the two heating strategies is expected to achieve high Mg extraction under mild, low pCO_2 conditions, suggesting that Al_2O_3-rich antigorite is not a desirable feedstock for low-cost carbonation under lean conditions (Du Breuil *et al.*, 2019b; Liu and Gadikota, 2020; Rim *et al.*, 2020).

3.6 Conclusions

The data presented here demonstrate that antigorite dehydroxylation is a complex multistep process that cannot be adequately represented by single-step kinetic models. A significant increase in activation energy coincides with the amorphous phase and forsterite formation, suggesting that local structural rearrangements have a considerable effect on dehydroxylation kinetics. The use of synchrotron radiation enables the identification of three distinct intermediate dehydroxylation products. The formation of the chlorite phase at $d \sim 14.3$ Å represents an additional reaction pathway for dehydroxylation of Al_2O_3-rich serpentine but likely contributes little to Mg extraction during subsequent carbonation. The close coupling between antigorite dehydroxylation and simultaneous formation of both amorphous components suggest that conventional heat treatment of antigorite is not suitable for preferential production of one of the amorphous phases relative to the other. The present findings also indicate that full extraction of Mg present in Al_2O_3-rich antigorite may not be possible in a practical process for mineral sequestration of CO_2 under lean operating conditions.

3.7 References

Alexander, G., Mercedes Maroto-Valer, M., Gafarova-Aksoy, P. (2007) Evaluation of reaction variables in the dissolution of serpentine for mineral carbonation. Fuel 86, 273-281.

Alizadehhesari, K., Golding, S.D., Bhatia, S.K. (2012) Kinetics of the dehydroxylation of serpentine. Energy & Fuels 26, 783-790.

Ashley, P.M., Brownlow, J.W. (1993) Silica-carbonate alteration zones in the Great Serpentinite Belt, southern New England Orogen: their nature and significance, In New England Orogen, (eds. P.G. Flood and J.C. Aitchison). University of New England, Armidale, Australia, 197-214.

Balucan, R.D., Dlugogorski, B.Z., Kennedy, E.M., Belova, I.V., Murch, G.E. (2013) Energy cost of heat activating serpentinites for CO_2 storage by mineralisation. International Journal of Greenhouse Gas Control 17, 225-239.

Balucan, R.D., Kennedy, E.M., Mackie, J.F., Dlugogorski, B.Z. (2011) Optimisation of antigorite heat pre-treatment via kinetic modelling of the dehydroxylation reaction for CO2 mineralisation. Greenhouse Gases: Science and Technology 1, 294-304.

Benhelal, E., Rashid, M.I., Rayson, M.S., Brent, G.F., Oliver, T., Stockenhuber, M., Kennedy, E.M. (2019) Direct aqueous carbonation of heat-activated serpentine: Discovery of undesirable side reactions reducing process efficiency. Applied Energy 242, 1369-1382.

Brindley, G.W., Hayami, R. (1963) Kinetics and mechanisms of dehydration and recrystallisation of serpentine—I. Clays and Clay Minerals 12, 35-47.

Brindley, G.W., Hayami, R. (1965) Mechanism of formation of forsterite and enstatite from serpentine. Mineralogical Magazine and Journal of the Mineralogical Society 35, 189-195.

Brindley, G.W., Zussman, J. (1957) A structural study of the thermal transformation of serpentine minerals to forsterite. American Mineralogist 42, 461-474.

Bromiley, G.D., Pawley, A.R. (2003) The stability of antigorite in the systems MgO-SiO_2-H_2O (MSH) and MgO-Al_2O_3-SiO_2-H_2O (MASH): The effects of Al^{3+} substitution on high-pressure stability. American Mineralogist 88, 99-108.

Candela, P.A., Crummett, C.D., Earnest, D.J., Frank, M.R., Wylie, A.G. (2007) Low-pressure decomposition of chrysotile as a function of time and temperature. American Mineralogist 92, 1704-1713.

Capitani, G., Mellini, M. (2004) The modulated crystal structure of antigorite: The m = 17 polysome. American Mineralogist 89, 147-158.

Chollet, M., Daniel, I., Koga, K.T., Morard, G., van de Moortèle, B. (2011) Kinetics and mechanism of antigorite dehydration: Implications for subduction zone seismicity. Journal of Geophysical Research: Solid Earth 116, B04203.

Dlugogorski, B.Z., Balucan, R.D. (2014) Dehydroxylation of serpentine minerals: Implications for mineral carbonation. Renewable and Sustainable Energy Reviews 31, 353-367.

Drief, A., Nieto, F. (1999) The effect of dry grinding on antigorite from Mulhacen, Spain. Clays and Clay Minerals 47, 417-424.

Du Breuil, C., Pasquier, L.-C., Dipple, G., Blais, J.-F., Iliuta, C.M., Mercier, G. (2019) Mineralogical transformations of heated serpentine and their impact on dissolution during aqueous-phase mineral carbonation reaction in flue gas conditions. Minerals 9.

Farhang, F., Rayson, M., Brent, G., Hodgins, T., Stockenhuber, M., Kennedy, E. (2017) Insights into the dissolution kinetics of thermally activated serpentine for CO_2 sequestration. Chemical Engineering Journal 330, 1174-1186.

Fedoročková, A., Hreus, M., Raschman, P., Sučik, G. (2012) Dissolution of magnesium from calcined serpentinite in hydrochloric acid. Minerals Engineering 32, 1-4.

Fouda, M.F.R., Amin, R.E.-S., Abd-Elzaher, M.M. (1996) Extraction of magnesia from Egyptian serpentine ore via reaction with different acids. I. Reaction with sulfuric acid. Bulletin of the Chemical Society of Japan 69, 1907-1912.

Fumagalli, P., Poli, S. (2004) Experimentally determined phase relations in hydrous peridotites to 6·5 GPa and their consequences on the dynamics of subduction zones. Journal of Petrology 46, 555-578.

Gao, W., Wen, J., Li, Z. (2014) Dissolution kinetics of magnesium from calcined serpentine in NH_4Cl solution. Industrial & Engineering Chemistry Research 53, 7947-7955.

Gerdemann, S.J., O'Connor, W.K., Dahlin, D.C., Penner, L.R., Rush, H. (2007) *Ex-situ* aqueous mineral carbonation. Environmental Science & Technology 41, 2587-2593.

Ghoorah, M., Dlugogorski, B.Z., Oskierski, H.C., Kennedy, E.M. (2014) Study of thermally conditioned and weak acid-treated serpentinites for mineralisation of carbon dioxide. Minerals Engineering 59, 17-30.

Gualtieri, A.F., Giacobbe, C., Viti, C. (2012) The dehydroxylation of serpentine group minerals. American Mineralogist 97, 666.

Hariharan, S., Mazzotti, M. (2017) Kinetics of flue gas CO_2 mineralisation processes using partially dehydroxylated lizardite. Chemical Engineering Journal 324, 397-413.

Hariharan, S., Werner, M., Hänchen, M., Zingaretti, D., Baciocchi, R., Mazzotti, M. (2014) Dissolution kinetics of thermally activated serpentine for mineralisation at flue gas conditions. Energy Procedia 63, 5887-5891.

He, S., Zhang, W., Liu, L., Huang, Y., He, J., Xie, W., Wu, P., Du, C. (2014) Baseline correction for Raman spectra using an improved asymmetric least squares method. Analytical Methods 6, 4402-4407.

Huijgen, W., Comans, R. (2005) Mineral CO_2 sequestration by carbonation of industrial residues. The Netherlands: Energy Research Centre of the Netherlands (ECN).

Kemache, N., Pasquier, L.-C., Cecchi, E., Mouedhen, I., Blais, J.-F., Mercier, G. (2017) Aqueous mineral carbonation for CO_2 sequestration: From laboratory to pilot scale. Fuel Processing Technology 166, 209-216.

Khawam, A., Flanagan, D.R. (2005) Role of isoconversional methods in varying activation energies of solid-state kinetics: I. isothermal kinetic studies. Thermochimica Acta 429, 93-102.

Kim, D.-J., Chung, H.-S. (2002) Effect of grinding on the structure and chemical extraction of metals from serpentine. Particulate Science and Technology 20, 159-168.

Kirchofer, A., Becker, A., Brandt, A., Wilcox, J. (2013) CO_2 mitigation potential of mineral carbonation with industrial alkalinity sources in the United States. Environmental Science & Technology 47, 7548-7554.

Lackner, K.S., Wendt, C.H., Butt, D.P., Joyce, E.L., Sharp, D.H. (1995) Carbon dioxide disposal in carbonate minerals. Energy 20, 1153-1170.

Li, W., Li, W., Li, B., Bai, Z. (2009) Electrolysis and heat pre-treatment methods to promote CO_2 sequestration by mineral carbonation. Chemical Engineering Research and Design 87, 210-215.

Liu, C., Wang, D., Shen, K., Liu, T., Yi, L. (2019) Kinetics of antigorite dehydration: Rapid dehydration as a trigger for lower-plane seismicity in subduction zones. American Mineralogist 104, 282-290.

Liu, M., Gadikota, G. (2018) Chemo-morphological coupling during serpentine heat treatment for carbon mineralisation. Fuel 227, 379-385.

Liu, M., Gadikota, G. (2020) Single-step, low temperature and integrated CO_2 capture and conversion using sodium glycinate to produce calcium carbonate. Fuel 275, 117887.

MacKenzie, K.J.D., Meinhold, R.H. (1994) Thermal reactions of chrysotile revisited: A 29Si and 25Mg MAS NMR study. American Mineralogist 79, 43-50.

Maroto-Valer, M.M., Fauth, D.J., Kuchta, M.E., Zhang, Y., Andrésen, J.M. (2005) Activation of magnesium rich minerals as carbonation feedstock materials for CO_2 sequestration. Fuel Processing Technology 86, 1627-1645.

McKelvy, M.J., Chizmeshya, A.V.G., Diefenbacher, J., Béarat, H., Wolf, G. (2004) Exploration of the role of heat activation in enhancing serpentine carbon sequestration reactions. Environmental Science & Technology 38, 6897-6903.

Mellini, M., Trommsdorff, V. & Compagnoni, R. (1987) Antigorite polysomatism: behaviour during progressive metamorphism. Contributions to Mineralogy and Petrology 97, 147-155.

Miller, Q.R.S., Schaef, H.T., Kaszuba, J.P., Gadikota, G., McGrail, B.P., Rosso, K.M. (2019) Quantitative review of olivine carbonation kinetics: Reactivity trends, mechanistic insights, and research frontiers. Environmental Science & Technology Letters 6, 431-442.

Molina-Montes, E., Donadio, D., Hernández-Laguna, A., Sainz-Díaz, C.I. (2008a) DFT Research on the Dehydroxylation Reaction of Pyrophyllite 2. Characterization of Reactants, Intermediates, And Transition States along the Reaction Path. The Journal of Physical Chemistry A 112, 6373-6383.

Molina-Montes, E., Donadio, D., Hernández-Laguna, A., Sainz-Díaz, C.I., Parrinello, M. (2008b) DFT research on the dehydroxylation reaction of pyrophyllite 1. First-principle molecular dynamics simulations. The Journal of Physical Chemistry B 112, 7051-7060.

Mouedhen, I., Kemache, N., Pasquier, L.-C., Cecchi, E., Blais, J.-F., Mercier, G. (2017) Effect of pCO_2 on direct flue gas mineral carbonation at pilot scale. Journal of Environmental Management 198, 1-8.

Ortega, A., Macías, M., Gotor, F.J. (2010) The Multistep Nature of the Kaolinite Dehydroxylation: Kinetics and Mechanism. Journal of the American Ceramic Society 93, 197-203.

Oskierski, H.C., Beinlich, A., Mavromatis, V., Altarawneh, M., Dlugogorski, B.Z. (2019) Mg isotope fractionation during continental weathering and low temperature carbonation of ultramafic rocks. Geochimica et Cosmochimica Acta 262, 60-77.

Oskierski, H.C., Dlugogorski, B.Z., Jacobsen, G. (2013a) Sequestration of atmospheric CO2 in a weathering-derived, serpentinite-hosted magnesite deposit: 14C tracing of carbon sources and age constraints for a refined genetic model. Geochimica et Cosmochimica Acta 122, 226-246.

Oskierski, H.C., Dlugogorski, B.Z., Jacobsen, G. (2013b) Sequestration of atmospheric CO_2 in chrysotile mine tailings of the Woodsreef Asbestos Mine, Australia: Quantitative mineralogy, isotopic fingerprinting and carbonation rates. Chemical Geology 358, 156-169.

Pasquier, L.-C., Mercier, G., Blais, J.-F., Cecchi, E., Kentish, S. (2014) Reaction mechanism for the aqueous-phase mineral carbonation of heat-activated serpentine at low temperatures and pressures in flue gas conditions. Environmental Science & Technology 48, 5163-5170.

Pawley, A. (2003) Chlorite stability in mantle peridotite: the reaction clinochlore+enstatite=forsterite+pyrope+H2O. Contributions to Mineralogy and Petrology 144, 449-456.

Peng, J., Peng, S., Jiang, A., Wei, J., Li, C., Tan, J. (2010) Asymmetric least squares for multiple spectra baseline correction. Analytica Chimica Acta 683, 63-68.

Perrillat, J.-P., Daniel, I., Koga, K.T., Reynard, B., Cardon, H., Crichton, W.A. (2005) Kinetics of antigorite dehydration: A real-time X-ray diffraction study. Earth and Planetary Science Letters 236, 899-913.

Power, I.M., Harrison, A.L., Dipple, G.M., Wilson, S.A., Kelemen, P.B., Hitch, M., Southam, G. (2013) Carbon mineralisation: From natural analogues to engineered systems. Reviews in Mineralogy and Geochemistry 77, 305.

Prigiobbe, V., Hänchen, M., Werner, M., Baciocchi, R., Mazzotti, M. (2009) Mineral carbonation process for CO_2 sequestration. Energy Procedia 1, 4885-4890.

Rausis, K., Ćwik, A., Casanova, I. (2020) Insights into the direct carbonation of activated lizardite: The identification a poorly reactive amorphous Mg-rich silicate phase. International Journal of Greenhouse Gas Control 100, 103114.

Rietmeijer, F.J.M., Nuth, J.A., Mackinnon, I.D.R. (1986) Analytical electron microscopy of Mg・SiO smokes: A comparison with infrared and XRD studies. Icarus 66, 211-222.

Rim, G., Marchese, A.K., Stallworth, P., Greenbaum, S.G., Park, A.-H.A. (2020) 29Si solid state MAS NMR study on leaching behaviors and chemical stability of different Mg-silicate structures for CO_2 sequestration. Chemical Engineering Journal 396, 125204.

Sanna, A., Uibu, M., Caramanna, G., Kuusik, R., Maroto-Valer, M.M. (2014) A review of mineral carbonation technologies to sequester CO_2. Chemical Society Reviews 43, 8049-8080.

Sawai, M., Katayama, I., Hamada, A., Maeda, M., Nakashima, S. (2013) Dehydration kinetics of antigorite using *in-situ* high-temperature infrared micro-spectroscopy. Physics and Chemistry of Minerals 40, 319-330.

Scambelluri, M., Pettke, T., Rampone, E., Godard, M., Reusser, E. (2014) Petrology and trace element budgets of high-pressure peridotites indicate subduction dehydration of serpentinised mantle (Cima di Gagnone, Central Alps, Switzerland). Journal of Petrology 55, 459-498.

Schmitt, B., Brönnimann, C., Eikenberry, E.F., Hülsen, G., Toyokawa, H., Horisberger, R., Gozzo, F., Patterson, B., Schulze-Briese, C., Tomizaki, T. (2004) Development of single photon counting detectors at the Swiss Light Source. Nuclear Instruments and Methods in Physics Research Section A: Accelerators, Spectrometers, Detectors and Associated Equipment 518, 436-439.

Stackhouse, S., Coveney, P.V., Benoit, D.M. (2004) Density-functional-theory-based study of the dehydroxylation behaviour of aluminous dioctahedral 2:1 layer-type clay minerals. The Journal of Physical Chemistry B 108, 9685-9694.

Staudigel, H., Schreyer, W. (1977) The upper thermal stability of clinochlore, $Mg_5Al[AlSi_3O_{10}](OH)_8$, at 10–35 kbar P_{H2O} Contributions to Mineralogy and Petrology 61, 187-198.

Trittschack, R., Grobéty, B. (2012) Dehydroxylation kinetics of lizardite. European Journal of Mineralogy 24, 47-57.

Trittschack, R., Grobéty, B., (2013) The dehydroxylation of chrysotile: A combined *in-situ* micro-Raman and micro-FTIR study, American Mineralogist, p. 1133.

Trittschack, R., Grobéty, B., Brodard, P. (2014) Kinetics of the chrysotile and brucite dehydroxylation reaction: a combined non-isothermal/isothermal thermogravimetric analysis

and high-temperature X-ray powder diffraction study. Physics and Chemistry of Minerals 41, 197-214.

Vickery, N.M., Brown, R.E., Percival, I.G. (2010) Manilla 1:100000 geological sheet 9036 explanatory notes. . NSW Geol. Surv., Maitland, Australia.

Viti, C. (2010) Serpentine minerals discrimination by thermal analysis. American Mineralogist 95, 631.

Viti, C., Giacobbe, C., Gualtieri, A.F. (2011) Quantitative determination of chrysotile in massive serpentinites using DTA: Implications for asbestos determinations. American Mineralogist 96, 1003-1011.

Vyazovkin, S., (2015a) Isoconversional methodology, Isoconversional kinetics of thermally stimulated processes. Springer International Publishing, Switzerland, pp. 27-62.

Vyazovkin, S., (2015b) Some basics en route to isoconversional methodology, Isoconversional Kinetics of Thermally Stimulated Processes. Springer, pp. 1-25.

Vyazovkin, S., Sbirrazzuoli, N. (2006) Isoconversional kinetic analysis of thermally stimulated processes in polymers. Macromolecular Rapid Communications 27, 1515-1532.

Vyazovkin, S., Wight, C.A. (1998) Isothermal and non-isothermal kinetics of thermally stimulated reactions of solids. International Reviews in Physical Chemistry 17, 407-433.

Wallwork, K.S., Kennedy, B.J., Wang, D. (2007) The high-resolution powder diffraction beamline for the Australian Synchrotron. AIP Conference Proceedings 879, 879-882.

Wang, D., Liu, X., Liu, T., Shen, K., Welch, D.O., Li, B. (2017) Constraints from the dehydration of antigorite on high-conductivity anomalies in subduction zones. Scientific Reports 7, 16893.

Werner, M., Hariharan, S., Mazzotti, M. (2014) Flue gas CO_2 mineralisation using thermally activated serpentine: From single- to double-step carbonation. Energy Procedia 63, 5912-5917.

White, C.E., Provis, J.L., Proffen, T., Riley, D.P., van Deventer, J.S.J. (2010) Density functional modelling of the local structure of kaolinite subjected to thermal dehydroxylation. The Journal of Physical Chemistry A 114, 4988-4996.

Whittaker, E.J.W., Zussman, J. (1956) The characterization of serpentine minerals by X-ray diffraction. Mineralogical Magazine and Journal of the Mineralogical Society 31, 107-126.

Wilson, S.A., Harrison, A.L., Dipple, G.M., Power, I.M., Barker, S.L.L., Ulrich Mayer, K., Fallon, S.J., Raudsepp, M., Southam, G. (2014) Offsetting of CO_2 emissions by air capture in mine tailings at the Mount Keith Nickel Mine, Western Australia: Rates, controls and prospects for carbon neutral mining. International Journal of Greenhouse Gas Control 25, 121-140.

Zhang, M., Redfern, S.A.T., Salje, E.K.H., Carpenter, M.A., Wang, L. (2010) H2O and the dehydroxylation of phyllosilicates: An infrared spectroscopic study. American Mineralogist 95, 1686-1693.

Chapter 4: The Effect of Partial Pressure of Water Vapour, Particle Size and Mineralogy on Dehydroxylation of Serpentine Minerals

4 Abstract

Dehydroxylation through heating and the associated amorphisation of serpentine minerals plays a vital role in effective sequestration of CO_2 through mineral carbonation. To achieve optimal reactivity during subsequent carbonation at the lowest possible energy cost, we must prevent the formation of less-reactive crystalline phases, *i.e.*, forsterite and enstatite through careful optimisation of the heating process. We employed synchrotron powder X-ray diffraction (PXRD), thermogravimetric (TG) and differential scanning calorimetric (DSC) analyses to provide the first *in-situ* record of the effects of the partial pressure of water vapours (P_{H2O}), grain size, and mineralogy on the structural changes during dehydroxylation. Higher P_{H2O} delayed the dehydroxylation of lizardite, whereas no effect was observed for antigorite, probably because of the high dehydroxylation temperature, less amorphous content and overlapping exothermic forsterite crystallisation, which prevent the chemisorption of water vapours on the surface of antigorite sample. Smaller grain sizes induced faster dehydroxylation due to the high surface area and better heat transfer. Lizardite dehydroxylation yields a high degree of amorphisation before the formation of less-reactive forsterite compared to antigorite, where sufficient amorphisation is only achieved when a significant amount of forsterite has formed. Overall,

fine-grained lizardite, heated under low P_{H2O}, is most promising for efficient dehydroxylation and subsequent carbonation.

4.1 Introduction

The dehydroxylation of serpentine minerals ($Mg_3Si_2O_5(OH)_4$) through heat treatment is a critical step for mineral carbonation, one of the promising techniques for large scale, permanent CO_2 sequestration (Alexander *et al.*, 2007; Dlugogorski and Balucan, 2014; Gerdemann *et al.*, 2007; Liu and Gadikota, 2018, 2020; Maroto-Valer *et al.*, 2005; McKelvy *et al.*, 2004; O'Connor *et al.*, 2005; Werner *et al.*, 2014). Reaction rate and efficiency of *ex-situ* reactor-based mineral carbonation are commonly limited by the slow dissolution kinetics of Mg-silicate feedstocks (Du Breuil *et al.*, 2019b; Farhang *et al.*, 2017; Hariharan *et al.*, 2014b; Liu and Gadikota, 2020; Rausis *et al.*, 2020; Rim *et al.*, 2020). For industrial application, dissolution has to occur on a timescale of hours, thus requiring thermal activation of the feedstock minerals, especially if mild, flue-gas conditions are used (Benhelal *et al.*, 2019; Du Breuil *et al.*, 2019b; Farhang *et al.*, 2017; Hariharan *et al.*, 2014b; Mouedhen *et al.*, 2017; Rausis *et al.*, 2020; Rim *et al.*, 2020; Werner *et al.*, 2014). Besides surface area, porosity and pore surface roughness (Liu and Gadikota, 2018), reactivity during dissolution and mineral carbonation is controlled by the mineralogy, *i.e.*, the crystal structure of the feedstock, which is modified during thermal treatment (Balucan *et al.*, 2013; Balucan *et al.*, 2011; Benhelal *et al.*, 2019; Dlugogorski and Balucan, 2014; Du Breuil *et al.*, 2019b; Farhang *et al.*, 2017; Rausis *et al.*, 2020; Rim *et al.*, 2020). Amorphisation and the formation of crystalline phases enhance and reduce the reactivity during mineral carbonation, respectively, and thermal treatment poses a significant additional energy requirement for the practical implementation of the mineral carbonation process (Dlugogorski and Balucan, 2014; Du Breuil *et al.*, 2019b; Rausis *et al.*, 2020; Rim *et al.*, 2020). It is thus vital to understand the

effect of operating and process parameters on structural changes during the dehydroxylation of serpentine minerals.

Type and flow rate of purge gas, grain size, dehydroxylation temperature, heating rate and feed material chemical and mineralogical composition affect the efficiency of thermal dehydroxylation and thus the feasibility of mineral carbonation (Balucan and Dlugogorski (2013); Bloise (2018); Brindley *et al.* (1967a); Dlugogorski and Balucan (2014); Kim and Chung (2002); Sanna *et al.* (2013); Viti (2010), Chapter 3). Balucan and Dlugogorski (2013), discussed the effect of flow rate, type of purge gas, grain size and heating rate on dehydroxylation of antigorite using thermal gravimetric (TGA) analysis (Balucan and Dlugogorski, 2013). This approach demonstrates the effect of these parameters on mass loss during thermal treatment but does not provide direct insights into crystal structural changes. Similarly, differential scanning calorimetry (DSC) reflects heat flow during phase transitions but requires complex peak deconvolution to resolve the overlapping phase transformations occurring during serpentine dehydroxylation (Michael *et al.*, 2018; Sandu and Singh, 1990). On the other hand, X-ray diffraction (XRD) records the evolution of individual phases and thus resolves phase transitions that overlap or occur without mass loss. Therefore, X-ray diffraction (XRD) provides crucial insights into serpentine heat treatment, that are not achievable by TGA or DSC analysis.

This study employs *in-situ* synchrotron PXRD to explore the influence of particle size, the partial pressure of water vapours and mineralogy on structural changes during the thermal dehydroxylation of serpentine minerals. The main aims of this study are a) to provide an in-depth insight into the effects of the partial pressure of water vapours, grain size and mineralogy

on the evolution of different phases during the dehydroxylation of serpentine minerals and b) the implication of these parameters for cost-effective thermal dehydroxylation of serpentine minerals. For the first time, this work presents the *in-situ* record of the effects of the dehydroxylation parameters on structural changes during the thermal dehydroxylation of serpentine minerals using PXRD analysis under flow-through condition.

4.2 Materials and methods

4.2.1 Characterisation of samples

The antigorite and lizardite samples were collected from the Great Serpentinite Belt, a dismembered ophiolite sequence in Northern New South Wales, Australia, (Sample AT1-1 and BS2-1 in Oskierski *et al.* (2019); Oskierski *et al.* (2013a). Initially, the samples were broken into small pieces using a hammer, ground in an agate ring mill for 2-3 minutes and sieved to obtain the particle size fractions 45-75 µm. After demagnetisation to remove the iron oxide (Balucan and Dlugogorski, 2013), the samples were further ground in McCrone mill using stacked Al_2O_3 pallets under the dry condition for 1 min and sieved to obtain particle size fraction < 45 µm.

The major and trace element concentrations of the demagnetised samples were determined using a PANalytical MagiX FAST at Bureau Veritas Minerals Pty Ltd, Western Australia. A flux of 66:34 lithium tetraborate and lithium metaborate along with 4 % lithium nitrate as an oxidising agent was used to prepare glass beads for XRF analysis. Loss on ignition (LOI) and particle size

distribution (PSD) were determined by a robotic thermogravimetric analyser, LabFit TGA-4000 and a Microtrac S3500 laser diffraction instrument in aqueous media, respectively. The chemical composition of serpentine samples with particle size fraction 45-75 μm used in the current study is shown in Table 4.1.

Table 4.1. Bulk chemical composition of the lizardite and antigorite samples

$\%_{w/w}$	**SiO_2**	**Al_2O_3**	**MgO**	**Fe_2O_3**	**Cr_2O_3**	**CaO**	**Na_2O**	**P_2O_5**	**SO_3**	**Ni✦**	**LOI***	**Total**
Antigorite	41.86	1.69	38.9	4.07	0.247	0.74	0.05	0.008	0.056	0.195	12.04	99.95
Lizardite	43.68	0.72	38.1	4.26	0.214	0.02	0.04	0.01	0.058	0.309	12.5	99.99

✦ Ni measured by trace element program

* LOI represents the volatile components based on loss of ignition at 1000 ℃.

Our values of 12.04 and 12.5 % for antigorite and lizardite sample, are consistent with the structural water content of respective serpentine polymorphs obtained by Balucan *et al.* (2013); Viti (2010).

Table 4.2. summarises the volumetric particle size distribution of the antigorite and lizardite samples.

Table 4.2. Particle size distribution for antigorite and lizardite samples for sieve fraction 45-75 µm and < 45 µm

Sample	$d_{4,3}$ (µm)	d_{90} (µm)	d_{50} (µm)	d_{10} (µm)	d_{80}^{*} (µm)
Antigorite ($Atg_{45\text{-}75\mu m}$)	61.7	51.1	12.2	2.02	37
Antigorite ($Atg_{<45\mu m}$)	44.6	26.2	5.97	1.54	18
Lizardite ($Liz_{45\text{-}75\mu m}$)	78.4	61.4	27.1	2.37	53
Lizardite ($Liz_{<45\mu m}$)	49.3	31.3	7.22	1.46	22

* $d_{4,3}$ represents the volume-weighted mean diameter. d_{10}, d_{50}, d_{80}, and d_{90} represent the 10, 50, 80, and 90 % volume of the particle mass diameter smaller than the size indicated, respectively. d_{80} is an interpolated value from d_{10}, d_{50}, and d_{90}. Particle size distributions are shown in Appendix B (Fig. S4.1)

4.2.2 Experimental setup for synchrotron powder X-ray diffraction

Powder X-ray diffraction (PXRD) beamline (Wallwork *et al.*, 2007) at the Australian synchrotron was employed to investigate the *in-situ* evolution of structural changes during the dehydroxylation of serpentine minerals under various process parameter. A NIST standard reference material (SRM) lanthanum hexaboride (LaB6) was used with 18 keV energy to calibrate the X-ray wavelength (0.688987(2) Å). The diffractograms were collected in the 2θ range between 2 and 80^{o} using a MYTHEN II detector (Schmitt *et al.*, 2004) at two detector positions,"2°" and "2.5°", with an acquisition time of one scan per minute for each position in a temperature range of 100 °C to 917 °C. The α to β quartz transition (573 °Cand the melting point of NaCl (801 °C) were used for temperature calibration ((see chapter 3 Appendix A Fig S3.1 for details). The uncertainty in the temperature measurements was ± 8 °C.

The high-temperature experiments were performed in a flow-through capillary (0.7 x 0.01 mm) with about 6 mg of sample, held in place by glass wool to avoid displacement of the sample with purge flow gas at 8 °C min^{-1} under the N_2 gas flow of 80 mL min^{-1}. Antigorite and lizardite samples with two different particle sizes were used to observe the influence of mineralogy and particle size on the dehydroxylation sequence. The effect of the partial pressure of water vapours was tested using dry and wet N_2 flow gas, the latter produced by bubbling the gas through the water.

We used PDViPeR software to process, merge and extract the synchrotron PXRD data for phase identification in Crystal Impact Match! software using crystallography open database (COD). The asymmetric least square fitting method in Origin software was used to model the capillary background and the amorphous background arising from the formation of amorphous phases during dehydroxylation. The capillary background was constant over the experimental temperature range. The growth of amorphous phases was determined as a difference between the integrating intensity between amorphous background and capillary background. Peak area measurements for non-overlapping peaks of different phases were performed using numerical integration after amorphous background subtraction. Reaction progress (α) was determined by normalising the integrated peak areas of amorphous and crystalline phases at any instant to the maximum integrated peak area of the respective phases.

Theoretical amorphous content was estimated using the balanced dehydroxylation reaction equation 4.1 (MacKenzie and Meinhold, 1994; Rim *et al.*, 2020) before the forsterite formation

(< 700 °C), as above this point amorphous content start to transform into forsterite and enstatite phases (Brindley and Hayami,1965).

Serpentine mineral → Amorphous α-MS + Amorphous β-MS + water (4.1)

$5Mg_3Si_2O_5(OH)_4 \rightarrow 7Mg_2SiO_4 + MgSi_3O_7 + 10H_2O$

According to Equation 4.1, all the dehydroxylated serpentine mineral converts to the amorphous content before the forsterite formation. However, the conversion of lizardite and antigorite is different due to their different structural stabilities and dehydroxylation temperatures, *i.e.*, lizardite completely dehydroxylates before the formation of forsterite whereas in antigorite severe overlap exits between the dehydroxylation and forsterite formation (Dlugogorski and Balucan (2014); Viti (2010), Chapter 3). Hence, the synchrotron PXRD-based conversion at the temperature before the onset of forsterite formation was used to estimate the theoretical amorphous content (refers to the sum of amorphous α- and β-metaserpentine) in antigorite and lizardite sample using stoichiometric Equation 4.1. Then we calculated the amount of antigorite needed to produce the same amount of amorphous content as in the lizardite sample (used as a reference), which is directly related to the ratio of amorphous production in lizardite to amorphous production in antigorite $(Am)_{Liz}/(Am)_{Atg}$ before forsterite formation.

4.2.3 Thermal analyses

Simultaneous thermogravimetric (TGA) and differential scanning calorimeter (DSC) analyses were carried out using Netzsch STA-449F3. Sensitivity calibration was performed using a sapphire standard disc (0.25 mm x 6 mm) in a covered platinum-rhodium (Pt-Rh) crucible under a constant flow of 40 mL min^{-1} of argon gas. A routine burn-off at 1000 °C for 10 min under a constant flow of 50 mL min^{-1} of synthetic air, served to remove the residual impurities in the furnace. The repeated non-isothermal experiments for 10 mg of both sieve fractions (45-75 µm and <45 µm) of lizardite and antigorite samples were performed at 8 °C min^{-1} in a temperature range of 25 -1000 °C under a constant argon flow of 40 mL min^{-1} in a covered crucible. Blank runs (without sample) for all the above experiments were performed under identical conditions to correct thermal buoyancy in TGA and the baseline in DSC. Maximum standard deviation in peak temperature, peak area, and mass loss in the repeated dehydroxylation TGA-DSC experiments are ± 1°C, ± 29 J g^{-1} and ± 0.08 %, respectively.

4.2.4 Calculation of energy requirements

The energy requirements for serpentine dehydroxylation were calculated at the temperature before the onset of forsterite during the dehydroxylation sequence. The extent of conversion, as determined from synchrotron PXRD for the above points, was applied to TGA data to identify the termination temperature for thermal treatment in the heat flow (DSC) curve. The energy requirement per unit mass was then calculated as the area under the heat flow curve up to the termination temperature using numerical integration (supporting information Figure S4.3). The respective DTG curve was used to mark the onset and end of dehydroxylation to calculate the

latent heat of dehydroxylation (Q_{Latent}) by measuring the area under the endothermic peak in the heat flow (DSC) curve. The sensible heat ($Q_{Sensible}$) was obtained by subtracting the latent heat, (Q_{Latent}) from the total heat (Q_{Total}) of dehydroxylation (Fig. S4.3; Balucan *et al.* (2013)).

In order to compare the energy requirements during dehydroxylation of serpentine polymorphs, we multiplied the energy required per unit mass of the sample with the ratio of the amount of antigorite and lizardite sample (Atg/Liz) needed to produce the same amorphous content (supporting information S4.3). The ratio of the amorphous phase produced $(Am)_{Liz}/(Am)_{Atg}$ is the same as the ratio of (Atg/Liz) to generate the same amorphous content during the thermal dehydroxylation. Lizardite sample with < 45 μm ($L_{<45\ \mu m}$) produces the highest amorphous content. Hence, it has been used as a reference for PXRD analysis, to measure the relative amounts of other samples to yield the same amorphous content.

4.3 Results and discussions

4.3.1 Effect of process parameters on serpentine dehydroxylation

2D (temperature resolved 2θ) plots for the *in-situ* synchrotron PXRD analysis and normalised integrated intensities and TGA-DSC traces illustrate the comparison of the effects of process parameters on the evolution of different phases and their respective formation and decomposition temperatures during the thermal dehydroxylation of two serpentine polymorphs (*i.e.*, antigorite

and lizardite) as shown in Figure 4.1 and 4.2 respectively. The details of the effects will be discussed in their respective sections.

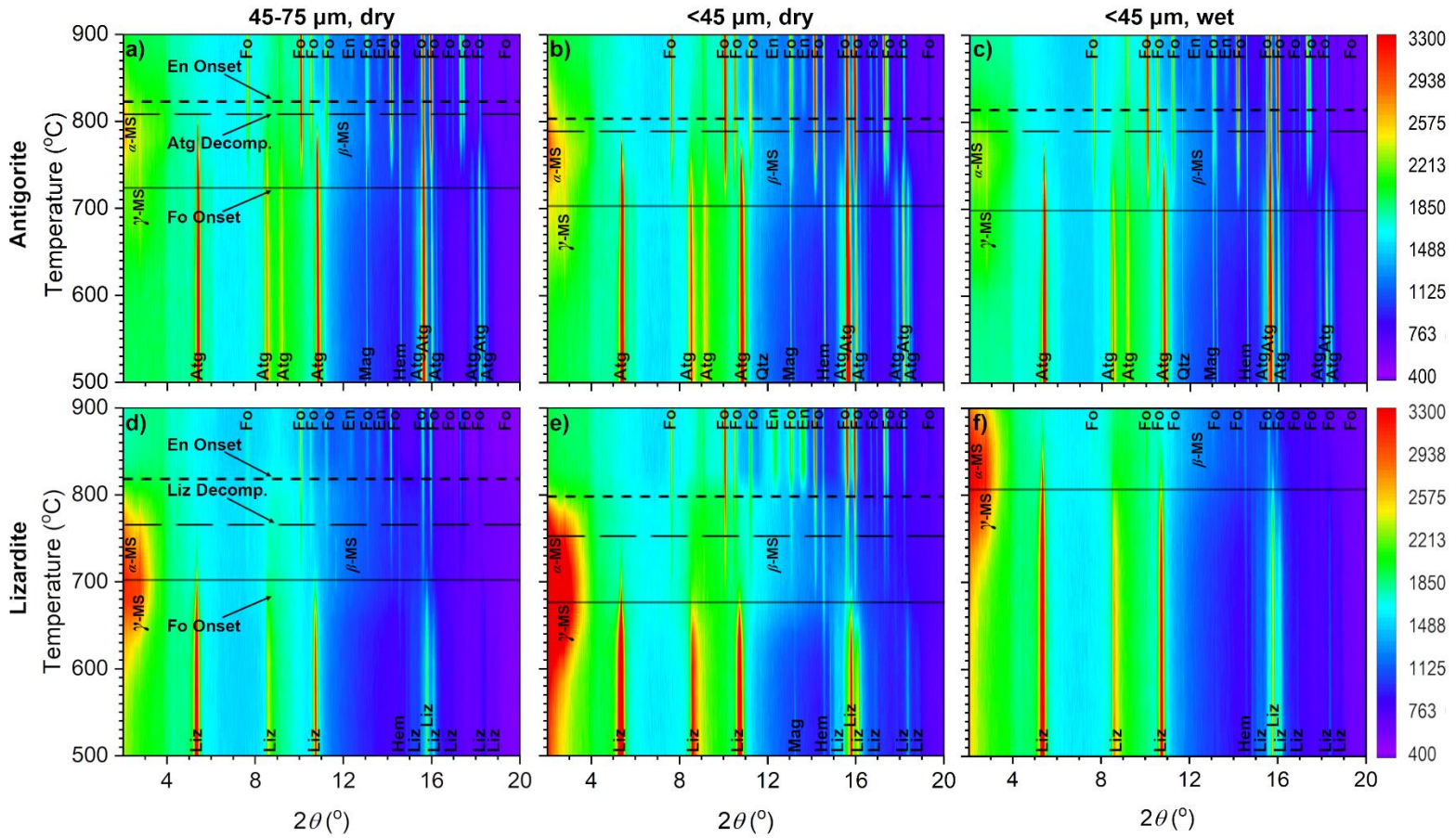

Figure 4.1. 2D (temperature resolved 2θ) synchrotron PXRD plot of the dehydroxylation of serpentine polymorphs of different particle size and partial pressure of water vapours. **a)** 45-75 µm and **b)** <45 µm sieve fraction under dry (low partial pressure of water vapours) and **c)** <45 µm sieve fraction under wet purge gas(high partial pressure of water vapours) conditions for antigorite **d)** 45-75 µm and **e)** <45 µm sieve fraction under dry and **f)** <45 µm sieve fraction under wet purge gas conditions for lizardite. Phases are labelled as Atg: antigorite, En: enstatite, Fo: forsterite, Liz: lizardite, α-MS: α-metaserpentine, β-MS: β-metaserpentine, and γ-MS: γ-metaserpentine. The onset of forsterite formation, complete decomposition of antigorite and onset of enstatite formation are shown

using solid, long dashed, and short dashed lines, respectively. Chlorite like γ-MS and amorphous α and β-metaserpentine components are present in all of the above 2D plots; however, their formation and decomposition temperatures are not shown for clarity (see Table S4.2 for details in Appendix B).

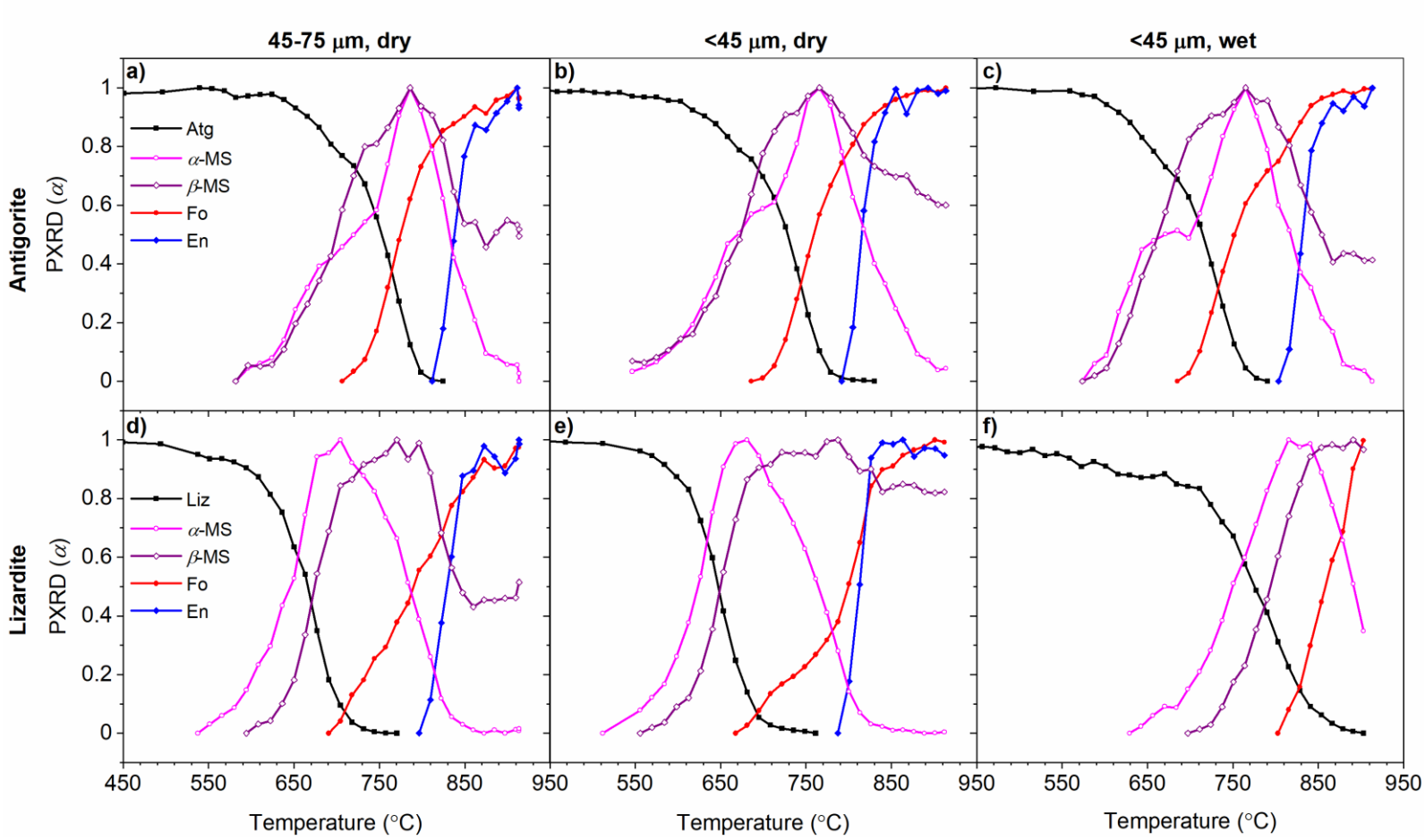

Figure 4.2. Normalised integrated intensities for the individual phases during the dehydroxylation of serpentine polymorphs of different grain size. **a)** 45-75 µm and **b)** <45 µm sieve fraction under dry and **c)** <45 µm sieve fraction under wet purge gas conditions for antigorite **d)** 45-75 µm and **e)** <45 µm sieve fraction under dry and **f)** <45 µm sieve fraction under wet purge gas conditions for lizardite. Phases are labelled as Atg: antigorite, En: enstatite, Fo: forsterite, Liz: lizardite, α-MS: α-metaserpentine, and β-MS: β-metaserpentine. Minor phases, *i.e.*, γ-MS, Qtz and Hem are not shown for clarity.

The selected synchrotron PXRD patterns in Figure 4.3 provide an overview of the reaction sequence during the dehydroxylation of antigorite and lizardite samples with 45-75 µm particle sizes.

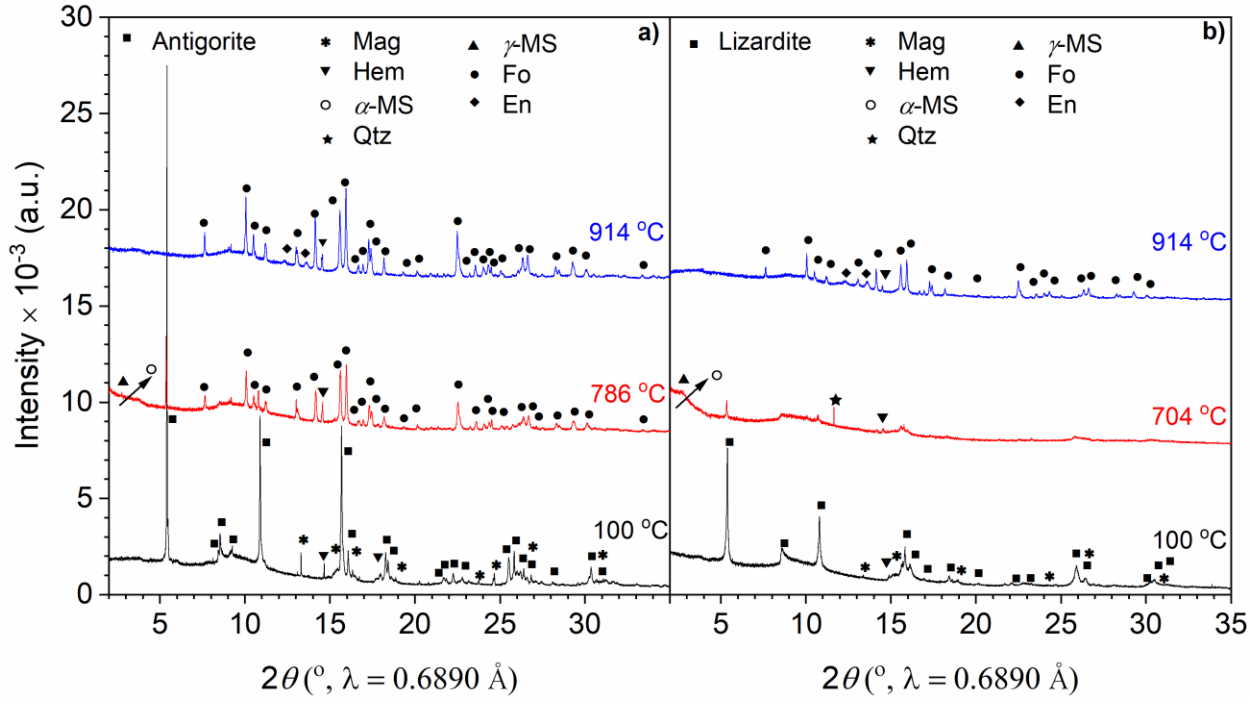

Figure 4.3. Selected synchrotron PXRD patterns for antigorite (a) and lizardite (b) with particle size 45 – 75 µm at 100 °C (black), at maximum amorphous content (786 °C and 704 °C, respectively; red) and after complete dehydroxylation at 914 °C (blue). The patterns are offset by 8000 counts, and the intensity is in arbitrary units (a.u.). Phases are labelled as Atg: antigorite, En: enstatite, Fo: forsterite, and Liz: lizardite, *α*-MS: *α*-metaserpentine and *γ*-MS: *γ*-metaserpentine. Open symbol exhibits the formation of the amorphous component during dehydroxylation.

The antigorite sample contains antigorite (COD ref. code: 96-900-3104) primarily with traces of magnetite (96-900-0927) and hematite (96-900-0140) (black diffractogram in Fig. 4.3a). In contrast, the lizardite sample mainly contains lizardite (96-901-6051) along with small impurity

of magnetite (96-900-6253) and hematite (96-900-0140) (black diffractogram in Fig. 4.3b). Antigorite has a diagnostic peak at d =1.56 Å (2θ = 25.5°), which is absent in the lizardite sample (Whittaker and Zussman, 1956). The dehydroxylation of both antigorite (Atg) and lizardite (Liz) results in the formation of intermediate phases, *i.e.*, amorphous α-MS for d > 9.9 Å (4° > 2θ) and amorphous β-MS component at 2.7 < d < 3.4 Å (2θ = 11.7 - 14.5°) and a minor amount of semi-crystalline chlorite-like phase (γ-MS) at d = 14.3 Å (2θ = 2.78°) as a result of the Al_2O_3 content in both samples (Fig. 4.1a, d; 4.2 a, d; 4.3a, b; Table 4.1) is consistent with the previous literature (Brindley and Zussman (1957); Chollet *et al.* (2011); Nakano *et al.* (2015); Pawley and Bromiley (2003); Chapter 3). Our PXRD analysis for the first time shows the formation of amorphous α-MS during the dehydroxylation of both antigorite and lizardite samples. In comparison to our PXRD data, a broad hump at 2.1 < d < 5.2 Å during the *ex-situ* XRD analysis has been referred to as amorphous meta serpentine component (McKelvy *et al.*, 2004; Rausis *et al.*, 2020). However, we observe a decrease in the amorphous background between 5.0 and 3.4 Å during thermal dehydroxylation probably because of the recrystallisation of amorphous serpentine consistent with a similar reduction in the amorphous background below the other serpentine peaks, *i.e.*, (00l) peak at d = 7.3 Å for both minerals (See Fig. S3.3 in Appendix A). On further heating, the amorphous α and β-metaserpentine components convert to forsterite (Fo) and enstatite (En), respectively (red and blue diffractograms in Fig. 4.3a and 4.3b, respectively). The amorphous α-MS and β-MS components are consistent with the behaviour of dehydroxylate I and dehydroxylate II observed during the ^{29}Si Nuclear magnetic resonance (^{29}Si NMR), respectively. For example, the formation of forsterite and enstatite occurs at the expense of dehydroxylate I and dehydroxylate II, respectively (MacKenzie and Meinhold, 1994).

TGA-DSC analysis illustrates the mass loss and heat flow during the dehydroxylation of antigorite and lizardite sample, as shown in Figure 4.4.

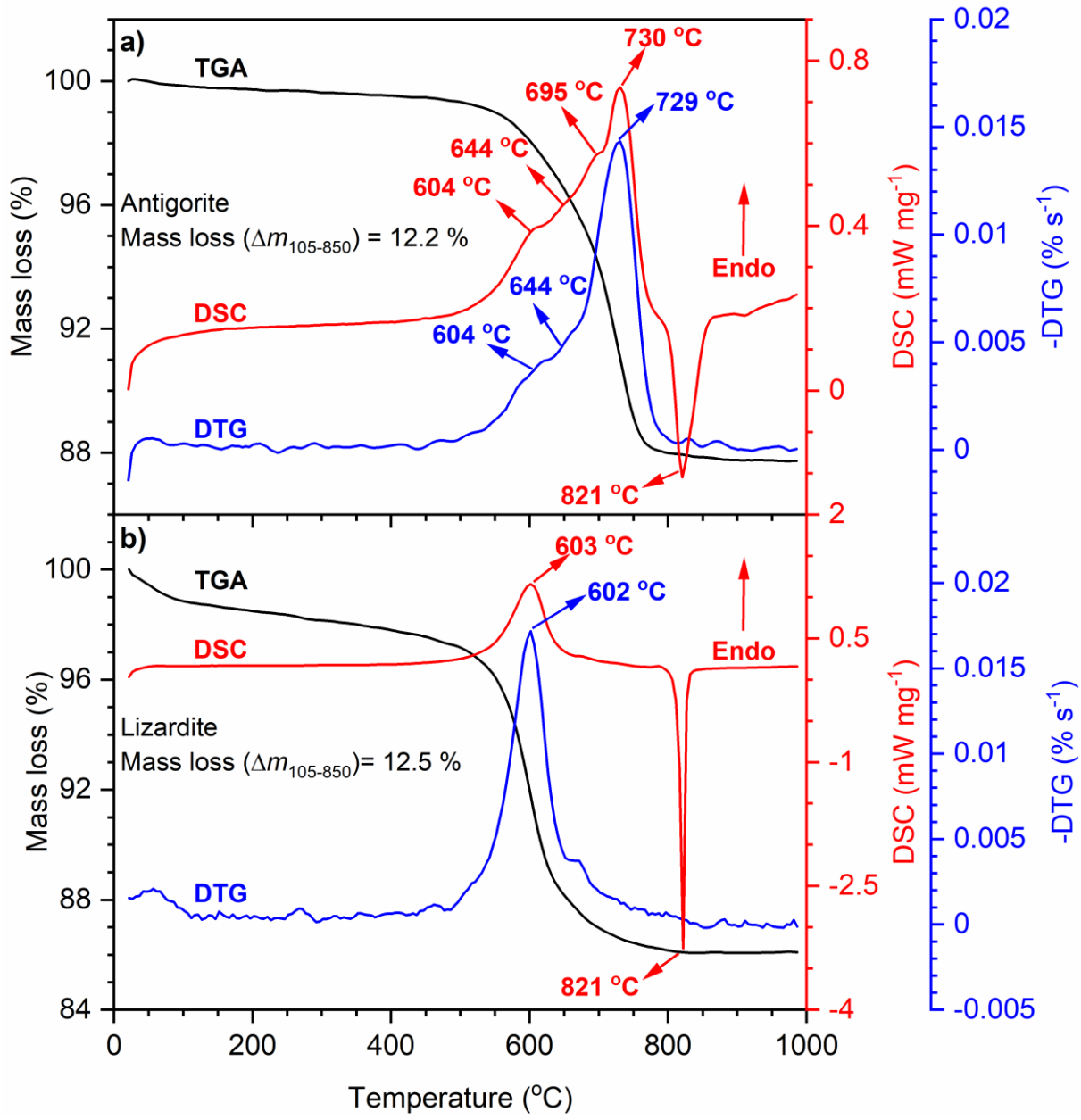

Figure 4.4. TGA (black), DTG (blue), and DSC (red) traces for the dehydroxylation of a) antigorite and b) lizardite sample at 8 °C min^{-1} under a constant flux of 40 mL min^{-1}of argon using 10 mg sample.

The major mass loss occurs in a temperature range of ~500-850 °C for both antigorite and lizardite samples (Fig. 4.4a and b). Heat flow curves (DSC) for both samples show endothermic peaks for dehydroxylation are associated with mass loss, which overlaps with exothermic crystallisation of forsterite above 700 °C. In comparison, the exothermic peak for crystallisation of forsterite and enstatite is not associated with any mass loss. The endothermic peak doublet at 695 and 730 °C during the dehydroxylation of antigorite (Balucan and Dlugogorski, 2013; Balucan *et al.*, 2013; Du Breuil *et al.*, 2019b) and endothermic peak at around 603 °C for lizardite sample (Ji *et al.*, 2018; Liu and Gadikota, 2018), are consistent with the behaviour of the serpentine polymorphs described in the literature. The exothermic peak is at the same temperature of ~821 °C for both serpentine polymorphs. However, antigorite sample shows a broader exothermic peak than lizardite (Balucan *et al.*, 2013), This might be linked to the rapid crystallisation of enstatite in lizardite as compared to antigorite sample (as shown in Fig. 4.3a, d).

The DSC analysis shows our latent heat (Q_{Latent}) value of 503 ± 20 MJ (t antigorite)$^{-1}$ is higher than all previously reported values ranging between 313 - 430 MJ (t antigorite)$^{-1}$ for antigorite sample (Balucan *et al.*, 2013; O'Connor *et al.*, 2001; O'Connor *et al.*, 2005; Weber and Greer, 1965), probably because of the relatively high Al_2O_3 content in our antigorite sample which increases the thermal stability of antigorite (Bromiley and Pawley (2003); Chapter 3). However, the latent heat value of 533 ± 29 MJ (t lizardite)$^{-1}$ for complete dehydroxylation of our lizardite sample is in close agreement with Weber and Greer's (1965) measurements of 565 ± 73 MJ (t serpentine)$^{-1}$ and higher than Balucan's *et al.* and O'Connor's *et al.* values of 479 ± 13 MJ and 432 MJ (t serpentine)$^{-1}$ respectively. However, total latent heat (Q_{Latent}) of 503 MJ (t serpentine)$^{-1}$ for dehydroxylation of antigorite ($A_{45\text{-}75\mu m}$) is lower than the 533 MJ (t serpentine)$^{-1}$ for lizardite

($Liz_{45\text{-}75\mu m}$). In contrast, total energy requirement ($Q = Q_{sensible} + Q_{Latent}$) of 1403 MJ (t serpentine)$^{-1}$ for the complete dehydroxylation of antigorite is higher than Q of 1370 MJ (t serpentine)$^{-1}$ for lizardite. The same was observed by Balucan *et al*. (2013).

4.3.2 Effect of mineralogy

2D plots for *in-situ* XRD analysis over selected 2θ range compares the evolution temperatures of non-overlapping peak reflection (hkl) of all the phases and their relative abundance during the thermal dehydroxylation of antigorite (Atg) and lizardite (Liz), as shown in Figure 4.5.

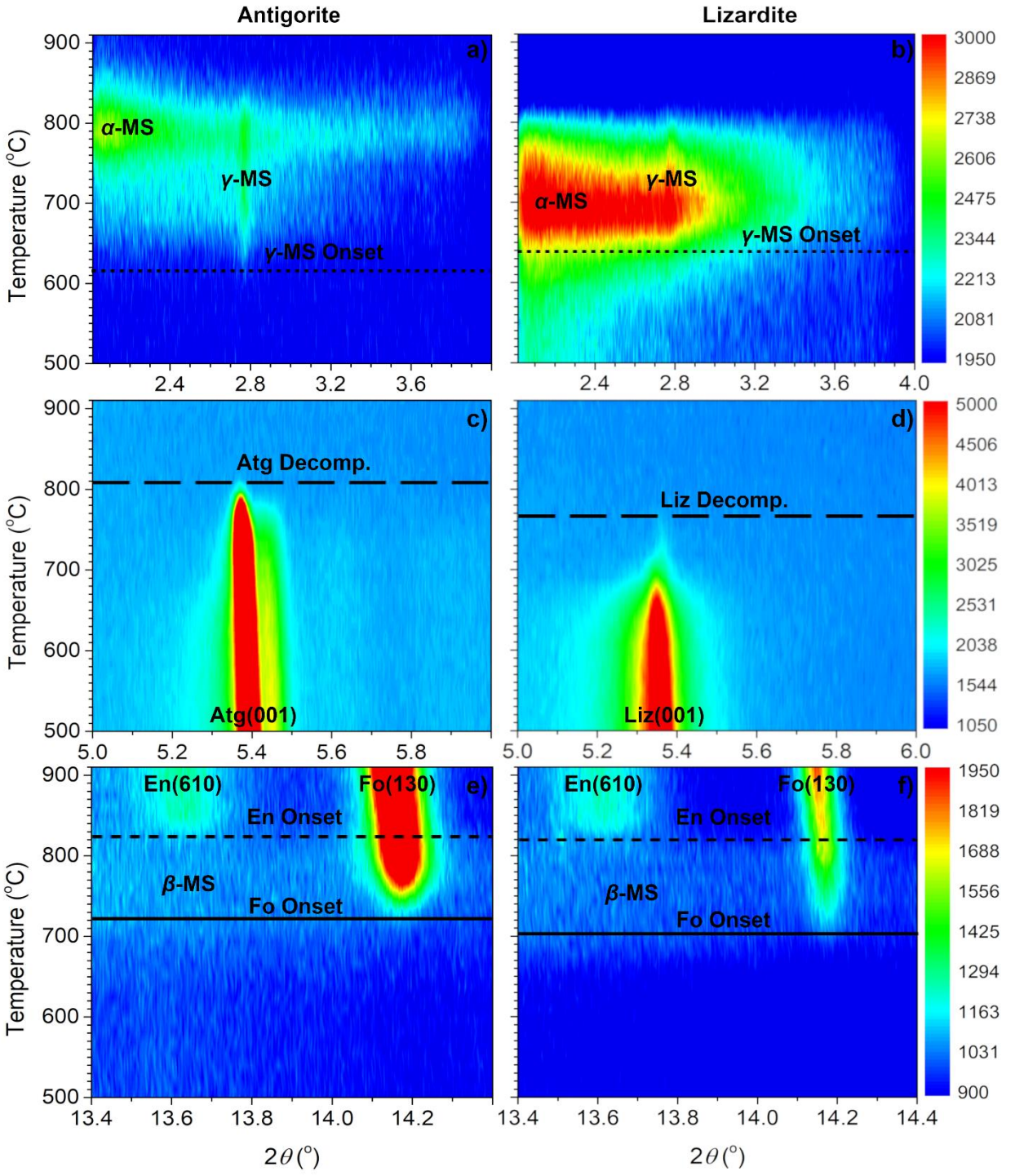

Figure 4.5. 2D synchrotron PXRD plots (temperature vs diffraction angle, 2θ) of the non-overlapping peak reflections (hkl) over the zoomed 2θ range for the evolution of individual phases during the dehydroxylation of antigorite (Atg) (panels a, c, e) and lizardite (Liz) (panels b, d, f) with particle size fraction 45-75 µm. Formation of α-metaserpentine and γ-metaserpentine (a, b), complete decomposition of antigorite (c) and lizardite (d) and

formation of forsterite, enstatite and β meta serpentine (e, f) are shown as dotted, long-dashed, short dashed and solid lines respectively. Phases are labelled as Atg: antigorite, En: enstatite, Fo: forsterite, Liz: lizardite, α-MS: α-metaserpentine, β-MS: β-metaserpentine, and γ-MS: γ-metaserpentine. The same colour scales for intensity are used for panels on the left and right side. The evolution of β-MS can be seen more clearly in Fig 4.2a and d.

The evolution of all phase changes during *in-situ* PXRD analysis of thermal dehydroxylation of antigorite occur at higher temperatures as compared to lizardite sample, except that the onset of chlorite-like phase (γ-MS) occurs at a lower temperature in antigorite, and the onset temperature for enstatite (En) formation remains unchanged in both samples (Fig. 4.5). Lower chlorite-like (γ-MS) formation due to lower Al_2O_3 content and higher amorphous content in the lizardite sample partially obscures the identification of chlorite-like phase (Table 4.1; Fig. 4.5a, b). Overall, the higher thermal stability of antigorite compared to lizardite, as reflected by higher evolution temperatures for all phases during dehydroxylation (Fig. 4.2a, b) is consistent with previous literature (Balucan *et al.*, 2013; Du Breuil *et al.*, 2019b; Liu and Gadikota, 2018). In the lizardite, the octahedral (brucite like) and tetrahedral (silica-like) layers are arranged alternatively giving it a planner structure whereas mismatched tetrahedral and octahedral sheets lead to the corrugated structured in antigorite sample (Dlugogorski and Balucan, 2014; Viti, 2010; Wicks and O'Hanley, 1988; Wicks and Whittaker, 1975). The corrugated structure makes antigorite thermodynamically more favourable compared to the planer lizardite structure (Ghaderi *et al.*, 2015), thereby giving the higher thermal stability to antigorite.

The dehydroxylation of both antigorite and lizardite samples produces the amorphous α and β-MS components (Fig. 4.2a, d). The formation of both amorphous components coincides in antigorite samples (~596 °C) whereas, in lizardite samples, the appearance of β-MS occurs at

~30-50 ℃ higher temperature compared to the α-MS. Moreover, both amorphous components achieve the maximum content at the same temperature for antigorite. However, for lizardite, β-MS reaches to ~80% of its maximum intensity at the maximum α-MS component, before the onset of forsterite. The α-MS transforms completely into forsterite, whereas β-MS component partially converts to enstatite phase in both minerals. The formation of two amorphous components and their conversion to crystalline forsterite and enstatite phases during the dehydroxylation of lizardite correspond to the similar behaviour observed for antigorite samples, consistent with the data presented in our previous work (Chapter 3).

The qualitative analysis of synchrotron PXRD demonstrates that significantly less amorphous content is formed during antigorite dehydroxylation compared to lizardite (Fig. 4.5a, b). Moreover, the formation of forsterite is higher in antigorite than lizardite, as shown in Figure 4.5e, f. Structural disorder produced by the amorphisation may delay the crysallisation process by hindering the rearrangement of atoms within the structure for non-overlapping amorphisation-crystallisation reactions. Brindley and co-workers also reported that high disorder delays the forsterite crystallisation by restricting the rearrangement of atoms within the structure (Brindley and Hayami, 1963; Brindley and Zussman, 1957). This may explain the more forsterite and less enstatite production in the antigorite sample as compared to the lizardite sample, as the higher thermal stability of the antigorite sample leads to the less amorphous production which maintains the necessary structural order for topotactic crystallisation of forsterite in the coupled amorphisation and crystallisation region during thermal dehydroxylation. In contrast, due to the decoupled amorphisation and crystallisation, lizardite sample completely converts to the amorphous content resulting in a highly disordered structure, which hinders the rearrangement of

atoms for the topotactic crystallisation of forsterite. This is also evident by our synchrotron PXRD analysis showing steeper forsterite formation in antigorite compared to the lizardite sample, as shown in Figure 4.2a, d.

4.3.3 Effect of grain size

All phase changes during *in-situ* synchrotron PXRD analysis of thermal dehydroxylation of serpentine polymorphs occur at a lower temperature in the smaller size fraction < 45 μm (Fig. 4.1a, b, d, e). The decrease in temperature (*e.g.*, $T(Atg_{45\text{-}75})$ - $T(Atg_{<45})$) is generally consistent for antigorite and lizardite, except for slightly larger reductions (~30 °C) observed for the onset of chlorite-like phase (γ-MS) formation and dehydroxylation in lizardite as shown in Figure 4.6.

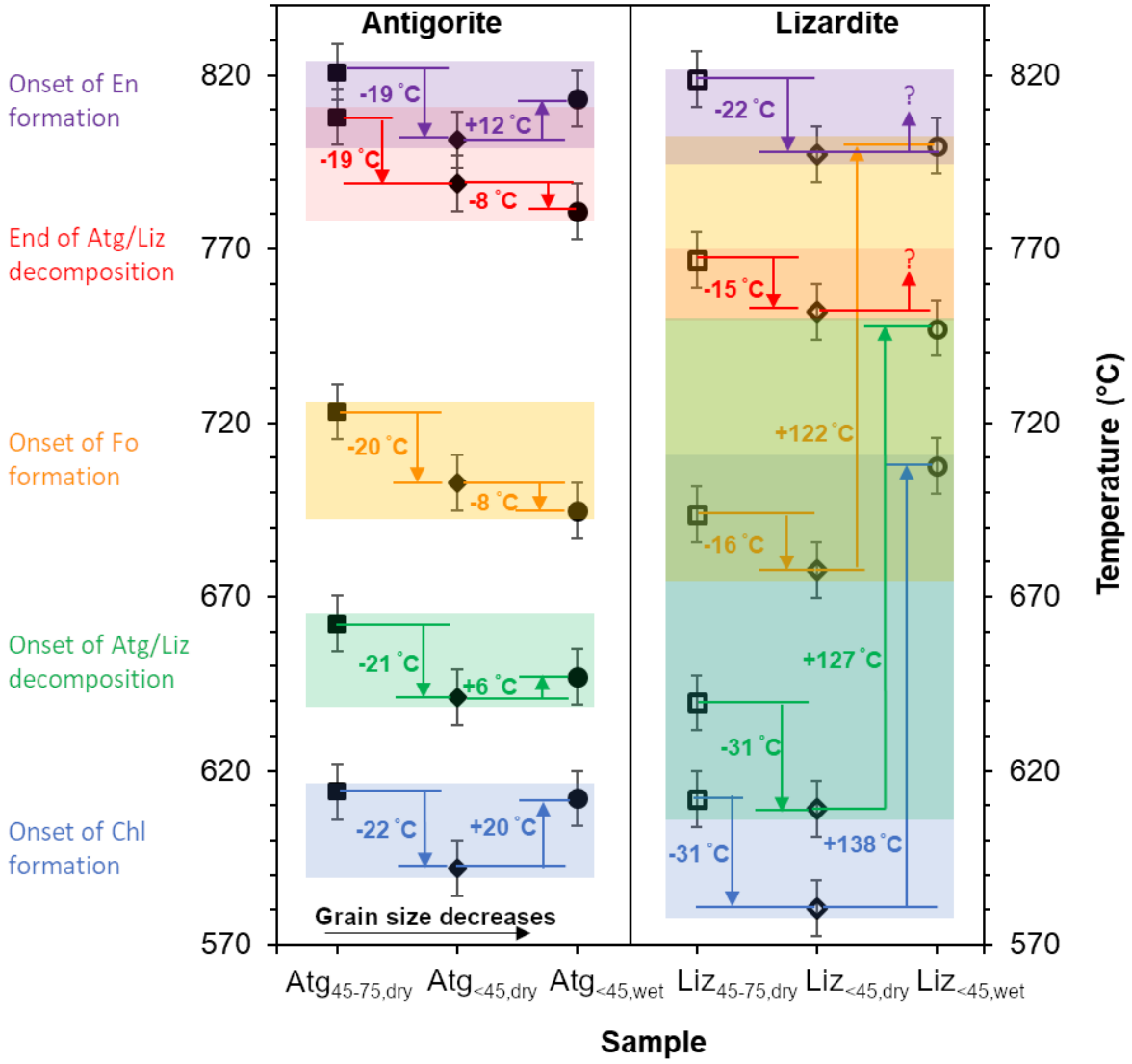

Figure 4.6. Schematic summary of the effects of mineralogy, grain size and partial pressure of water vapours on the phase evolution temperatures during dehydroxylation of serpentine polymorphs observed by *in-situ* synchrotron PXRD. $Atg_{45\text{-}75,\ dry}$, $Atg_{<45,\ dry}$ and $Atg_{<45,\ wet}$ refer to antigorite with a sample size of 45-75 µm and <45 µm, heated under dry and wet conditions, respectively. Similar abbreviations are used for the lizardite (Liz) sample. Under wet conditions, the lizardite sample does not completely decompose in the studied temperature range.

The reduction in dehydroxylation temperatures of serpentine minerals with the particle size is consistent with the previous literature as it affects the dehydroxylation temperature by increasing

specific surface area and shortening the distance of heat and volatile transfer between particle surfaces and interior (Bloise, 2018; Brindley and Hayami, 1963; Drief and Nieto, 1999; Martinez, 1961). For antigorite, a reduction in particle size leads to consistent lowering of temperatures of decomposition, forsterite formation and enstatite formation by 20 °C (Table S4.2). Albeit more variable, a similar decrease in temperatures is observed for lizardite. This reflects the increased heat transfer into smaller serpentine particles and the close coupling of forsterite and enstatite formation to serpentine dehydroxylation. Smaller particle size also reduces the γ-MS formation temperature for antigorite and lizardite, but its decomposition temperature is not affected by particle size. This suggests that γ-MS formation is affected by the increased heat transfer to the finer material, but its decomposition temperatures are decoupled from formation temperature. Consequently, the particle size of the initial feedstock may influence not only decomposition temperatures of serpentine but also the formation temperatures of the crystalline phases forming at a higher temperature.

4.3.4 Effect of the partial pressure of water vapours

The evolution of different phases during the dehydroxylation of antigorite and lizardite under dry and wet conditions is shown in Figure 4.1 (b, c and e, f) and 4.2 (b, c and e, f). Using wet purge gas does not have a significant effect on temperatures of antigorite decomposition, forsterite and enstatite formation but chlorite formation and decomposition occur at about 20 °C higher temperatures in wet conditions (Fig 4.6; Table S4.2). In contrast, the wet condition has a severe effect on lizardite dehydroxylation, leading to significantly increased temperatures for the onset

of dehydroxylation (+127 °C) and formation of chlorite like γ-MS (+138 °C) and forsterite (+122 °C) relative to dry conditions (Fig. 4.6). However, under wet conditions, the lizardite sample does not completely decompose in the studied temperature range.

The water vapours produced due to thermal dehydroxylation of serpentine minerals may initiate the back reaction and slow down the dehydroxylation process (Balucan and Dlugogorski, 2013; Brindley *et al.*, 1967a; Brindley and Millhollen, 1966; Brindley *et al.*, 1967b). However, *in-situ* PXRD analysis shows the dehydroxylation of antigorite is not affected by the variation in P_{H2O}. In contrast, lizardite shows a considerable increase in the evolution temperatures during the dehydroxylation under high P_{H2O} condition (Fig. 4.6). The negligible effect of P_{H2O} may be explained due to the small amount of amorphous phase in the antigorite sample, which offers less hindrance to the diffusion of water vapour from the structure. Additionally, the coupled exothermic forsterite crystallisation and high dehydroxylation temperature inhibit the formation of the chemisorption layer of water vapours over the antigorite surface. This is in line with Brindley and co-workers who reported that the effect of chemisorption of water vapour is negligible at high temperature, *i.e.*, ≥ 657 °C for 10^{-3} mmHg and ≥ 698 °C for 47 mmHg water vapour pressure (Brindley *et al.*, 1967a; Brindley and Millhollen, 1966; Brindley *et al.*, 1967b)

On the other hand, an increase in phase evolution temperatures under high P_{H2O} condition in lizardite might be explained based on the high amorphous content production during dehydroxylation which hinders the diffusion of water (H_2O) from the surface of particles during the dehydroxylation of lizardite. Previous literature also reports an increase in activation energy and dehydroxylation temperature with the increase in water vapour pressure for kaolinite and

lizardite minerals, having a similar parallel layered structure and both convert to the amorphous phase before the onset of crystalline phases (Brindley and Hayami, 1963; Brindley and Millhollen, 1966; Brindley *et al.*, 1967b; Levy, 1990). High P_{H2O} blocks the portion of the mineral surface for the dehydroxylation reaction through chemisorption of water on the surface at a lower temperature. Unlike antigorite, the water vapour at a lower temperature and high amorphous content before exothermic crystalline forsterite formation (~700 °C) in lizardite results in higher chemisorption and delays the lizardite dehydroxylation. Hence, the chemisorption of water favoured by lower temperatures and high amorphous content delays lizardite dehydroxylation.

In contrast, the high temperature, exothermic crystallisation of forsterite and less amorphous formation in antigorite does not favour the production of chemisorption layer of water. It is generally accepted that the dehydroxylation of serpentine under high vapour pressure conditions shifts the dehydroxylation reaction to more elevated temperatures based on TGA data (Balucan and Dlugogorski, 2013; Brindley *et al.*, 1967a). However, our PXRD observations support that the P_{H2O} increases the dehydroxylation temperature only for lizardite sample; however, it does not appreciably affect the dehydroxylation temperature for antigorite sample. Therefore, we recommend the continuous flow of air or proper ventilation to remove the water vapours generated during thermal dehydroxylation to avoid the loss of energy and quick conversion to the desired products.

4.3.5 Heat requirements

The reactivity of serpentine depends on the mineral carbonation conditions along with amorphous and crystalline phases formed during thermal dehydroxylation. Higher amorphous content yield during thermal dehydroxylation, ease the Mg dissolution even under the mild acidic conditions (Du Breuil *et al.*, 2019b; Farhang *et al.*, 2017; Mouedhen *et al.*, 2017; Rim *et al.*, 2020). In comparison, crystalline forsterite formation is not favourable under these conditions (Balucan *et al.*, 2011; Farhang *et al.*, 2017; Mouedhen *et al.*, 2017; Saadatkhah *et al.*, 2020). Although mineral carbonation using strong acid or higher pCO_2 results the higher dissolution rates as Mg is also released by forsterite dissolution (Du Breuil *et al.*, 2019b; Ortega *et al.*, 2010; Rim *et al.*, 2020; Stopic *et al.*, 2019; Stopic *et al.*, 2018), the cost of recovery and recycling the strong acids, limits its feasibility. However, higher amorphous content is most favourable in either case and must be considered to estimate the realistic energy requirement for thermal dehydroxylation. Rausis *et al.* (2020) reported that the amorphous metaserpentine ($2.1 < d < 5.2$ Å) is not affected by the carbonation of the heat-treated lizardite sample under low temperature and pressure conditions; hence it is a poorly reactive amorphous phase (Rausis *et al.*, 2020). However, they did not observe amorphous α-MS ($d > 9.9$ Å) due to the limitation of the laboratory scale *ex-situ* XRD analysis. Our *in-situ* synchrotron PXRD analysis shows two amorphous components α-MS and β-MS along with the formation of chlorite-like γ-MS (d =14.3 Å). Hence, practical heating strategies must be designed to perform heat treatment before the onset temperature of forsterite formation. Balucan *et al*. (2013) have already shown that the complete dehydroxylation of serpentine minerals is not energy efficient due to the production of high-temperature crystalline phases, *i.e.*, forsterite and enstatite (Balucan *et al.*, 2013). Hence, in

the current study, the energy requirements are compared based on the amount of the amorphous content produced during heat treatment before the formation of forsterite as shown in Table 4.3 for practical heat treatment strategies of the investigated samples.

Table 4.3. Comparison of energy for 1 tonne of serpentine mineral (*i.e.*, antigorite and lizardite) required to produce the same amorphous content during the thermal dehydroxylation of serpentine before the onset of forsterite formation.

Sample	% conv.	% OH_{Res}	Total Energy	Am. Production	Relative Am production in serpentine	Energy required (Q_S) to produce the same Am content as in ref	$Q_S/Q_{ref.}$
	PXRD	(TGA)	Q	Theoretical.	Theoretical.	Q .(S)/$(Liz)_{ref}$	Theoretical.
	%	%	MJ$(tonne)^{-1}$	tonnes	$(Am)_{ref,,Liz}/(Am)_S$	MJ $(tonne)^{-1}$	
Liz_{45-75}	90	10	1230	0.78	0.94	1161	1.00
$Liz_{<45}$	85	15	1212	0.74	1.00	1212	1.00
Atg_{45-75}	26	74	880	0.23	3.27	2877	2.37
$Atg_{<45}$	30	70	951	0.26	2.84	2703	2.23

Note: Am = Amorphous content, Atg = antigorite, Liz = lizardite, subscript in $(Liz)_{<45}$ represents the particle size fraction, *i.e.*<45 µm, $(Am)_{ref,\ Liz}$ represents the amorphous content produced in reference lizardite sample (*i.e.*, $Liz_{<45}$ used as a reference due to highest amorphous production). $(Am)_{ref,Liz}/(Am)_s$ is the ratio of Amorphous phase production in the reference sample to the current sample. It is equal to the ratio of the amount of sample to reference lizardite (S/Liz_{ref}) to produce the same amorphous content. Multiplying $(Am)_{ref,Liz}/(Am)_s$ to the total energy provides the Q_S to produce same amorphous content. ($Q_S/Q_{ref.}$) provides us with the relative energy required for the sample to produce the same amorphous content as in ref. Liz sample.

% conv. represents the % dehydroxylated antigorite and lizardite phase during *in-situ* synchrotron PXRD analysis

% OH_{res} exhibits the residual OH extracted from TGA, based on α from PXRD to calculate the terminal temperature for the energy requirements from DSC. $\%OH_{res} = 1-\alpha$

Theoretical values refer to the stoichiometric calculations based on the dehydroxylation Reaction equation 4.1

Table 4.3 shows that antigorite requires nearly 3.3 times more sample than the lizardite to produce the same amount of amorphous material while avoiding the forsterite formation. However, the energy requirements for antigorite are ~2.37 times than the lizardite for heat-treating the serpentine before the onset of forsterite formation (Table 4.3).

4.4 Conclusion

This study combines *in-situ* synchrotron PXRD and TGA-DSC analysis to show the effects of the partial pressure of water vapours, grain size, and mineralogy on the dehydroxylation of serpentine minerals and its implication for effective dehydroxylation. The results suggest that lizardite is more suitable for dehydroxylation than antigorite as it a) produces higher amorphous content per unit mass of sample b) achieves maximum amorphous content before the formation of less reactive crystalline, *i.e.*, forsterite and enstatite phases c) reduces the energy consumption to nearly half compared to antigorite for heat treatment due to higher production of amorphous phase and dehydroxylation at a lower temperature.

Additionally, smaller particle sizes lower the dehydroxylation temperature due to the increase in surface area and heat transfer, leading to lower energy requirements for heat transfer. Moreover, the high partial pressure of water vapours does not affect the dehydroxylation in antigorite, whereas it inhibits the dehydroxylation in lizardite sample. Hence, for practical heating during the dehydroxylation of lizardite sample, it is essential to ensure adequate ventilation and air circulation to avoid the formation of chemisorption layer which may generate due to the

entrapment of water vapours and thereby hindering the dehydroxylation. This can be achieved by the use of fluidised bed reactor and purging with a dry N_2 or argon gas.

4.5 References:

Alexander, G., Mercedes Maroto-Valer, M., Gafarova-Aksoy, P. (2007) Evaluation of reaction variables in the dissolution of serpentine for mineral carbonation. Fuel 86, 273-281.

Balucan, R.D., Dlugogorski, B.Z. (2013) Thermal activation of antigorite for mineralisation of CO_2. Environmental Science & Technology 47, 182-190.

Balucan, R.D., Dlugogorski, B.Z., Kennedy, E.M., Belova, I.V., Murch, G.E. (2013) Energy cost of heat activating serpentinites for CO_2 storage by mineralisation. International Journal of Greenhouse Gas Control 17, 225-239.

Balucan, R.D., Kennedy, E.M., Mackie, J.F., Dlugogorski, B.Z. (2011) Optimisation of antigorite heat pre-treatment via kinetic modelling of the dehydroxylation reaction for CO_2 mineralisation. Greenhouse Gases: Science and Technology 1, 294-304.

Benhelal, E., Rashid, M.I., Rayson, M.S., Brent, G.F., Oliver, T., Stockenhuber, M., Kennedy, E.M. (2019) Direct aqueous carbonation of heat-activated serpentine: Discovery of undesirable side reactions reducing process efficiency. Applied Energy 242, 1369-1382.

Bloise, A.C., Manuela; Gualtieri, Alessandro F. (2018) Effect of grinding on chrysotile, amosite and crocidolite and implications for thermal treatment. Minerals 8.

Brindley, G.W., Achar, B.N.N., Sharp, J.H. (1967a) Kinetics and mechanism of dehydroxylation processes: II. Temperature and vapour pressure dependence of dehydroxylation of serpentine. American Mineralogist 52, 1697-1705.

Brindley, G.W., Hayami, R. (1963) Kinetics and mechanisms of dehydration and recrystallisation of serpentine—I. Clays and Clay Minerals 12, 35-47.

Brindley, G.W., Millhollen, G.L. (1966) Chemisorption of water at high temperatures on kaolinite: Effect on dehydroxylation. Science 152, 1385.

Brindley, G.W., Sharp, J.H., Patterson, J.H., Narahari, B.N. (1967b) Kinetics and mechanism of dehydroxylation processes, I. Temperature and vapour pressure dependence of dehydroxylation of kaolinite. American Mineralogist 52, 201-211.

Brindley, G.W., Zussman, J. (1957) A structural study of the thermal transformation of serpentine minerals to forsterite. American Mineralogist 42, 461-474.

Bromiley, G.D., Pawley, A.R. (2003) The stability of antigorite in the systems MgO-SiO_2-H_2O (MSH) and MgO-Al_2O_3-SiO_2-H_2O (MASH): The effects of Al^{3+} substitution on high-pressure stability. American Mineralogist 88, 99-108.

Chollet, M., Daniel, I., Koga, K.T., Morard, G., van de Moortèle, B. (2011) Kinetics and mechanism of antigorite dehydration: Implications for subduction zone seismicity. Journal of Geophysical Research: Solid Earth 116, B04203.

Dlugogorski, B.Z., Balucan, R.D. (2014) Dehydroxylation of serpentine minerals: Implications for mineral carbonation. Renewable and Sustainable Energy Reviews 31, 353-367.

Drief, A., Nieto, F. (1999) The effect of dry grinding on antigorite from Mulhacen, Spain. Clays and Clay Minerals 47, 417-424.

Du Breuil, C., César-Pasquier, L., Dipple, G., Blais, J.-F., Iliuta, C.M., Mercier, G. (2019a) Mineralogical transformations of heated serpentine and their impact on dissolution during aqueous-phase mineral carbonation reaction in flue gas conditions. Minerals 9.

Du Breuil, C., Pasquier, L.-C., Dipple, G., Blais, J.-F., Iliuta, C.M., Mercier, G. (2019b) Mineralogical transformations of heated serpentine and their impact on dissolution during aqueous-phase mineral carbonation reaction in flue gas conditions. Minerals 9.

Farhang, F., Rayson, M., Brent, G., Hodgins, T., Stockenhuber, M., Kennedy, E. (2017) Insights into the dissolution kinetics of thermally activated serpentine for CO_2 sequestration. Chemical Engineering Journal 330, 1174-1186.

Gerdemann, S.J., O'Connor, W.K., Dahlin, D.C., Penner, L.R., Rush, H. (2007) *Ex-situ* aqueous mineral carbonation. Environmental Science & Technology 41, 2587-2593.

Ghaderi, N., Zhang, H., Sun, T. (2015) Relative stability and contrasting elastic properties of serpentine polymorphs from first-principles calculations. Journal of Geophysical Research: Solid Earth 120, 4831-4842.

Hariharan, S., Werner, M., Hänchen, M., Zingaretti, D., Baciocchi, R., Mazzotti, M. (2014) Dissolution kinetics of thermally activated serpentine for mineralisation at flue gas conditions. Energy Procedia 63, 5887-5891.

Ji, S., Zhu, J., He, H., Tao, Q., Zhu, R., Ma, L., Chen, M., Li, S., Zhou, J. (2018) Conversion of serpentine to smectite under hydrothermal condition: Implication for solid-state transformation. American Mineralogist 103, 241-251.

Kim, D.-J., Chung, H.-S. (2002) Effect of grinding on the structure and chemical extraction of metals from serpentine. Particulate Science and Technology 20, 159-168.

Levy, J.H. (1990) Effect of water vapour pressure on the dehydration and dehydroxylation of kaolinite and smectite isolated from Australian tertiary oil shales. Energy & Fuels 4, 146-151.

Liu, M., Gadikota, G. (2018) Chemo-morphological coupling during serpentine heat treatment for carbon mineralisation. Fuel 227, 379-385.

Liu, M., Gadikota, G. (2020) Single-step, low temperature and integrated CO_2 capture and conversion using sodium glycinate to produce calcium carbonate. Fuel 275, 117887.

MacKenzie, K.J.D., Meinhold, R.H. (1994) Thermal reactions of chrysotile revisited: A 29Si and 25Mg MAS NMR study. American Mineralogist 79, 43-50.

Maroto-Valer, M.M., Fauth, D.J., Kuchta, M.E., Zhang, Y., Andrésen, J.M. (2005) Activation of magnesium rich minerals as carbonation feedstock materials for CO_2 sequestration. Fuel Processing Technology 86, 1627-1645.

Martinez, E. (1961) The effect of particle size on the thermal properties of serpentine minerals. American Mineralogist 46, 901-912.

McKelvy, M.J., Chizmeshya, A.V.G., Diefenbacher, J., Béarat, H., Wolf, G. (2004) Exploration of the role of heat activation in enhancing serpentine carbon sequestration reactions. Environmental Science & Technology 38, 6897-6903.

Michael, A., Zhou, Y.N., Yavuz, M., Khan, M.I. (2018) Deconvolution of overlapping peaks from differential scanning calorimetry analysis for multi-phase NiTi alloys. Thermochimica Acta 665, 53-59.

Mouedhen, I., Kemache, N., Pasquier, L.-C., Cecchi, E., Blais, J.-F., Mercier, G. (2017) Effect of pCO_2 on direct flue gas mineral carbonation at pilot scale. Journal of Environmental Management 198, 1-8.

O'Connor, W.K., Dahlin, D.C., Nilsen, D.N., Gerdemann, S.J., Rush, G.E., Walters, R.P., Turner, P.C., (2001) Research status on the sequestration of carbon dioxide by direct aqueous mineral carbonation. Pittsburgh Coal Conference, University of Pittsburgh, 1249 Benedum Hall, Pittsburgh, PA 15261, United States.

O'Connor, W.K., Dahlin, D.C., Rush, G.E., Gerdemann, S.J., Penner, L.R., (2005) Energy and economic evaluation of *ex-situ* aqueous mineral carbonation, Rubin, E.S., Keith, D.W., Gilboy, C.F., Wilson, M., Morris, T., Gale, J., Thambimuthu, K. (Eds.), Greenhouse Gas Control Technologies 7. Elsevier Science Ltd, Oxford, pp. 2011-2015.

Oskierski, H.C., Beinlich, A., Mavromatis, V., Altarawneh, M., Dlugogorski, B.Z. (2019) Mg isotope fractionation during continental weathering and low-temperature carbonation of ultramafic rocks. Geochimica et Cosmochimica Acta 262, 60-77.

Oskierski, H.C., Dlugogorski, B.Z., Jacobsen, G. (2013) Sequestration of atmospheric CO2 in a weathering-derived, serpentinite-hosted magnesite deposit: 14C tracing of carbon sources and age constraints for a refined genetic model. Geochimica et Cosmochimica Acta 122, 226-246.

Pawley, A.R., Bromiley, G.D. (2003) The stability of antigorite in the systems $MgO\text{-}SiO_2\text{-}H_2O$ (MSH) and $MgO\text{-}Al_2O_3\text{-}SiO_2\text{-}H_2O$ (MASH): The effects of Al^{3+} substitution on high-pressure stability. American Mineralogist 88, 99-108.

Rausis, K., Ćwik, A., Casanova, I. (2020) Insights into the direct carbonation of activated lizardite: The identification of a poorly reactive amorphous Mg-rich silicate phase. International Journal of Greenhouse Gas Control 100, 103114.

Rim, G., Marchese, A.K., Stallworth, P., Greenbaum, S.G., Park, A.-H.A. (2020) ^{29}Si solid-state MAS NMR study on leaching behaviours and chemical stability of different Mg-silicate structures for CO_2 sequestration. Chemical Engineering Journal 396, 125204.

Sandu, C., Singh, R.K. (1990) Modelling differential scanning calorimetry. Thermochimica Acta 159, 267-298.

Sanna, A., Wang, X., Lacinska, A., Styles, M., Paulson, T., Maroto-Valer, M.M. (2013) Enhancing Mg extraction from lizardite-rich serpentine for CO_2 mineral sequestration. Minerals Engineering 49, 135-144.

Schmitt, B., Brönnimann, C., Eikenberry, E.F., Hülsen, G., Toyokawa, H., Horisberger, R., Gozzo, F., Patterson, B., Schulze-Briese, C., Tomizaki, T. (2004) Development of single photon counting detectors at the Swiss Light Source. Nuclear Instruments and Methods in Physics Research Section A: Accelerators, Spectrometers, Detectors and Associated Equipment 518, 436-439.

Viti, C. (2010) Serpentine minerals discrimination by thermal analysis. American Mineralogist 95, 631.

Wallwork, K.S., Kennedy, B.J., Wang, D. (2007) The high-resolution powder diffraction beamline for the Australian Synchrotron. AIP Conference Proceedings 879, 879-882.

Weber, J.N., Greer, R.T. (1965) Dehydration of serpentine: heat of reaction and reaction kinetics at PH_2O=1 ATM. American Mineralogist 50, 450-464.

Werner, M., Hariharan, S., Mazzotti, M. (2014) Flue gas CO_2 mineralisation using thermally activated serpentine: From single- to double-step carbonation. Energy Procedia 63, 5912-5917.

Whittaker, E.J.W., Zussman, J. (1956) The characterization of serpentine minerals by X-ray diffraction. Mineralogical Magazine and Journal of the Mineralogical Society 31, 107-126.

Wicks, F.J., O'Hanley, D.S. (1988) Serpentine minerals; structures and petrology. Reviews in Mineralogy and Geochemistry 19, 91-167.

Wicks, F.J., Whittaker, E.J.W. (1975) A reappraisal of the structures of the serpentine minerals. The Canadian Mineralogist 13, 227-243.

Chapter 5: Comparison of TGA, DSC and XRD-based Kinetic Analysis of Antigorite Dehydroxylation

5 Abstract

Thermal dehydroxylation of serpentine minerals proceeds via intermediate amorphous phases to the formation of forsterite and enstatite at higher temperatures. It significantly enhances the reactivity of serpentine minerals for CO_2 storage through mineral carbonation, but practical implementation requires high energy inputs and thus intimate understanding of kinetic parameters of the dehydroxylation process. In this study, deploying the *in-situ* synchrotron PXRD, we investigate the isoconversional kinetics and compare them with those obtained from the TGA and DSC measurements. *In-situ* synchrotron PXRD can resolve processes affecting individual mineral phases and thus provide independent records of antigorite decomposition and forsterite formation kinetics, which overlap in conventional TGA and DSC analyses and the associated kinetic analysis. Our insights from synchrotron PXRD are consistent with an initially gentle increase in activation energies associated with increasing distance between hydroxyls that need to combine and diffuse for dehydroxylation to proceed. At around 703 °C, the temperature at which forsterite begins forming, TGA and DSC-based activation energies increase sharply. The synchrotron PXRD-based kinetics suggest that this increase is due to forsterite formation, which requires the breaking of strong Si-O and Mg-O bonds. Consequently, forsterite formation has to be avoided during energy-efficient heat treatment, as it is associated with a significant kinetic barrier.

5.1 Introduction

Mineral carbonation, a promising technology to safely and permanently sequester CO_2 emissions (Bobicki *et al.*, 2012; Gerdemann *et al.*, 2007; Huijgen and Comans, 2005; Kirchofer *et al.*, 2013; Lackner *et al.*, 1995; Liu and Gadikota, 2018, 2020; Maroto-Valer *et al.*, 2005; McKelvy *et al.*, 2004; Miller *et al.*, 2019; Prigiobbe *et al.*, 2009; Werner *et al.*, 2014) mimics the natural weathering of Ca/Mg silicate rocks to stable carbonates (Oskierski *et al.*, 2019; Oskierski *et al.*, 2013b; Wilson *et al.*, 2014). Thermal dehydroxylation helps to increase the Mg extraction from the serpentine minerals through amorphisation of the structure, necessary for mineral carbonation to occur at industrially relevant rates. However, the energy requirements for thermal dehydroxylation to enhance the dissolution kinetics of serpentine minerals for the industrial applications are currently a challenge (Alexander *et al.*, 2007; Dlugogorski and Balucan, 2014; Drief and Nieto, 1999; Kim and Chung, 2002; Maroto-Valer *et al.*, 2005; McKelvy *et al.*, 2004; Sanna *et al.*, 2014b). Additionally, the literature lacks a comprehensive thermo-kinetic and mineralogical analyses of the most stable form of the serpentine mineral, antigorite. The current study explores using *in-situ* synchrotron PXRD to unravel the kinetics of the overlapping reactions occurring during antigorite dehydroxylation.

Thermal dehydroxylation proceeds through the formation of intermediate amorphous phases between 500 to 800 °C, which transform into less-reactive crystalline forsterite and enstatite, above 700 °C and 800 °C, respectively (Du Breuil *et al.*, 2019b; Farhang *et al.*, 2017; MacKenzie and Meinhold, 1994; McKelvy *et al.*, 2004; Rausis *et al.*, 2020; Rim *et al.*, 2020). Isoconversional kinetic analysis for thermal dehydroxylation of antigorite, using

thermogravimetric (TGA) and differential scanning calorimetry (DSC), shows that the activation energy of antigorite dehydroxylation varies with reaction process, suggesting a complex multi-step nature of dehydroxylation reaction (Chapter 3, Liu *et al.* (2019)). However, there is limited understanding about the significant increase in E_α at around 700 °C, when only ~49 % (51 % OH_{res}) of antigorite is dehydroxylated (Chapter 3). This is likely related to the inability of commonly used TGA and DSC methods to resolve the overlapping reactions during antigorite dehydroxylation (Muravyev *et al.*, 2017; Nakano *et al.*, 2015; Saadatkhah *et al.*, 2020).

On the other hand, X-ray diffraction (XRD) can resolve the individual phase transformation, and their kinetics (Svoboda, 2019). Therefore, for the first time, this study uses *in-situ* synchrotron PXRD to separately analyse the kinetics of antigorite decomposition and forsterite formation. This new approach gives hitherto unavailable insights into the overall kinetics of antigorite dehydroxylation and explains the increase in activation energies at higher degrees of antigorite dehydroxylation observed in TGA and DSC-based kinetic analysis. Our data indicate that the increase in the energetic barrier to dehydroxylation is due to forsterite formation, which should thus be avoided during the practical implementation of thermal treatment.

5.2 Materials and methods

5.2.1 Sample preparation

This study investigates an antigorite-rich serpentinised harzburgite sample from Attunga, New South Wales, Australia (Oskierski *et al.*, 2013a; Oskierski *et al.*, 2013b). The sample was crushed using a hammer and ground in an agate ring mill for 2 – 3 min, and finally, sieved to obtain a narrow size fraction of 48 – 53 µm. Additionally, we demagnetised the samples using a hand-magnet.

5.2.2 Synchrotron powder X-ray diffraction (PXRD)

The heat treatment of antigorite has been studied with *in-situ* powder X-Ray diffraction (PXRD) beamline at the Australian Synchrotron (Wallwork *et al.*, 2007). We introduced the antigorite sample into 0.3 mm quartz capillary, continuously purged with inert nitrogen using a custom-made stainless steel sample holder designed by Norby (Norby, 1997). The X-ray wavelength (0.774479(6) Å) was calibrated using a lanthanum hexaboride (LaB_6) standard (NIST SRM 660b), and X-ray energy was 16 keV. The instrument recorded the diffractograms within the 2θ range of 3 – 80°, with an acquisition rate of one scan per minute by a position-sensitive MYTHEN II detector at two positions p1 and p2 at 3° and 3.5° respectively (Schmitt *et al.*, 2004). We applied the heating rates of 2, 4 and 8 °C min^{-1} from room temperature to 964 °C, using a hot air blower located beneath the capillary. A K-type thermocouple monitored the temperature of the capillary. Temperature calibration was based on the α to β-quartz transition in a quartz sample and the melting point of reagent grade NaCl (Section 1of Appendix C). The maximum uncertainty in the temperature measurements is ± 8 °C.

We processed, merged and extracted the synchrotron PXRD data using PDViPeR software for further qualitative analysis in Crystal Impact Match! Software, using the crystallographic open database (COD). Origin software served to perform the baseline subtraction for synchrotron PXRD patterns and peak integration for non-overlapping peaks of different phases. The evolution of amorphous phases was determined as the difference in integrated intensity between the amorphous background and the capillary background; both modelled with the asymmetric least square smoothing method in Origin software (see Fig. S3.2 in section 2 of Appendix A) (He *et al.*, 2014; Peng *et al.*, 2010). The integrated peak intensities of amorphous and crystalline phases were normalised to the maximum intensity of the respective phases and transformed into the extent of conversion (α) during the dehydroxylation of the antigorite sample.

The sample consists of antigorite (COD ref. code: 96-900-3104) as a primary phase along with traces of magnesite (96-900-0972), quartz (96-900-0776) and hematite (96-900-0140; Fig. 5.1).

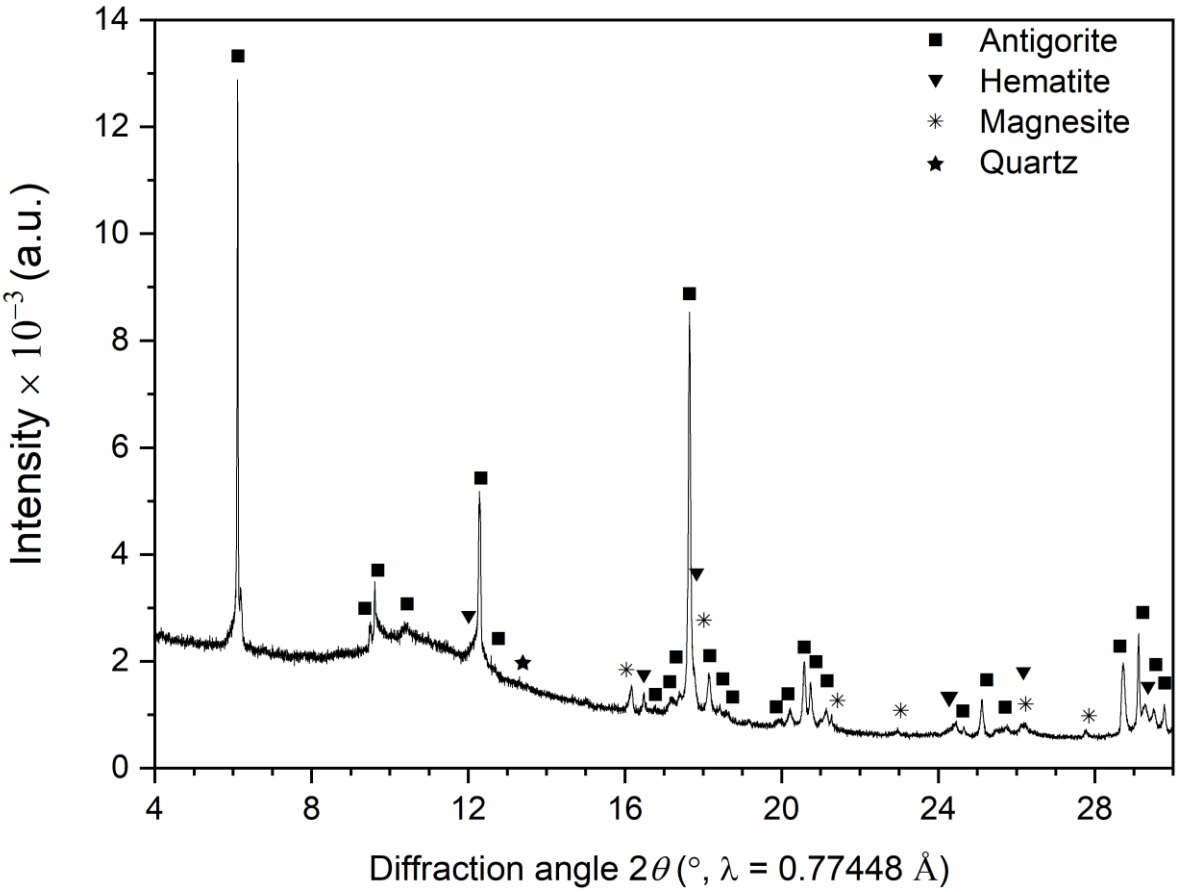

Figure 5.1. Room temperature synchrotron PXRD pattern of the antigorite sample. The intensity is in arbitrary units (a.u.).

5.2.3 X-Ray fluorescence (XRF) and LOI analyses

The chemical composition of the demagnetised powdered sample was determined using lithium tetraborate/metaborate glass bead and a PANalytical MagiX FAST XRF (Table 5.1). A robotic thermogravimetric analyser, LabFit TGA-4000 afforded, measuring the loss on ignition (LOI).

Table 5.1

The chemical composition of the demagnetised antigorite sample

Species	SiO_2	Al_2O_3	MgO	Fe_2O_3	Cr_2O_3	CaO	Na_2O	P_2O_5	SO_3	LOI	Total
(wt. %)	40.15	0.96	39.40	4.29	0.41	0.24	0.05	0.01	0.06	13.89	99.37

LOI (loss on ignition) denotes the release of volatile components at 1000 ℃.

5.2.4 Thermal analyses

Simultaneous thermogravimetric (TGA) and differential scanning calorimetric (DSC) analyses were performed using Netzsch STA 449 F3. Sensitivity calibration employed a 0.25 mm × 6 mm sapphire disc standard in a covered Pt-Rh crucible, under a constant argon flow of 40 mL min^{-1}. Moreover, the routine burning out of the residue remaining in the furnace from a completed run, at 1100 ℃ for 10 min under the 100 mL min^{-1} flow of synthetic air, eliminated any residual contaminants prior to subsequent experiments.

Non-isothermal experiments were performed using powdered antigorite samples (10.0 ± 0.05 mg) in a Pt-Rh crucible (Pt:Rh = 80:20, Ø 6.8 mm × 4 mm), at the nominal heating rates of 5, 10 and 20 ℃.min^{-1} from 20 – 1000 ℃ under an argon flow of 40 mL min^{-1}. We performed all experiments in triplicate. Blank runs (*i.e.*, without sample), completed under identical conditions to the production experiments, yielded the TGA thermal buoyancy and DSC baseline corrections. The maximum uncertainty in the temperature measurement corresponds ± 2 ℃.

5.2.5 Isoconversional kinetic modelling

Isoconversional kinetic treatment was employed to estimate the activation energies for thermal dehydroxylation of antigorite using *in-situ* synchrotron PXRD, as well as TGA and DSC. TGA and DSC-based kinetic analysis is described in detail in Chapter 3. TGA and DSC follow the same treatment as described here for synchrotron PXRD in detail except that the extent of conversion is determined based on TGA and DSC analysis of Chapter 3. The extent of conversion based on *in-situ* synchrotron PXRD was performed using Equations 5.1.

$$\alpha = \left(\frac{I_{p,i} - I_{p,t}}{I_{p,i} - I_{p,f}}\right) \quad \textbf{(5.1)}$$

Where I_i, I_t, and I_f exhibits the initial integrated intensity (peak area), the integrated intensity at any instant, and final integrated intensity, respectively, during *in-situ* synchrotron PXRD analysis (Eq. 5.1).

The basic kinetic equation describing the rate of solid-state reaction can be written as Equation 5.2.

$$\frac{d\alpha}{dt} = A.e^{\frac{-E}{RT(t)}}.f(\alpha) \quad \textbf{(5.2)}$$

Where t is the time (s), α is the extent of conversion (dimensionless), A is the Arrhenius constant (s^{-1}), E is the activation energy (J mol^{-1}), T is the absolute temperature (K), R is the universal gas constant (8.3145 J mol^{-1} K^{-1}), and $f(\alpha)$ represents the differential reaction model.

The generalised kinetic equation for non-isothermal conditions can be cast into Equation 5.3 by substituting a constant heating rate (β = dT/dt) into Equation 5.2.

$$\frac{d\alpha}{dT} = \frac{A}{\beta}.e^{\frac{-E}{RT(t)}}.f(\alpha) \quad \textbf{(5.3)}$$

where β represents a constant heating rate (K s^{-1}).

The solution to Equation 5.3 can be performed using numerical differentiation of the experimental extent of conversion (Vyazovkin and Sbirrazzuoli, 2006). However, the differential method tends to be numerically unstable due to its higher sensitivity to experimental noise. Alternatively, we can apply its integral form (Equation 5.4) to obtain an approximate solution:

$$\int_0^{\alpha} \frac{d\alpha}{A\,f(\alpha)} = \frac{1}{\beta}\int_0^{T} e^{\frac{-E}{RT(t)}}\,dT = \frac{1}{\beta}[I\,(E_\alpha, T_\alpha)] \quad \textbf{(5.4)}$$

Among the available integral solutions for Equation 5.4, the advanced Vyazovkin method provides excellent accuracy. It calculates the activation energy (E_α) by minimising Equation 5.5 at a particular extent of conversion (Vyazovkin, 2015b; Vyazovkin and Sbirrazzuoli, 2006; Vyazovkin and Wight, 1998), for a set of n experiments carried out at different heating rates.

$$n(n-1) = \emptyset(E_\alpha) = \sum_{i=1}^{n}\sum_{j\neq i}^{n}\frac{I\,(E_\alpha, T_{\alpha,i})\beta_j}{I\,(E_\alpha, T_{\alpha,j})\beta_i} \quad \textbf{(5.5)}$$

The parameters *i* and *j* represent repeated experiments performed at different heating rates. The isoconversional method assumes that the reaction model remains constant over a small degree of conversion and does not depend on the heating rate (Vyazovkin and Sbirrazzuoli, 2006). We used numerical linear interpolation of synchrotron PXRD, TGA, and DSC data for different heating rates to extract the temperatures (T) at the desired extent of conversion (α) to estimate the isoconversional activation energy based on Equation 5.5 (Vyazovkin, 2015a). That is, we interpolated the temperatures between adjacent values, to obtain the temperature values corresponding to the selected interval of 0.025 over the fractional conversion range of 0.1 to 0.9 (*i.e.*, α = 0.1, 0.125, ..., 0.875, 0.9).

5.3 Results and discussion

5.3.1 Phase changes, heat, and mass flow during thermal dehydroxylation of antigorite

2D synchrotron PXRD plots elucidate the phase evolution during antigorite dehydroxylation (Fig. 5.2).

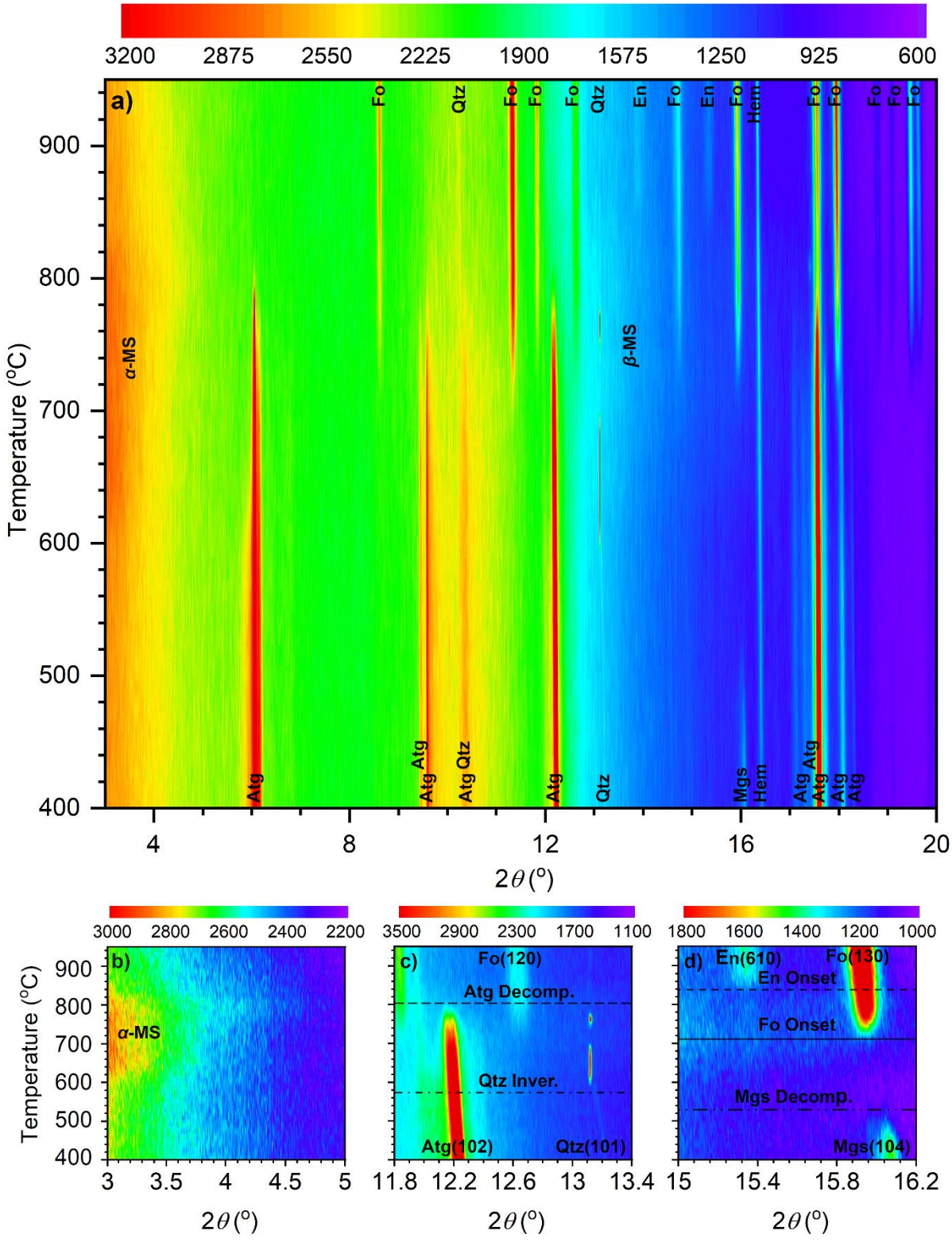

Figure 5.2. a) Temperature resolved *in-situ* synchrotron PXRD for dehydroxylation of antigorite at 8 °C min^{-1}. Peaks are labelled as Atg: antigorite, En: enstatite, Fo: forsterite, Hem: hematite, Mgs: magnesite, Qtz: quartz, α-MS: α-metaserpentine and β-MS: β-metaserpentine **b)** 2D *in-situ* synchrotron PXRD showing detail of α-metaserpentine at $2\theta < 4.5°$ **c)** 2D *in-situ* synchrotron PXRD showing detail of (102) peak of antigorite (2θ =

6.1°) and of the transition from α to β-quartz for (101) peak of quartz at 2θ = 13.2°, **d)** 2D *in-situ* synchrotron PXRD showing detail of (104) peak of magnesite at 2θ =16.1°,.(130) peak of forsterite at 2θ = 15.9° and (610) peak of enstatite at 2θ = 15.3°.

The magnesite impurity in the antigorite sample decomposes at ~523 ℃, as evident by the disappearance of the magnesite peaks, *e.g.*, (104) reflection at d = 2.74 Å (2θ =16.1°) (Fig. 5.2a and 5.2d). In contrast, hematite, *e.g.*, (104) reflection at d = 2.70 Å (2θ =16.5°) remains unchanged over the studied temperature range (Fig. 5.2a). As the dehydroxylation of antigorite proceeds above 580 ℃, α-metaserpentine (α-MS; Fig 5b) and β-metaserpentine (β-MS; Fig. 5a) start to form, characterised by broad peaks at d > 9.9 Å (2θ < 4.5°) and 3.4 < d < 2.7 Å (13.3° < 2θ <16.2°), respectively. Forsterite, *e.g.*, peaks at d = 3.9 Å (2θ = 11.3°) and d = 2.8 Å (2θ = 15.9°), forms at around 703 ℃, with the complete decomposition of antigorite, *e.g.* peak reflections (001) at d = 7.3 Å (2θ = 6.1°) and (102) at d = 3.6 Å (2θ = 12.3°), occurring at around 805 ℃ (Fig. 5.2a and c). Enstatite reflections, *e.g.*, at d = 3.2 Å (2θ = 13.9°) and d = 2.9 Å (2θ = 15.1°), appear at 837 ℃, only after the complete decomposition of antigorite (Fig. 5.2d). Quartz undergoes α to β-transition at 573 ℃ (Fig. 5.2c), and the β-quartz peak at 13.1° (d = 3.3 Å) appears temporarily between 590 – 700 ℃ and 750 – 780 ℃ (Fig. 5.2a and Fig. 5.2c). Overall, the temperatures of dehydroxylation events during the heat treatment of antigorite agree well with previous literature (Balucan *et al.*, 2011; Gualtieri *et al.*, 2012; Viti, 2010).

Figure 5.3 exhibits the simultaneous TGA/DTG and DSC record for the thermal dehydroxylation of antigorite.

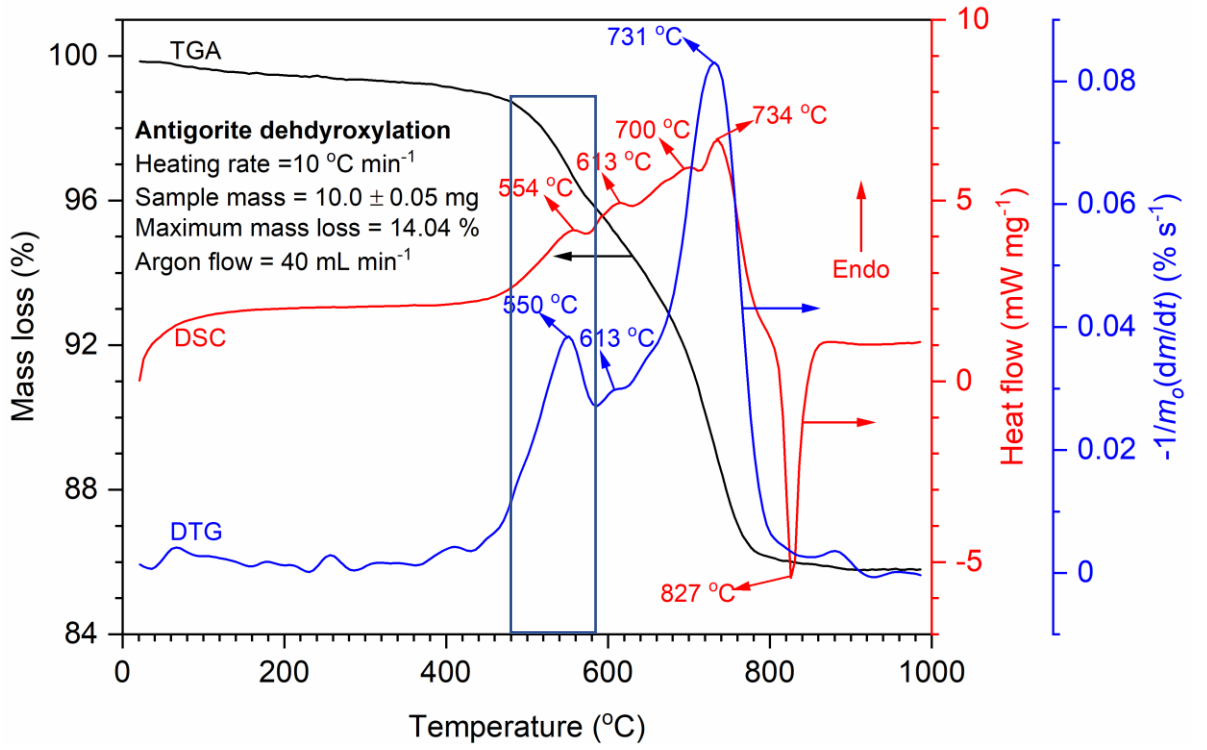

Figure 5.3. TGA, DTG and DSC results for the thermal dehydroxylation of antigorite in a covered crucible under the constant flow of argon purge gas at a heating rate of 10 °C min^{-1}.

DTG and DSC curves show multiple maxima and minima, during the dehydroxylation of antigorite. The first DTG and DSC peak at ~550 °C relates to the decomposition of magnesite, consistent with previously reported magnesite decomposition temperatures between 500 to 600 °C (Demir *et al.*, 2003; Samtani *et al.*, 2002; Sheila, 1993; Subagjo *et al.*, 2017). Total mass loss of 14 % in our antigorite sample is higher than the stoichiometric mass loss of 12.4 % from the typical composition of antigorite (m = 17) in the literature (Mellini, 1987), suggesting that ~1.6 % mass loss relates to the magnesite impurity. The DSC peak doublet at 700 and 734 °C with a shoulder at 613 °C and exothermic peak above 800 °C agree well with DSC traces of antigorite in the literature (Balucan and Dlugogorski, 2013), and the observed peak doublet is absent in the other polymorphs lizardite and chrysotile (Viti, 2010). The exothermic peak above 800 °C is commonly assigned to enstatite crystallisation (Balucan *et al.*, 2013; Dlugogorski and Balucan, 2014; McKelvy *et al.*, 2004;

Viti, 2010). On the other hand, there is an overlap between endothermic dehydroxylation (500 – 800 ℃) (Balucan *et al.*, 2013; Viti, 2010) and exothermic forsterite crystallisation (Kimura *et al.*, 2011)

5.3.2 Isoconversional kinetic modelling of antigorite dehydroxylation

The relationship between the experimental extent of conversion (α) and temperature (T) is shown in Figure 5.4 for synchrotron PXRD, TGA and DSC data.

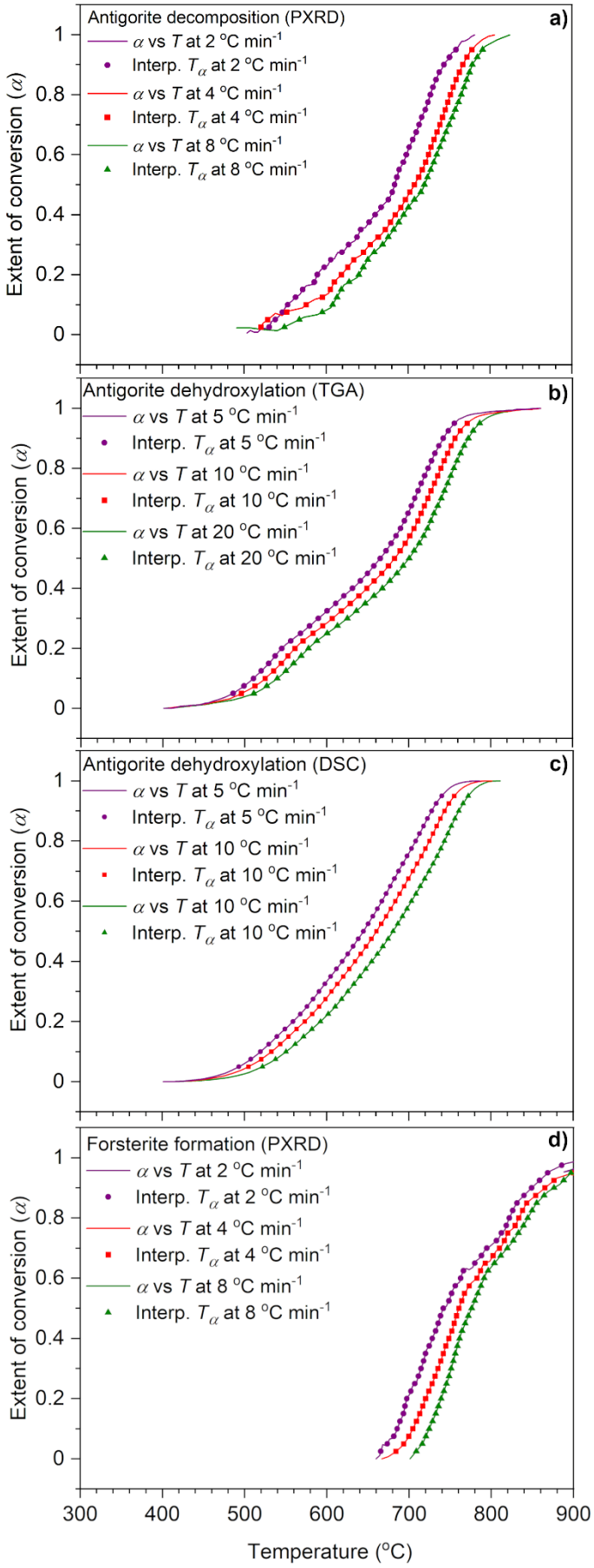
Antigorite decomposition (PXRD)
a)
α vs T at 2 °C min-1
Interp. Tα at 2 °C min-1
α vs T at 4 °C min-1
Interp. Tα at 4 °C min-1
α vs T at 8 °C min-1
Interp. Tα at 8 °C min-1
Antigorite dehydroxylation (TGA)
b)
α vs T at 5 °C min-1
Interp. Tα at 5 °C min-1
α vs T at 10 °C min-1
Interp. Tα at 10 °C min-1
α vs T at 20 °C min-1
Interp. Tα at 20 °C min-1
Antigorite dehydroxylation (DSC)
c)
α vs T at 5 °C min-1
Interp. Tα at 5 °C min-1
α vs T at 10 °C min-1
Interp. Tα at 10 °C min-1
α vs T at 10 °C min-1
Interp. Tα at 10 °C min-1
Forsterite formation (PXRD)
d)
α vs T at 2 °C min-1
Interp. Tα at 2 °C min-1
α vs T at 4 °C min-1
Interp. Tα at 4 °C min-1
α vs T at 8 °C min-1
Interp. Tα at 8 °C min-1
Extent of conversion (α)
0
0.2
0.4
0.6
0.8
1
300
400
500
600
700
800
900
Temperature (°C)

Figure 5.4. The extent of conversion (α) vs temperature (T) for antigorite dehydroxylation in the temperature range of 400 to 900 °C based on **a)** synchrotron PXRD, **b)** TGA, **c)** DSC and **d)** forsterite formation based on synchrotron PXRD. Interp. T_α represents the interpolated temperature at the particular extent of conversion.

The increase in heating rate consistently shifts the extent of conversion to higher temperatures (Fig. 5.4; Fig.S5.2 in Appendix C). This is due to the lag in the heat and mass transfer at the higher heating rate (Balucan *et al.*, 2011; El Hazzat *et al.*, 2020; Hu *et al.*, 2016; Moine *et al.*, 2016; Trittschack and Grobéty, 2012)

Figure 5.5 displays the activation energy (E_α) derived from prograde synchrotron PXRD, TGA and DSC data calculated using Vyazovkin's isoconversional method (Vyazovkin and Sbirrazzuoli, 2006).

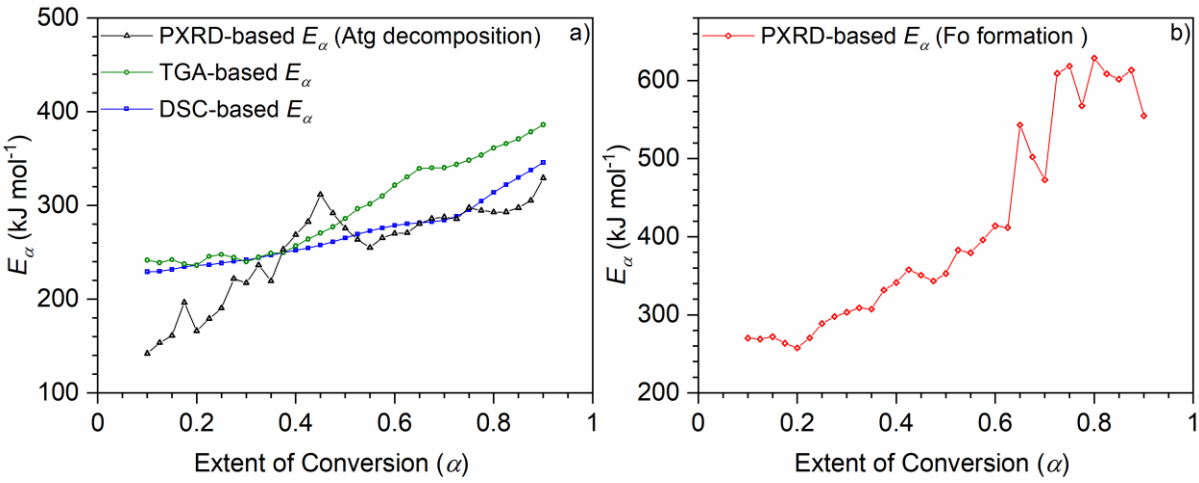

Figure 5.5. a) Variation of activation energy (E_α) with the extent of conversion (α) for dehydroxylation of antigorite based on synchrotron Powder X-ray diffraction (PXRD), TGA and DSC **b)** Variation in activation energy with the extent of conversion for forsterite formation based on synchrotron PXRD data. Labels Atg and Fo represent antigorite and forsterite, respectively.

The *in-situ* synchrotron PXRD-based E_α for antigorite decomposition increases from 142 kJ mol^{-1} to around 300 kJ mol^{-1}, with a maximum of 310 kJ mol^{-1} at α = 0.45 (slope of linear fit to = 188). TGA-based E_α is varying between 240 - 256 kJ mol^{-1} for $0.1 \leq \alpha \leq 0.4$, followed by a steep increase from 256 mol^{-1} to 340 kJ mol^{-1} for $0.4 \leq \alpha \leq 0.65$ (slope = 332) and a gentle increase to 390 kJ mol^{-1} at α = 0.90 (slope = 213). DSC-based E_α gradually increases from 229 to 284kJ mol^{-1} at α = 0.7 (slope = 102), followed by a steeper increase to 360 kJ mol^{-1} at α = 0.90 (slope = 320). PXRD-based E_α for forsterite formation varies between 260 - 270 kJ mol^{-1} for $\alpha < 0.2$ but exhibits a steep increase to 618 kJ mol^{-1} at α = 0.75 (slope = 549).

The increase in TGA and DSC-based E_α over the dehydroxylation process is generally smaller and smoother than for XRD-based E_α. TGA and DSC-based E_α initially develop similarly, but TGA-based E_α diverts to higher values above α = 0.4.

5.3.3 Comparison of information from TGA, DSC and PXRD techniques

The isoconversional kinetic analysis of antigorite dehydroxylation shows significant variation in activation energy (Fig. 5.5a), demonstrating that it is a multi-step reaction with one or more changes in the rate-limiting step. This is consistent with previous results showing that dehydroxylation of the other serpentine polymorphs chrysotile and lizardite is also a multi-step reaction (Chapter 3, Trittschack and Grobéty (2012); Trittschack *et al.* (2014)) and indicates that single step reaction models are not sufficient to describe the kinetics of serpentine dehydroxylation (Trittschack and Grobéty, 2012, 2013). An intimate understanding of the reaction mechanism and kinetics is required to optimise thermal treatment of serpentine minerals for maximum amorphous content and reactivity at the lowest

possible energy cost (Du Breuil *et al.*, 2019a; Farhang *et al.*, 2019; Rausis *et al.*, 2020; Rim *et al.*, 2020).

TGA-DSC analyses are well established, and the most widely used thermal analysis techniques to obtain isoconversional kinetic parameters of solid-state reactions (Vyazovkin *et al.*, 2020). TGA measures changes in mass, most commonly mass loss during heating, and can thus not provide information about mass-invariant reactions (Saadatkhah *et al.*, 2020), such as crystallisation or phase inversions (Abdullah *et al.*, 2019). In the current study, TGA records mass loss due to both magnesite decomposition and antigorite dehydroxylation (Fig. 5.3). Due to the overlap of the two at lower temperatures, this results in a 'mixed-signal' which can only be resolved by peak deconvolution routines that lower the precision of the evaluated data (Muravyev *et al.*, 2017; Nakano *et al.*, 2015; Vyazovkin *et al.*, 2020). After magnesite decomposition, TGA-based E_α reflects the changes in kinetic barrier associated with mass loss during dehydroxylation and thus diffusion of hydroxyl groups or water through the surrounding crystal structure, evolving from antigorite via amorphous phases to forsterite. Also, the combination of hydroxyl groups into water molecules, either within the structure or on particle surfaces, may indirectly influence diffusion kinetics (Ortega *et al.*, 2010; Trittschack and Grobéty, 2012, 2013).

DSC measures the amount of heat absorbed or released (heat flow) during endothermic and exothermic reactions, respectively. Unlike TGA, it can provide reliable kinetic information about mass-invariant reactions such as phase transitions (Muravyev *et al.*, 2017; Nakano *et al.*, 2015; Vyazovkin *et al.*, 2020). The application of DSC-based kinetics to antigorite dehydroxylation is complicated by the fact that the endothermic dehydroxylation partly overlaps with exothermic forsterite formation (*cf.* Fig. 5.6; Balucan and Dlugogorski,

McKelvy). Although endothermic and exothermic reactions can be deconvoluted to decipher the kinetics of multi-step reactions, the deconvolution introduces additional uncertainty (Muravyev *et al.*, 2017; Nakano *et al.*, 2015; Vyazovkin *et al.*, 2020). During endothermic antigorite dehydroxylation, exothermic forsterite formation provides an additional, internal heat source, reducing the overall heat requirement of the dehydroxylation above 703 °C.

As an alternative to TGA and DSC-based kinetics, this study provides kinetics based on *in-situ* synchrotron PXRD, using a signal that is not affected by the limitation discussed above. Synchrotron PXRD can resolve the evolution of individual phases and thus provides the opportunity to study antigorite decomposition kinetics and forsterite formation kinetics independently. However, PXRD is generally limited by high detection limits e.g., 0.5 - 5 wt % (Newman *et al.*, 2015) and large uncertainties in phase quantification, *e.g.* ± 5-10 % relative error in Wilson et al. (2006), especially when using normalised integrated peak intensities as in this study. Integrated peak intensities depend on factors such as sample preparation and preferred orientation, crystallite sizes and quantification/integration method used, which could be largely avoided during Rietveld refinements, Full pattern fitting or the use of an inert, internal standard (Madsen *et al.*, 2011; Purba, 2010). Overall, this results in considerable uncertainties in the XRD-based activation energies (Vyazovkin *et al.*, 2020; Vyazovkin *et al.*, 2014) compared to TGA and DSC, reflected in much smoother E_α variation curves for the latter (Fig. 5.5). However, our data demonstrate that the variation in synchrotron PXRD-based E_α trends are mainly consistent with those in TGA and DSC-based E_α (Fig. 5.5). Hence synchrotron PXRD-based kinetic analysis provides excellent potential for unravelling complex, overlapping multi-step processes, such as antigorite dehydroxylation, based on the ability to analyse the kinetics of individual reaction steps.

5.3.4 Evolution of activation energy relative to structural changes

PXRD-based reaction progress at 8 °C min^{-1} and activation energy relative to average temperature, *i.e.*, mean temperature over three different heating rates (5, 10 and 20 °C min^{-1} for TGA-DSC and 2, 4 and 8 °C min^{-1} for PXRD) at a constant extent of conversion, are shown in Figure 5.6.

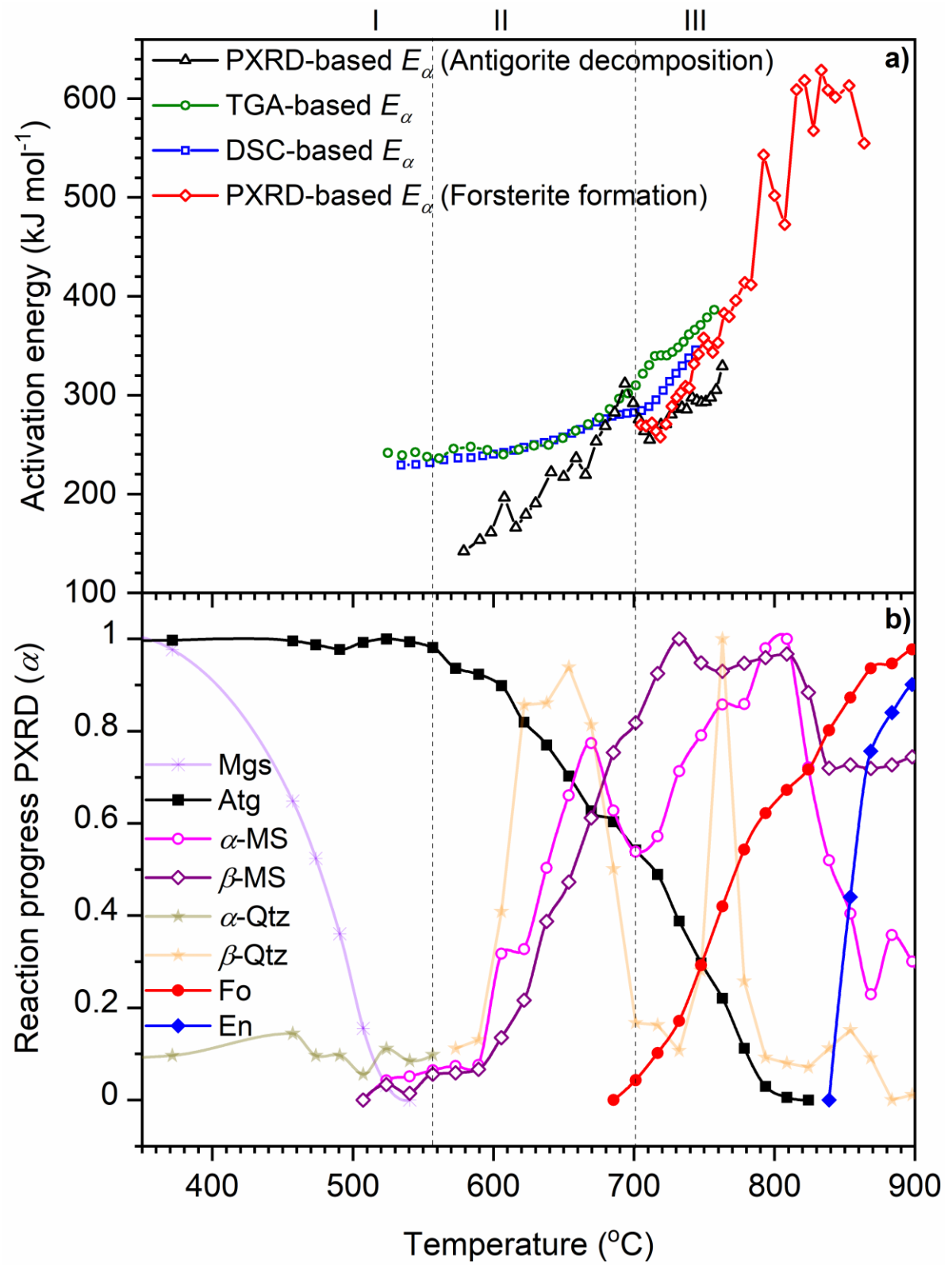

Figure 5.6. Variation in activation energy **a)** and PXRD-based reaction progress **b)** relative to average temperature based on the constant extent of conversion over three different heating rates (5, 10 and 20 °C min^{-1}). Antigorite decomposition and forsterite formation are based on PXRD, dehydroxylation of antigorite is based on TGA (mass loss) and DSC (heat flow). PXRD-based reaction progress reflects the evolution of normalised

integrated peak intensities during heating at 8 °C min^{-1}. The phases are labelled as Atg: antigorite, En: enstatite, Fo: forsterite, Mgs: magnesite, Qtz: quartz, α-MS: α-metaserpentine and β-MS: β metaserpentine**.**

Region (I) between 500 and 558 °C is initially characterised by the decomposition of magnesite, in line with the disappearance of magnesite peaks at around 523 °C recorded by *in-situ* PXRD (Fig. 5.2d). However, it is important to keep in mind the slight mismatch between the TGA-DSC data and PXRD data is due to the use of lower heating rates used in the latter. Overlap of magnesite decomposition ($MgCO_3 \rightarrow MgO + CO_2$) with the initial stages of thermal dehydroxylation of antigorite obscures the identification of the antigorite dehydroxylation onset in TGA and DSC and results in increased mass-loss rate as indicated by the first DTG peak in Figure 5.3. Synchrotron PXRD-based E_α is initially lower than TGA and DSC-based E_α, after magnesite decomposition, both reflect antigorite dehydroxylation.

Region (II) from 558 to 703 °C is dominated by initial antigorite dehydroxylation and the formation of amorphous dehydroxylates (α-MS and β-MS). The formation of intermediate hydrous amorphous components (α-MS and β-MS) in this temperature range (Fig. 5.6b) is consistent with the lower mass-loss rate commonly observed during the initial thermal treatment of antigorite (see Fig. 3.3 and 3.5). The gradual increase in activation energies in this temperature range is most pronounced in synchrotron PXRD-based E_α and commonly interpreted to reflect the increasing distance between OH-groups during progressive dehydroxylation (Trittschack and Grobéty, 2012). This interpretation is based on ab initio quantum mechanical modelling of the dehydroxylation of the dioctahedral phyllosilicate pyrophyllite, which demonstrate that the increase of E_α during pyrophyllite dehydroxylation can be rationalised through increasing distances between hydroxyls groups (Molina-Montes

et al., 2008). At 680 °C, just before the onset of forsterite formation, synchrotron PXRD-based E_α has increased to similar values as TGA and DSC-based E_α. TGA-based E_α diverges to higher values than DSC-based E_α and remains higher until the end of the dehydroxylation. This divergence may reflect the hindrance of outward migration of hydroxyls by the intermediate amorphous components (Ortega *et al.*, 2010; Trittschack and Grobéty, 2012, 2013), resulting in higher TGA-based E_α or the contribution of exothermic forsterite formation to heat flow, resulting in lower DSC-based E_α or both.

Region (III), above 703 °C, is characterised by antigorite dehydroxylation with concurrent forsterite formation, consistent with higher mass loss rates (*cf.* Fig. 5.3). A steep increase in TGA and DSC-based E_α as well as forsterite formation activation energies occurs in this temperature region, consistent with local structural rearrangement and breakage of stronger Si-O and Mg-O bonds with bond dissociation energies of 452 and 400 kJ mol^{-1}, respectively (Cotton and Jenkins, 1969; Kildahl, 1995). Additionally, the amorphous structure may hinder the structural rearrangement required for the topotactic crystallisation of forsterite (Brindley and Zussman, 1957). Trittschack *et al.* (2014) attributed this increase in activation energy to the conversion from 2-dimensional to 3-dimensional diffusion due to the breakdown or final dehydroxylation of the inner layers of serpentine particles. Our data, especially the sharp increase in synchrotron PXRD-based E_α observed for forsterite formation (Fig. 5.6a) suggests that the overall increase in E_α during later stages of dehydroxylation is caused by forsterite formation. This indicates that forsterite formation may become the rate-limiting step at the end of the dehydroxylation reaction, imposing a significant kinetic barrier to practical heating strategies.

5.4 Implication and concluding remarks

The isoconversional kinetic analysis presented in this study shows that antigorite dehydroxylation is a complex, multi-step reaction with different kinetic barriers associated to changes in the rate-limiting step. Antigorite dehydroxylation is coupled to the forsterite formation through a reaction involving intermediate amorphous phases (Atg→*α*-Am→Fo). The overlap between endothermic antigorite dehydroxylation and exothermic, mass-invariant forsterite formation above 703 °C make it challenging to interpret variations in kinetic parameters based on TGA and DSC data, which rely on mass loss and heat flow, respectively. Therefore, this study employs kinetic analysis based on *in-situ* synchrotron PXRD, which has the ability to resolve antigorite decomposition from forsterite formation and thus to establish independent kinetic parameters for both processes. TGA, DSC and synchrotron PXRD-based kinetics consistently show a gradual increase in activation energy during initial antigorite dehydroxylation between 558 and 703 °C. This has been explained to reflect an increasing kinetic barrier associated with increasing distance between hydroxyl groups that need to combine and diffuse for dehydroxylation to proceed (Ortega *et al.*, 2010; Trittschack and Grobéty, 2012; Trittschack *et al.*, 2014). At around 680 °C, TGA-based activation energies diverge to higher values than DSC-based activation energies, either due to an increased kinetic barrier to diffusion or a reduction in heat flow, resulting from the overlapping exothermic forsterite crystallisation. Our synchrotron PXRD data show that the steep increase in activation energies above 703 °C is related to forsterite formation and the associated breaking of Si-O and Mg-O bonds. This demonstrates that forsterite formation has to be avoided during practical heat treatment, as it is associated with a significantly higher energy barrier compared to serpentine dehydroxylation before forsterite formation onset. Our study

demonstrates the utility of *in-situ* synchrotron PXRD in resolving the kinetics of complex, overlapping, multi-step reactions.

5.1 References

Abdullah, A.A., Oskierski, H.C., Altarawneh, M., Senanayake, G., Lumpkin, G., Dlugogorski, B.Z. (2019) Phase transformation mechanism of spodumene during its calcination. Minerals Engineering 140, 105883.

Alexander, G., Mercedes Maroto-Valer, M., Gafarova-Aksoy, P. (2007) Evaluation of reaction variables in the dissolution of serpentine for mineral carbonation. Fuel 86, 273-281.

Alizadehhesari, K., Golding, S.D., Bhatia, S.K. (2012) Kinetics of the dehydroxylation of serpentine. Energy & Fuels 26, 783-790.

Aminu, M.D., Nabavi, S.A., Rochelle, C.A., Manovic, V. (2017) A review of developments in carbon dioxide storage. Applied Energy 208, 1389-1419.

Arce Ferrufino, G.L.A., Okamoto, S., Dos Santos, J.C., de Carvalho, J.A., Avila, I., Romero Luna, C.M., Gomes Soares Neto, T. (2018) CO_2 sequestration by pH-swing mineral carbonation based on HCl/NH_4OH system using iron-rich lizardite 1T. Journal of CO2 Utilization 24, 164-173.

Ashley, P.M., Brownlow, J.W. (1993) Silica-carbonate alteration zones in the Great Serpentinite Belt, southern New England Orogen: their nature and significance, In New England Orogen, (eds. P.G. Flood and J.C. Aitchison). University of New England, Armidale, Australia, 197-214.

Assima, G.P., Larachi, F., Molson, J., Beaudoin, G. (2014) Comparative study of five Québec ultramafic mining residues for use in direct ambient carbon dioxide mineral sequestration. Chemical Engineering Journal 245, 56-64.

Azadi, M., Edraki, M., Farhang, F., Ahn, J. (2019) Opportunities for mineral carbonation in Australia's mining industry. Sustainability 11.

Azdarpour, A., Asadullah, M., Mohammadian, E., Hamidi, H., Junin, R., Karaei, M.A. (2015) A review on carbon dioxide mineral carbonation through pH-swing process. Chemical Engineering Journal 279, 615-630.

Balucan, R.D., Dlugogorski, B.Z. (2013) Thermal activation of antigorite for mineralisation of CO_2. Environmental Science & Technology 47, 182-190.

Balucan, R.D., Dlugogorski, B.Z., Kennedy, E.M., Belova, I.V., Murch, G.E. (2013) Energy cost of heat activating serpentinites for CO_2 storage by mineralisation. International Journal of Greenhouse Gas Control 17, 225-239.

Balucan, R.D., Kennedy, E.M., Mackie, J.F., Dlugogorski, B.Z. (2011) Optimisation of antigorite heat pre-treatment via kinetic modelling of the dehydroxylation reaction for CO_2 mineralisation. Greenhouse Gases: Science and Technology 1, 294-304.

Béarat, H., McKelvy, M.J., Chizmeshya, A.V.G., Gormley, D., Nunez, R., Carpenter, R.W., Squires, K., Wolf, G.H. (2006) Carbon sequestration via aqueous olivine mineral carbonation: Role of passivating layer formation. Environmental Science & Technology 40, 4802-4808.

Béarat, H., McKelvy, M.J., Chizmeshya, A.V.G., Sharma, R., Carpenter, R.W. (2002) Magnesium hydroxide dehydroxylation/carbonation reaction processes: Implications for carbon dioxide mineral sequestration. Journal of the American Ceramic Society 85, 742-748.

Benhelal, E., Rashid, M.I., Rayson, M.S., Brent, G.F., Oliver, T., Stockenhuber, M., Kennedy, E.M. (2019) Direct aqueous carbonation of heat activated serpentine: Discovery of undesirable side reactions reducing process efficiency. Applied Energy 242, 1369-1382.

Bloise, A.C., Manuela; Gualtieri, Alessandro F. (2018) Effect of grinding on chrysotile, amosite and crocidolite and implications for thermal treatment. Minerals 8.

Bobicki, E.R., Liu, Q., Xu, Z., Zeng, H. (2012) Carbon capture and storage using alkaline industrial wastes. Progress in Energy and Combustion Science 38, 302-320.

Brindley, G.W., Achar, B.N.N., Sharp, J.H. (1967a) Kinetics and mechanism of dehydroxylation processes: II. Temperature and vapor pressure dependence of dehydroxylation of serpentine. American Mineralogist 52, 1697-1705.

Brindley, G.W., Hayami, R. (1963) Kinetics and mechanisms of dehydration and recrystallization of serpentine—I. Clays and Clay Minerals 12, 35-47.

Brindley, G.W., Hayami, R. (1965) Mechanism of formation of forsterite and enstatite from serpentine. Mineralogical Magazine and Journal of the Mineralogical Society 35, 189-195.

Brindley, G.W., Millhollen, G.L. (1966) Chemisorption of water at high temperatures on kaolinite: Effect on dehydroxylation. Science 152, 1385.

Brindley, G.W., Sharp, J.H., Patterson, J.H., Narahari, B.N. (1967b) Kinetics and mechanism of dehydroxylation processes, I. Temperature and vapor pressure dependence of dehydroxylation of kaolinite. American Mineralogist 52, 201-211.

Brindley, G.W., Zussman, J. (1957) A structural study of the thermal transformation of serpentine minerals to forsterite. American Mineralogist 42, 461-474.

Bromiley, G.D., Pawley, A.R. (2003) The stability of antigorite in the systems MgO-SiO_2-H_2O (MSH) and MgO-Al_2O_3-SiO_2-H_2O (MASH): The effects of Al^{3+} substitution on high-pressure stability. American Mineralogist 88, 99-108.

Burnham, A.K., Dinh, L. (2007) A comparison of isoconversional and model-fitting approaches to kinetic parameter estimation and application predictions. Journal of Thermal Analysis and Calorimetry 89, 479-490.

Candela, P.A., Crummett, C.D., Earnest, D.J., Frank, M.R., Wylie, A.G. (2007) Low-pressure decomposition of chrysotile as a function of time and temperature. American Mineralogist 92, 1704-1713.

Capitani, G., Mellini, M. (2004) The modulated crystal structure of antigorite: The m = 17 polysome. American Mineralogist 89, 147-158.

Cattaneo, A., Gualtieri, A.F., Artioli, G. (2003) Kinetic study of the dehydroxylation of chrysotile asbestos with temperature by in situ XRPD. Physics and Chemistry of Minerals 30, 177-183.

Chang, E.E., Pan, S.-Y., Chen, Y.-H., Tan, C.-S., Chiang, P.-C. (2012) Accelerated carbonation of steelmaking slags in a high-gravity rotating packed bed. Journal of Hazardous Materials 227-228, 97-106.

Chollet, M., Daniel, I., Koga, K.T., Morard, G., van de Moortèle, B. (2011) Kinetics and mechanism of antigorite dehydration: Implications for subduction zone seismicity. Journal of Geophysical Research: Solid Earth 116, B04203.

Cotton, D.H., Jenkins, D.R. (1969) Bond-dissociation energy of gaseous magnesium oxide. Transactions of the Faraday Society 65, 376-379.

Critelli, T., Marini, L., Schott, J., Mavromatis, V., Apollaro, C., Rinder, T., De Rosa, R., Oelkers, E.H. (2015) Dissolution rate of antigorite from a whole-rock experimental study of serpentinite dissolution from $2<pH<9$ at 25°C: Implications for carbon mitigation via enhanced serpentinite weathering. Applied Geochemistry 61, 259-271.

Demir, F., Dönmez, B., Okur, H., Sevim, F. (2003) Calcination kinetic of magnesite from thermogravimetric data. Chemical Engineering Research and Design 81, 618-622.

Dessert, C., Dupré, B., Gaillardet, J., François, L.M., Allègre, C.J. (2003) Basalt weathering laws and the impact of basalt weathering on the global carbon cycle. Chemical Geology 202, 257-273.

Dey, S., Dhal, G.C. (2019) Materials progress in the control of CO and CO_2 emission at ambient conditions: An overview. Materials Science for Energy Technologies 2, 607-623.

Ding, W., Yang, H., Ouyang, J., Long, H. (2016) Modified wollastonite sequestrating CO_2 and exploratory application of the carbonation products. RSC Advances 6, 78090-78099.

Dlugogorski, B.Z., Balucan, R.D. (2014) Dehydroxylation of serpentine minerals: Implications for mineral carbonation. Renewable and Sustainable Energy Reviews 31, 353-367.

Drief, A., Nieto, F. (1999) The effect of dry grinding on antigorite from Mulhacen, Spain. Clays and Clay Minerals 47, 417-424.

Du Breuil, C., César-Pasquier, L., Dipple, G., Blais, J.-F., Iliuta, C.M., Mercier, G. (2019a) Mineralogical transformations of heated serpentine and their impact on dissolution during aqueous-phase mineral carbonation reaction in flue gas conditions. Minerals 9.

Du Breuil, C., Pasquier, L.-C., Dipple, G., Blais, J.-F., Iliuta, C.M., Mercier, G. (2019b) Mineralogical transformations of heated serpentine and their impact on dissolution during aqueous-phase mineral carbonation reaction in flue gas conditions. Minerals 9.

Durand, B., (2011) Carbon dioxide capture and storage, France, p. 32.

El Hazzat, M., Sifou, A., Arsalane, S., El Hamidi, A. (2020) Novel approach to thermal degradation kinetics of gypsum: application of peak deconvolution and Model-Free isoconversional method. Journal of Thermal Analysis and Calorimetry 140, 657-671.

Fabian, M., Shopska, M., Paneva, D., Kadinov, G., Kostova, N., Turianicová, E., Briančin, J., Mitov, I., Kleiv, R.A., Baláž, P. (2010) The influence of attrition milling on carbon dioxide sequestration on magnesium–iron silicate. Minerals Engineering 23, 616-620.

Fagerlund, J., Teir, S., Nduagu, E., Zevenhoven, R. (2009) Carbonation of magnesium silicate mineral using a pressurised gas/solid process. Energy Procedia 1, 4907-4914.

Farhang, F., Oliver, T.K., Rayson, M.S., Brent, G.F., Molloy, T.S., Stockenhuber, M., Kennedy, E.M. (2019) Dissolution of heat activated serpentine for CO_2 sequestration: The effect of silica precipitation at different temperature and pH values. Journal of CO2 Utilization 30, 123-129.

Farhang, F., Rayson, M., Brent, G., Hodgins, T., Stockenhuber, M., Kennedy, E. (2017) Insights into the dissolution kinetics of thermally activated serpentine for CO_2 sequestration. Chemical Engineering Journal 330, 1174-1186.

Fedoročková, A., Hreus, M., Raschman, P., Sučik, G. (2012) Dissolution of magnesium from calcined serpentinite in hydrochloric acid. Minerals Engineering 32, 1-4.

Field, C.B., Raupach, M.R. (2004) The global carbon cycle: integrating humans, climate and the natural world. Island Press, Washington.

Flynn, J.H., Wall, L.A. (1966) General treatment of thermogravimetry of polymers. Journal of Research of the National Bureau of Standards Section a-Physics and Chemistry A 70, 487-+.

Fouda, M.F.R., Amin, R.E.-S., Abd-Elzaher, M.M. (1996) Extraction of magnesia from Egyptian serpentine ore via reaction with different acids. I. Reaction with sulfuric acid. Bulletin of the Chemical Society of Japan 69, 1907-1912.

Friedlingstein, P., Jones, M.W., O'Sullivan, M., Andrew, R.M., Hauck, J., Peters, G.P., Peters, W., Pongratz, J., Sitch, S., Le Quéré, C., Bakker, D.C.E., Canadell, J.G., Ciais, P., Jackson, R.B., Anthoni, P., Barbero, L., Bastos, A., Bastrikov, V., Becker, M., Bopp, L., Buitenhuis, E., Chandra, N., Chevallier, F., Chini, L.P., Currie, K.I., Feely, R.A., Gehlen, M., Gilfillan, D., Gkritzalis, T., Goll, D.S., Gruber, N., Gutekunst, S., Harris, I., Haverd, V., Houghton, R.A., Hurtt, G., Ilyina, T., Jain, A.K., Joetzjer, E., Kaplan, J.O., Kato, E., Klein Goldewijk, K., Korsbakken, J.I., Landschützer, P., Lauvset, S.K., Lefèvre, N., Lenton, A., Lienert, S., Lombardozzi, D., Marland, G., McGuire, P.C., Melton, J.R., Metzl, N., Munro, D.R., Nabel, J.E.M.S., Nakaoka, S.I., Neill, C., Omar, A.M., Ono, T., Peregon, A., Pierrot, D., Poulter, B., Rehder, G., Resplandy, L., Robertson, E., Rödenbeck, C., Séférian, R., Schwinger, J., Smith, N., Tans, P.P., Tian, H., Tilbrook, B., Tubiello, F.N., van der Werf, G.R., Wiltshire, A.J., Zaehle, S. (2019) Global carbon budget 2019. Earth Syst. Sci. Data 11, 1783-1838.

Friedman, H.L. (1964) Kinetics of thermal degradation of char-forming plastics from thermogravimetry. Application to a phenolic plastic. Journal of Polymer Science Part C: Polymer Symposia 6, 183-195.

Fumagalli, P., Poli, S. (2004) Experimentally determined phase relations in hydrous peridotites to 6·5 GPa and their consequences on the dynamics of subduction zones. Journal of Petrology 46, 555-578.

Galwey, A.K. (2003) Perennial problems and promising prospects in the kinetic analysis of nonisothermal rate data. Thermochimica Acta 407, 93-103.

Gao, W., Wen, J., Li, Z. (2014) Dissolution kinetics of magnesium from calcined serpentine in NH_4Cl solution. Industrial & Engineering Chemistry Research 53, 7947-7955.

Gerdemann, S.J., O'Connor, W.K., Dahlin, D.C., Penner, L.R., Rush, H. (2007) *Ex-situ* aqueous mineral carbonation. Environmental Science & Technology 41, 2587-2593.

Ghaderi, N., Zhang, H., Sun, T. (2015) Relative stability and contrasting elastic properties of serpentine polymorphs from first-principles calculations. Journal of Geophysical Research: Solid Earth 120, 4831-4842.

Ghoorah, M., Dlugogorski, B.Z., Oskierski, H.C., Kennedy, E.M. (2014) Study of thermally conditioned and weak acid-treated serpentinites for mineralisation of carbon dioxide. Minerals Engineering 59, 17-30.

Gualtieri, A.F., Giacobbe, C., Viti, C. (2012) The dehydroxylation of serpentine group minerals. American Mineralogist 97, 666.

Gysi, A.P., Stefánsson, A. (2008) Numerical modelling of CO_2-water-basalt interaction. Mineralogical Magazine 72, 55.

Hariharan, S., Mazzotti, M. (2017a) Growth kinetics of synthetic hydromagnesite at 90 °C. Crystal Growth & Design 17, 317-327.

Hariharan, S., Mazzotti, M. (2017b) Kinetics of flue gas CO_2 mineralisation processes using partially dehydroxylated lizardite. Chemical Engineering Journal 324, 397-413.

Hariharan, S., Repmann-Werner, M., Mazzotti, M. (2016) Dissolution of dehydroxylated lizardite at flue gas conditions: III. Near-equilibrium kinetics. Chemical Engineering Journal 298, 44-54.

Hariharan, S., Werner, M., Hänchen, M., Mazzotti, M. (2014a) Dissolution of dehydroxylated lizardite at flue gas conditions: II. Kinetic modelling. Chemical Engineering Journal 241, 314-326.

Hariharan, S., Werner, M., Hänchen, M., Zingaretti, D., Baciocchi, R., Mazzotti, M. (2014b) Dissolution kinetics of thermally activated serpentine for mineralisation at flue gas conditions. Energy Procedia 63, 5887-5891.

Hariharan, S.B., Werner, M., Zingaretti, D., Baciocchi, R., Mazzotti, M. (2013) Dissolution of activated serpentine for direct flue-gas mineralisation. Energy Procedia 37, 5938-5944.

Harrison, A.L., Power, I.M., Dipple, G.M. (2013) Accelerated carbonation of brucite in mine tailings for carbon sequestration. Environmental Science & Technology 47, 126-134.

He, S., Zhang, W., Liu, L., Huang, Y., He, J., Xie, W., Wu, P., Du, C. (2014) Baseline correction for Raman spectra using an improved asymmetric least squares method. Analytical Methods 6, 4402-4407.

Hu, M., Chen, Z., Wang, S., Guo, D., Ma, C., Zhou, Y., Chen, J., Laghari, M., Fazal, S., Xiao, B., Zhang, B., Ma, S. (2016) Thermogravimetric kinetics of lignocellulosic biomass slow pyrolysis using distributed activation energy model, Fraser–Suzuki deconvolution, and isoconversional method. Energy Conversion and Management 118, 1-11.

Huijgen, W., Comans, R. (2005) Mineral CO_2 sequestration by carbonation of industrial residues. The Netherlands: Energy Research Centre of the Netherlands (ECN).

Huijgen, W.J.J., Comans, R.N.J. (2006) Carbonation of steel slag for CO_2 sequestration: Leaching of products and reaction mechanisms. Environmental Science & Technology 40, 2790-2796.

Huntzinger, D.N., Gierke, J.S., Kawatra, S.K., Eisele, T.C., Sutter, L.L. (2009) Carbon dioxide sequestration in cement kiln dust through mineral carbonation. Environmental Science & Technology 43, 1986-1992.

Huot, F., Beaudoin, G., Hebert, R., Constantin, M., Bonin, G., Dipple, G.M., (2003) Evaluation of southern Quebec asbestos residues for CO_2 sequestration by mineral carbonation : preliminary result. Geological Association of Canada, St. John's, NF (Canada), Canada.

IPCC, (2014) Climate change 2014: Mitigation of climate change. IPCC.

Ji, S., Zhu, J., He, H., Tao, Q., Zhu, R., Ma, L., Chen, M., Li, S., Zhou, J. (2018) Conversion of serpentine to smectite under hydrothermal condition: Implication for solid-state transformation. American Mineralogist 103, 241-251.

Kelemen, P., Benson, S.M., Pilorgé, H., Psarras, P., Wilcox, J. (2019) An overview of the status and challenges of CO_2 storage in minerals and geological formations. Frontiers in Climate 1, 9.

Kelemen, P.B., Hirth, G. (2012) Reaction-driven cracking during retrograde metamorphism: Olivine hydration and carbonation. Earth and Planetary Science Letters 345-348, 81-89.

Kelemen, P.B., Matter, J. (2008) *In-situ* carbonation of peridotite for CO_2 storage. Proceedings of the National Academy of Sciences 105, 17295-17300.

Kelly, K.E., Silcox, G.D., Sarofim, A.F., Pershing, D.W. (2011) An evaluation of *ex-situ*, industrial-scale, aqueous CO_2 mineralisation. International Journal of Greenhouse Gas Control 5, 1587-1595.

Kemache, N., Pasquier, L.-C., Cecchi, E., Mouedhen, I., Blais, J.-F., Mercier, G. (2017) Aqueous mineral carbonation for CO_2 sequestration: From laboratory to pilot scale. Fuel Processing Technology 166, 209-216.

Khawam, A., Flanagan, D.R. (2005) Role of isoconversional methods in varying activation energies of solid-state kinetics: I. isothermal kinetic studies. Thermochimica Acta 429, 93-102.

Khoo, H.H., Sharratt, P.N., Bu, J., Yeo, T.Y., Borgna, A., Highfield, J.G., Bjorklof, T.G., Zevenhoven, R. (2011) Carbon capture and mineralisation in Singapore: preliminary environmental impacts and costs via LCA. Industrial & Engineering Chemistry Research 50, 11350-11357.

Kildahl, N.K. (1995) Bond energy data summarised. Journal of Chemical Education 72, 423.

Kim, D.-J., Chung, H.-S. (2002) Effect of grinding on the structure and chemical extraction of metals from serpentine. Particulate Science and Technology 20, 159-168.

Kimura, Y., Nuth Iii, J.A., Tsukamoto, K., Kaito, C. (2011) Laboratory annealing experiments of refractory silicate grain analogs using differential scanning calorimetry. Meteoritics & Planetary Science 46, 92-102.

Kirchofer, A., Becker, A., Brandt, A., Wilcox, J. (2013) CO_2 mitigation potential of mineral carbonation with industrial alkalinity sources in the United States. Environmental Science & Technology 47, 7548-7554.

Lackner, K.S., Butt, D.P., Wendt, C.H. (1997) Progress on binding CO2 in mineral substrates. Energy Conversion and Management 38, S259-S264.

Lackner, K.S., Wendt, C.H., Butt, D.P., Joyce, E.L., Sharp, D.H. (1995) Carbon dioxide disposal in carbonate minerals. Energy 20, 1153-1170.

Larachi, F., Aksenova, D., Yousefi, B., Maldague, X.P.V., Beaudoin, G. (2018) Thermochemical monitoring of brucite carbonation using passive infrared thermography. Chemical Engineering and Processing - Process Intensification 130, 43-52.

Levy, J.H. (1990) Effect of water vapour pressure on the dehydration and dehydroxylation of kaolinite and smectite isolated from Australian tertiary oil shales. Energy & Fuels 4, 146-151.

Li, J., Hitch, M. (2018) Mechanical activation of magnesium silicates for mineral carbonation, a review. Minerals Engineering 128, 69-83.

Li, J., Hitch, M., Power, I.M., Pan, Y. (2018) Integrated mineral carbonation of ultramafic mine deposits—a review. Minerals 8.

Li, W., Li, W., Li, B., Bai, Z. (2009) Electrolysis and heat pretreatment methods to promote CO_2 sequestration by mineral carbonation. Chemical Engineering Research and Design 87, 210-215.

Liu, C., Wang, D., Shen, K., Liu, T., Yi, L. (2019) Kinetics of antigorite dehydration: Rapid dehydration as a trigger for lower-plane seismicity in subduction zones. American Mineralogist 104, 282-290.

Liu, M., Gadikota, G. (2018) Chemo-morphological coupling during serpentine heat treatment for carbon mineralisation. Fuel 227, 379-385.

Liu, M., Gadikota, G. (2020) Single-step, low temperature and integrated CO_2 capture and conversion using sodium glycinate to produce calcium carbonate. Fuel 275, 117887.

Loo, L., Maaten, B., Konist, A., Siirde, A., Neshumayev, D., Pihu, T. (2017) Carbon dioxide emission factors for oxy-fuel CFBC and aqueous carbonation of the Ca-rich oil shale ash. Energy Procedia 128, 144-149.

MacKenzie, K.J.D., Meinhold, R.H. (1994) Thermal reactions of chrysotile revisited: A 29Si and 25Mg MAS NMR study. American Mineralogist 79, 43-50.

Madsen, I.C., Scarlett, N.V.Y., Kern, A. (2011) Description and survey of methodologies for the determination of amorphous content via X-ray powder diffraction. Zeitschrift fur Kristallographie 226, 944.

Maroto-Valer, M.M., Fauth, D.J., Kuchta, M.E., Zhang, Y., Andrésen, J.M. (2005) Activation of magnesium rich minerals as carbonation feedstock materials for CO_2 sequestration. Fuel Processing Technology 86, 1627-1645.

Martinez, E. (1961) The effect of particle size on the thermal properties of serpentine minerals. American Mineralogist 46, 901-912.

Matter, J.M., Stute, M., Snæbjörnsdottir, S., Oelkers, E.H., Gislason, S.R., Aradottir, E.S., Sigfusson, B., Gunnarsson, I., Sigurdardottir, H., Gunnlaugsson, E., Axelsson, G., Alfredsson, H.A., Wolff-Boenisch, D., Mesfin, K., Fernandez de la Reguera Taya, D., Hall, J., Dideriksen, K., Broecker, W.S. (2016) Rapid carbon mineralisation for permanent disposal of anthropogenic carbon dioxide emissions. Science 352, 1312-1314.

Matus, C., Stopic, S., Etzold, S., Kremer, D., Wotruba, H., Dertmann, C., Telle, R., Friedrich, B., Knops, P. (2020) Mechanism of Nickel, Magnesium, and Iron Recovery from Olivine Bearing Ore during Leaching with Hydrochloric Acid Including a Carbonation Pre-Treatment. Metals 10.

McKelvy, M.J., Chizmeshya, A.V.G., Diefenbacher, J., Béarat, H., Wolf, G. (2004) Exploration of the role of heat activation in enhancing serpentine carbon sequestration reactions. Environmental Science & Technology 38, 6897-6903.

McKelvy, M.J., Diefenbacher, J., Nunez, R., Carpenter, R.W., Chizmeshya, A.V.G., (2005) Simultaneous mechanical and heat activation: A new route to enhance serpentine carbonation reactivity and lower CO_2 mineral sequestration process cost, United States.

McKelvy, M.J., Sharma, R., Chizmeshya, A.V.G., Bearat, H., Carpenter, R.W., (2000) $Mg(OH)_2$ dehydroxylation: Implications for enhancing CO_2 mineral sequestration reaction processes. Coal Technology Association, Rockville, MD (US), United States.

Mellini, M., Trommsdorff, V. & Compagnoni, R. (1987) Antigorite polysomatism: behaviour during progressive metamorphism. Contributions to Mineralogy and Petrology 97, 147-155.

Metz, B., Davidson, O., Coninck, H.d., Loos, M., Meyer, L. (2005) IPCC special report on carbon dioxide capture and storage. Cambridge University Press, New York, NY (United States), United States.

Michael, A., Zhou, Y.N., Yavuz, M., Khan, M.I. (2018) Deconvolution of overlapping peaks from differential scanning calorimetry analysis for multi-phase NiTi alloys. Thermochimica Acta 665, 53-59.

Miller, Q.R.S., Schaef, H.T., Kaszuba, J.P., Gadikota, G., McGrail, B.P., Rosso, K.M. (2019) Quantitative review of olivine carbonation kinetics: Reactivity trends, mechanistic insights, and research frontiers. Environmental Science & Technology Letters 6, 431-442.

Moine, E.c., Groune, K., El Hamidi, A., Khachani, M., Halim, M., Arsalane, S. (2016) Multi-step process kinetics of the non-isothermal pyrolysis of Moroccan RIF oil shale. Energy 115, 931-941.

Molina-Montes, E., Donadio, D., Hernández-Laguna, A., Sainz-Díaz, C.I., Parrinello, M. (2008) DFT research on the dehydroxylation reaction of pyrophyllite 1. First-principle molecular dynamics simulations. The Journal of Physical Chemistry B 112, 7051-7060.

Montes-Hernandez, G., Pérez-López, R., Renard, F., Nieto, J.M., Charlet, L. (2009) Mineral sequestration of CO_2 by aqueous carbonation of coal combustion fly-ash. Journal of Hazardous Materials 161, 1347-1354.

Moody, J.B. (1976) Serpentinisation: a review. Lithos 9, 125-138.

Mouedhen, I., Kemache, N., Pasquier, L.-C., Cecchi, E., Blais, J.-F., Mercier, G. (2017) Effect of pCO_2 on direct flue gas mineral carbonation at pilot scale. Journal of Environmental Management 198, 1-8.

Muravyev, N.V., Koga, N., Meerov, D.B., Pivkina, A.N. (2017) Kinetic analysis of overlapping multistep thermal decomposition comprising exothermic and endothermic processes: thermolysis of ammonium dinitramide. Physical Chemistry Chemical Physics 19, 3254-3264.

Nakano, M., Wada, T., Koga, N. (2015) Exothermic behaviour of thermal decomposition of sodium percarbonate: Kinetic deconvolution of successive endothermic and exothermic processes. The Journal of Physical Chemistry A 119, 9761-9769.

Neeraj, Yadav, S. (2020) Carbon storage by mineral carbonation and industrial applications of CO_2. Materials Science for Energy Technologies 3, 494-500.

Newman, J.A., Schmitt, P.D., Toth, S.J., Deng, F., Zhang, S., Simpson, G.J. (2015) Parts per million powder X-ray diffraction. Analytical chemistry 87, 10950-10955.

Norby, P. (1997) Hydrothermal conversion of zeolites: An *in-situ* synchrotron X-ray powder diffraction study. Journal of the American Chemical Society 119, 5215-5221.

O'Connor, W.K., Dahlin, D.C., Nilsen, D.N., Gerdemann, S.J., Rush, G.E., Walters, R.P., Turner, P.C., (2001) Research status on the sequestration of carbon dioxide by direct aqueous mineral carbonation. Pittsburgh Coal Conference, University of Pittsburgh, 1249 Benedum Hall, Pittsburgh, PA 15261, United States.

O'Connor, W.K., Dahlin, D.C., Rush, G.E., Gerdemann, S.J., Penner, L.R., (2004) Energy and economic considerations for ex-situ and aqueous mineral carbonation. Coal Technology Association, 601 Suffield Drive, Gaithersburg, MD 20878, United States.

O'Connor, W.K., Dahlin, D.C., Rush, G.E., Gerdemann, S.J., Penner, L.R., (2005) Energy and economic evaluation of ex situ aqueous mineral carbonation, in: Rubin, E.S., Keith, D.W., Gilboy, C.F., Wilson, M., Morris, T., Gale, J., Thambimuthu, K. (Eds.), Greenhouse Gas Control Technologies 7. Elsevier Science Ltd, Oxford, pp. 2011-2015.

O'Connor, W.K., Dahlin, D.C., Turner, P.C., and Walters, R.P., (2000) Carbon dioxide sequestration by ex-situ mineral carbonation. Cognizant Communication Corporation, 3 Hartsdale Road, Elmsford, NY 10523, United States.

O'connor, W., Dahlin, D., Rush, G., Gerdemann, S., Penner, L., Nilsen, D. (2005) Aqueous mineral carbonation: Mineral availability, pretreatment, reaction parametrics, and process studies. National Energy Technology Laboratory, US DOE. Available online: http://www. webcitation. org/query.

Oelkers, E.H., Gislason, S.R., Matter, J. (2008) Mineral carbonation of CO_2. Elements 4, 333.

Ortega, A., Macías, M., Gotor, F.J. (2010) The multi-step nature of the kaolinite dehydroxylation: Kinetics and mechanism. Journal of the American Ceramic Society 93, 197-203.

Oskierski, H.C., Beinlich, A., Mavromatis, V., Altarawneh, M., Dlugogorski, B.Z. (2019) Mg isotope fractionation during continental weathering and low temperature carbonation of ultramafic rocks. Geochimica et Cosmochimica Acta 262, 60-77.

Oskierski, H.C., Dlugogorski, B.Z., Jacobsen, G. (2013a) Sequestration of atmospheric CO2 in a weathering-derived, serpentinite-hosted magnesite deposit: 14C tracing of carbon sources and age constraints for a refined genetic model. Geochimica et Cosmochimica Acta 122, 226-246.

Oskierski, H.C., Dlugogorski, B.Z., Jacobsen, G. (2013b) Sequestration of atmospheric CO_2 in chrysotile mine tailings of the Woodsreef Asbestos Mine, Australia: Quantitative mineralogy, isotopic fingerprinting and carbonation rates. Chemical Geology 358, 156-169.

Ozawa, T. (1965) A new method of analysing thermogravimetric data. Bulletin of the Chemical Society of Japan 38, 1881-1886.

Park, A.-H.A., Fan, L.-S. (2004) Mineral sequestration: physically activated dissolution of serpentine and pH swing process. Chemical Engineering Science 59, 5241-5247.

Pasquier, L.-C., Mercier, G., Blais, J.-F., Cecchi, E., Kentish, S. (2014) Reaction mechanism for the aqueous-phase mineral carbonation of heat-activated serpentine at low temperatures and pressures in flue gas conditions. Environmental Science & Technology 48, 5163-5170.

Pawley, A. (2003) Chlorite stability in mantle peridotite: the reaction clinochlore+enstatite=forsterite+pyrope+H_2O. Contributions to Mineralogy and Petrology 144, 449-456.

Pawley, A.R., Bromiley, G.D. (2003) The stability of antigorite in the systems MgO-SiO_2-H_2O (MSH) and MgO-Al_2O_3-SiO_2-H_2O (MASH): The effects of Al^{3+} substitution on high-pressure stability. American Mineralogist 88, 99-108.

Peng, J., Peng, S., Jiang, A., Wei, J., Li, C., Tan, J. (2010) Asymmetric least squares for multiple spectra baseline correction. Analytica Chimica Acta 683, 63-68.

Perrillat, J.-P., Daniel, I., Koga, K.T., Reynard, B., Cardon, H., Crichton, W.A. (2005) Kinetics of antigorite dehydration: A real-time X-ray diffraction study. Earth and Planetary Science Letters 236, 899-913.

Power, I.M., Harrison, A.L., Dipple, G.M., Wilson, S.A., Kelemen, P.B., Hitch, M., Southam, G. (2013) Carbon mineralisation: From natural analogues to engineered systems. Reviews in Mineralogy and Geochemistry 77, 305.

Prigiobbe, V., Hänchen, M., Werner, M., Baciocchi, R., Mazzotti, M. (2009) Mineral carbonation process for CO_2 sequestration. Energy Procedia 1, 4885-4890.

Pronost, J., Beaudoin, G., Tremblay, J., Larachi, F., Duchesne, J., Hébert, R., Constantin, M. (2011) Carbon sequestration kinetic and storage capacity of ultramafic mining waste. Environmental Science & Technology 45, 9413-9420.

Purba, E. (2010) Determination of reaction kinetics using online X-ray diffraction. Indonesian Journal of Chemistry 8.

R. Perez-Lopez, G.M.-H., J.-M. Nieto, F. Renard, L. Charlet (2008) Carbonation of alkaline paper mill waste to reduce CO_2 greenhouse gas emissions into the atmosphere. Applied Geochemistry, Elsevier 23 8.

Rahmani, O. (2018) CO_2 sequestration by indirect mineral carbonation of industrial waste red gypsum. Journal of CO2 Utilization 27, 374-380.

Rausis, K., Ćwik, A., Casanova, I. (2020) Insights into the direct carbonation of activated lizardite: The identification a poorly reactive amorphous Mg-rich silicate phase. International Journal of Greenhouse Gas Control 100, 103114.

Reddy, K.R., Gopakumar, A., Chetri, J.K. (2019) Critical review of applications of iron and steel slags for carbon sequestration and environmental remediation. Reviews in Environmental Science and Bio/Technology 18, 127-152.

Rietmeijer, F.J.M., Nuth, J.A., Mackinnon, I.D.R. (1986) Analytical electron microscopy of Mg-SiO smokes: A comparison with infrared and XRD studies. Icarus 66, 211-222.

Rim, G., Marchese, A.K., Stallworth, P., Greenbaum, S.G., Park, A.-H.A. (2020) ^{29}Si solid state MAS NMR study on leaching behaviors and chemical stability of different Mg-silicate structures for CO_2 sequestration. Chemical Engineering Journal 396, 125204.

Romanov, V., Soong, Y., Carney, C., Rush, G.E., Nielsen, B., O'Connor, W. (2015) Mineralisation of carbon dioxide: A literature review. ChemBioEng Reviews 2, 231-256.

Saadatkhah, N., Carillo Garcia, A., Ackermann, S., Leclerc, P., Latifi, M., Samih, S., Patience, G.S., Chaouki, J. (2020) Experimental methods in chemical engineering: Thermogravimetric analysis—TGA. The Canadian Journal of Chemical Engineering 98, 34-43.

Samtani, M., Dollimore, D., Alexander, K.S. (2002) Comparison of dolomite decomposition kinetics with related carbonates and the effect of procedural variables on its kinetic parameters. Thermochimica Acta 392-393, 135-145.

Sandu, C., Singh, R.K. (1990) Modelling differential scanning calorimetry. Thermochimica Acta 159, 267-298.

Sanna, A., Gaubert, J., Maroto-Valer, M.M. (2016) Alternative regeneration of chemicals employed in mineral carbonation towards technology cost reduction. Chemical Engineering Journal 306, 1049-1057.

Sanna, A., Lacinska, A., Styles, M., Maroto-Valer, M.M. (2014a) Silicate rock dissolution by ammonium bisulphate for pH swing mineral CO_2 sequestration. Fuel Processing Technology 120, 128-135.

Sanna, A., Uibu, M., Caramanna, G., Kuusik, R., Maroto-Valer, M.M. (2014b) A review of mineral carbonation technologies to sequester CO_2. Chemical Society Reviews 43, 8049-8080.

Sanna, A., Wang, X., Lacinska, A., Styles, M., Paulson, T., Maroto-Valer, M.M. (2013) Enhancing Mg extraction from lizardite-rich serpentine for CO_2 mineral sequestration. Minerals Engineering 49, 135-144.

Sarperi, L., Surbrenat, A., Kerihuel, A., Chazarenc, F. (2014) The use of an industrial by-product as a sorbent to remove CO_2 and H_2S from biogas. Journal of Environmental Chemical Engineering 2, 1207-1213.

Sawai, M., Katayama, I., Hamada, A., Maeda, M., Nakashima, S. (2013) Dehydration kinetics of antigorite using *in-situ* high-temperature infrared microspectroscopy. Physics and Chemistry of Minerals 40, 319-330.

Sbirrazzuoli, N., Vincent, L., Mija, A., Guigo, N. (2009) Integral, differential and advanced isoconversional methods: Complex mechanisms and isothermal predicted conversion–time curves. Chemometrics and Intelligent Laboratory Systems 96, 219-226.

Scambelluri, M., Pettke, T., Rampone, E., Godard, M., Reusser, E. (2014) Petrology and trace element budgets of high-pressure peridotites indicate subduction dehydration of serpentinized mantle (Cima di Gagnone, Central Alps, Switzerland). Journal of Petrology 55, 459-498.

Schaef, H.T., Windisch Jr, C.F., McGrail, B.P., Martin, P.F., Rosso, K.M. (2011) Brucite $Mg(OH)_2$ carbonation in wet supercritical CO_2: An *in-situ* high pressure X-ray diffraction study. Geochimica et Cosmochimica Acta 75, 7458-7471.

Schmitt, B., Brönnimann, C., Eikenberry, E.F., Hülsen, G., Toyokawa, H., Horisberger, R., Gozzo, F., Patterson, B., Schulze-Briese, C., Tomizaki, T. (2004) Development of single photon counting detectors at the Swiss Light Source. Nuclear Instruments and Methods in Physics Research Section A: Accelerators, Spectrometers, Detectors and Associated Equipment 518, 436-439.

Seifritz, W. (1990) CO_2 disposal by means of silicates. Nature 345, 486.

Sheila, D. (1993) Thermal analysis studies on the decomposition of magnesite. International Journal of Mineral Processing 37, 73-88.

Sigfusson, B., Gislason, S.R., Matter, J.M., Stute, M., Gunnlaugsson, E., Gunnarsson, I., Aradottir, E.S., Sigurdardottir, H., Mesfin, K., Alfredsson, H.A., Wolff-Boenisch, D., Arnarsson, M.T., Oelkers, E.H. (2015) Solving the carbon-dioxide buoyancy challenge: The design and field testing of a dissolved CO_2 injection system. International Journal of Greenhouse Gas Control 37, 213-219.

Sipilä, J., Teir, S., Zevenhoven, R. (2008) Carbon dioxide sequestration by mineral carbonation: Literature review update 2005–2007. Åbo Akademi Rep. VT 1.

Snæbjörnsdóttir, S.Ó., Gislason, S.R., Galeczka, I.M., Oelkers, E.H. (2018) Reaction path modelling of in-situ mineralisation of CO_2 at the CarbFix site at Hellisheidi, SW-Iceland. Geochimica et Cosmochimica Acta 220, 348-366.

Snæbjörnsdóttir, S.Ó., Sigfússon, B., Marieni, C., Goldberg, D., Gislason, S.R., Oelkers, E.H. (2020) Carbon dioxide storage through mineral carbonation. Nature Reviews Earth & Environment 1, 90-102.

Song, X., Xiaoyu, C., Lin, Q., Yanna, L. (2019) A review of mineral carbonation from industrial waste. IOP Conference Series: Earth and Environmental Science 401, 012008.

Stackhouse, S., Coveney, P.V., Benoit, D.M. (2004) Density-functional-theory-based study of the dehydroxylation behaviour of aluminous dioctahedral 2:1 layer-type clay minerals. The Journal of Physical Chemistry B 108, 9685-9694.

Staudigel, H., Schreyer, W. (1977) The upper thermal stability of clinochlore, $Mg_5Al[AlSi_3O_{10}](OH)_8$, at 10–35 kbar P_{H2O} Contributions to Mineralogy and Petrology 61, 187-198.

Stolaroff, J.K., Lowry, G.V., Keith, D.W. (2005) Using CaO and MgO-rich industrial waste streams for carbon sequestration. Energy Conversion and Management 46, 687-699.

Subagjo, Wulandari, W., Adinata, P.M., Fajrin, A. (2017) Thermal decomposition of dolomite under CO_2-air atmosphere. AIP Conference Proceedings 1805, 040006.

Svoboda, R. (2019) Reaction/crystallisation kinetics studied via *in-situ* XRD: experimental conditions versus methods of kinetic analysis. Philosophical Magazine 99, 2941-2956.

Tamilselvi Dananjayan, R.R., Kandasamy, P., Andimuthu, R. (2016) Direct mineral carbonation of coal fly ash for CO_2 sequestration. Journal of Cleaner Production 112, 4173-4182.

Tarling, M.S., Smith, S.A.F., Viti, C., Scott, J.M. (2018) Dynamic earthquake rupture preserved in a creeping serpentinite shear zone. Nature Communications 9, 3552.

Teir, S., Kuusik, R., Fogelholm, C.-J., Zevenhoven, R. (2007) Production of magnesium carbonates from serpentinite for long-term storage of CO_2. International Journal of Mineral Processing 85, 1-15.

Thom, J.G.M., Dipple, G.M., Power, I.M., Harrison, A.L. (2013) Chrysotile dissolution rates: Implications for carbon sequestration. Applied Geochemistry 35, 244-254.

Trittschack, R., Grobéty, B. (2012) Dehydroxylation kinetics of lizardite. European Journal of Mineralogy 24, 47-57.

Trittschack, R., Grobéty, B., (2013) The dehydroxylation of chrysotile: A combined *in-situ* micro-Raman and micro-FTIR study, American Mineralogist, p. 1133.

Trittschack, R., Grobéty, B., Brodard, P. (2014) Kinetics of the chrysotile and brucite dehydroxylation reaction: a combined non-isothermal/isothermal thermogravimetric analysis and high-temperature X-ray powder diffraction study. Physics and Chemistry of Minerals 41, 197-214.

Ukwattage, N.L., Ranjith, P.G., Li, X. (2017) Steel-making slag for mineral sequestration of carbon dioxide by accelerated carbonation. Measurement 97, 15-22.

Ukwattage, N.L., Ranjith, P.G., Wang, S.H. (2013) Investigation of the potential of coal combustion fly ash for mineral sequestration of CO_2 by accelerated carbonation. Energy 52, 230-236.

UNFCCC, P.A. (2015) United Nations framework convention on climate change. report of the conference of the parties on itss twenty first session, held in Paris from 30 November to 13 December 2015.

Vickery, N.M., Brown, R.E., Percival, I.G. (2010) Manilla 1:100000 geological sheet 9036 explanatory notes. . NSW Geol. Surv., Maitland, Australia.

Viti, C. (2010) Serpentine minerals discrimination by thermal analysis. American Mineralogist 95, 631.

Viti, C., Giacobbe, C., Gualtieri, A.F. (2011) Quantitative determination of chrysotile in massive serpentinites using DTA: Implications for asbestos determinations. American Mineralogist 96, 1003-1011.

Vyazovkin, S., (2015a) Isoconversional methodology, Isoconversional kinetics of thermally stimulated processes. Springer International Publishing, Switzerland, pp. 27-62.

Vyazovkin, S., (2015b) Some basics en route to isoconversional methodology, Isoconversional Kinetics of Thermally Stimulated Processes. Springer, pp. 1-25.

Vyazovkin, S., Burnham, A.K., Favergeon, L., Koga, N., Moukhina, E., Pérez-Maqueda, L.A., Sbirrazzuoli, N. (2020) ICTAC Kinetics Committee recommendations for analysis of multi-step kinetics. Thermochimica Acta 689, 178597.

Vyazovkin, S., Chrissafis, K., Di Lorenzo, M.L., Koga, N., Pijolat, M., Roduit, B., Sbirrazzuoli, N., Suñol, J.J. (2014) ICTAC Kinetics Committee recommendations for collecting experimental thermal analysis data for kinetic computations. Thermochimica Acta 590, 1-23.

Vyazovkin, S., Sbirrazzuoli, N. (2006) Isoconversional kinetic analysis of thermally stimulated processes in polymers. Macromolecular Rapid Communications 27, 1515-1532.

Vyazovkin, S., Wight, C.A. (1998) Isothermal and non-isothermal kinetics of thermally stimulated reactions of solids. International Reviews in Physical Chemistry 17, 407-433.

Wallwork, K.S., Kennedy, B.J., Wang, D. (2007) The high resolution powder diffraction beamline for the Australian Synchrotron. AIP Conference Proceedings 879, 879-882.

Wang, D., Liu, X., Liu, T., Shen, K., Welch, D.O., Li, B. (2017) Constraints from the dehydration of antigorite on high-conductivity anomalies in subduction zones. Scientific Reports 7, 16893.

Wang, F., Dreisinger, D., Jarvis, M., Hitchins, T. (2019) Kinetics and mechanism of mineral carbonation of olivine for CO_2 sequestration. Minerals Engineering 131, 185-197.

Wang, X., Maroto-Valer, M. (2011a) Integration of CO_2 capture and storage based on pH-swing mineral carbonation using recyclable ammonium salts. Energy Procedia 4, 4930-4936.

Wang, X., Maroto-Valer, M.M. (2011b) Dissolution of serpentine using recyclable ammonium salts for CO_2 mineral carbonation. Fuel 90, 1229-1237.

Weber, J.N., Greer, R.T. (1965) Dehydration of serpentine: heat of reaction and reaction kinetics at PH_2O=1 ATM. American Mineralogist 50, 450-464.

Werner, M., Hariharan, S., Mazzotti, M. (2014) Flue gas CO_2 mineralisation using thermally activated serpentine: From single- to double-step carbonation. Energy Procedia 63, 5912-5917.

Werner, M., Hariharan, S.B., Bortolan, A.V., Zingaretti, D., Baciocchi, R., Mazzotti, M. (2013) Carbonation of activated serpentine for direct flue gas mineralisation. Energy Procedia 37, 5929-5937.

White, C.E., Provis, J.L., Proffen, T., Riley, D.P., van Deventer, J.S.J. (2010) Density functional modelling of the local structure of kaolinite subjected to thermal dehydroxylation. The Journal of Physical Chemistry A 114, 4988-4996.

Whittaker, E.J.W., Zussman, J. (1956) The characterisation of serpentine minerals by X-ray diffraction. Mineralogical Magazine and Journal of the Mineralogical Society 31, 107-126.

Wicks, F.J., O'Hanley, D.S. (1988) Serpentine minerals; structures and petrology. Reviews in Mineralogy and Geochemistry 19, 91-167.

Wicks, F.J., Whittaker, E.J.W. (1975) A reappraisal of the structures of the serpentine minerals. The Canadian Mineralogist 13, 227-243.

Wilson, S.A., Dipple, G.M., Power, I.M., Thom, J.M., Anderson, R.G., Raudsepp, M., Gabites, J.E., Southam, G. (2009) Carbon dioxide fixation within mine wastes of ultramafic-hosted ore deposits: Examples from the Clinton Creek and Cassiar Chrysotile deposits, Canada. Economic Geology 104, 95-112.

Wilson, S.A., Harrison, A.L., Dipple, G.M., Power, I.M., Barker, S.L.L., Ulrich Mayer, K., Fallon, S.J., Raudsepp, M., Southam, G. (2014) Offsetting of CO_2 emissions by air capture in mine tailings at the Mount Keith Nickel Mine, Western Australia: Rates, controls and prospects for carbon neutral mining. International Journal of Greenhouse Gas Control 25, 121-140.

Wilson, S.A., Raudsepp, M., Dipple, G.M. (2006) Verifying and quantifying carbon fixation in minerals from serpentine-rich mine tailings using the Rietveld method with X-ray powder diffraction data. American Mineralogist 91, 1331-1341.

Xu, X., Liu, W., Chu, G., Zhang, G., Luo, D., Yue, H., Liang, B., Li, C. (2019) Energy-efficient mineral carbonation of $CaSO_4$ derived from wollastonite via a roasting-leaching route. Hydrometallurgy 184, 151-161.

Yan, H., Zhang, J., Zhao, Y., Zheng, C. (2013) CO_2 sequestration from flue gas by direct aqueous mineral carbonation of wollastonite. Science China Technological Sciences 56, 2219-2227.

Zhang, M., Redfern, S.A.T., Salje, E.K.H., Carpenter, M.A., Wang, L. (2010) H_2O and the dehydroxylation of phyllosilicates: An infrared spectroscopic study. American Mineralogist 95, 1686-1693.

Zhou, S., Wei, Y., Li, B., Ma, B., Wang, C., Wang, H. (2017) Kinetics study on the dehydroxylation and phase transformation of $Mg_3Si_2O_5(OH)_4$. Journal of Alloys and Compounds 713, 180-186.

Zhu, W., Fusseis, F., Lisabeth, H., Xing, T., Xiao, X., De Andrade, V., Karato, S.-i. (2016) Experimental evidence of reaction-induced fracturing during olivine carbonation. Geophysical Research Letters 43, 9535-9543.

Zulumyan, N., Isahakyan, A., Beglaryan, H., Melikyan, S. (2018) A study of thermal decomposition of antigorite from dunite and lizardite from peridotite. Journal of Thermal Analysis and Calorimetry 131, 1201-1211.

Chapter 6: Conclusions and Recommendations for Future Research

6 Introduction

This chapter summarises the major research outcomes of this thesis along with the recommendations for potential future research. Overall, this thesis contributed towards a comprehensive understanding of mineralogical changes and kinetics pertinent to thermal dehydroxylation of serpentine minerals ($Mg_3Si_2O_5(OH)_4$) and to provide potent strategies for the energy-efficient development of a dehydroxylation process, necessary for reducing the cost of this pre-treatment step for viable CO_2 sequestration via mineral carbonation. Firstly, this thesis explores kinetics of thermal dehydroxylation of Al-rich antigorite using isoconversional kinetics by employing simultaneous thermal gravimetric and differential scanning calorimetric (TGA-DSC) analysis. Concurrent use of *in-situ* synchrotron powder X-ray diffraction (PXRD) analysis provided insights into phase evolution and thus into the limitations of using Al-rich antigorite as a feedstock for mineral carbonation. Secondly, the investigation on the impact of grain size, feedstock mineralogy and vapour pressure on the structural changes during thermal dehydroxylation using a flow-through synchrotron PXRD analysis further enhanced our comprehension of why lizardite (serpentine polymorph) is a more suitable candidate for the mineral carbonation, as compared to antigorite and how the operating conditions can affect the energy requirements of thermal dehydroxylation. Lastly, this research compares the use of TGA, DSC and *in-situ* synchrotron PXRD data for

isoconversional kinetic analysis of antigorite dehydroxylation. It explores the potential of *in-situ* synchrotron PXRD-based isoconversional kinetic analysis of individual phases to decipher the kinetics of the complex, multistep dehydroxylation reaction.

Thermal dehydroxylation of serpentine minerals produces the amorphous α-MS and β-MS components (500 - 800 °C) which are responsible for the higher reactivity during the subsequent CO_2 sequestration through mineral carbonation under flue gas conditions (Du Breuil *et al.*, 2019b; Farhang *et al.*, 2017; Rim *et al.*, 2020). However, further heating converts these amorphous contents to less-reactive crystalline forsterite (above 700 °C) and enstatite (above 800 °C) phases (Alizadehhesari *et al.*, 2012; Dlugogorski and Balucan, 2014; Du Breuil *et al.*, 2019b; Gualtieri *et al.*, 2012; Liu *et al.*, 2019; McKelvy *et al.*, 2004; Viti, 2010). Mineral carbonation at high temperature and high CO_2 pressure may dissolve the less reactive forsterite phase, but this is not an economically viable solution (Rim *et al.*, 2020). Hence, thermal dehydroxylation to an appropriate temperature for the highest production of amorphous content is crucial for the implementation of mineral carbonation of serpentine minerals. Therefore, we employed the *in-situ* synchrotron PXRD analysis, which helped us identify the two amorphous components during the thermal dehydroxylation and the desired dehydroxylation temperature for the highest amorphous content. Until now, literature provides no detailed record of amorphous phase formation during serpentine dehydroxylation, as it was believed that PXRD could not provide the required information about amorphous content and researchers used other techniques such as ^{29}Si Nuclear magnetic resonance (NMR) and Raman to identify the amorphous phases (Rausis *et al.*, 2020; Rim *et al.*, 2020).

6.1 Conclusions

Literature lacks a link between the *α*-metaserpentine and amorphous metaserpentine components observed in XRD analysis (McKelvy *et al.*, 2004) and dehydroxylate I and dehydroxylate II discovered via ^{29}Si NMR for lizardite and chrysotile (MacKenzie and Meinhold, 1994; Rim *et al.*, 2020). However, a rigorous *in-situ* synchrotron PXRD analysis allowed us to rectify the existing significant discrepancies regarding the nomenclature of these amorphous phases. This study reports a new amorphous component called *α*-metaserpentine (*α*-MS at d < 9.9 Å), which has not been previously reported using XRD analysis (McKelvy *et al.*, 2004). Amorphous *α*-MS observed in our study behaves similarly to the dehydroxylate I (σ = -72 ppm) observed in ^{29}Si NMR, *e.g.*, the formation of forsterite occurs at the expense of dehydroxylate I (MacKenzie and Meinhold, 1994). Additionally, a significant discrepancy exists in the kinetic parameters for the thermal dehydroxylation of serpentine which may have originated from the inappropriate use of single-step kinetic model-fitting to a multi-step dehydroxylation reaction (Alizadehhesari *et al.*, 2012; Balucan *et al.*, 2011; Chollet *et al.*, 2011; Gualtieri *et al.*, 2012; Perrillat *et al.*, 2005; Sawai *et al.*, 2013). Therefore, this study implemented the isoconversional kinetic analysis to address this issue. A variation in activation energy (E_α) from 290 to 515 kJ mol^{-1} for progressive antigorite dehydroxylation suggested a multistep reaction. The combined kinetic and mineralogical variation exhibited that the antigorite could only be dehydroxylated to 49 % (51 % OH_{res}), as above this, the activation energy starts to increase with the onset of less reactive forsterite formation. Hence Al-rich antigorite is not a suitable feedstock for mineral carbonation under flue gas conditions.

The effect of operating parameters (*e.g.*, grain size, heating rate, flow rate and type of purge gas) on the dehydroxylation of serpentine minerals have been previously explored by many researchers using simultaneous thermal analyses (TGA-DSC) analyses (Balucan and Dlugogorski, 2013; Brindley and Hayami, 1963; Brindley and Zussman, 1957; Drief and Nieto, 1999; Gualtieri *et al.*, 2012; Kim and Chung, 2002). However, the record of mass loss (TGA) and heat flow (DSC) during thermal dehydroxylation does not provide valuable insight into the structural variation which is a vital factor defining the reactivity in the successive stage of carbonation for CO_2 sequestration. Therefore, *in-situ* PXRD analysis was explored due to its ability to track the evolution of structural changes for individual crystalline and amorphous phases during overlapping reactions occurring without mass loss. We employed *in-situ* synchrotron PXRD analysis to explore the effect of mineralogy (*i.e.*, antigorite and lizardite), grain size (45-75 µm and < 45 µm) and partial pressure of water vapour (dry and wet) conditions on the formation of amorphous phases. Consistent with our previous study (Chapter 3), both antigorite and lizardite sample showed the formation of two amorphous components [α-metaserpentine (d > 9.9 Å) and β-metaserpentine (2.7 < d < 3.4 Å)] and their transformation to forsterite and enstatite, respectively. However, in the antigorite sample, these two phases form simultaneously, whereas amorphous β-metaserpentine formation lags behind the amorphous α-metaserpentine formation in the lizardite sample. Although amorphous β-metaserpentine is less reactive under mild carbonation conditions (Rausis *et al.*, 2020), the selective production of α-MS is not possible in the studied serpentine polymorphs. The comparison of antigorite and lizardite showed that lizardite, at 90% conversion (10 % OH_{res}), contains the highest amorphous content before the onset of less-reactive forsterite formation and that the maximum amorphous content in lizardite is ~3 times higher than in antigorite. Antigorite, on the other hand, produces less amorphous content and overlapping of dehydroxylation with forsterite formation (~60 %

forsterite at highest amorphous content) renders it unfeasible for carbonation at the flue gas conditions. Additionally, energy requirements double for the dehydroxylation of antigorite to provide the same amount of amorphous content as in the lizardite.

The study of different particle sizes suggests that smaller particle size decreases the dehydroxylation temperature for both serpentine polymorphs due to better heat and mass transfer. The partial pressure of water vapour (p_{H2O}) affects the thermal dehydroxylation of lizardite but not that of antigorite. Our PXRD data show that the higher p_{H2O} delays the dehydroxylation in lizardite to higher temperature due to the formation of a chemisorption layer over the surface of particles, consistent with the literature (Brindley *et al.*, 1967a; Brindley and Hayami, 1963). In contrast, p_{H2O} does not favour the formation of the chemisorption layer due to lower amorphous content, high dehydroxylation temperature and simultaneous exothermic forsterite formation.

This thesis has demonstrated that the energy-efficient development of a dehydroxylation process for CO_2 sequestration through mineral carbonation relies on profound mineralogical changes and kinetic understanding of the thermal dehydroxylation of serpentine minerals. While lizardite is most abundant and provides most amorphous content upon dehydroxylation, it is crucial to understand the kinetics of most stable serpentine polymorphs to provide the benchmark for the extreme energy requirement during thermal dehydroxylation. Isoconversional kinetic analysis based on TGA and DSC analyses provides the overall variation in activation energy during thermal dehydroxylation (Chapter 3). However, some aspects of the overlapping dehydroxylation reactions are obscured in TGA-DSC, *i.e.*, TGA-based E_α does not reflect reactions occurring without mass loss (*i.e.*, forsterite formation) and DSC-based kinetics do not reflect overlapping endothermic

(dehydroxylation) and exothermic (forsterite crystallisation) reactions. Therefore, for the first time, PXRD-based isoconversional kinetic analysis of the evolution of individual phases (antigorite and forsterite) during thermal dehydroxylation of antigorite was explored. TGA, DSC and synchrotron PXRD-based activation energies for antigorite dehydroxylation are consistent in that they show a gentle increase prior to the onset of forsterite formation. This has been explained though an increasing kinetic barrier associated with increasing distance between hydroxyl groups that need to combine to be removed from the mineral in the form of water vapour (Ortega *et al.*, 2010; Trittschack and Grobéty, 2012; Trittschack *et al.*, 2014). The divergence of TGA and DSC-based activation energies around 700 °C is either associated with increased hindrance of the diffusion of volatile species or with a contribution to heat flow by the exothermic formation of forsterite. The sharp increase in TGA and DSC-based activation energies above 700 °C has previously been ascribed to increasing distance of hydroxyl groups (Molina-Montes *et al.*, 2008; Trittschack and Grobéty, 2012; Ukwattage *et al.*, 2013). However, independent PXRD-based activation energies of antigorite decomposition and forsterite formation determined in this thesis show that the sharp increase is due to forsterite formation and the associated breaking of strong Si-O and Mg-O bonds. Therefore, energy-efficient dehydroxylation of serpentine mineral must consider the kinetic barrier posed by formation of forsterite. Isoconversional kinetic analysis performed using *in-situ* PXRD data for individual phases is able to enhance the understanding of similar multistep reaction kinetics.

6.2 Recommendations

Based on the series of investigations presented in this dissertation, future research directions may focus on the following aspects:

- Al-rich antigorite mineral is not suitable for mineral carbonation at mild temperature and pressure conditions due to higher thermal stability. However, if the antigorite has to be used at some location due to the unavailability of other serpentine polymorphs, the reactivity of antigorite sample heat-treated at a temperature a) before the onset of forsterite and b) maximum amorphous production should be further investigated for mineral carbonation at high temperature and pressure conditions.

- As feedstock mineralogy affects the dehydroxylation temperatures, and natural serpentine minerals may coexist in nature, investigating the kinetics of mixtures of serpentine polymorphs may be beneficial for designing an optimised thermal dehydroxylation reactor. The underlying aim may be to operate under varying feedstock compositions.

- In the current study, amorphous α and β-metaserpentine components appeared to be the precursors of forsterite and enstatite, respectively. However, both amorphous components reach the maximum amount nearly at the same temperature in antigorite, implying the limitation of producing one amorphous phase over another for subsequent carbonation, whereas in lizardite, β-metaserpentine lags behind the α-metaserpentine. Therefore, the combined use of *in-situ* ^{29}Si NMR and XRD analysis for both thermal dehydroxylation and most economical carbonation scheme under mild temperature and pressure conditions may help to further optimise dehydroxylation process for serpentine minerals in general.

- Density functional theory (DFT) computations should be coupled with isoconversional kinetic analysis to attain an in-depth mechanistic understanding of the dehydroxylation of antigorite and to verify that combination, diffusion and removal of increasingly distant hydroxyl groups is responsible for increasing activation energies during progressive dehydroxylation.

6.3 **References**

Abdullah, A.A., Oskierski, H.C., Altarawneh, M., Senanayake, G., Lumpkin, G., Dlugogorski, B.Z. (2019) Phase transformation mechanism of spodumene during its calcination. Minerals Engineering 140, 105883.

Alexander, G., Mercedes Maroto-Valer, M., Gafarova-Aksoy, P. (2007) Evaluation of reaction variables in the dissolution of serpentine for mineral carbonation. Fuel 86, 273-281.

Alizadehhesari, K., Golding, S.D., Bhatia, S.K. (2012) Kinetics of the dehydroxylation of serpentine. Energy & Fuels 26, 783-790.

Aminu, M.D., Nabavi, S.A., Rochelle, C.A., Manovic, V. (2017) A review of developments in carbon dioxide storage. Applied Energy 208, 1389-1419.

Arce Ferrufino, G.L.A., Okamoto, S., Dos Santos, J.C., de Carvalho, J.A., Avila, I., Romero Luna, C.M., Gomes Soares Neto, T. (2018) CO_2 sequestration by pH-swing mineral carbonation based on HCl/NH_4OH system using iron-rich lizardite 1T. Journal of CO2 Utilization 24, 164-173.

Ashley, P.M., Brownlow, J.W. (1993) Silica-carbonate alteration zones in the Great Serpentinite Belt, southern New England Orogen: their nature and significance, In New England Orogen, (eds. P.G. Flood and J.C. Aitchison). University of New England, Armidale, Australia, 197-214.

Assima, G.P., Larachi, F., Molson, J., Beaudoin, G. (2014) Comparative study of five Québec ultramafic mining residues for use in direct ambient carbon dioxide mineral sequestration. Chemical Engineering Journal 245, 56-64.

Azadi, M., Edraki, M., Farhang, F., Ahn, J. (2019) Opportunities for mineral carbonation in Australia's mining industry. Sustainability 11.

Azdarpour, A., Asadullah, M., Mohammadian, E., Hamidi, H., Junin, R., Karaei, M.A. (2015) A review on carbon dioxide mineral carbonation through pH-swing process. Chemical Engineering Journal 279, 615-630.

Balucan, R.D., Dlugogorski, B.Z. (2013) Thermal activation of antigorite for mineralisation of CO_2. Environmental Science & Technology 47, 182-190.

Balucan, R.D., Dlugogorski, B.Z., Kennedy, E.M., Belova, I.V., Murch, G.E. (2013) Energy cost of heat activating serpentinites for CO_2 storage by mineralisation. International Journal of Greenhouse Gas Control 17, 225-239.

Balucan, R.D., Kennedy, E.M., Mackie, J.F., Dlugogorski, B.Z. (2011) Optimisation of antigorite heat pre-treatment via kinetic modelling of the dehydroxylation reaction for CO_2 mineralisation. Greenhouse Gases: Science and Technology 1, 294-304.

Béarat, H., McKelvy, M.J., Chizmeshya, A.V.G., Gormley, D., Nunez, R., Carpenter, R.W., Squires, K., Wolf, G.H. (2006) Carbon sequestration via aqueous olivine mineral carbonation: Role of passivating layer formation. Environmental Science & Technology 40, 4802-4808.

Béarat, H., McKelvy, M.J., Chizmeshya, A.V.G., Sharma, R., Carpenter, R.W. (2002) Magnesium hydroxide dehydroxylation/carbonation reaction processes: Implications for carbon dioxide mineral sequestration. Journal of the American Ceramic Society 85, 742-748.

Benhelal, E., Rashid, M.I., Rayson, M.S., Brent, G.F., Oliver, T., Stockenhuber, M., Kennedy, E.M. (2019) Direct aqueous carbonation of heat activated serpentine: Discovery of undesirable side reactions reducing process efficiency. Applied Energy 242, 1369-1382.

Bloise, A.C., Manuela; Gualtieri, Alessandro F. (2018) Effect of grinding on chrysotile, amosite and crocidolite and implications for thermal treatment. Minerals 8.

Bobicki, E.R., Liu, Q., Xu, Z., Zeng, H. (2012) Carbon capture and storage using alkaline industrial wastes. Progress in Energy and Combustion Science 38, 302-320.

Brindley, G.W., Achar, B.N.N., Sharp, J.H. (1967a) Kinetics and mechanism of dehydroxylation processes: II. Temperature and vapor pressure dependence of dehydroxylation of serpentine. American Mineralogist 52, 1697-1705.

Brindley, G.W., Hayami, R. (1963) Kinetics and mechanisms of dehydration and recrystallization of serpentine—I. Clays and Clay Minerals 12, 35-47.

Brindley, G.W., Hayami, R. (1965) Mechanism of formation of forsterite and enstatite from serpentine. Mineralogical Magazine and Journal of the Mineralogical Society 35, 189-195.

Brindley, G.W., Millhollen, G.L. (1966) Chemisorption of water at high temperatures on kaolinite: Effect on dehydroxylation. Science 152, 1385.

Brindley, G.W., Sharp, J.H., Patterson, J.H., Narahari, B.N. (1967b) Kinetics and mechanism of dehydroxylation processes, I. Temperature and vapor pressure dependence of dehydroxylation of kaolinite. American Mineralogist 52, 201-211.

Brindley, G.W., Zussman, J. (1957) A structural study of the thermal transformation of serpentine minerals to forsterite. American Mineralogist 42, 461-474.

Bromiley, G.D., Pawley, A.R. (2003) The stability of antigorite in the systems MgO-SiO_2-H_2O (MSH) and MgO-Al_2O_3-SiO_2-H_2O (MASH): The effects of Al^{3+} substitution on high-pressure stability. American Mineralogist 88, 99-108.

Burnham, A.K., Dinh, L. (2007) A comparison of isoconversional and model-fitting approaches to kinetic parameter estimation and application predictions. Journal of Thermal Analysis and Calorimetry 89, 479-490.

Candela, P.A., Crummett, C.D., Earnest, D.J., Frank, M.R., Wylie, A.G. (2007) Low-pressure decomposition of chrysotile as a function of time and temperature. American Mineralogist 92, 1704-1713.

Capitani, G., Mellini, M. (2004) The modulated crystal structure of antigorite: The m = 17 polysome. American Mineralogist 89, 147-158.

Cattaneo, A., Gualtieri, A.F., Artioli, G. (2003) Kinetic study of the dehydroxylation of chrysotile asbestos with temperature by in situ XRPD. Physics and Chemistry of Minerals 30, 177-183.

Chang, E.E., Pan, S.-Y., Chen, Y.-H., Tan, C.-S., Chiang, P.-C. (2012) Accelerated carbonation of steelmaking slags in a high-gravity rotating packed bed. Journal of Hazardous Materials 227-228, 97-106.

Chollet, M., Daniel, I., Koga, K.T., Morard, G., van de Moortèle, B. (2011) Kinetics and mechanism of antigorite dehydration: Implications for subduction zone seismicity. Journal of Geophysical Research: Solid Earth 116, B04203.

Cotton, D.H., Jenkins, D.R. (1969) Bond-dissociation energy of gaseous magnesium oxide. Transactions of the Faraday Society 65, 376-379.

Critelli, T., Marini, L., Schott, J., Mavromatis, V., Apollaro, C., Rinder, T., De Rosa, R., Oelkers, E.H. (2015) Dissolution rate of antigorite from a whole-rock experimental study of serpentinite dissolution from $2<pH<9$ at 25°C: Implications for carbon mitigation via enhanced serpentinite weathering. Applied Geochemistry 61, 259-271.

Demir, F., Dönmez, B., Okur, H., Sevim, F. (2003) Calcination kinetic of magnesite from thermogravimetric data. Chemical Engineering Research and Design 81, 618-622.

Dessert, C., Dupré, B., Gaillardet, J., François, L.M., Allègre, C.J. (2003) Basalt weathering laws and the impact of basalt weathering on the global carbon cycle. Chemical Geology 202, 257-273.

Dey, S., Dhal, G.C. (2019) Materials progress in the control of CO and CO_2 emission at ambient conditions: An overview. Materials Science for Energy Technologies 2, 607-623.

Ding, W., Yang, H., Ouyang, J., Long, H. (2016) Modified wollastonite sequestrating CO_2 and exploratory application of the carbonation products. RSC Advances 6, 78090-78099.

Dlugogorski, B.Z., Balucan, R.D. (2014) Dehydroxylation of serpentine minerals: Implications for mineral carbonation. Renewable and Sustainable Energy Reviews 31, 353-367.

Drief, A., Nieto, F. (1999) The effect of dry grinding on antigorite from Mulhacen, Spain. Clays and Clay Minerals 47, 417-424.

Du Breuil, C., César-Pasquier, L., Dipple, G., Blais, J.-F., Iliuta, C.M., Mercier, G. (2019a) Mineralogical transformations of heated serpentine and their impact on dissolution during aqueous-phase mineral carbonation reaction in flue gas conditions. Minerals 9.

Du Breuil, C., Pasquier, L.-C., Dipple, G., Blais, J.-F., Iliuta, C.M., Mercier, G. (2019b) Mineralogical transformations of heated serpentine and their impact on dissolution during aqueous-phase mineral carbonation reaction in flue gas conditions. Minerals 9.

Durand, B., (2011) Carbon dioxide capture and storage, France, p. 32.

El Hazzat, M., Sifou, A., Arsalane, S., El Hamidi, A. (2020) Novel approach to thermal degradation kinetics of gypsum: application of peak deconvolution and Model-Free isoconversional method. Journal of Thermal Analysis and Calorimetry 140, 657-671.

Fabian, M., Shopska, M., Paneva, D., Kadinov, G., Kostova, N., Turianicová, E., Briančin, J., Mitov, I., Kleiv, R.A., Baláž, P. (2010) The influence of attrition milling on carbon dioxide sequestration on magnesium–iron silicate. Minerals Engineering 23, 616-620.

Fagerlund, J., Teir, S., Nduagu, E., Zevenhoven, R. (2009) Carbonation of magnesium silicate mineral using a pressurised gas/solid process. Energy Procedia 1, 4907-4914.

Farhang, F., Oliver, T.K., Rayson, M.S., Brent, G.F., Molloy, T.S., Stockenhuber, M., Kennedy, E.M. (2019) Dissolution of heat activated serpentine for CO_2 sequestration: The effect of silica precipitation at different temperature and pH values. Journal of CO2 Utilization 30, 123-129.

Farhang, F., Rayson, M., Brent, G., Hodgins, T., Stockenhuber, M., Kennedy, E. (2017) Insights into the dissolution kinetics of thermally activated serpentine for CO_2 sequestration. Chemical Engineering Journal 330, 1174-1186.

Fedoročková, A., Hreus, M., Raschman, P., Sučik, G. (2012) Dissolution of magnesium from calcined serpentinite in hydrochloric acid. Minerals Engineering 32, 1-4.

Field, C.B., Raupach, M.R. (2004) The global carbon cycle: integrating humans, climate and the natural world. Island Press, Washington.

Flynn, J.H., Wall, L.A. (1966) General treatment of thermogravimetry of polymers. Journal of Research of the National Bureau of Standards Section a-Physics and Chemistry A 70, 487-+.

Fouda, M.F.R., Amin, R.E.-S., Abd-Elzaher, M.M. (1996) Extraction of magnesia from Egyptian serpentine ore via reaction with different acids. I. Reaction with sulfuric acid. Bulletin of the Chemical Society of Japan 69, 1907-1912.

Friedlingstein, P., Jones, M.W., O'Sullivan, M., Andrew, R.M., Hauck, J., Peters, G.P., Peters, W., Pongratz, J., Sitch, S., Le Quéré, C., Bakker, D.C.E., Canadell, J.G., Ciais, P., Jackson, R.B., Anthoni, P., Barbero, L., Bastos, A., Bastrikov, V., Becker, M., Bopp, L., Buitenhuis, E., Chandra, N., Chevallier, F., Chini, L.P., Currie, K.I., Feely, R.A., Gehlen, M., Gilfillan, D., Gkritzalis, T., Goll, D.S., Gruber, N., Gutekunst, S., Harris, I., Haverd, V., Houghton, R.A., Hurtt, G., Ilyina, T., Jain, A.K., Joetzjer, E., Kaplan, J.O., Kato, E., Klein Goldewijk, K., Korsbakken, J.I., Landschützer, P., Lauvset, S.K., Lefèvre, N., Lenton, A., Lienert, S., Lombardozzi, D., Marland, G., McGuire, P.C., Melton, J.R., Metzl, N., Munro, D.R., Nabel, J.E.M.S., Nakaoka, S.I., Neill, C., Omar, A.M., Ono, T., Peregon, A., Pierrot, D., Poulter, B., Rehder, G., Resplandy, L., Robertson, E., Rödenbeck, C., Séférian, R., Schwinger, J., Smith, N., Tans, P.P., Tian, H., Tilbrook, B., Tubiello, F.N., van der Werf, G.R., Wiltshire, A.J., Zaehle, S. (2019) Global carbon budget 2019. Earth Syst. Sci. Data 11, 1783-1838.

Friedman, H.L. (1964) Kinetics of thermal degradation of char-forming plastics from thermogravimetry. Application to a phenolic plastic. Journal of Polymer Science Part C: Polymer Symposia 6, 183-195.

Fumagalli, P., Poli, S. (2004) Experimentally determined phase relations in hydrous peridotites to 6·5 GPa and their consequences on the dynamics of subduction zones. Journal of Petrology 46, 555-578.

Galwey, A.K. (2003) Perennial problems and promising prospects in the kinetic analysis of nonisothermal rate data. Thermochimica Acta 407, 93-103.

Gao, W., Wen, J., Li, Z. (2014) Dissolution kinetics of magnesium from calcined serpentine in NH_4Cl solution. Industrial & Engineering Chemistry Research 53, 7947-7955.

Gerdemann, S.J., O'Connor, W.K., Dahlin, D.C., Penner, L.R., Rush, H. (2007) *Ex-situ* aqueous mineral carbonation. Environmental Science & Technology 41, 2587-2593.

Ghaderi, N., Zhang, H., Sun, T. (2015) Relative stability and contrasting elastic properties of serpentine polymorphs from first-principles calculations. Journal of Geophysical Research: Solid Earth 120, 4831-4842.

Ghoorah, M., Dlugogorski, B.Z., Oskierski, H.C., Kennedy, E.M. (2014) Study of thermally conditioned and weak acid-treated serpentinites for mineralisation of carbon dioxide. Minerals Engineering 59, 17-30.

Gualtieri, A.F., Giacobbe, C., Viti, C. (2012) The dehydroxylation of serpentine group minerals. American Mineralogist 97, 666.

Gysi, A.P., Stefánsson, A. (2008) Numerical modelling of CO_2-water-basalt interaction. Mineralogical Magazine 72, 55.

Hariharan, S., Mazzotti, M. (2017a) Growth kinetics of synthetic hydromagnesite at 90 °C. Crystal Growth & Design 17, 317-327.

Hariharan, S., Mazzotti, M. (2017b) Kinetics of flue gas CO_2 mineralisation processes using partially dehydroxylated lizardite. Chemical Engineering Journal 324, 397-413.

Hariharan, S., Repmann-Werner, M., Mazzotti, M. (2016) Dissolution of dehydroxylated lizardite at flue gas conditions: III. Near-equilibrium kinetics. Chemical Engineering Journal 298, 44-54.

Hariharan, S., Werner, M., Hänchen, M., Mazzotti, M. (2014a) Dissolution of dehydroxylated lizardite at flue gas conditions: II. Kinetic modelling. Chemical Engineering Journal 241, 314-326.

Hariharan, S., Werner, M., Hänchen, M., Zingaretti, D., Baciocchi, R., Mazzotti, M. (2014b) Dissolution kinetics of thermally activated serpentine for mineralisation at flue gas conditions. Energy Procedia 63, 5887-5891.

Hariharan, S.B., Werner, M., Zingaretti, D., Baciocchi, R., Mazzotti, M. (2013) Dissolution of activated serpentine for direct flue-gas mineralisation. Energy Procedia 37, 5938-5944.

Harrison, A.L., Power, I.M., Dipple, G.M. (2013) Accelerated carbonation of brucite in mine tailings for carbon sequestration. Environmental Science & Technology 47, 126-134.

He, S., Zhang, W., Liu, L., Huang, Y., He, J., Xie, W., Wu, P., Du, C. (2014) Baseline correction for Raman spectra using an improved asymmetric least squares method. Analytical Methods 6, 4402-4407.

Hu, M., Chen, Z., Wang, S., Guo, D., Ma, C., Zhou, Y., Chen, J., Laghari, M., Fazal, S., Xiao, B., Zhang, B., Ma, S. (2016) Thermogravimetric kinetics of lignocellulosic biomass slow pyrolysis using distributed activation energy model, Fraser–Suzuki deconvolution, and isoconversional method. Energy Conversion and Management 118, 1-11.

Huijgen, W., Comans, R. (2005) Mineral CO_2 sequestration by carbonation of industrial residues. The Netherlands: Energy Research Centre of the Netherlands (ECN).

Huijgen, W.J.J., Comans, R.N.J. (2006) Carbonation of steel slag for CO_2 sequestration: Leaching of products and reaction mechanisms. Environmental Science & Technology 40, 2790-2796.

Huntzinger, D.N., Gierke, J.S., Kawatra, S.K., Eisele, T.C., Sutter, L.L. (2009) Carbon dioxide sequestration in cement kiln dust through mineral carbonation. Environmental Science & Technology 43, 1986-1992.

Huot, F., Beaudoin, G., Hebert, R., Constantin, M., Bonin, G., Dipple, G.M., (2003) Evaluation of southern Quebec asbestos residues for CO_2 sequestration by mineral carbonation : preliminary result. Geological Association of Canada, St. John's, NF (Canada), Canada.

IPCC, (2014) Climate change 2014: Mitigation of climate change. IPCC.

Ji, S., Zhu, J., He, H., Tao, Q., Zhu, R., Ma, L., Chen, M., Li, S., Zhou, J. (2018) Conversion of serpentine to smectite under hydrothermal condition: Implication for solid-state transformation. American Mineralogist 103, 241-251.

Kelemen, P., Benson, S.M., Pilorgé, H., Psarras, P., Wilcox, J. (2019) An overview of the status and challenges of CO_2 storage in minerals and geological formations. Frontiers in Climate 1, 9.

Kelemen, P.B., Hirth, G. (2012) Reaction-driven cracking during retrograde metamorphism: Olivine hydration and carbonation. Earth and Planetary Science Letters 345-348, 81-89.

Kelemen, P.B., Matter, J. (2008) *In-situ* carbonation of peridotite for CO_2 storage. Proceedings of the National Academy of Sciences 105, 17295-17300.

Kelly, K.E., Silcox, G.D., Sarofim, A.F., Pershing, D.W. (2011) An evaluation of *ex-situ*, industrial-scale, aqueous CO_2 mineralisation. International Journal of Greenhouse Gas Control 5, 1587-1595.

Kemache, N., Pasquier, L.-C., Cecchi, E., Mouedhen, I., Blais, J.-F., Mercier, G. (2017) Aqueous mineral carbonation for CO_2 sequestration: From laboratory to pilot scale. Fuel Processing Technology 166, 209-216.

Khawam, A., Flanagan, D.R. (2005) Role of isoconversional methods in varying activation energies of solid-state kinetics: I. isothermal kinetic studies. Thermochimica Acta 429, 93-102.

Khoo, H.H., Sharratt, P.N., Bu, J., Yeo, T.Y., Borgna, A., Highfield, J.G., Bjorklof, T.G., Zevenhoven, R. (2011) Carbon capture and mineralisation in Singapore: preliminary environmental impacts and costs via LCA. Industrial & Engineering Chemistry Research 50, 11350-11357.

Kildahl, N.K. (1995) Bond energy data summarised. Journal of Chemical Education 72, 423.

Kim, D.-J., Chung, H.-S. (2002) Effect of grinding on the structure and chemical extraction of metals from serpentine. Particulate Science and Technology 20, 159-168.

Kimura, Y., Nuth Iii, J.A., Tsukamoto, K., Kaito, C. (2011) Laboratory annealing experiments of refractory silicate grain analogs using differential scanning calorimetry. Meteoritics & Planetary Science 46, 92-102.

Kirchofer, A., Becker, A., Brandt, A., Wilcox, J. (2013) CO_2 mitigation potential of mineral carbonation with industrial alkalinity sources in the United States. Environmental Science & Technology 47, 7548-7554.

Lackner, K.S., Butt, D.P., Wendt, C.H. (1997) Progress on binding CO2 in mineral substrates. Energy Conversion and Management 38, S259-S264.

Lackner, K.S., Wendt, C.H., Butt, D.P., Joyce, E.L., Sharp, D.H. (1995) Carbon dioxide disposal in carbonate minerals. Energy 20, 1153-1170.

Larachi, F., Aksenova, D., Yousefi, B., Maldague, X.P.V., Beaudoin, G. (2018) Thermochemical monitoring of brucite carbonation using passive infrared thermography. Chemical Engineering and Processing - Process Intensification 130, 43-52.

Levy, J.H. (1990) Effect of water vapour pressure on the dehydration and dehydroxylation of kaolinite and smectite isolated from Australian tertiary oil shales. Energy & Fuels 4, 146-151.

Li, J., Hitch, M. (2018) Mechanical activation of magnesium silicates for mineral carbonation, a review. Minerals Engineering 128, 69-83.

Li, J., Hitch, M., Power, I.M., Pan, Y. (2018) Integrated mineral carbonation of ultramafic mine deposits—a review. Minerals 8.

Li, W., Li, W., Li, B., Bai, Z. (2009) Electrolysis and heat pretreatment methods to promote CO_2 sequestration by mineral carbonation. Chemical Engineering Research and Design 87, 210-215.

Liu, C., Wang, D., Shen, K., Liu, T., Yi, L. (2019) Kinetics of antigorite dehydration: Rapid dehydration as a trigger for lower-plane seismicity in subduction zones. American Mineralogist 104, 282-290.

Liu, M., Gadikota, G. (2018) Chemo-morphological coupling during serpentine heat treatment for carbon mineralisation. Fuel 227, 379-385.

Liu, M., Gadikota, G. (2020) Single-step, low temperature and integrated CO_2 capture and conversion using sodium glycinate to produce calcium carbonate. Fuel 275, 117887.

Loo, L., Maaten, B., Konist, A., Siirde, A., Neshumayev, D., Pihu, T. (2017) Carbon dioxide emission factors for oxy-fuel CFBC and aqueous carbonation of the Ca-rich oil shale ash. Energy Procedia 128, 144-149.

MacKenzie, K.J.D., Meinhold, R.H. (1994) Thermal reactions of chrysotile revisited: A 29Si and 25Mg MAS NMR study. American Mineralogist 79, 43-50.

Madsen, I.C., Scarlett, N.V.Y., Kern, A. (2011) Description and survey of methodologies for the determination of amorphous content via X-ray powder diffraction. Zeitschrift fur Kristallographie 226, 944.

Maroto-Valer, M.M., Fauth, D.J., Kuchta, M.E., Zhang, Y., Andrésen, J.M. (2005) Activation of magnesium rich minerals as carbonation feedstock materials for CO_2 sequestration. Fuel Processing Technology 86, 1627-1645.

Martinez, E. (1961) The effect of particle size on the thermal properties of serpentine minerals. American Mineralogist 46, 901-912.

Matter, J.M., Stute, M., Snæbjörnsdottir, S., Oelkers, E.H., Gislason, S.R., Aradottir, E.S., Sigfusson, B., Gunnarsson, I., Sigurdardottir, H., Gunnlaugsson, E., Axelsson, G., Alfredsson, H.A., Wolff-Boenisch, D., Mesfin, K., Fernandez de la Reguera Taya, D., Hall, J., Dideriksen, K., Broecker, W.S. (2016) Rapid carbon mineralisation for permanent disposal of anthropogenic carbon dioxide emissions. Science 352, 1312-1314.

Matus, C., Stopic, S., Etzold, S., Kremer, D., Wotruba, H., Dertmann, C., Telle, R., Friedrich, B., Knops, P. (2020) Mechanism of Nickel, Magnesium, and Iron Recovery from Olivine Bearing Ore during Leaching with Hydrochloric Acid Including a Carbonation Pre-Treatment. Metals 10.

McKelvy, M.J., Chizmeshya, A.V.G., Diefenbacher, J., Béarat, H., Wolf, G. (2004) Exploration of the role of heat activation in enhancing serpentine carbon sequestration reactions. Environmental Science & Technology 38, 6897-6903.

McKelvy, M.J., Diefenbacher, J., Nunez, R., Carpenter, R.W., Chizmeshya, A.V.G., (2005) Simultaneous mechanical and heat activation: A new route to enhance serpentine carbonation reactivity and lower CO_2 mineral sequestration process cost, United States.

McKelvy, M.J., Sharma, R., Chizmeshya, A.V.G., Bearat, H., Carpenter, R.W., (2000) $Mg(OH)_2$ dehydroxylation: Implications for enhancing CO_2 mineral sequestration reaction processes. Coal Technology Association, Rockville, MD (US), United States.

Mellini, M., Trommsdorff, V. & Compagnoni, R. (1987) Antigorite polysomatism: behaviour during progressive metamorphism. Contributions to Mineralogy and Petrology 97, 147-155.

Metz, B., Davidson, O., Coninck, H.d., Loos, M., Meyer, L. (2005) IPCC special report on carbon dioxide capture and storage. Cambridge University Press, New York, NY (United States), United States.

Michael, A., Zhou, Y.N., Yavuz, M., Khan, M.I. (2018) Deconvolution of overlapping peaks from differential scanning calorimetry analysis for multi-phase NiTi alloys. Thermochimica Acta 665, 53-59.

Miller, Q.R.S., Schaef, H.T., Kaszuba, J.P., Gadikota, G., McGrail, B.P., Rosso, K.M. (2019) Quantitative review of olivine carbonation kinetics: Reactivity trends, mechanistic insights, and research frontiers. Environmental Science & Technology Letters 6, 431-442.

Moine, E.c., Groune, K., El Hamidi, A., Khachani, M., Halim, M., Arsalane, S. (2016) Multi-step process kinetics of the non-isothermal pyrolysis of Moroccan RIF oil shale. Energy 115, 931-941.

Molina-Montes, E., Donadio, D., Hernández-Laguna, A., Sainz-Díaz, C.I., Parrinello, M. (2008) DFT research on the dehydroxylation reaction of pyrophyllite 1. First-principle molecular dynamics simulations. The Journal of Physical Chemistry B 112, 7051-7060.

Montes-Hernandez, G., Pérez-López, R., Renard, F., Nieto, J.M., Charlet, L. (2009) Mineral sequestration of CO_2 by aqueous carbonation of coal combustion fly-ash. Journal of Hazardous Materials 161, 1347-1354.

Moody, J.B. (1976) Serpentinisation: a review. Lithos 9, 125-138.

Mouedhen, I., Kemache, N., Pasquier, L.-C., Cecchi, E., Blais, J.-F., Mercier, G. (2017) Effect of pCO_2 on direct flue gas mineral carbonation at pilot scale. Journal of Environmental Management 198, 1-8.

Muravyev, N.V., Koga, N., Meerov, D.B., Pivkina, A.N. (2017) Kinetic analysis of overlapping multistep thermal decomposition comprising exothermic and endothermic processes: thermolysis of ammonium dinitramide. Physical Chemistry Chemical Physics 19, 3254-3264.

Nakano, M., Wada, T., Koga, N. (2015) Exothermic behaviour of thermal decomposition of sodium percarbonate: Kinetic deconvolution of successive endothermic and exothermic processes. The Journal of Physical Chemistry A 119, 9761-9769.

Neeraj, Yadav, S. (2020) Carbon storage by mineral carbonation and industrial applications of CO_2. Materials Science for Energy Technologies 3, 494-500.

Newman, J.A., Schmitt, P.D., Toth, S.J., Deng, F., Zhang, S., Simpson, G.J. (2015) Parts per million powder X-ray diffraction. Analytical chemistry 87, 10950-10955.

Norby, P. (1997) Hydrothermal conversion of zeolites: An *in-situ* synchrotron X-ray powder diffraction study. Journal of the American Chemical Society 119, 5215-5221.

O'Connor, W.K., Dahlin, D.C., Nilsen, D.N., Gerdemann, S.J., Rush, G.E., Walters, R.P., Turner, P.C., (2001) Research status on the sequestration of carbon dioxide by direct aqueous mineral carbonation. Pittsburgh Coal Conference, University of Pittsburgh, 1249 Benedum Hall, Pittsburgh, PA 15261, United States.

O'Connor, W.K., Dahlin, D.C., Rush, G.E., Gerdemann, S.J., Penner, L.R., (2004) Energy and economic considerations for ex-situ and aqueous mineral carbonation. Coal Technology Association, 601 Suffield Drive, Gaithersburg, MD 20878, United States.

O'Connor, W.K., Dahlin, D.C., Rush, G.E., Gerdemann, S.J., Penner, L.R., (2005) Energy and economic evaluation of ex situ aqueous mineral carbonation, in: Rubin, E.S., Keith, D.W., Gilboy, C.F., Wilson, M., Morris, T., Gale, J., Thambimuthu, K. (Eds.), Greenhouse Gas Control Technologies 7. Elsevier Science Ltd, Oxford, pp. 2011-2015.

O'Connor, W.K., Dahlin, D.C., Turner, P.C., and Walters, R.P., (2000) Carbon dioxide sequestration by ex-situ mineral carbonation. Cognizant Communication Corporation, 3 Hartsdale Road, Elmsford, NY 10523, United States.

O'connor, W., Dahlin, D., Rush, G., Gerdemann, S., Penner, L., Nilsen, D. (2005) Aqueous mineral carbonation: Mineral availability, pretreatment, reaction parametrics, and process studies. National Energy Technology Laboratory, US DOE. Available online: http://www. webcitation. org/query.

Oelkers, E.H., Gislason, S.R., Matter, J. (2008) Mineral carbonation of CO_2. Elements 4, 333.

Ortega, A., Macías, M., Gotor, F.J. (2010) The multi-step nature of the kaolinite dehydroxylation: Kinetics and mechanism. Journal of the American Ceramic Society 93, 197-203.

Oskierski, H.C., Beinlich, A., Mavromatis, V., Altarawneh, M., Dlugogorski, B.Z. (2019) Mg isotope fractionation during continental weathering and low temperature carbonation of ultramafic rocks. Geochimica et Cosmochimica Acta 262, 60-77.

Oskierski, H.C., Dlugogorski, B.Z., Jacobsen, G. (2013a) Sequestration of atmospheric CO2 in a weathering-derived, serpentinite-hosted magnesite deposit: 14C tracing of carbon sources and age constraints for a refined genetic model. Geochimica et Cosmochimica Acta 122, 226-246.

Oskierski, H.C., Dlugogorski, B.Z., Jacobsen, G. (2013b) Sequestration of atmospheric CO_2 in chrysotile mine tailings of the Woodsreef Asbestos Mine, Australia: Quantitative mineralogy, isotopic fingerprinting and carbonation rates. Chemical Geology 358, 156-169.

Ozawa, T. (1965) A new method of analysing thermogravimetric data. Bulletin of the Chemical Society of Japan 38, 1881-1886.

Park, A.-H.A., Fan, L.-S. (2004) Mineral sequestration: physically activated dissolution of serpentine and pH swing process. Chemical Engineering Science 59, 5241-5247.

Pasquier, L.-C., Mercier, G., Blais, J.-F., Cecchi, E., Kentish, S. (2014) Reaction mechanism for the aqueous-phase mineral carbonation of heat-activated serpentine at low temperatures and pressures in flue gas conditions. Environmental Science & Technology 48, 5163-5170.

Pawley, A. (2003) Chlorite stability in mantle peridotite: the reaction clinochlore+enstatite=forsterite+pyrope+H_2O. Contributions to Mineralogy and Petrology 144, 449-456.

Pawley, A.R., Bromiley, G.D. (2003) The stability of antigorite in the systems MgO-SiO_2-H_2O (MSH) and MgO-Al_2O_3-SiO_2-H_2O (MASH): The effects of Al^{3+} substitution on high-pressure stability. American Mineralogist 88, 99-108.

Peng, J., Peng, S., Jiang, A., Wei, J., Li, C., Tan, J. (2010) Asymmetric least squares for multiple spectra baseline correction. Analytica Chimica Acta 683, 63-68.

Perrillat, J.-P., Daniel, I., Koga, K.T., Reynard, B., Cardon, H., Crichton, W.A. (2005) Kinetics of antigorite dehydration: A real-time X-ray diffraction study. Earth and Planetary Science Letters 236, 899-913.

Power, I.M., Harrison, A.L., Dipple, G.M., Wilson, S.A., Kelemen, P.B., Hitch, M., Southam, G. (2013) Carbon mineralisation: From natural analogues to engineered systems. Reviews in Mineralogy and Geochemistry 77, 305.

Prigiobbe, V., Hänchen, M., Werner, M., Baciocchi, R., Mazzotti, M. (2009) Mineral carbonation process for CO_2 sequestration. Energy Procedia 1, 4885-4890.

Pronost, J., Beaudoin, G., Tremblay, J., Larachi, F., Duchesne, J., Hébert, R., Constantin, M. (2011) Carbon sequestration kinetic and storage capacity of ultramafic mining waste. Environmental Science & Technology 45, 9413-9420.

Purba, E. (2010) Determination of reaction kinetics using online X-ray diffraction. Indonesian Journal of Chemistry 8.

R. Perez-Lopez, G.M.-H., J.-M. Nieto, F. Renard, L. Charlet (2008) Carbonation of alkaline paper mill waste to reduce CO_2 greenhouse gas emissions into the atmosphere. Applied Geochemistry, Elsevier 23 8.

Rahmani, O. (2018) CO_2 sequestration by indirect mineral carbonation of industrial waste red gypsum. Journal of CO2 Utilization 27, 374-380.

Rausis, K., Ćwik, A., Casanova, I. (2020) Insights into the direct carbonation of activated lizardite: The identification a poorly reactive amorphous Mg-rich silicate phase. International Journal of Greenhouse Gas Control 100, 103114.

Reddy, K.R., Gopakumar, A., Chetri, J.K. (2019) Critical review of applications of iron and steel slags for carbon sequestration and environmental remediation. Reviews in Environmental Science and Bio/Technology 18, 127-152.

Rietmeijer, F.J.M., Nuth, J.A., Mackinnon, I.D.R. (1986) Analytical electron microscopy of Mg-SiO smokes: A comparison with infrared and XRD studies. Icarus 66, 211-222.

Rim, G., Marchese, A.K., Stallworth, P., Greenbaum, S.G., Park, A.-H.A. (2020) ^{29}Si solid state MAS NMR study on leaching behaviors and chemical stability of different Mg-silicate structures for CO_2 sequestration. Chemical Engineering Journal 396, 125204.

Romanov, V., Soong, Y., Carney, C., Rush, G.E., Nielsen, B., O'Connor, W. (2015) Mineralisation of carbon dioxide: A literature review. ChemBioEng Reviews 2, 231-256.

Saadatkhah, N., Carillo Garcia, A., Ackermann, S., Leclerc, P., Latifi, M., Samih, S., Patience, G.S., Chaouki, J. (2020) Experimental methods in chemical engineering: Thermogravimetric analysis—TGA. The Canadian Journal of Chemical Engineering 98, 34-43.

Samtani, M., Dollimore, D., Alexander, K.S. (2002) Comparison of dolomite decomposition kinetics with related carbonates and the effect of procedural variables on its kinetic parameters. Thermochimica Acta 392-393, 135-145.

Sandu, C., Singh, R.K. (1990) Modelling differential scanning calorimetry. Thermochimica Acta 159, 267-298.

Sanna, A., Gaubert, J., Maroto-Valer, M.M. (2016) Alternative regeneration of chemicals employed in mineral carbonation towards technology cost reduction. Chemical Engineering Journal 306, 1049-1057.

Sanna, A., Lacinska, A., Styles, M., Maroto-Valer, M.M. (2014a) Silicate rock dissolution by ammonium bisulphate for pH swing mineral CO_2 sequestration. Fuel Processing Technology 120, 128-135.

Sanna, A., Uibu, M., Caramanna, G., Kuusik, R., Maroto-Valer, M.M. (2014b) A review of mineral carbonation technologies to sequester CO_2. Chemical Society Reviews 43, 8049-8080.

Sanna, A., Wang, X., Lacinska, A., Styles, M., Paulson, T., Maroto-Valer, M.M. (2013) Enhancing Mg extraction from lizardite-rich serpentine for CO_2 mineral sequestration. Minerals Engineering 49, 135-144.

Sarperi, L., Surbrenat, A., Kerihuel, A., Chazarenc, F. (2014) The use of an industrial by-product as a sorbent to remove CO_2 and H_2S from biogas. Journal of Environmental Chemical Engineering 2, 1207-1213.

Sawai, M., Katayama, I., Hamada, A., Maeda, M., Nakashima, S. (2013) Dehydration kinetics of antigorite using *in-situ* high-temperature infrared microspectroscopy. Physics and Chemistry of Minerals 40, 319-330.

Sbirrazzuoli, N., Vincent, L., Mija, A., Guigo, N. (2009) Integral, differential and advanced isoconversional methods: Complex mechanisms and isothermal predicted conversion–time curves. Chemometrics and Intelligent Laboratory Systems 96, 219-226.

Scambelluri, M., Pettke, T., Rampone, E., Godard, M., Reusser, E. (2014) Petrology and trace element budgets of high-pressure peridotites indicate subduction dehydration of serpentinized mantle (Cima di Gagnone, Central Alps, Switzerland). Journal of Petrology 55, 459-498.

Schaef, H.T., Windisch Jr, C.F., McGrail, B.P., Martin, P.F., Rosso, K.M. (2011) Brucite $Mg(OH)_2$ carbonation in wet supercritical CO_2: An *in-situ* high pressure X-ray diffraction study. Geochimica et Cosmochimica Acta 75, 7458-7471.

Schmitt, B., Brönnimann, C., Eikenberry, E.F., Hülsen, G., Toyokawa, H., Horisberger, R., Gozzo, F., Patterson, B., Schulze-Briese, C., Tomizaki, T. (2004) Development of single photon counting detectors at the Swiss Light Source. Nuclear Instruments and Methods in Physics Research Section A: Accelerators, Spectrometers, Detectors and Associated Equipment 518, 436-439.

Seifritz, W. (1990) CO_2 disposal by means of silicates. Nature 345, 486.

Sheila, D. (1993) Thermal analysis studies on the decomposition of magnesite. International Journal of Mineral Processing 37, 73-88.

Sigfusson, B., Gislason, S.R., Matter, J.M., Stute, M., Gunnlaugsson, E., Gunnarsson, I., Aradottir, E.S., Sigurdardottir, H., Mesfin, K., Alfredsson, H.A., Wolff-Boenisch, D., Arnarsson, M.T., Oelkers, E.H. (2015) Solving the carbon-dioxide buoyancy challenge: The design and field testing of a dissolved CO_2 injection system. International Journal of Greenhouse Gas Control 37, 213-219.

Sipilä, J., Teir, S., Zevenhoven, R. (2008) Carbon dioxide sequestration by mineral carbonation: Literature review update 2005–2007. Åbo Akademi Rep. VT 1.

Snæbjörnsdóttir, S.Ó., Gislason, S.R., Galeczka, I.M., Oelkers, E.H. (2018) Reaction path modelling of in-situ mineralisation of CO_2 at the CarbFix site at Hellisheidi, SW-Iceland. Geochimica et Cosmochimica Acta 220, 348-366.

Snæbjörnsdóttir, S.Ó., Sigfússon, B., Marieni, C., Goldberg, D., Gislason, S.R., Oelkers, E.H. (2020) Carbon dioxide storage through mineral carbonation. Nature Reviews Earth & Environment 1, 90-102.

Song, X., Xiaoyu, C., Lin, Q., Yanna, L. (2019) A review of mineral carbonation from industrial waste. IOP Conference Series: Earth and Environmental Science 401, 012008.

Stackhouse, S., Coveney, P.V., Benoit, D.M. (2004) Density-functional-theory-based study of the dehydroxylation behaviour of aluminous dioctahedral 2:1 layer-type clay minerals. The Journal of Physical Chemistry B 108, 9685-9694.

Staudigel, H., Schreyer, W. (1977) The upper thermal stability of clinochlore, $Mg_5Al[AlSi_3O_{10}](OH)_8$, at 10–35 kbar P_{H2O} Contributions to Mineralogy and Petrology 61, 187-198.

Stolaroff, J.K., Lowry, G.V., Keith, D.W. (2005) Using CaO and MgO-rich industrial waste streams for carbon sequestration. Energy Conversion and Management 46, 687-699.

Stopic, S., Dertmann, C., Koiwa, I., Kremer, D., Wotruba, H., Etzold, S., Telle, R., Knops, P., Friedrich, B. (2019) Synthesis of Nanosilica via Olivine Mineral Carbonation under High Pressure in an Autoclave. Metals 9.

Stopic, S., Dertmann, C., Modolo, G., Kegler, P., Neumeier, S., Kremer, D., Wotruba, H., Etzold, S., Telle, R., Rosani, D., Knops, P., Friedrich, B. (2018) Synthesis of Magnesium Carbonate via Carbonation under High Pressure in an Autoclave. Metals 8.

Subagjo, Wulandari, W., Adinata, P.M., Fajrin, A. (2017) Thermal decomposition of dolomite under CO_2-air atmosphere. AIP Conference Proceedings 1805, 040006.

Svoboda, R. (2019) Reaction/crystallisation kinetics studied via *in-situ* XRD: experimental conditions versus methods of kinetic analysis. Philosophical Magazine 99, 2941-2956.

Tamilselvi Dananjayan, R.R., Kandasamy, P., Andimuthu, R. (2016) Direct mineral carbonation of coal fly ash for CO_2 sequestration. Journal of Cleaner Production 112, 4173-4182.

Tarling, M.S., Smith, S.A.F., Viti, C., Scott, J.M. (2018) Dynamic earthquake rupture preserved in a creeping serpentinite shear zone. Nature Communications 9, 3552.

Teir, S., Kuusik, R., Fogelholm, C.-J., Zevenhoven, R. (2007) Production of magnesium carbonates from serpentinite for long-term storage of CO_2. International Journal of Mineral Processing 85, 1-15.

Thom, J.G.M., Dipple, G.M., Power, I.M., Harrison, A.L. (2013) Chrysotile dissolution rates: Implications for carbon sequestration. Applied Geochemistry 35, 244-254.

Trittschack, R., Grobéty, B. (2012) Dehydroxylation kinetics of lizardite. European Journal of Mineralogy 24, 47-57.

Trittschack, R., Grobéty, B., (2013) The dehydroxylation of chrysotile: A combined *in-situ* micro-Raman and micro-FTIR study, American Mineralogist, p. 1133.

Trittschack, R., Grobéty, B., Brodard, P. (2014) Kinetics of the chrysotile and brucite dehydroxylation reaction: a combined non-isothermal/isothermal thermogravimetric analysis and high-temperature X-ray powder diffraction study. Physics and Chemistry of Minerals 41, 197-214.

Ukwattage, N.L., Ranjith, P.G., Li, X. (2017) Steel-making slag for mineral sequestration of carbon dioxide by accelerated carbonation. Measurement 97, 15-22.

Ukwattage, N.L., Ranjith, P.G., Wang, S.H. (2013) Investigation of the potential of coal combustion fly ash for mineral sequestration of CO_2 by accelerated carbonation. Energy 52, 230-236.

UNFCCC, P.A. (2015) United Nations framework convention on climate change. report of the conference of the parties on itss twenty first session, held in Paris from 30 November to 13 December 2015.

Vickery, N.M., Brown, R.E., Percival, I.G. (2010) Manilla 1:100000 geological sheet 9036 explanatory notes. . NSW Geol. Surv., Maitland, Australia.

Viti, C. (2010) Serpentine minerals discrimination by thermal analysis. American Mineralogist 95, 631.

Viti, C., Giacobbe, C., Gualtieri, A.F. (2011) Quantitative determination of chrysotile in massive serpentinites using DTA: Implications for asbestos determinations. American Mineralogist 96, 1003-1011.

Vyazovkin, S., (2015a) Isoconversional methodology, Isoconversional kinetics of thermally stimulated processes. Springer International Publishing, Switzerland, pp. 27-62.

Vyazovkin, S., (2015b) Some basics en route to isoconversional methodology, Isoconversional Kinetics of Thermally Stimulated Processes. Springer, pp. 1-25.

Vyazovkin, S., Burnham, A.K., Favergeon, L., Koga, N., Moukhina, E., Pérez-Maqueda, L.A., Sbirrazzuoli, N. (2020) ICTAC Kinetics Committee recommendations for analysis of multi-step kinetics. Thermochimica Acta 689, 178597.

Vyazovkin, S., Chrissafis, K., Di Lorenzo, M.L., Koga, N., Pijolat, M., Roduit, B., Sbirrazzuoli, N., Suñol, J.J. (2014) ICTAC Kinetics Committee recommendations for collecting experimental thermal analysis data for kinetic computations. Thermochimica Acta 590, 1-23.

Vyazovkin, S., Sbirrazzuoli, N. (2006) Isoconversional kinetic analysis of thermally stimulated processes in polymers. Macromolecular Rapid Communications 27, 1515-1532.

Vyazovkin, S., Wight, C.A. (1998) Isothermal and non-isothermal kinetics of thermally stimulated reactions of solids. International Reviews in Physical Chemistry 17, 407-433.

Wallwork, K.S., Kennedy, B.J., Wang, D. (2007) The high resolution powder diffraction beamline for the Australian Synchrotron. AIP Conference Proceedings 879, 879-882.

Wang, D., Liu, X., Liu, T., Shen, K., Welch, D.O., Li, B. (2017) Constraints from the dehydration of antigorite on high-conductivity anomalies in subduction zones. Scientific Reports 7, 16893.

Wang, F., Dreisinger, D., Jarvis, M., Hitchins, T. (2019) Kinetics and mechanism of mineral carbonation of olivine for CO_2 sequestration. Minerals Engineering 131, 185-197.

Wang, X., Maroto-Valer, M. (2011a) Integration of CO_2 capture and storage based on pH-swing mineral carbonation using recyclable ammonium salts. Energy Procedia 4, 4930-4936.

Wang, X., Maroto-Valer, M.M. (2011b) Dissolution of serpentine using recyclable ammonium salts for CO_2 mineral carbonation. Fuel 90, 1229-1237.

Weber, J.N., Greer, R.T. (1965) Dehydration of serpentine: heat of reaction and reaction kinetics at PH_2O=1 ATM. American Mineralogist 50, 450-464.

Werner, M., Hariharan, S., Mazzotti, M. (2014) Flue gas CO_2 mineralisation using thermally activated serpentine: From single- to double-step carbonation. Energy Procedia 63, 5912-5917.

Werner, M., Hariharan, S.B., Bortolan, A.V., Zingaretti, D., Baciocchi, R., Mazzotti, M. (2013) Carbonation of activated serpentine for direct flue gas mineralisation. Energy Procedia 37, 5929-5937.

White, C.E., Provis, J.L., Proffen, T., Riley, D.P., van Deventer, J.S.J. (2010) Density functional modelling of the local structure of kaolinite subjected to thermal dehydroxylation. The Journal of Physical Chemistry A 114, 4988-4996.

Whittaker, E.J.W., Zussman, J. (1956) The characterisation of serpentine minerals by X-ray diffraction. Mineralogical Magazine and Journal of the Mineralogical Society 31, 107-126.

Wicks, F.J., O'Hanley, D.S. (1988) Serpentine minerals; structures and petrology. Reviews in Mineralogy and Geochemistry 19, 91-167.

Wicks, F.J., Whittaker, E.J.W. (1975) A reappraisal of the structures of the serpentine minerals. The Canadian Mineralogist 13, 227-243.

Wilson, S.A., Dipple, G.M., Power, I.M., Thom, J.M., Anderson, R.G., Raudsepp, M., Gabites, J.E., Southam, G. (2009) Carbon dioxide fixation within mine wastes of ultramafic-hosted ore deposits: Examples from the Clinton Creek and Cassiar chrysotile deposits, Canada. Economic Geology 104, 95-112.

Wilson, S.A., Harrison, A.L., Dipple, G.M., Power, I.M., Barker, S.L.L., Ulrich Mayer, K., Fallon, S.J., Raudsepp, M., Southam, G. (2014) Offsetting of CO_2 emissions by air capture in mine tailings at the Mount Keith Nickel Mine, Western Australia: Rates, controls and prospects for carbon neutral mining. International Journal of Greenhouse Gas Control 25, 121-140.

Wilson, S.A., Raudsepp, M., Dipple, G.M. (2006) Verifying and quantifying carbon fixation in minerals from serpentine-rich mine tailings using the Rietveld method with X-ray powder diffraction data. American Mineralogist 91, 1331-1341.

Xu, X., Liu, W., Chu, G., Zhang, G., Luo, D., Yue, H., Liang, B., Li, C. (2019) Energy-efficient mineral carbonation of $CaSO_4$ derived from wollastonite via a roasting-leaching route. Hydrometallurgy 184, 151-161.

Yan, H., Zhang, J., Zhao, Y., Zheng, C. (2013) CO_2 sequestration from flue gas by direct aqueous mineral carbonation of wollastonite. Science China Technological Sciences 56, 2219-2227.

Zhang, M., Redfern, S.A.T., Salje, E.K.H., Carpenter, M.A., Wang, L. (2010) H_2O and the dehydroxylation of phyllosilicates: An infrared spectroscopic study. American Mineralogist 95, 1686-1693.

Zhou, S., Wei, Y., Li, B., Ma, B., Wang, C., Wang, H. (2017) Kinetics study on the dehydroxylation and phase transformation of $Mg_3Si_2O_5(OH)_4$. Journal of Alloys and Compounds 713, 180-186.

Zhu, W., Fusseis, F., Lisabeth, H., Xing, T., Xiao, X., De Andrade, V., Karato, S.-i. (2016) Experimental evidence of reaction-induced fracturing during olivine carbonation. Geophysical Research Letters 43, 9535-9543.

Zulumyan, N., Isahakyan, A., Beglaryan, H., Melikyan, S. (2018) A study of thermal decomposition of antigorite from dunite and lizardite from peridotite. Journal of Thermal Analysis and Calorimetry 131, 1201-1211.

Appendix A: Supplementary Information for Chapter 3

Section 1: Synchrotron PXRD temperature calibration

Section 2: *In-situ* PXRD peak integration and amorphous phase calculation

Section 3: Thermogravimetry and differential scanning analyses

Section 4: Sample characterisation

Section 5: Calculations for isoconversional kinetic analysis

Section 6: Reaction scheme

Section 1: Synchrotron PXRD temperature calibration

Figure S3.1 shows the temperature calibration curve for the *in-situ* Synchrotron PXRD experiment using a heating rate of 8 °C min^{-1}. A 2^{nd} order polynomial function was used to model the calibration curve based on room temperature (25 °C), quartz transition (584.2 °C) and NaCl melting point (852 °C) measured at 8 °C min^{-1}.

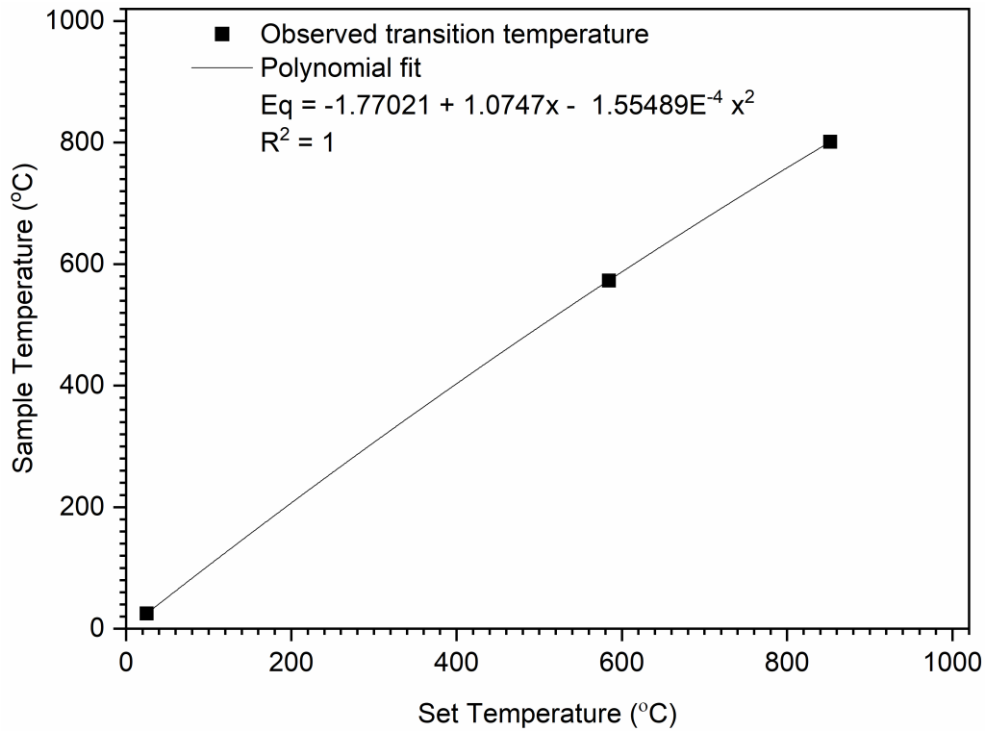

Figure S3.1. Temperature calibration for *in-situ* synchrotron powder X-ray diffraction (PXRD) at 8 °C min^{-1}.

Section 2: *In-situ* PXRD peak integration and amorphous phase calculation

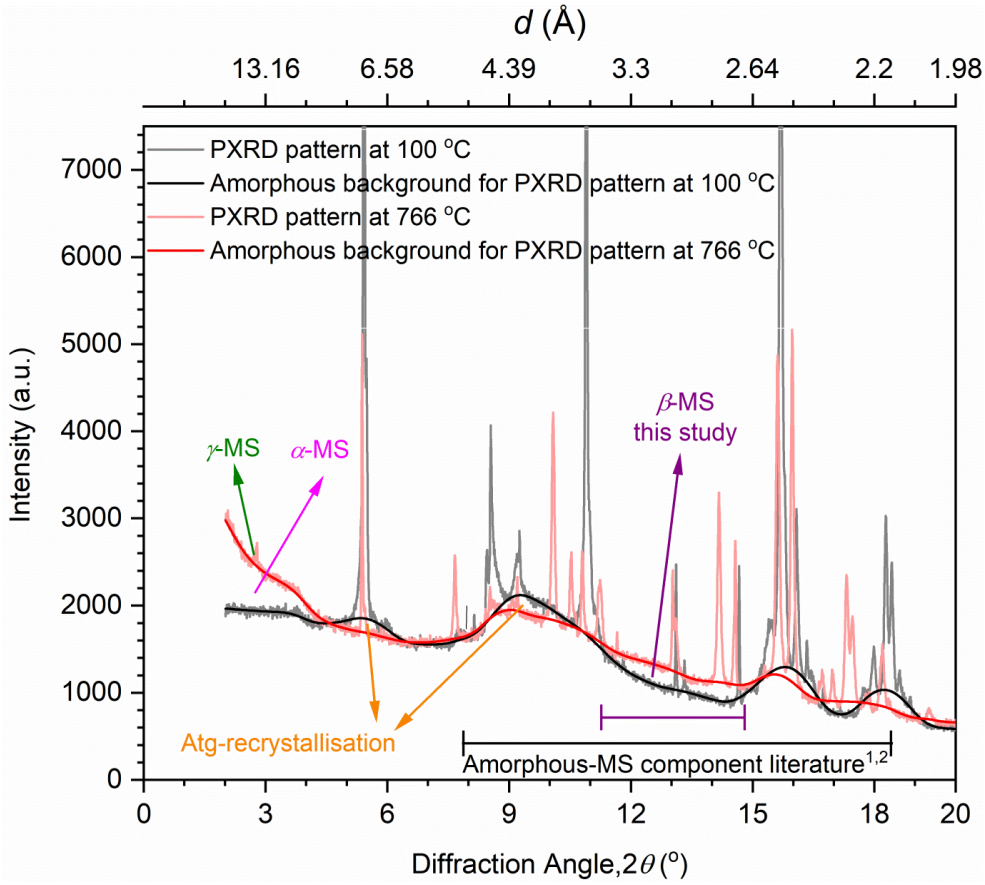

Figure S3.2. Amorphous phase modelling using asymmetric least square fitting method using Origin software during the dehydroxylation of antigorite dehydroxylation at 100 ℃ (starting temperature) and 766 ℃ (maximum αmetaserpentine component). Intermediate phases during dehydroxylation are labelled as α-MS: α-metaserpentine, β-MS: β-metaserpentine, γ-MS: γ-metaserpentine component

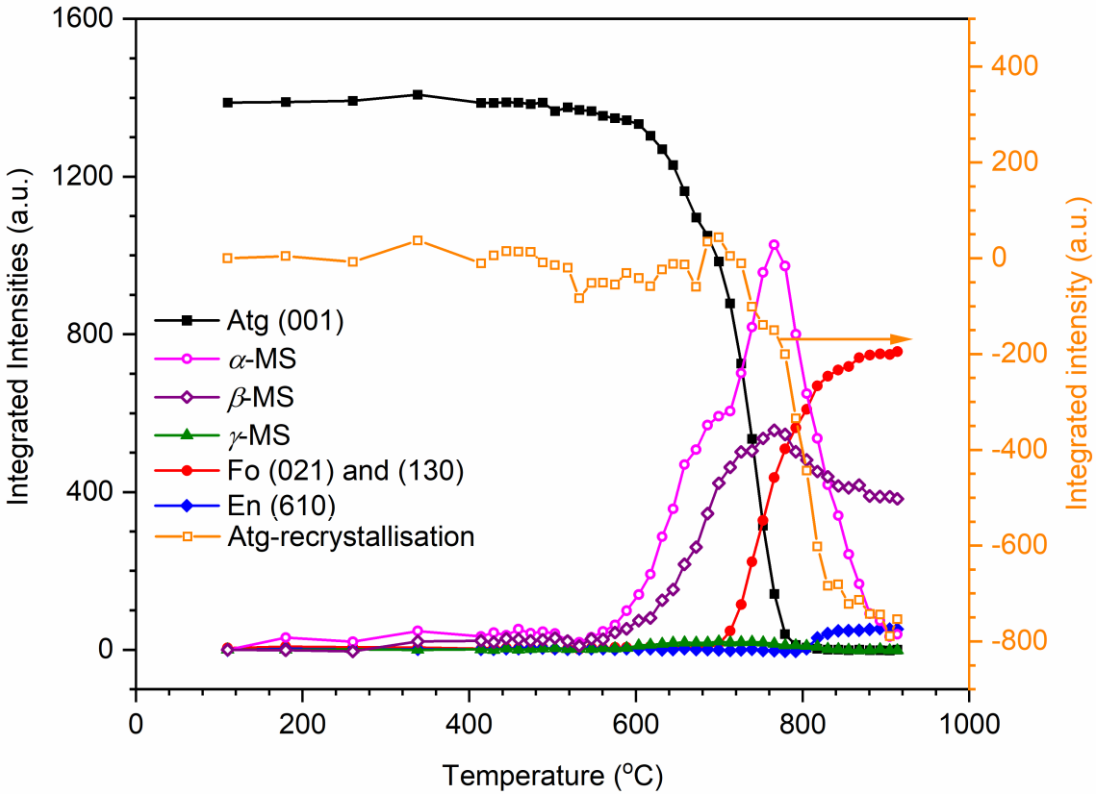

Figure S3.3. Evolution of Integrated peak intensities with temperature for selected non-overlapping (*hkl*) reflections of different phases during thermal dehydroxylation of antigorite using *in-situ* synchrotron PXRD at 8 °C min^{-1}. Phases are labelled as Atg: antigorite, En: enstatite, Fo: forsterite, *α*-MS: *α* metaserpentine, *β*-MS: *β*-metaserpentine, and *γ*-MS: *γ*-metaserpentine. Solid and open symbols show the crystalline and amorphous phases, respectively.

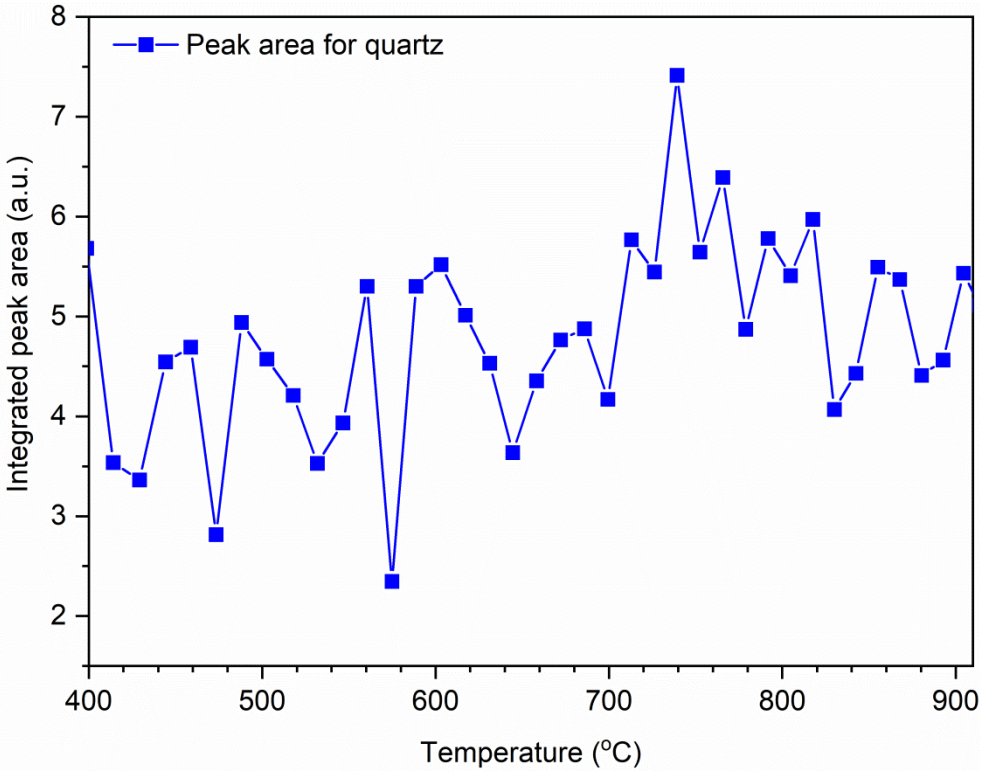

Figure S3.4. Integrated peak intensity for quartz (Qtz), (101) reflections during *in-situ* synchrotron PXRD analysis for antigorite dehydroxylation.

Section 3: Thermogravimetry and differential scanning analyses

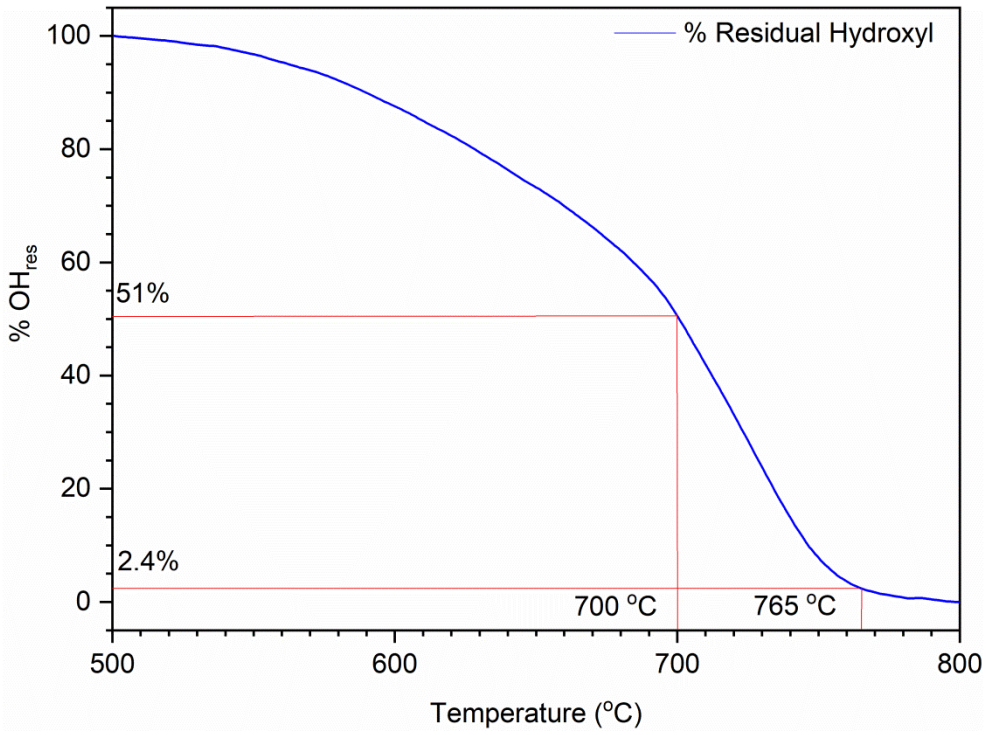

Figure S3.5. Percentage residual hydroxyl (% OH_{res}) for the dehydroxylation of antigorite based on TGA data in the temperature range of 500 – 800 °C.

Table S3.1.

Summary of mass loss percentage, peak temperatures in DTG and DSC during dehydroxylation of antigorite at 10 °C min^{-1}.

TGA		DTG	DSC	
***T* range (°C)**	**Mass Loss %**	**Peak *T*** (°C)	**Heat Direction**	**Peak *T*** (°C)
0-558	1.2	611 (w)	Endo	611 (sh)
558-725	7.1	653 (w)	Endo	660 (sh)
725-816	3.8	713 (s)	Endo	697(s)
Sum at 816	12.1	731 (s)	Endo	732 (vs)
Total losses at 985	12.3	--	Exo	827 (s)

Note: w = weak, s = strong, vs = very strong, sh = shoulder, endo = endothermic peak, exo = exothermic peak.

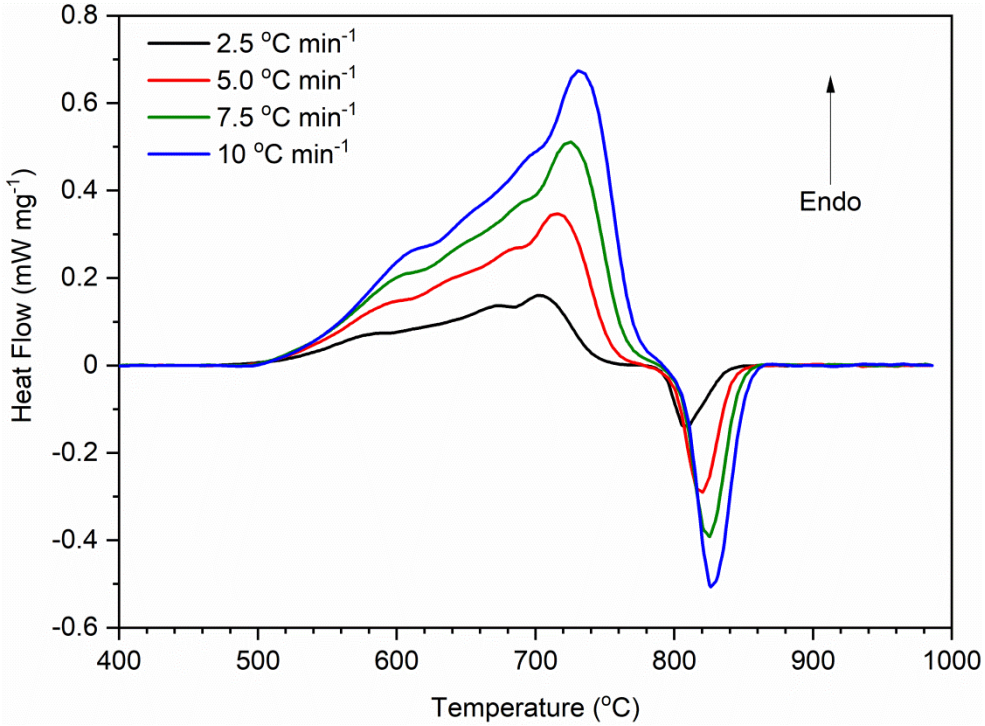

Figure S3.6. Baseline-subtracted heat flow (DSC) traces for the temperature ramps of 2.5, 5, 7.5 and 10 °C min^{-1} for the extent of conversion measurements for isoconversional kinetic analysis of thermal dehydroxylation of antigorite.

Section 4: Sample characterisation

Peak identification for the starting sample at 100 ℃ is shown in Figure S3.1.

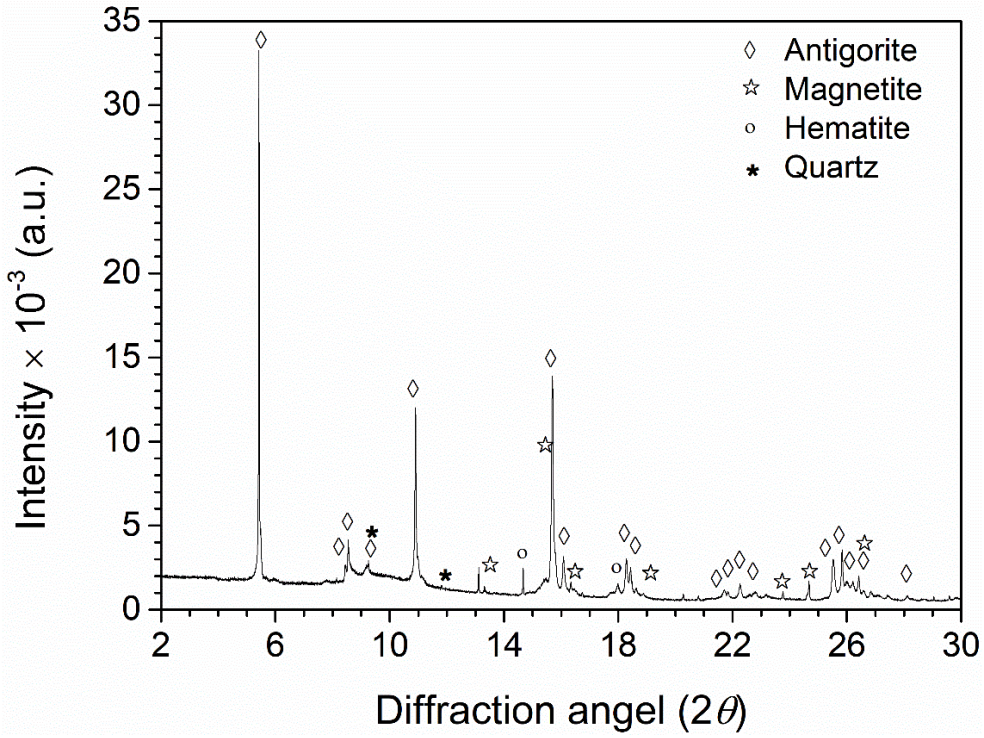

Figure S3.7. Synchrotron PXRD pattern for the demagnetised antigorite sample at 100 °C. Intensity represented in arbitrary units (a.u.)

Section 5: Calculations for isoconversional kinetic analysis

Temperature vs extent of conversion profiles for isoconversional kinetics

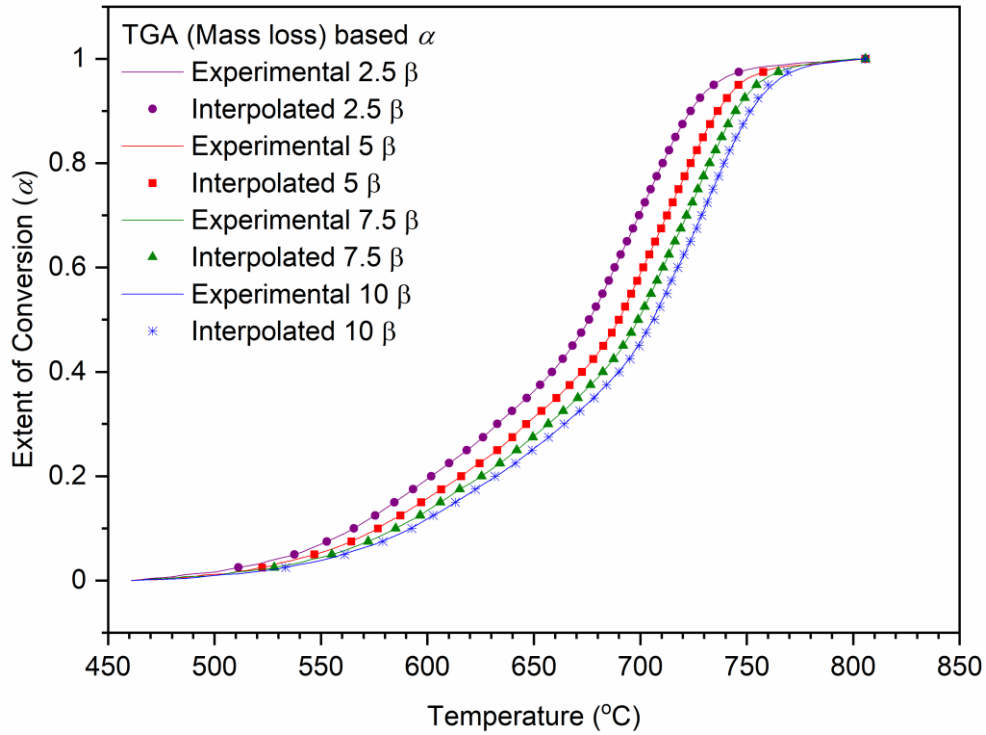

Figure S3.8 Experimental and Interpolated temperatures at a specific extent of conversion for TGA results using numerical linear interpolation at 2.5, 5, 7.5 and 10 ℃ min^{-1}.

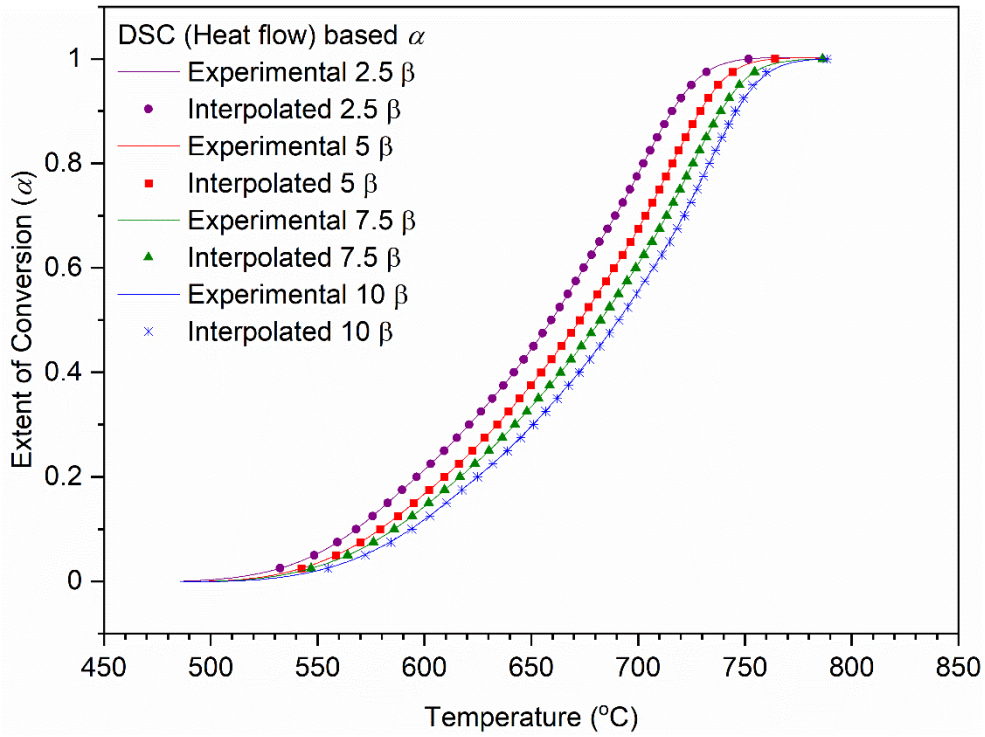

Figure S3.9. Experimental and Interpolated temperatures at a specific extent of conversion for DSC results using numerical linear interpolation at 2.5, 5, 7.5 and 10 °C min^{-1}.

Isoconversional pre-exponential factor

Calculation of the isoconversional pre-exponential factor is based on the compensation effect which is based on the following equation.

$$\ln A_i = \frac{E_i}{RT} + \ln\left(\frac{(\frac{d\alpha}{dt})}{f(\alpha)}\right)_i \qquad \text{S3.1}$$

The compensation effect requires the estimation of several kinetic triples (E_i, $f(\alpha)/g(\alpha)$ and A_i) over a wide range of reaction models $f(\alpha)$ shown in Table S3.2 which can be achieved by applying the integral form of Coats-Redfern to equation S3.1.

$$\ln\left(\frac{g_i(\alpha)}{T_\alpha^2}\right) = ln\left(\frac{A_i R}{\beta E_i}\right) - \frac{E_i}{RT_\alpha} \qquad \text{S3.2}$$

E_i and $\ln A_i$ pair for all reaction models were calculated from the slope and intercepts of the straight-line plots between $\ln(\beta g(\alpha)/T^2)$ and $1/T$ for all the models mentioned in Table S3.2.

Table S3.2.

List of solid-state reaction models and integral forms of these models

No.	Reaction models	Symbol	$f(\alpha)$	$g(\alpha)$
1	Power law	P1	$4\,\alpha^{3/4}$	$\alpha^{¼}$
2	Power law	P2	$3\,\alpha^{2/3}$	$\alpha^{1/3}$
3	Power law	P3	$2\,\alpha^{1/2}$	$A^{1/2}$
4	Power law	P4	$2/3\,\alpha^{-1/2}$	$\alpha^{3/2}$
5	One-dimensional diffusion	D1	$1/2\,\alpha^{-1}$	α^{2}
6	Mampel (1st order)	F1	$1-\alpha$	$-\ln(1-\alpha)$
7	Avrami–Erofeev	A4	$4(1-\alpha)[-\ln(1-\alpha)]^{3/4}$	$[-\ln(1-\alpha)]^{1/4}$
8	Avrami–Erofeev	A3	$3(1-\alpha)[-\ln(1-\alpha)]^{2/3}$	$[-\ln(1-\alpha)]^{1/3}$
9	Avrami–Erofeev	A2	$2(1-\alpha)[-\ln(1-\alpha)]^{1/2}$	$[-\ln(1-\alpha)]^{1/2}$
10	Three-dimensional diffusion	D3	$3/2(1-\alpha)^{2/3}[1-(1-\alpha)1/3]^{-1}$	$[1-(1-\alpha)^{1/3}]^2$
11	Contracting sphere	R3	$3(1-\alpha)^{2/3}$	$1-(1-\alpha)^{1/3}$
12	Contracting cylinder	R2	$2(1-\alpha)^{1/2}$	$1-(1-\alpha)^{1/2}$
13	Two-dimensional diffusion	D2	$[-\ln(1-\alpha)]^{-1}$	$(1-\alpha)\ln(1-\alpha)+\alpha$
14	Second order	F2	$(1-\alpha)^2$	$(1-\alpha)^{-1}-1$

However, models P4, A4, A3 appreciably deviate from linearity (Figure S3.11. and S3.12.). Consequently, these are excluded from the estimation of "*a*" and "*b*" values. The linear fit for the 5 °C min^{-1} heating rate is shown in Figures S3.10. and S3.11., for $0.2 < \alpha < 0.8$ range while 2.5, 7.5 and 10 °C min^{-1} runs show similar results (shown in Table S3.3.). Finally, the graphs between E and ln$A$ for all the reaction models giving $r^2 > 0.99$ are selected for the estimation of the coefficients "*a*" and "*b*" using equation S3.3. The results are given in Figure S3.12.

$$ln\,A_i = a + bE_i \qquad \text{S3.3}$$

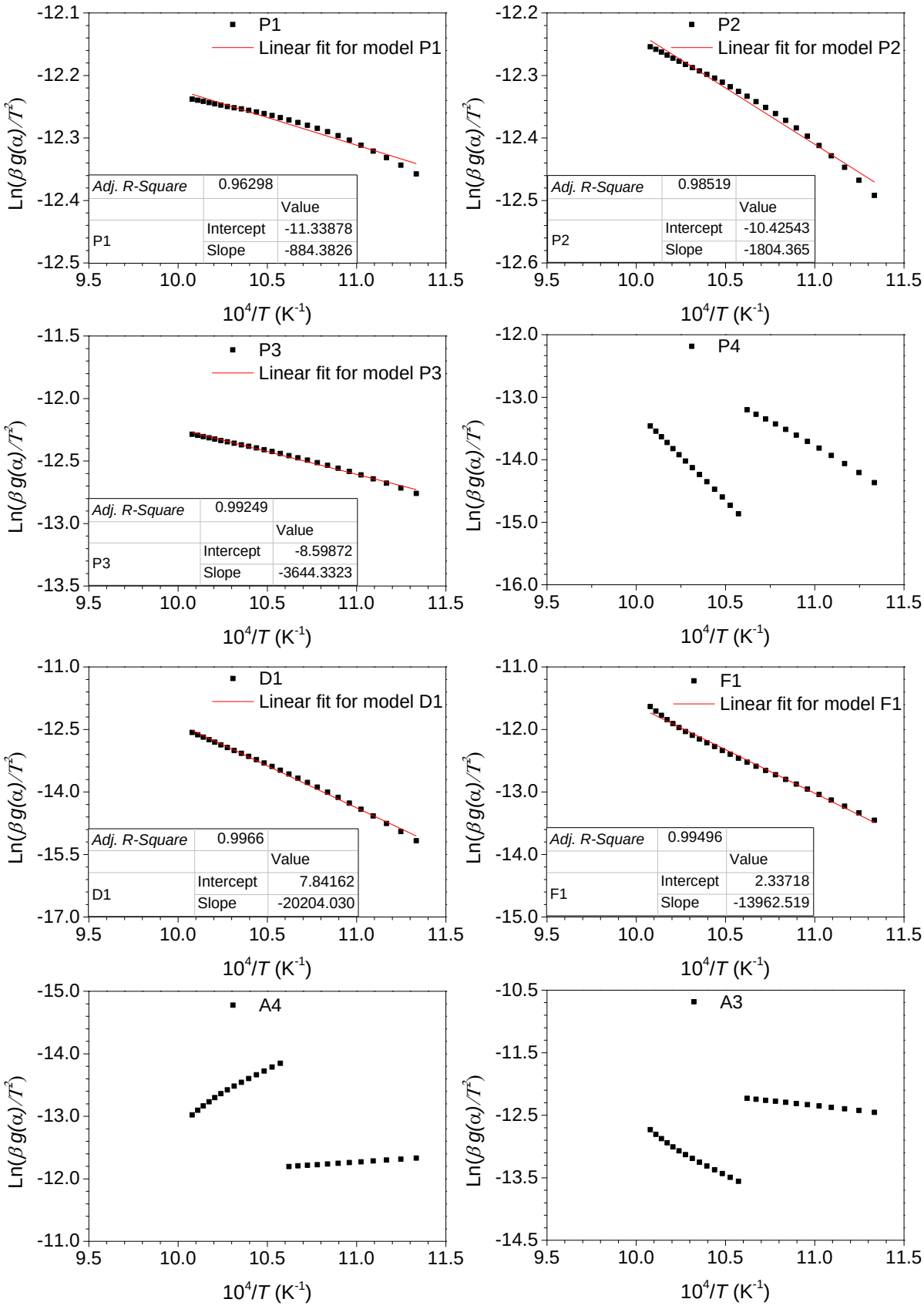

Figure S3.10. Model fitting for 1-8 solid state reaction models (Table S1-1) using 5 °C min^{-1} in $0.2 < \alpha < 0.8$.

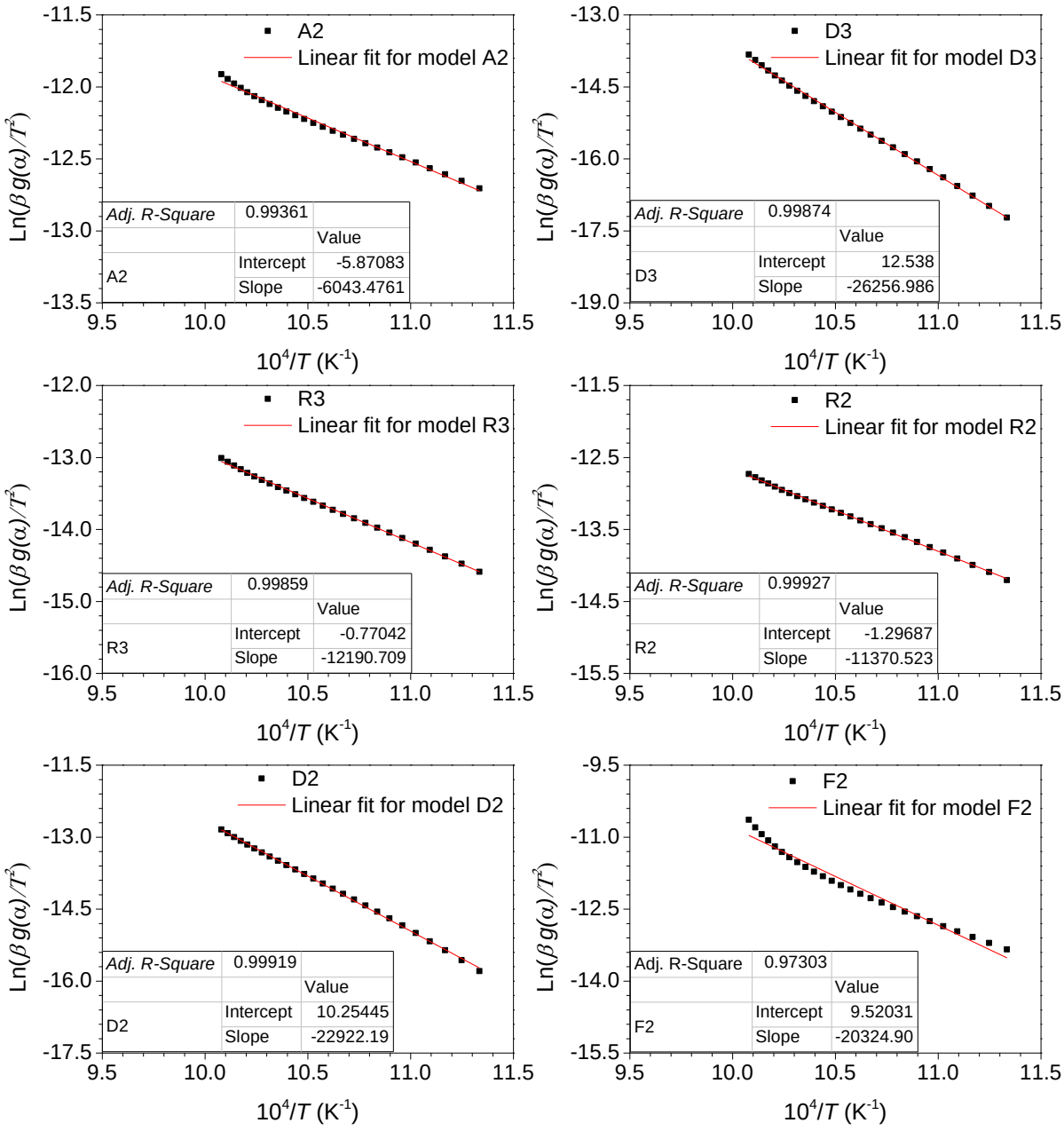

Figure S3.11. Model fitting for 8-14 solid state reaction models (Table S1-1) using 5 °C min^{-1} in $0.2 < \alpha < 0.8$.

Table S3.3

E and Ln*A* values for different reaction models at 10, 7.5. 5 and 2.5 °C min^{-1}.

Reaction	**10 °C min^{-1}**			**7.5 °C min^{-1}**			**5 °C min^{-1}**			**2.5 °C min^{-1}**		
Model	***E* (kJ mol^{-1})**	**Ln*A***	**R^2**	***E* (kJ mol^{-1})**	**Ln*A***	**R^2**	***E* (kJ mol^{-1})**	**Ln*A***	**R^2**	***E* (kJ mol^{-1})**	**Ln*A***	**R^2**
P1	0.0076	-10.7566	0.9789	7.2244	-4.2107	0.9721	7.4641	-4.5241	0.9652	7.3314	-5.2100	0.9679
P2	15.4291	-2.2248	0.9917	14.8696	-2.5849	0.9892	15.1415	-2.8998	0.9859	14.8895	-3.5855	0.9871
P3	31.0678	0.3087	0.9959	30.1607	-0.0708	0.9947	30.4958	-0.3656	0.9928	30.0061	-1.0531	0.9935
D1	171.8171	18.5216	0.9982	167.7765	17.9093	0.9977	168.6827	17.8521	0.9967	166.0555	17.1435	0.9971
F1	116.6039	12.3293	0.9943	113.8685	11.8198	0.9952	114.6667	11.6841	0.9965	112.8709	10.9833	0.9968
A2	50.3787	3.3907	0.9928	49.0767	2.9864	0.9938	49.5506	2.7312	0.9956	48.7633	2.0406	0.9960
D3	220.7118	23.1647	0.9983	215.6735	22.4816	0.9986	216.9200	22.5274	0.9992	213.5368	21.8106	0.9994
R3	102.4368	9.6392	0.9981	99.9758	8.7092	0.9985	100.6742	8.5430	0.9991	99.0946	7.8444	0.9994
R2	95.8438	10.0536	0.9991	93.5242	8.1711	0.9993	94.1727	7.9907	0.9994	92.6928	7.2932	0.9998
D2	193.9241	20.9383	0.9995	189.4260	20.2928	0.9994	190.4821	20.2824	0.9992	187.5056	19.5691	0.9995
F2	167.0033	19.4248	0.9745	163.2537	18.8448	0.9763	164.4509	18.8208	0.9794	161.8819	18.1128	0.9797

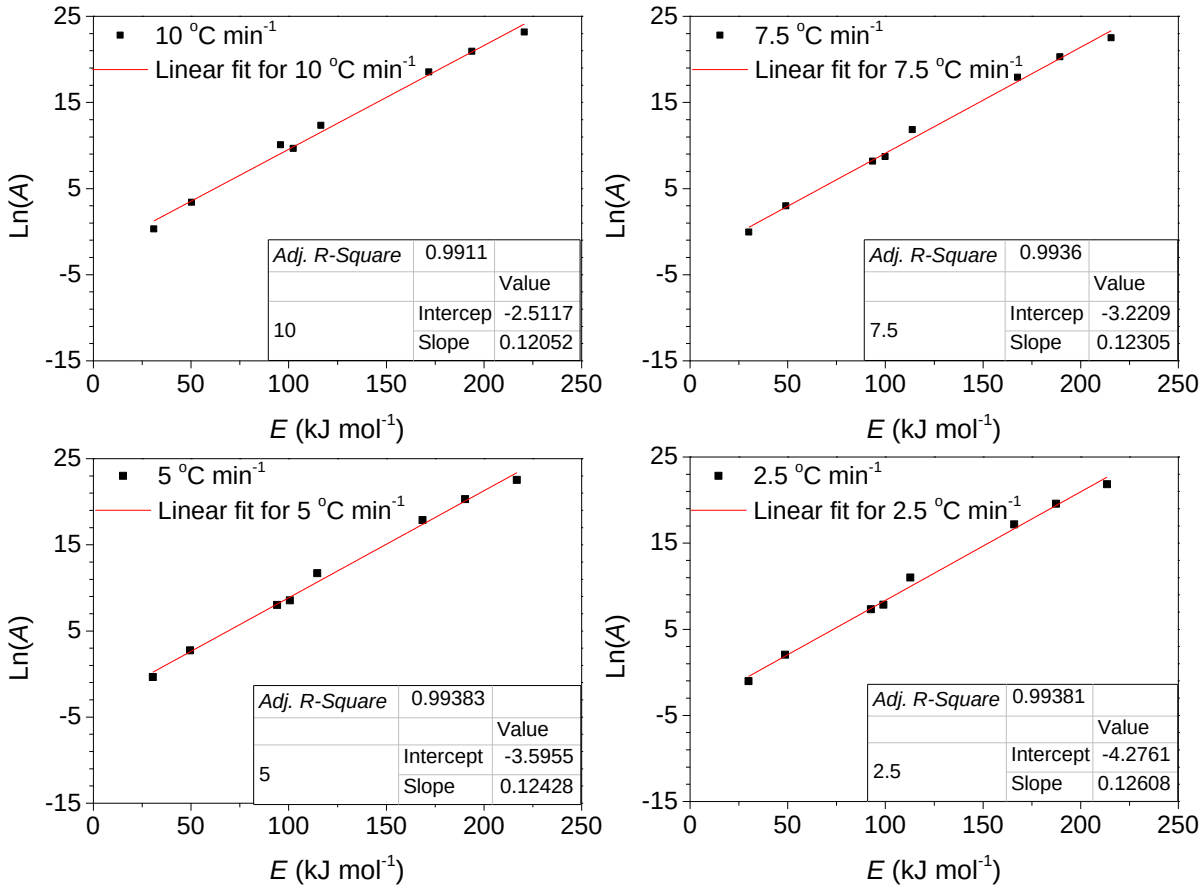

Figure S3.12. Graph between E and Ln(A) pair for solid-state reaction models (Table S1-1) having R^2> 0.99 (excluding P1, P2, P4, A4 A3, and F1).

Section 6: Reaction scheme

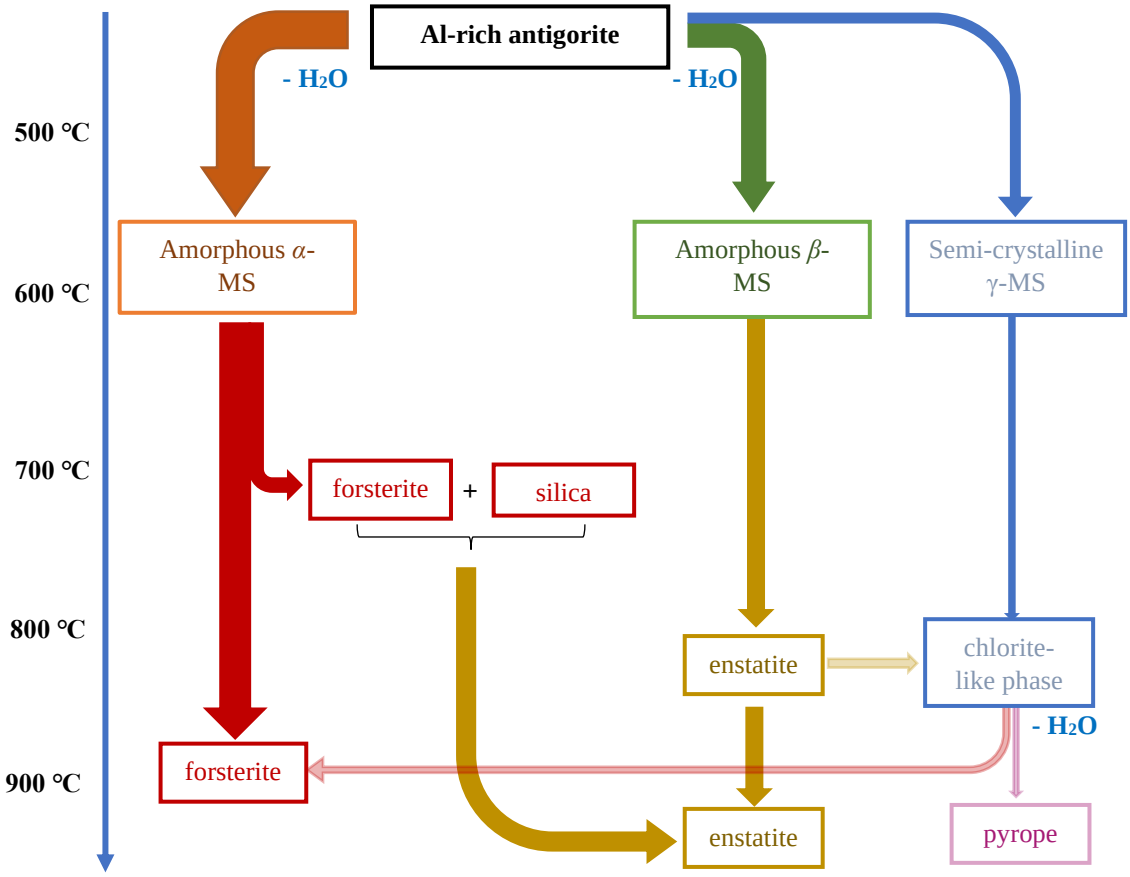

Figure S3.13. Schematic of proposed reaction pathways for thermal decomposition of Al-rich antigorite. *α*-MS, *β*-MS and *γ*-MS represents the *α*, *β* and *γ* metaserpentine compenents formed during dehdyroxylation.

Appendix B: Supplementary Information for Chapter 4

Section 1: particle size distribution

Section 2: TGA-DSC analysis reproducibility

Section 3: Partial integration for energy calculation at various % residual hydroxyl (%OHres)

Section 4: Comparison of phase formation in serpentine polymorphs

Section 5: *In-situ* PXRD analysis for the effect of partial pressure of water vapours and grain size on dehydroxylation

Section 1: Particle size distribution

Figure S4.1 and Table S4.1 illustrate the detailed particle size distribution of the antigorite and lizardite samples with sieve fractions 45-75 µm and <45 µm.

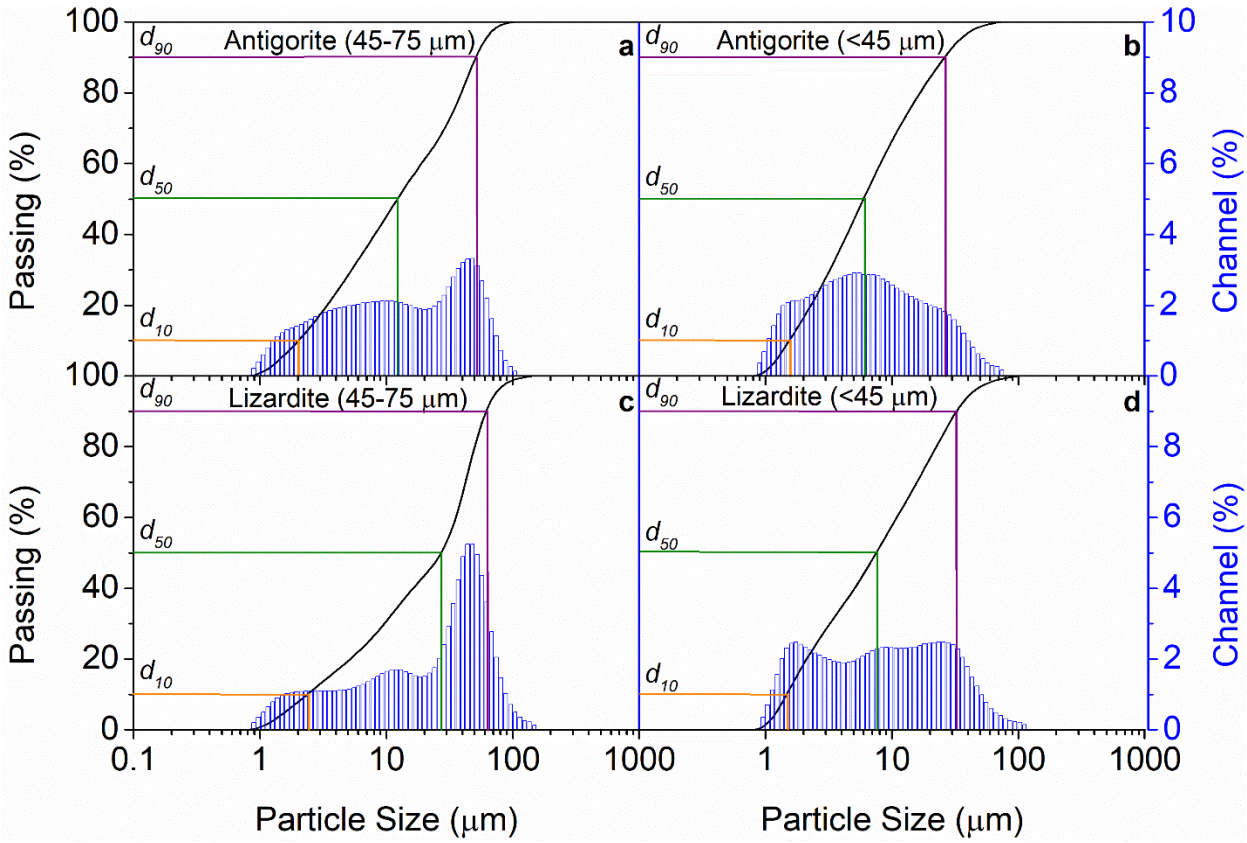

Figure S4.1. The volumetric particle size distribution of antigorite with sieve fraction **a)** 45-75 µm and **b)** < 45 µm and lizardite sample with sieve fraction **c)** 45-75 µm and **d)** < 45 µm

Section 2: TGA-DSC analysis reproducibility

Figure S4.2. shows the repeated runs for the dehydroxylation of lizardite, and Table S4.2. reports the corresponding peak temperature for DTG and DSC traces and % mass loss.

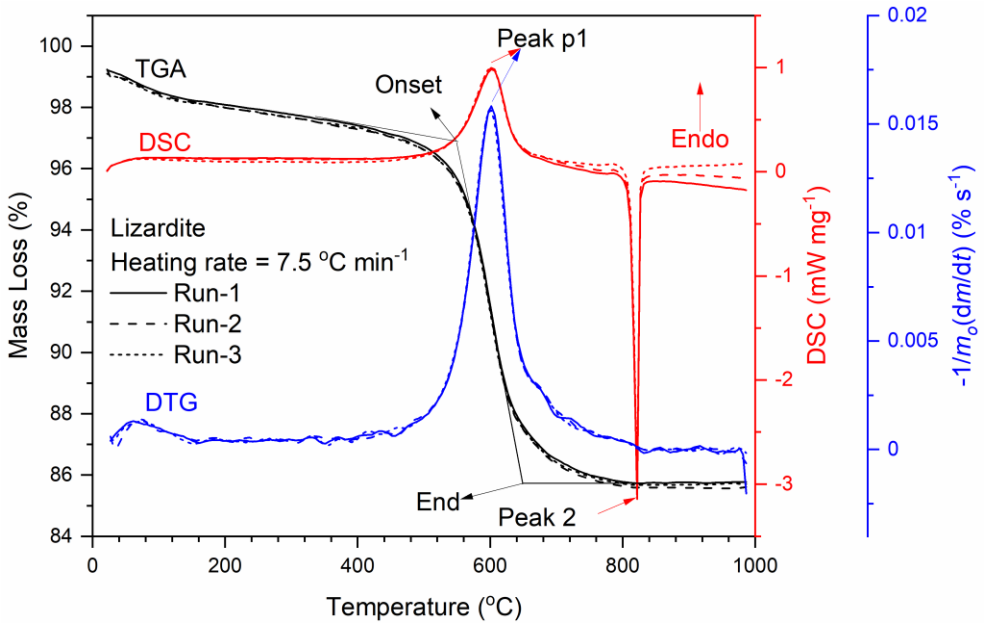

Figure S4.2. Repeated runs for the TGA, DSC, and DTG traces showing the reproducibility of results.

Table S4.1.

Peak temperatures for DTG and DSC curves along with mass loss during the two repeated dehydroxylation runs of lizardite sample

	DTG	**Mass loss (%)**			**DSC**			
	Peak temperature (°C)	Onset	End	$\Delta m_{105\text{-}850}$	Peak temperature (°C)		Peak area (J g^{-1})	
	T_{p1} (°C)	T (°C)	T (°C)	%	T_{p1} (Endo)	T_{p2} (Exo)	Endo	Exo
Run-1	601.2	561	640.2	12.74	602.8	820.8	592.8	206.3
Run-2	601.2	560.6	639.7	12.84	603.4	820.6	594.8	208.3
Run-3	599.8	560.3	639.1	12.69	601.5	820.8	542.6	212.1
Average	600.7	560.6	639.7	12.76	602.6	820.7	576.7	208.9
STDEV	0.81	0.35	0.55	0.08	0.97	0.12	29.6	2.95

Section 3: Partial integration for energy calculation at various % residual hydroxyl (%OHres)

Energy to produce the same amount of amorphous phase for both serpentine minerals were calculated by the following steps

1. The percentage conversion of serpentine was estimated from the synchrotron PXRD data at maximum amorphous content, and before the onset of forsterite formation
2. The termination temperature/time was determined by matching the percentage conversion from PXRD to residual hydroxyl from the TGA data.
3. The partial area under the heat flow curve was determined using the termination time, as in Figure S4.3 which gives the energy requirement per unit mass of the sample.

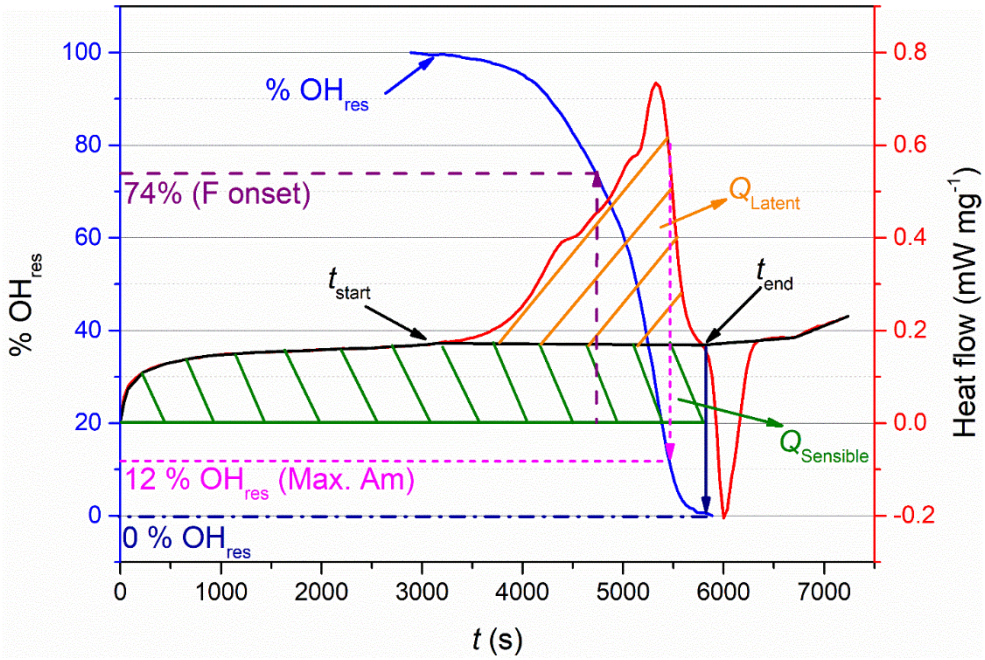

Figure S4.3. Schematic for the heat calculations through partial integration of the heat flow curves for serpentine minerals. This particular sample is the antigorite used in the current study at a heating rate of 8 °C min^{-1} in the temperature range of 25 - 1000 °C.

4. Finally, the amount of the sample to produce the same amount of amorphous content was computed using balanced stoichiometric equation.4.1. As, according to equation 4.1, all the serpentine mineral dehydroxylates to the amorphous content before forsterite formation, therefore the percentage conversions from synchrotron PXRD data before the forsterite formation was used to find the theoretical amount of dehydroxylated antigorite and lizardite samples. The ratio of Atg/Liz to produce the same amorphous content is the same as the stoichiometrically calculated ratio of $(Am)_{Liz,\ calc}/(Am)_{Atg,\ calc}$ amorphous content in lizardite to antigorite. This ratio factor is then used to roughly estimate the energy requirement for antigorite relative to lizardite to produce same amorphous content.
5. However, in antigorite, the amorphous phase also starts to convert to forsterite before the theoretical estimate of amorphous content was made at the temperature of highest amorphous content point for the antigorite by back calculating the unconverted amorphous phase using PXRD-based normalised forsterite conversion (% reaction progress for forsterite) in equation 4.2. due to the difficulty in finding the conversion of amorphous content to forsterite. Since the ratios of amorphous phase production in synchrotron PXRD closely relates to the theoretical values, we used the ratio of amorphous production of lizardite to antigorite as observed in synchrotron PXRD at the high amorphous content point to compare the energy requirements for serpentine samples.

Section 4: Comparison of phase formation in serpentine polymorphs

The overlay synchrotron PXRD plots in Figure S4.4 for the selected patterns at the same dehydroxylation event shows the comparison of antigorite and lizardite sample before dehydroxylation, at maximum amorphous content and after dehydroxylation.

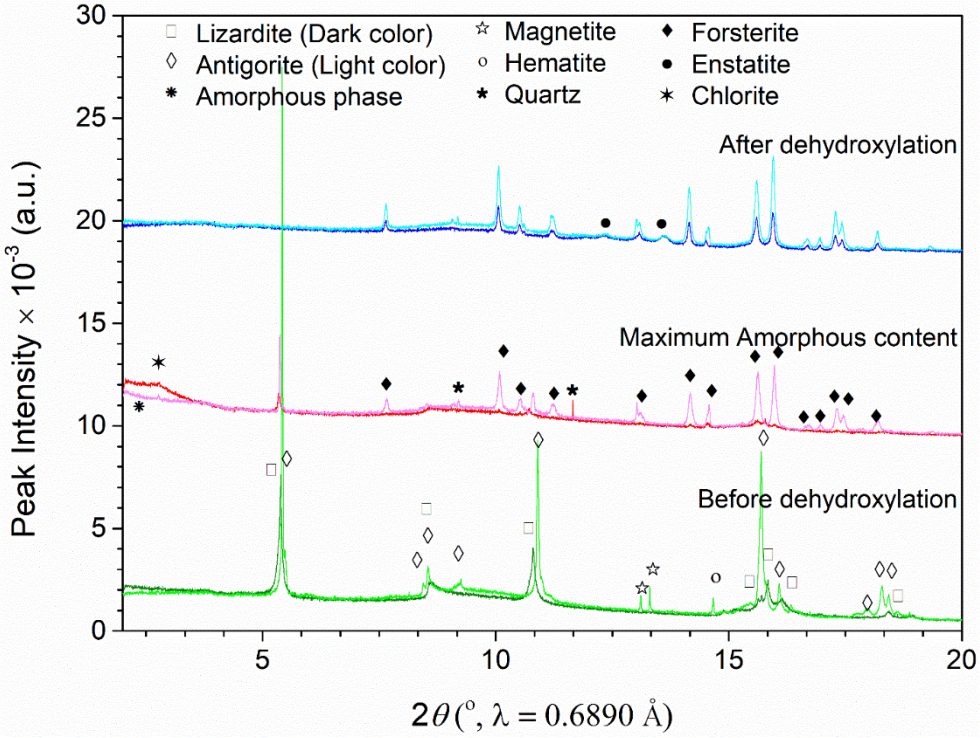

Figure S4.4. Overlaying synchrotron PXRD plots for the comparison of same dehydroxylation points in serpentine polymorphs (*i.e.*, antigorite and lizardite)

Section 5: *In-situ* PXRD analysis for the effect of the partial pressure of water vapours and grain size on dehydroxylation

Table S4.2

Onset temperatures for the evolution of different phases during the dehydroxylation of antigorite and lizardite samples for two different grain sizes under dry or wet conditions using synchrotron PXRD analysis in the temperature range of 100 - 917 °C

Events	$T_{(45\text{-}75,dry)}$* (°C)	$T(Atg_{<45,dry})$* (°C)	$T(Atg_{<45,wet})$* (°C)	$T(Atg_{45\text{-}75}) - T(Atg_{<45})$ (°C)	$T(Atg_{<45,wet}) - T(Atg_{<45,dry})$ (°C)	$T(Liz_{45\text{-}75,dry})$* (°C)	$T(Liz_{<45,dry})$* (°C)	$T(Liz_{<45,wet})$* (°C)	$T(Liz_{45\text{-}75}) - T(Liz_{<45})$ (°C)	$T(Liz_{<45,wet}) - T(Liz_{<45,dry})$ (°C)
Onset of Chl form.	614	592	612	**22**	**20**	640	609	747	**31**	**138**
Onset of Atg/Liz decomp.	662	641	647	**21**	**6**	612	581	708	**31**	**127**
Onset of Fo form.	723	703	695	**20**	**-8**	694	678	800	**16**	**122**
End of Atg/Liz decomp.	808	789	781	**19**	**-8**	767	752	n.d.	**15**	**n.d.**
Onset of En form.	821	801	813	**19**	**12**	819	797	n.d.	**22**	**n.d.**
End of Chl decomp.	840	833	857	**7**	**24**	819	816	n.d.	**3**	**n.d.**

n.d. = not detected in the temperature range used in synchrotron PXRD experiments

*Abbreviation refers to temperature observed for serpentine polymorph and grain size and dry or wet conditions, *e.g.* $A_{45\text{-}75,dry}$ = antigorite, 45 to 75 µm fraction under dry purge gas conditions.

Appendix C: Supplementary Information for Chapter 5

Section 1: Temperature calibration synchrotron PXRD

Section 2: Non-isothermal TGA-DSC data for isoconversional kinetic analysis

Section 1: Temperature calibration synchrotron PXRD

Figure S5.1 shows the temperature calibration curves for heating rates (β) of 2, 4 and 8 °C min $^{-1}$. Observed room temperature (25 °C), α to β-quartz transition (535.1 °C) and NaCl melting point (772 °C) at 8 °C min $^{-1}$ were used to establish the relationship between set temperature and sample temperature. The resulting 2nd order polynomial function was fitted to match the quartz transition temperatures (575.4 °C) and 549.9 °C measured at heating rates of 2 and 4 °C min $^{-1}$, respectively.

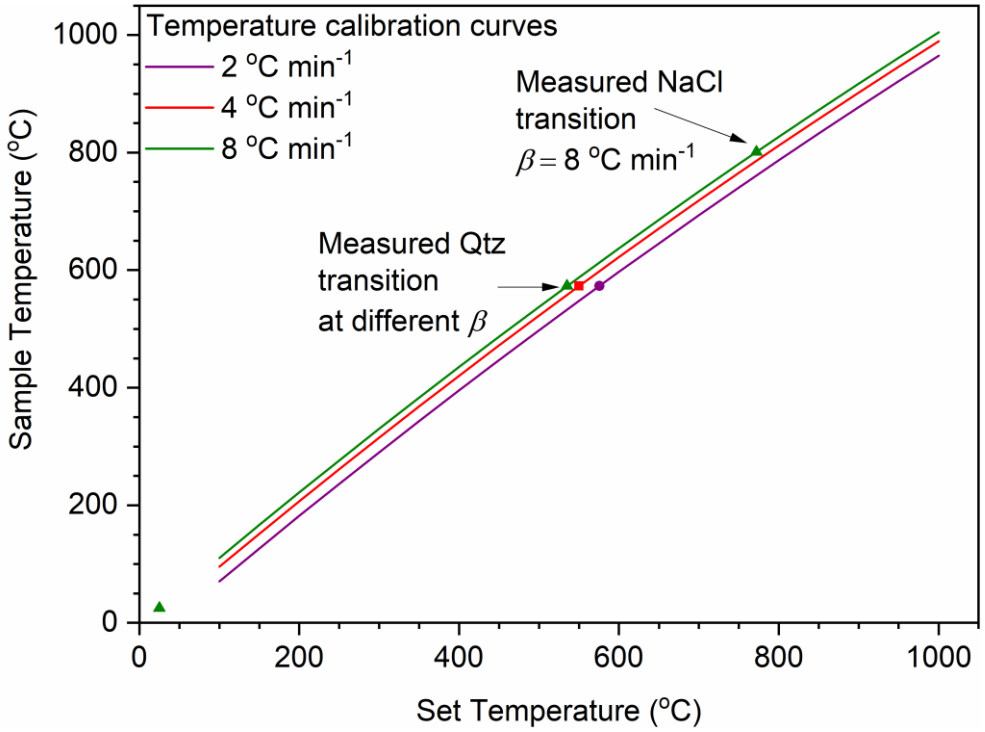

Figure S5.1 Temperature calibration curves for *in-situ* synchrotron PXRD at β = 2, 4 and 8 °C min^{-1}.

Section 2: Non isothermal TGA-DSC data for isoconversional kinetic analysis

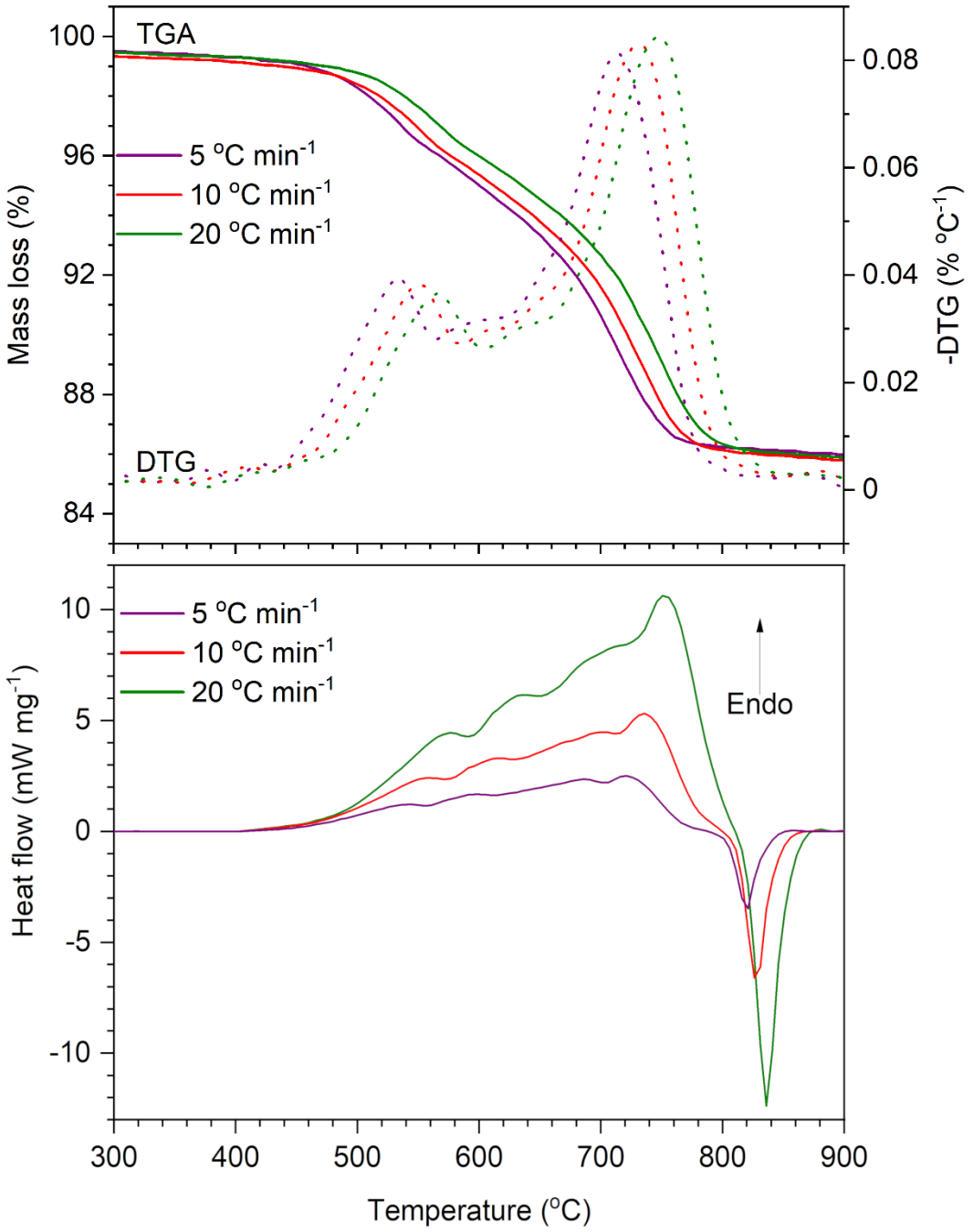

Figure S5.2 Non-isothermal record of simultaneous TGA/DTG-DSC at 5, 10 and 20 °C min^{-1} during the thermal dehydroxylation of antigorite.